# Temporal and genetical constraints of the Cu-Co Vena-Dampetorp deposit, Bergslagen, Sweden

*Dino Leopardi*

**Dissertations in Geology at Lund University,**
**Master's thesis, no 582**
**(45 hp/ECTS credits)**

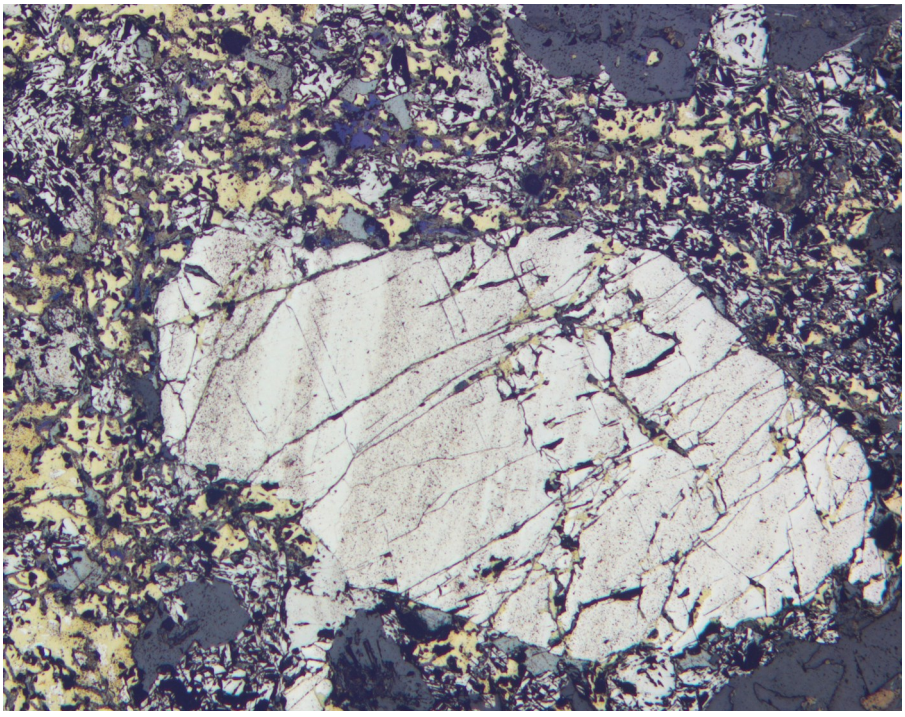

**Department of Geology**
**Lund University**
**2020**

# Temporal and genetical constraints of the Cu-Co Vena-Dampetorp deposit, Bergslagen, Sweden

Master's thesis

Dino Leopardi

Department of Geology
Lund University
2020

# Contents



**Cover Picture:** Photomicrograph in polarized reflected light of a fractured cobaltite crystal surrounded by subhedral carrolite and interstitial chalcopyrite as part of a sulphide vein. Photo: Dino Leopardi.

# Contents, continuation

# Contents, continuation

# Temporal and genetical constraints of the Cu-Co Vena-Dampetorp deposit, Bergslagen, Sweden

DINO LEOPARDI

Leopardi, D., 2020: Temporal and genetical constraints of the Cu-Co Vena-Dampetorp deposit, Bergslagen, Sweden . *Dissertations in Geology at Lund University*, No. 582, 111 pp. 45 hp (45 ECTS credits) .

**Abstract:** The Bergslagen Province is known for containing major Zn-Pb-Ag and Zn-Pb-Cu-Ag sulphide mineralizations with associated iron-oxide skarns and a lot of research have focused on understanding them. However, Cu-Co deposits like the Vena-Dampetorp deposit have received less attention. The Vena-Dampetorp deposit is a disseminated and vein Cu-Co mineralization hosted primarily in a 1.89 Ga rhyolitic to dacitic volcanoclastic sequence with thin interbedded calcareous horizons and associated mafic and granodioritic intrusions. Two stages of deformation and regional high-temperature and low-pressure metamorphism affected this shallow subaqueous back-arc assemblage. The aim of this study is to constrain the spatial, temporal and genetical relationships of ore minerals and the effects of metamorphism on the host rocks and their assemblages. Building on existing work, it aims to explore the origin and processes responsible for the concentration of Co and genesis of Cu-Co deposits in the Bergslagen area.

Textural relationships and geochemical data of drill cores show that the mineralization is zoned from pyrite-pyrrhotite zones to chalcopyrite-sphalerite richer zones, with localized Cu-Co areas. At the deposit scale, Co rich zones occur in the SE while Pb-Sb enriched zones concentrate in the NW. The U-Pb dating of metamorphic titanite with LA-ICP-MS gave a mean concordant $^{207}Pb/^{206}Pb$ date of 1882±16 Ma for a skarn sample. This age is interpreted as the onset of regional metamorphism. In contrast, the lower intercept age of 1882±16 Ma obtained for titanite in one metavolcanic sample could either represent the onset of metamorphism or a cooling age. Sulphide thermobarometric estimates, EDS-SEM mapping, and the presence of sulphosalt-rich associations together with deformational features in the ore minerals, indicate that the Fe-oxide mineralization at the Vena-Dampetorp deposit occurred as a Bastnäs-type deposit due to the interaction of magmatic fluid with carbonate horizons. In comparison, the sulphide Cu-Co-rich mineralization was deposited in a sub-seafloor hydrothermal exhalative system, where the higher Cu-Co concentrations are related to high temperature stringers near the feeder zone. Later mechanical, hydrothermal and melt-assisted re-mobilization during metamorphism concentrated certain metals like Co in secondary veins and assemblages.

**Keywords:** Bergslagen, Vena, Dampetorp, Cu-Co, sulphide melting, Bastnäs-type, cobaltite, arsenopyrite, titanite dating, sulphide mineralization, sulphide re-mobilisation.

**Supervisor(s):** Charlotte Möller (LU), Alex Lewerentz (SGU)

**Subject:** Bedrock Geology

*Dino Leopardi, Department of Geology, Lund University, Sölvegatan 12, SE-223 62 Lund, Sweden. E-mail: d.leopardin@gmail.com*

# Tidsmässiga och genetiska begränsningar av Cu-Co-förekomsten i Vena-Dampetorpförekomst, Bergslagen, Sverige

DINO LEOPARDI

Leopardi, D., 2020: Tidsmässiga och genetiska begränsningar av Cu-Co-förekomsten i Vena-Dampetorpförekomst, Bergslagen, Sverige. *Examensarbeten i geologi vid Lunds universitet*, Nr. 582, 111 sid. 45 hp.

**Sammanfattning:** Bergslagens malmprovins är känd för att innehålla stora Zn-Pb-Ag- och Zn-Pb-Cu-Ag-sulfidförekomster med tillhörande järnoxidskarn och många studier har fokuserat på att förstå dessa förekomster. Cu-Co-förekomster som Vena-Dampetorp-förekomsten har emellertid fått mindre uppmärksamhet. Vena-Dampetorp-förekomsten är en disseminerad och åderstödd Cu-Co-mineralisering som förekommer i en 1,89 Ga ryolitisk till dacitisk vulkaniklastisk sekvens med tunna inbäddade kalkhaltiga horisonter och tillhörande mafiska och granodioritiska intrusioner. Två deformationsstadier med regional högtemperatur- och lågtrycksmetamorfos har påverkat denna sekvens som avsattes i grund, subakvatisk miljö i en sedimentär bassäng i en öbågemiljö. Syftet med denna studie är att begränsa de rumsliga, temporala och genetiska förhållandena mellan malmmineral och effekterna av metamorfos på värdbergarterna och deras sammansättningar. Utifrån befintligt Målet är att utifrån befintlig forskning utforska ursprung och processer som givit upphov till koncentrationen av Co och uppkomsten av Cu-Co-avlagringar i Bergslagen.

Texturella förhållanden och geokemiska data från borrkärnor visar att mineraliseringen är zonerad från pyrit-magnetkiszoner till kopparkis-zinkblände-rikare zoner, med lokala Cu-Co-områden. På avlagringskala förekommer Co-rika zoner i SO medan Pb-Sb-anrikade zoner koncentreras i NV. U-Pb-datering av metamorf titanit med LA-ICP-MS gav ett $^{207}Pb$ / $^{206}Pb$ medelvärde datum av1882 ± 16 Ma för ett skarnprov. Denna ålder tolkas som början av den regionala metamorfosen. Däremot kan den lägre avlyssningsåldern 1882 ± 16 Ma erhållen för titanit i ett metavulkaniskt prov antingen representera början av metamorfosen eller en kylningsålder. Sulfidtermobarometriska uppskattningar, EDS-SEM-kartläggning och närvaron av sulfosalt rika föreningar tillsammans med deformationstexturer i malmmineralen indikerar att Fe-oxidmineraliseringen vid Vena-Dampetorp bildades som en Bastnäsavlagring på grund av interaktionen mellan magmatiska/hydrotermala vätskor och karbonathorisonter. Som jämförelse avsattes den sulfidiska Cu-Co-rika mineraliseringen i ett hydrotermalt system på havsbotten, där de högre Cu-Co-koncentrationerna är relaterade till högtemperaturströngar nära matarzonen. Senare mekanisk, hydrotermal och smältmedierad återmobilisering under metamorfos koncentrerade vissa metaller som Co i sekundära ådror och parageneser.

**Nyckelord:** Bergslagen, Vena, Dampetorp, Cu-Co, sulfidsmältning, Bastnäs-typ, kobaltit, arsenopyrit, titanit-datering, sulfidmineralisering, sulfid-remobilisering.

**Handledare**: Charlotte Möller (LU), Alex Lewerentz (SGU)

**Ämnesinriktning**: Berggrundsgeologi

*Dino Leopardi, Department of Geology, Lund University, Sölvegatan 12, SE-223 62 Lund, Sweden. E-mail: d.leopardin@gmail.com*

# 1 Introduction

The Vena mining field is located roughly 2 km NE of Åmmeberg in the prolific Bergslagen Province (Figure 1). It consists of over one hundred individual mines, aligned in a NW-SE direction, where historically Cu and Co were mined between the 18th and the late 19th centuries (Tegengren et al. 1924). Similarly, the Dampetorp mining field, located approximately 4.5 km NW of the Vena mining field on the opposite side of lake Åmmelången, consists of several smaller abandoned mines from which presumably copper and maybe cobalt was extracted. Both areas have a stratiform mineralization hosted mainly in Paleoproterozoic metavolcanics with amphibolite intercalations, and later granodioritic and granitic intrusions (Tegengren et al. 1924; Wikström & Karis 1991; Persson & Wikström 1993; Lewerentz et al. 2019).

Previous studies of the Vena and Dampetorp areas (Tegengren et al. 1924; Wikström & Karis 1991) have focused on a general characterization of the host rocks and general descriptions of the mineralization. So far, the mode of occurrence, mineralogical associations, alterations, geochronology and processes involved in the mineralization remain widely unconstrained.

As a part of the Bergslagen Project, the Geological Survey of Sweden (SGU) has undertaken a general characterization of the mineralization in the study area (Lewerentz et al. 2019). This study aims to improve our understanding of the relationships between the hosts rocks and the ore minerals, and to investigate the effects of metamorphism on the deposit as a complement to the ongoing research by SGU. Furthermore, this study seeks to discern the spatial, mineralogical, temporal and genetical constrains of the deposit by answering the following specific questions:

- What are the temporal relationships between metamorphism and mineralization?
- How do the different ore minerals relate to each other?
- What is the general distribution of ore minerals and economic metals in the deposit?
- At which temperature and pressure conditions did the sulphides precipitate?

In this thesis, the issues above are addressed by doing petrographic of gangue and ore minerals, microprobe and whole–rock chemical studies, drill-core observations, thermobarometric sulphide estimatios and U-Pb dating of metamorphic titanite Altogether, these investigations aim at to increased understanding of the specific origin, distribution, and controls of the cobalt occurrence.

This study is part of the of the first efforts towards a comprehensive overview of the mineralization in the Vena-Dampetorp (see Lewerentz et al. 2019) and should serve as strong base for future research of the deposit and similar Cu-Co deposits of the Bergslagen area.

# 2 Geological Background

## 2.1 Bergslagen province

The Bergslagen Province (Figure 1) is a region in south-central Sweden that forms part of the Svecokarelian orogen (a part of the Baltic Shield; Gorbatschev 1962; Gáal & Gorbatschev 1987; Oen 1987; Stephens et al. 2009; Beunk & Kuipers 2012). Bergslagen is an approximately 200 km long curved belt which is dominated by Paleoproterozoic volcano-sedimentary rocks and associated plutonic rocks formed between 1.9 and 1.8 Ga (Oen et al. 1982; Oen 1987; Allen et al. 1996; Stephens et al. 2009). Although the basement to these rocks is mostly unknown, inherited zircon crystals and εNd values suggest both an Archean crystalline and metasedimentary components and juvenile Proterozoic intrusions (Bergman et al. 2008; Stephens et al. 2009).

The volcano-sedimentary succession of rocks is known as the Bergslagen Supracrustal Sequence (Oen et al. 1982) or the Bergslagen Group (Beunk & Kuipers 2012), and is stratigraphically divided into: 1) a lower unit composed of metamorphosed turbidites, greywackes, arkose, pelites, migmatites and quartzites, 2) a thick metavolcanic unit that overlies the metasedimentary unit, and 3) an upper metaturbiditic and locally pelitic sequence (Allen et al. 1996; Jansson et al. 2017). Rhyolitic compositions predominate within the metavolcanic unit. Dacitic-andesitic varieties are present but are, otherwise, completely absent in the eastern part of the Bergslagen Province (Allen et al. 1996).

The metavolcanic unit can be separated into two parts; the lower part is dominated by pyroclastic flow deposits and subaqueous pyroclastic debris flows interbedded with thin marble beds and some siliceous iron formations, whereas the upper section is more stratified and contains reworked volcanoclastics with abundant limestone beds and calc-silicate rock (skarn), interfingering towards the top with the upper metasedimentary sequence (Oen et al. 1982; Allen et al. 1996; Stephens et al. 2009).

Both parts of the metavolcanic unit have been interpreted by Allen et al. (1996) to have formed either in rhyolitic, pyroclastic caldera volcanoes or dacitic-rhyolite complexes with subaerial deposition, and probably in shallow-water conditions within an extensional back-arc setting. The lower section was deposited during the intense volcanism and extensional stage, in which the increased volcanic activity and the constant subsidence maintained continuously shallow oceans. In contrast, the upper part of the metavolcanics represents the waning stage of volcanism, during which a decreased volcanic activity and continued subsidence generated deeper depositional conditions.

U-Pb ages of zircon from the whole metavolcanic sequence span between 1906±3 Ma and 1887 ±5 Ma. The onset of intense volcanism has been dated at 1906±3 and 1904±4 Ma (Lundström et al. 1998; Stephens et al. 2009) and continued until around 1895 Ma. The waning stage of volcanism has been constrained at 1892±5 and 1891±2 Ma by Stephens et al. (2009). New preliminary U-Pb zircon data indicate that the rhyolitic ash-siltstones from the Vena area crystallized at 1884±8 Ma (unpublished data; Lewerentz 2020), which within error overlaps with previous studies but could indicate an even more prolonged volcanism.

The supracrustal rocks are intruded by several generations of igneous rocks which Stephens et al. (2009) grouped into three main compositionally dis-

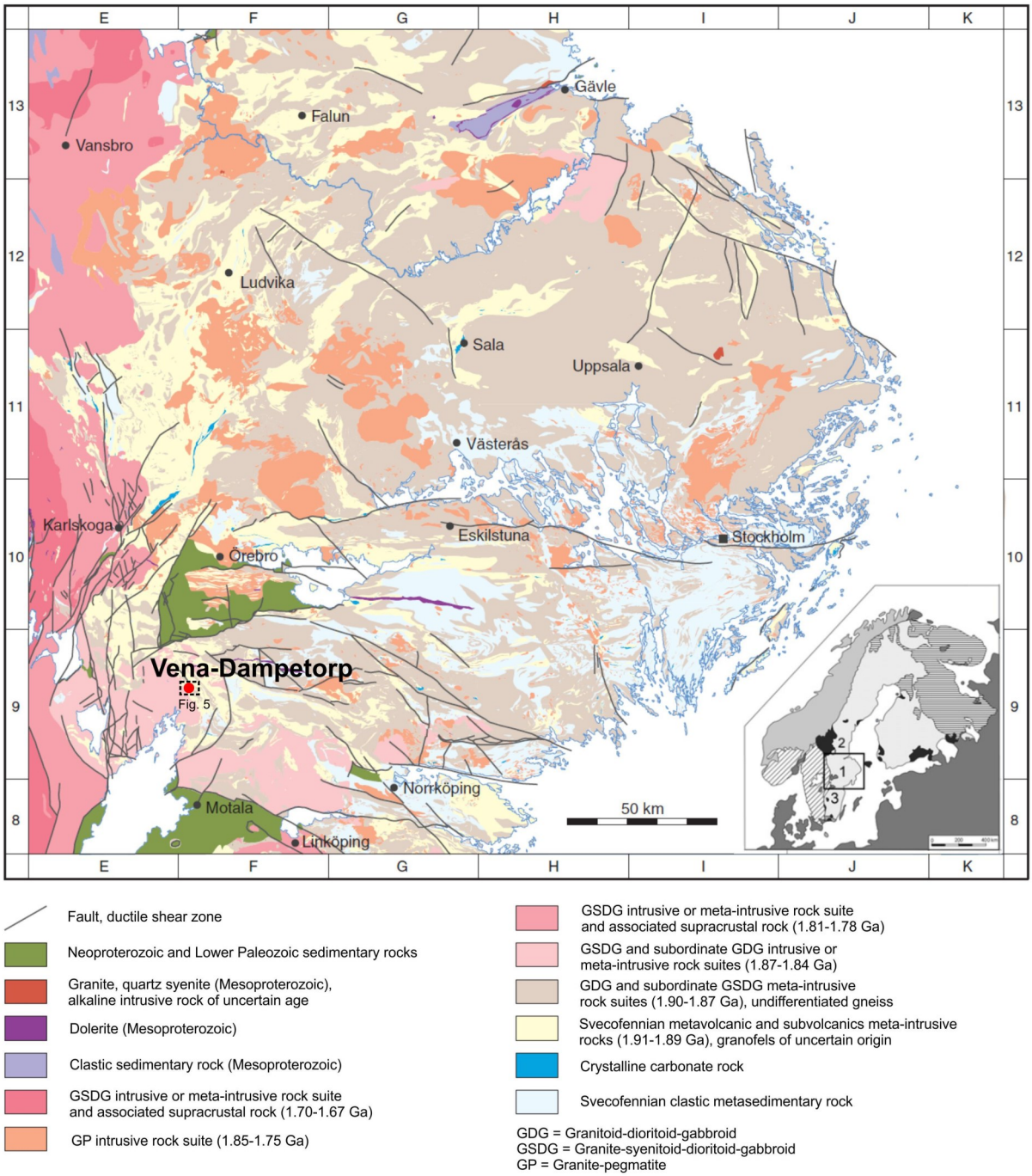


Figure 1.Simplified geological map of the Bedrock in the Bergslagen area (from Stephens et al. 2009). Inset: major tectonic units in the Fennoscandian shield, (from Beunk & Kuipers 2012), with location of the Bergslagen area and this figure; light grey = Svecofennian orogen, horizontal ruling = Archean and pre-Svecofennian Paleoproterozoic rocks, partly affected by Svecofennian reworking, black = Post-Svecofennian Paleoproterozoic igneous and sedimentary rocks, diagonal hatch = Sveconorwegian orogen, medium grey = Caledonian orogen, dark grey = Neo-Proterozoic and Phanerozoic cover rocks; 1 = Bergslagen, 2 = Ljusdal batholith, and 3 = Oskarshamn–Jönköping Belt. The dashed rectangle shows the location of the area of study and of Figure 4.

tinct suites: (1) Granitoid-dioritoid-gabbroid (GDG), (2) Granitoid-syenitoid-dioritoid-gabbroid (GSDG), and (3) Granite-pegmatite (GP). The GDG suite is composed mainly of plutonic rocks that vary from tonalite to granodiorite and granite with some spatially associated intermediate and mafic compositions. These rocks where emplaced before tectonic deformation as they vary from weakly to strongly deformed or migmatitic. Most zircon ages of the GDG suite range between 1907 and 1861 Ma (Figure 2), overlapping with the ages of metavolcanics. Towards the southern and western parts of the Bergslagen Province, the GSDG intrudes the Supracrustal Sequence of Bergslagen and the majority of the GDG rocks. Metadolerites occur throughout the Bergslagen region as conformable or discordant amphibolitic rocks. These are thought to be

emplaced between 1891 and 1857 Ma (Hermansson et al. 2008; Stephens et al. 2009). The GSDG can be divided temporally into three phases. The first two phases from 1.89 to 1.84 Ga and 1.81 to 1.78 Ga, respectively, were intruded during the later stages of the Svecokarelian orogeny. The third phase was emplaced between 1.70 and 1.67 Ga and is post-tectonic. The three phases include granitic to gabbroic and even noritic varieties, however, the syenitic compositions are restricted to the 1.81 to 1.78 Ga phase.

The GSDG suite have also been referred as the Transcandinavian Igneous Belt (TIB) (e.g. Andersson 1991; Högdahl et al. 2004) but has been disregarded by Stephens et al. (2009) based on deviations in the temporal and compositional ranges that are grouped within such term. The GP suite includes granites and associated pegmatites that intruded as post-tectonic or late magmatic bodies. The rocks within this suite crystallized between 1.82 and 1.75 Ga (Stephens & Jansson 2020).

## 2.2 Svecokarelian Orogeny

The rocks of the Bergslagen Province (and a large part of the Baltic Shield) were affected by the tectonic processes of the Svecokarelian orogeny from 2.1 to 1.8 Ga (Gáal & Gorbatschev 1987; Lahtinen et al. 2005; Andersson et al. 2006; Stephens et al. 2009; Beunk & Kuipers 2012), sometimes also referred to as Svecofennian orogeny (Gáal & Gorbatschev 1987). During the Svecokarelian orogeny, the Bergslagen region was subjected to metamorphic conditions from greenschist-facies temperatures up to locally granulite facies (400 to 800ºC) and pressures from 0.2 to 0.6 GPa; most rocks attained amphibolite-facies conditions, (Andersson 2005; Stephens et al. 2009; Skelton et al. 2018; Stephens & Jansson 2020). A large part of the region to the west has, however, been overprinted by the Sveconorwegian orogeny between 1.0 and 0.9 Ga, and locally, in the Karlskoga area, by contact metamorphism around 1.7 Ga (Stephens et al. 2009).

With respect to metamorphic grade, the Bergslagen area can be divided into the northern migmatitic, the central low-grade, the central medium-grade, and the southern migmatitic domain. Peak metamorphism occurred between 1.87 and 1.86 Ga in the northern migmatitic domain, whereas the central medium-grade domain is constrained to 1.88-1.86 Ga. In the southern migmatitic domain, however, two distinct metamorphic events can be recognized. The first episode of metamorphism ($M_1$), dated between 1.87 and 1.84 Ga, is thought to be related to the same metamor-

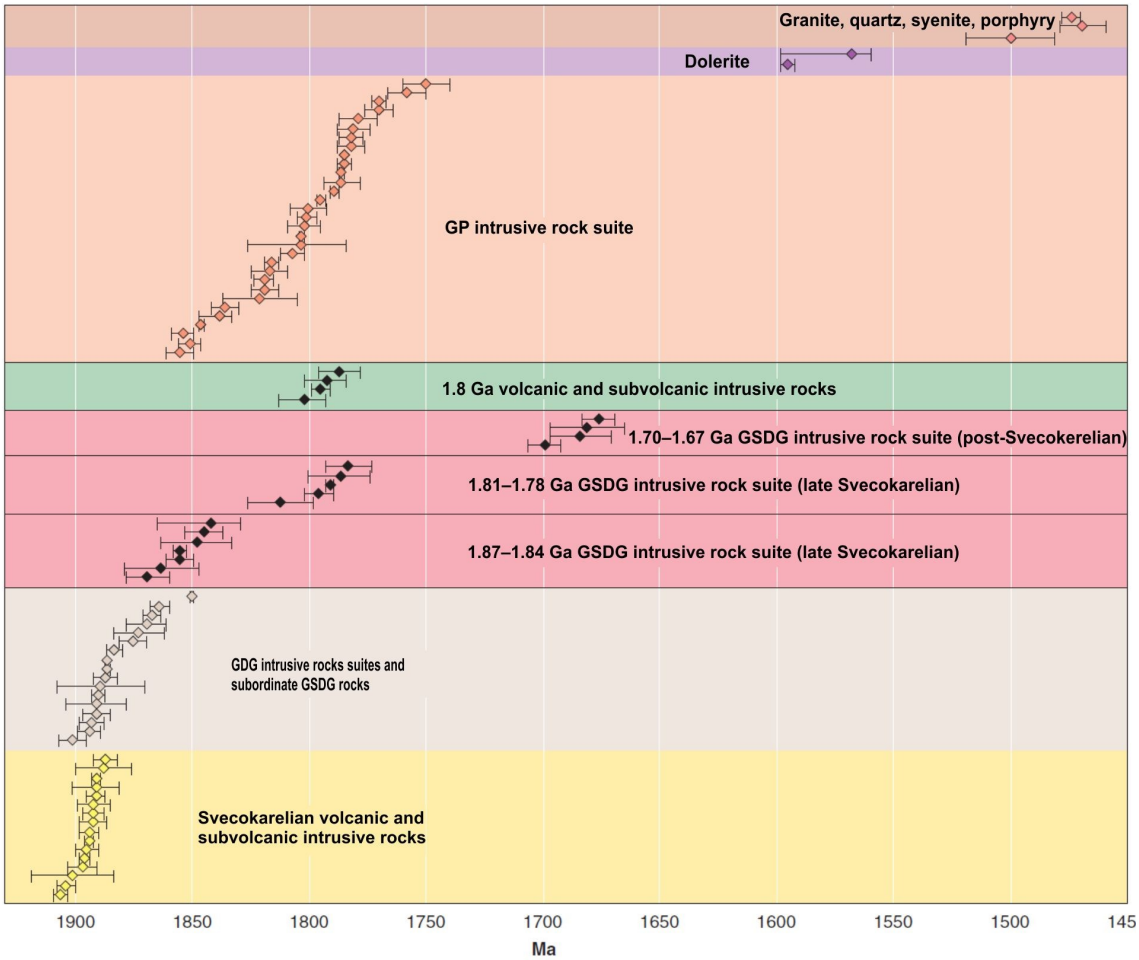


Figure 2. Summary of U-Pb ages (zircon, titanite) from intrusive and volcanic rocks in the Bergslagen area (from Stephens et al. 2009).

phic events as the northern migmatitic and central medium-grade domains (Stephens et al. 2009). The post 1.85 Ga evolution after the first $M_1$ event is attributed to either a single major thermal event (Stephens et al. 2009) or two thermal events at 1.83-1.82 Ga and 1.80-1.79 (Persson & Sjöström 2002).

Stephens et al. (2009) divided the Bergslagen region into four structural domains based on the style of deformation: 1) northern domain, 2) central domain, 3) southern domain, and 4) western domain. Both the northern and the southern domains contain steeply dipping strained belts of amphibolite facies with an overall strike WNW-ESE, with dextral strike-slip and south-side-up shear. These areas are affected by N-NW verging tight folding. In the southern domain, a later generation with more open folding occurs. Most of the high strained belts formed between 1.87 to 1.86 Ga; however, younger ductile deformation events that affected the GSDG suite have been recognized (Stephens & Jansson, 2020).

The central domain is influenced by one early and one later generation of folding. Fold axis strike E-W to NE-SW. A third folding generation can be found in the western areas, which axial planes strike NW-SE to NNW-SSE. The ductile belts formed before the second folding generation and sinistral and NW-side-up shear dominate this domain. The western structural domain is characterized by interference structures associated to the Sveconorwegian overprint, the structures formed before the Sveconorwegian orogeny strike WNW-ESE, whereas structures overprinted by later Sveconorwegian tectonics show a deflected N-S strike. A west-side-up shear sense can be recognized in the domain, later overprinted by Sveconorwegian E-W compression.

Several tectonic models have been invoked for the Svecokarelian orogeny since the first one was proposed by Hietanen (1975). Gáal and Gorbatschev's (1987) original model proposed three continuous orogenic processes that were responsible for crustal generation during the Archean (Lopian orogeny) and during the Proterozoic (Svecofennian and Gothian orogenies). In their model, the Bergslagen and the Skellefte districts are volcanic belts. These developed in a continental margin that formed an embayment in the Archean craton in which the Bothnian basin represents the centre. These models also recognize early, late- and post-orogenic magmatic episodes, where the early granitoids were emplaced in an extensive regime, whereas the late granitoids are of S-type associated with the migmatization and reworking of the crust.

Lastly, post-orogenic rapakivi granitoids were emplaced in intra-cratonic settings. Gáal & Gorbatschev (1987) suggested that deformation and metamorphism occurred in two periods closely, where each period was closely related in time with either the early or the late granites. They recognized either crustal thickening or a high heat flow associated with repeated igneous intrusions as the cause of high-grade metamorphism.

Nironen (1997), also proposed a three staged model; however, his model involves the accretion of island arc complexes into the Archean craton. In the Archean, between 2.1 and 2.0, the craton broke down into microcontinents due to fragmentation or as result of a passive aulacogen. Around 1.91 Ga, an arc complex collided with the Archean craton margin at the SW while subduction continued active on the west side. Afterwards, another two Archean blocks were accreted to the north of the craton between 1.91 and 1.90 Ga, which caused either a subduction polarity reversal or the approach of another microplate from the south. The Tampere volcanics developed in the continental margin with a subduction zone beneath them, whereas the Bothnian basin and the Skellefte volcanics formed part of an island arc. The Bergslagen volcanics were, on the other hand, extruded within extensional basins in the older crust and were separated from the forearc volcanics of the Häme area by a shallow back-arc or intra-arc basin. Together, the Bergslagen and the Häme volcanics formed another arc complex with a subduction zone to the south. The Häme-Bergslagen arc complex collided with the Tampere-Skellefte arc complex by 1.89 Ga, which led to the closure of the Bothnian basin, disappearance of the two subduction zones, and mergence of the accretionary prisms. After the orogeny, the crust cooled down and became denser and around 1.89 Ga the lithosphere started to delaminate, which in turn produced an astenospheric rise and re-melting of the lower crust. The high temperatures produced by these processes resulted in regional high-temperature metamorphism. Post-orogenic magmatism took place in a continental arc setting with an east-dipping subduction zone.

In contrast, a later model presented by Lahtinen et al. (2005) suggested an evolution with five individual orogenies related to microcontinental accretion (Model 2; Figure 3). In their model, the Archean craton experienced multiple rifting events between 2.5 to 2.1 Ga. Continental breakup occurred in the western margin of the Karelian craton at 2.06 Ga. In the Lapland-Kola area, a subduction zone was active towards the SW between 1.96 and 1.93 Ga and had an associated back-arc basin. Between 1.93 and 1.91 Ga, the back-arc basin shortened as a result of the collision of the Kola and the Karelian craton, which resulted in the Lapland-Kola orogen. Collapse of the orogen and crustal thinning of the crust happened around 1.88 and 1.87 Ga. Island-arc magmatism was active between 1.93 and 1.92 Ga in the Savo belt, which was part of the Keitele microcontinent. The Karelian and Keitele collision occurred probably around 1.91 Ga. Around the same time, the Bothnian microcontinent continued approaching the accreted Keitele microcontinent from the east and collided at 1.90 Ga; together they formed the Lapland-Savo orogen.

The collision and accretion of the Keitele microcontinent caused a subduction reversal and switch-over resulting in extension on the continental margin. With the collision of the Bothnian microcontinent, a north-northwest-dipping subduction system was established between 1.89 to 1.87 Ga. Towards the south, an island arc complex developed between 1.90 and 1.88 Ga, composed of a volcanic arc (Häme belt) with back-arc volcanism (Bergslagen area). At 1.89 Ga the subduction zone to the north migrated towards the continent, which caused the subduction slab lock and started a compressive regime in the region. The collision of the Bergslagen microcontinent to the Keitele continental margin started the Fennian orogeny.

Around 1.87 Ga, the subduction to the west of the Fennoscandian shield migrated towards the south of the continent, which in turn resulted in a subduction reversal at the southern margin. With change in plate dynamics, an extensional stage happened between 1.86-1.84 Ga, which caused thinning and astenospheric upwelling in the Bergslagen-Häme and Bothnian areas. It is understood that the mantellic rise was responsible for migmatization and granite generation in these areas. Between 1.85-1.79 Ga, an Andean-type margin was initiated along the SW part of the Fennoscandian Shield with a northwest dipping subduction zone. A continent-continent collision started to the southeast of the shield with the collision of Sarmatia until 1.82 Ga, producing the Svecobaltic orogen. The oblique continental collision led to inversion and extension between 1.86 and 1.84 Ga, resulting in granite generation and migmatization in the Bergslagen area (Lahtinen et al. 2005).

The Nordic orogeny is proposed as the result of a NW-SE to E-W collision that occurred between 1.82 and 1.80 Ga in the southwestern margin of the Fennoscandian shield. Magmatism (TIB) developed in an extensional or intra-cratonic setting. Afterwards, the Nordic orogeny orogenic collapse took place between 1.79 to 1.77 Ga with an extensional regime. The Gothian orogeny occurred between 1.73 and 1.55 Ga as a complex period with several growth stages.

Most of the later models are built upon the Lahtinen et al. (2005) model (e.g. Weihed et al. 2005; Korja et al. 2006; Lahtinen et al. 2009; Stephens et al. 2009), each with minor differences compared to the others. However, the latest models (Hermansson et al. 2008; Stephens et al. 2009; Beunk & Kuipers 2012; Johansson & Stephens 2017) focus on the evolution of the Bergslagen area in the context of the Svecokarelian orogeny. Hermansson et al. (2008) presented two different models to explain the tectonic evolution of the Bergslagen Province. The first one (Figure 3) considers a subduction zone SW from a continental margin where the migration subduction hinge caused two cycles of extension compression. The second model (Figure 3) involves extension and later accretion of a continent into another microcontinent, where originally a southwest-dipping zone was reversed into a northeast-dipping subduction zone that later experienced extension due to hinge retreat. Both Stephens et al. (2009) and Beunk & Kuipers (2012) prefer the first scenario, in which two periods of extension and later accretion characterized the evolution of the Bergslagen area, the first one as part of the Fennian orogeny (1.89-1.87 Ga) and the second one responsible for the Svecobaltic orogeny (1.86-1.83 Ga; Beunk & Kuipers 2012). More recently, Johansson & Stephens (2017) presented new geochronological evidence that further supports the extension-accretion model of Hermansson et al. (2008).

## 2.3 Ore deposits

The Bergslagen mining district contains several different deposit types, including Mg-skarns, Fe-oxide carbonate and calc-silicate skarns, W-skarns, carbonate-hosted Fe-oxide ores, apatite-bearing iron ores, banded iron formations (BIF), stratiform and stratabound base metal sulfide deposits, minor Mo-sulfide deposits, greisen and pegmatitic deposits (Allen et al. 1996; Allen et al. 2008; Stephens et al. 2009). The sulphide ores were originally subdivided in two genetic types: the Åmmeberg type and the Falun type (Magnusson 1953). The Falun type, referred to as stratabound volcanic associated limestone skarns (SVALS type) by Allen et al. (1996), consists of stratabound irregular and pod like Zn-Pb-Ag-(Cu-Au), massive or disseminated, sulfide deposits hosted by felsic metavolcanics and associated carbonate rocks. Examples of deposits of this type include the Falun, Sala and Garpenberg deposits. On the other hand, the Åmmeberg type, or stratiform ash-siltstone (SAS type) in Allen et al. (1996), comprises stratiform or sheet-like Zn-Pb-Ag-Cu sulfide deposits, hosted by felsic ash-siltstone metavolcanics, calc-silicate skarns, carbonate rocks and siliceous beds. A classic example of this type is the Zinkgruvan deposit (Allen et al. 1996; Stephens et al. 2009; Jansson et al. 2018).

Most base metal sulfide deposits have a low tonnage (below 1 Mt) and are not economically viable, except for the Garpenberg Odalfält (16 Mt), Garpenberg Norra (17 Mt), Sala (2 Mt), Saxberget (6 Mt), Zinkgruvan (43 Mt) and Falun (28 Mt) deposits. Typically, base metal sulfide deposits in Bergslagen are rich in Zn and contain an average of 4.5% Zn, 2.5% Pb and 0.5% Cu. The content of Ag varies in most deposits from a major commodity to a by-product (Allen et al. 2008; Stephens et al. 2009). Cobalt is mostly present in some Cu-rich deposits and minor Co-Ni sulphide deposits, traditionally being locally extracted as a by-product (Allen et al. 2008; Stephens et al. 2009; Stephens & Jansson 2020). Examples of Co deposits include the Tunaberg (Johansson 1919) and the Vena (Tegengren et al. 1924) deposits.

Early studies (e.g. Gorbatschev 1969), have recognized regional elemental enrichments or alterations in the Bergslagen area. Stephens et al. (2009) groups them into four categories: 1) sodium alteration, 2) potassium alteration, 3) magnesium alteration and 4) skarn alteration. Sodium enrichment or sodium alteration affects mostly mineralized rocks (Stephens et al. 2009) and lower stratigraphic levels (Lundström 1985). Potassium and sodium enrichment are probably the most common types of alterations recognized in the metavolcanic successions of the Bergslagen area (e.g. Allen et al. 1996), and have been interpreted to be the result of sub-sea floor heated seawater interaction with felsic rocks rich in feldspars (de Groot 1990). Magnesium alteration is commonly recognized by mineral assemblages that can include chlorite, phlogopite, biotite, muscovite, gedrite, anthophyllite or cordierite, which are thought to represent the metamorphic products of Mg-alteration minerals (Helmers 1984; Trädgårdh 1991; Ripa 1994). The Mg-alteration has been interpreted as the replacement of feldspar by phyllosilicates in zones of hydrothermal fluid conduction in a sub-sea floor environment (Baker & Groot 1983). This alteration can in places overprint an earlier sodium enrichment in highly porous areas (Stephens et al 2009).

The first ideas about the origin of the base metal sulfide ore deposits in Bergslagen included magmatic ore-forming fluids related to the GDG intrusions (Geijer 1917), and a primary magmatic differentiation

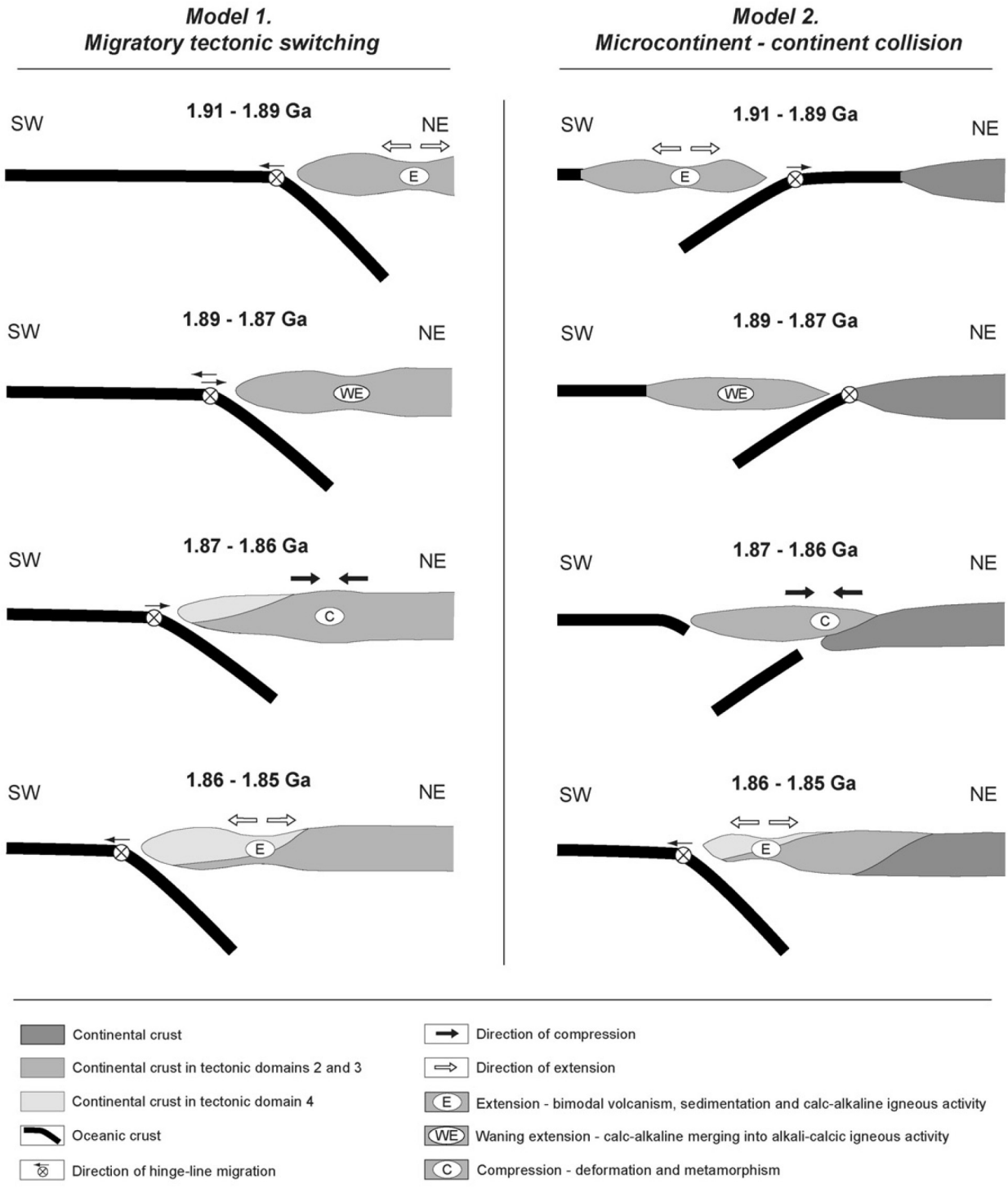


Figure 3. Two different models explaining the tectonic evolution of the Bergslagen Province. Model 1 involves a continuous subduction where hinge retreat and advance produces episodes of compression and extension. Model 2 includes microcontinental collision and accretion with a later subduction polarity change and hinge retreat. From Hermansson et al. 2008

that controlled the variety of alterations and compositions (Tegengren et al. 1924). Recent models, however, consider that the sulfides deposits were formed by syn-volcanic sub-seafloor replacement (Allen et al. 1996), seafloor exhalative (Henriques 1964; Oen et al. 1982; Oen et. al. 1987; Jansson et al. 2017) or a combination of both processes (Allen et al. 1996).

# 3 Local Geology

## 3.1 Stratigraphy

The stratigraphy of the Åmmeberg mining district, including the Vena, Dampetorp and Zinkgruvan mining fields, was originally described by Henriques (1964) and later further detailed by Kumpulainen et al. (1996). Collectively, the volcanosedimentary succession is referred to as the Emme Group (Figure 4; Kumpulainen et al. 1996), and consists of the lower Mösjön unit that comprises a lensoidal rhyodacitic body overlain by the Gökberget unit as well as a quartzofeldespatic rock with different degrees of metamorphic grades and hydrothermal alteration. These units are in turn overlain, in ascending order, by the Igelfors, Närkesberg and the Mariedamm and Godegård formations. The Igelfors formation is composed of rhyolitic volcanoclastics and quartz porphyries deposited from pyroclastic flows. The Närkesberg formation is a sedimentary succession dominated by continentally derived arkoses with minor shales and debris flow-associated deposits towards the top of the succession. Overlying the Närkesberg formation are both the Mariedamm and the Godegård volcanic units. The Mariedamm volcanic unit varies in composition between rhyodacite and rhyolite, whereas the Godegård volcanic unit has rhyolitic to dacitic compositions. A limestone unit, defined as the Höksjön limestone, overlies the Godegård volcanic unit and appears as discontinuous tabular bodies (Kompulainen et al. 1996). The Vintergölen formation is the stratigraphically highest volcano-sedimentary succession of the Emme Group and consist of migmatitic and non-migmatitic metapelites that represent sandy to shaly turbiditic deposits (Kumpulainen et al. 1996; Jansson et al. 2017). Underlying the Vintergölen formation lies what Hedström et al. (1989) defined as a discontinuous metatuffite unit, that is later referred to by Jansson et al. (2017) as the Zinkgruvan formation. The metavolcanic of the Zinkgruvan formation contain interbedded limestone horizons and lenses (Kumpulainen et al. 1996; Jansson et al. 2017).

Most of the metavolcanic rocks that outcrop in the Vena and Dampetorp area belong to the Mariedamm volcanic unit (Kumpulainen et al. 1996) and range from rhyolite to andesite in composition (Lewerentz et al. 2019). Within the metavolcanic rocks, elongate lenses of amphibolites are found, which are interpreted to be the metamorphosed mafic intrusive bodies (Wikström & Karis 1991; Lewerentz et al. 2019). Svecokarelian fine grained granodiorite and tonalites (GDG granitoids; Stephens et al. 2009) intrude the metavolcanic rocks locally with metamorphic garnet porphyroblasts. These rocks are also foliated, similar to the metavolcanic and amphibolitic rocks (Lewerentz et al. 2019).

The Svecokarelian metavolcanic rocks and associated intrusions are crosscut by undeformed pegmatites consisting of quartz and potassium feldspar with minor mica, plagioclase and tourmaline. Towards the south and southwestern margins of the study area, the 1.84 Ga (Persson & Wikström 1993) post-orogenic Askersund granite, along with genetically related syenites outcrop (Lewerentz et al. 2019).

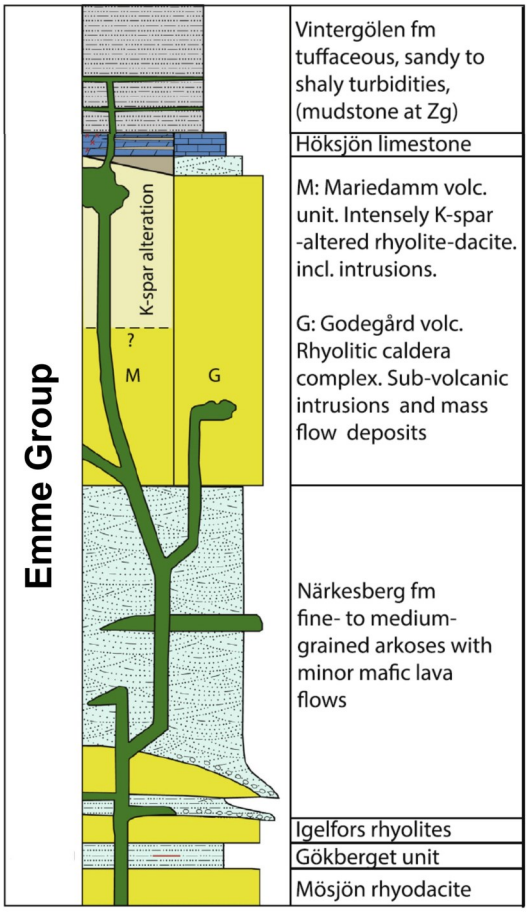


Figure 4. Emme Group stratigraphic column that comprised the regional stratigraphy of the Åmmeberg mining district. The total thickness is approximately 10 km. Zg=Zinkgruvan. Modified from Jansson et al. (2017).

## 3.2 Structural Geology

Most Svecokarelian rocks in the Vena area have a penetrative foliation or a mineral foliation in a NW-SE direction related to a $D_1$ deformational event during the Svecokarelian orogeny (Lewerentz et al. 2019). Sometimes foliation can vary 180° from the NW-SE general trend, particularly near the mines, which has been interpreted as a series of small-scale folds that form a part of an open fold structure with approximately 150° between the limbs and with a flat dipping axial plane with NE strike direction, representing a $D_2$ event. This last event has been interpreted as refolding of the $D_1$ foliation in an isoclinal fold with a steeply dipping SW striking axial plane (Wikström & Karis 1991; Lewerentz et al. 2019).

# 4 Methods

## 4.1 Sampling

Field work and sampling was carried out during May 2019 in the Vena-Dampetorp Area. The sampling was mainly focused on mineralized samples to study ore textures and their relationships. A total of six samples were collected (Table 1 and figure 5): three from different "waste piles" within the Vena area and three samples from "waste piles" in the Dampetorp area. In addition, one sample was taken from the wall of the "Långgruvan" mine pit. These waste piles were generated during the intermittent mining of the deposit between 1770 and 1880 (Tegengren at al. 1924). The exact mine or original location of each rock sample is not known as they were collected from the waste piles; however, it is inferred that they originate from any of the mines near the piles where they were taken from. Therefore, they are thought to represent typical (possibly lower grade) samples from the mineralized areas.

In addition to the samples collected in field, data and thin sections (Table 1) were made available for this thesis by SGU, originally sampled as part of their "Bergslagen, etapp 1" and "Regeringsuppdrag om innovationskritiska metaller och mineral" projects. Out of a total of 98 SGU samples, 29 were taken from outcrops, 69 from waste piles, and 26 from drill cores.

## 4.2 Core Logging

Previous exploration of the Vena area included the drilling of 12 exploration bore holes. The shorter drill cores were described by Henriques (1957; 1979) and Åberg (1987), while the four longer cores by Wasström (1991a; 1991b, 1991c) and Simeonov (1990). These logs were used as a base for interpretation of the simplified stratigraphy. In addition, an alteration log was created based on the previous observation and reinterpretations of those descriptions.

Additionally, drill cores DH9002 and DH9004 from the Vena area were logged at the Zinkgruvan mine facilities. The logging of these cores focused on the mineralized zones and adjoining areas. Detailed descriptions of the lithology and the styles of mineralization for the ore-bearing intervals were combined with the previous lithological descriptions done by Wasström (1991a; 1991b, 1991c) and Simeonov (1990). The SGU took samples from the main mineralized areas in cores 9004 and 9002, which were also included in the whole rock analyses. A total of four samples were taken for thin sections from cores, as summarized in Table 2.

## 4.3 Microscopy

### 4.3.1 Optical Microscopy

For the petrographic description, 22 thin sections were selected from the SGU samples. In addition, 10 thin sections of the samples collected during field work were prepared and described. Observations were performed using a polarized transmitted light Olympus BX53 microscope. For the petrographic descriptions of ore minerals, a total of 27 mineralized samples were chosen and examined under reflected light using a Nikon E400 Pol microscope; these include 17 thin sections from SGU and 10 thin sections from the samples collected during this study.

### 4.3.2 Electron Microscopy

Electron microscopy was used to investigate the elemental distribution of cobalt and other elements within ore phases, as well as to determine mineral phases that could not be identified through optical microscopy. The analyses were performed at Lund University using a Tescan Mira 3 Field Emission Scanning Electron Microscope (SEM).

The SEM uses an electron beam in vacuum conditions, generated by passing a high voltage through a tungsten filament. The beam is focused into the sample by means of magnetic lenses (i.e. condenser lenses). In this type of microscope, the electron beam is fixed and the sample can move in the x and y directions.

The interaction of the electron beam with the sample produces four main products: (1) secondary electrons (SE), (2) back-scattered electrons (BSE), (3) cathodoluminescence (CL), and (4) X-rays. Secondary electrons are produced from the valence electrons of the sample that are striped when hit by the beam. In comparison, the BSE are high energy electrons from the beam that are reflected when hitting the sample. In contrast, the CL is produced as a response to excitation of the atom outer orbitals during the interaction with the electron beam. Lastly, X-rays are emitted from the sample as part of the de-excitation of the outer orbital electrons. These X-rays have a characteristic wavelength that depends on the atomic number of the atom (Egerton 2005).

An analysis of the X-ray emissions, known as X-ray energy-dispersive spectroscopy (XEDS or EDS) in which a diode collects photons and their energy produced by the X-rays. A quantitative analysis can compare the intensity of the peaks with the specific wavelengths or intensities that correspond to specific elements (Egerton 2005).

A total of 11 samples were selected and coated with 20 nm of carbon. Each sample was analysed using an acceleration voltage of 15 kV and a beam intensity of 17 nA. Chemical compositions were determined using the equipment's BSE detector and calibrated with the built-in standards of the instrument. In addition to these analyses, the study includes SEM-EDS analyses for 11 samples performed by SGU.

Based on the results obtained from the SEM-EDS analysis, mineral compositions were calculated. Analyses with wt% total sums between 96 to 104 were considered reliable for the quantitative composition calculations. Hydrous and carbonaceous phases could have totals well below 100 wt% as the technique cannot detect these components and thus, low totals are expected. All other analyses below 96 or above 104 wt% were considered unreliable and have been excluded from this thesis; however, in some cases no reliable analysis was obtained for a specific mineral in which case the data was normalized to 100 wt% for qualitative comparisons only. Additionally, mixed results (i.e. results were the beam hit two or more minerals at the time) were discarded.

For non-sulphide minerals, compositions were calculated primarily based on the number of oxygens. The amount of $Fe^{3+}$ was determined and corrected us-

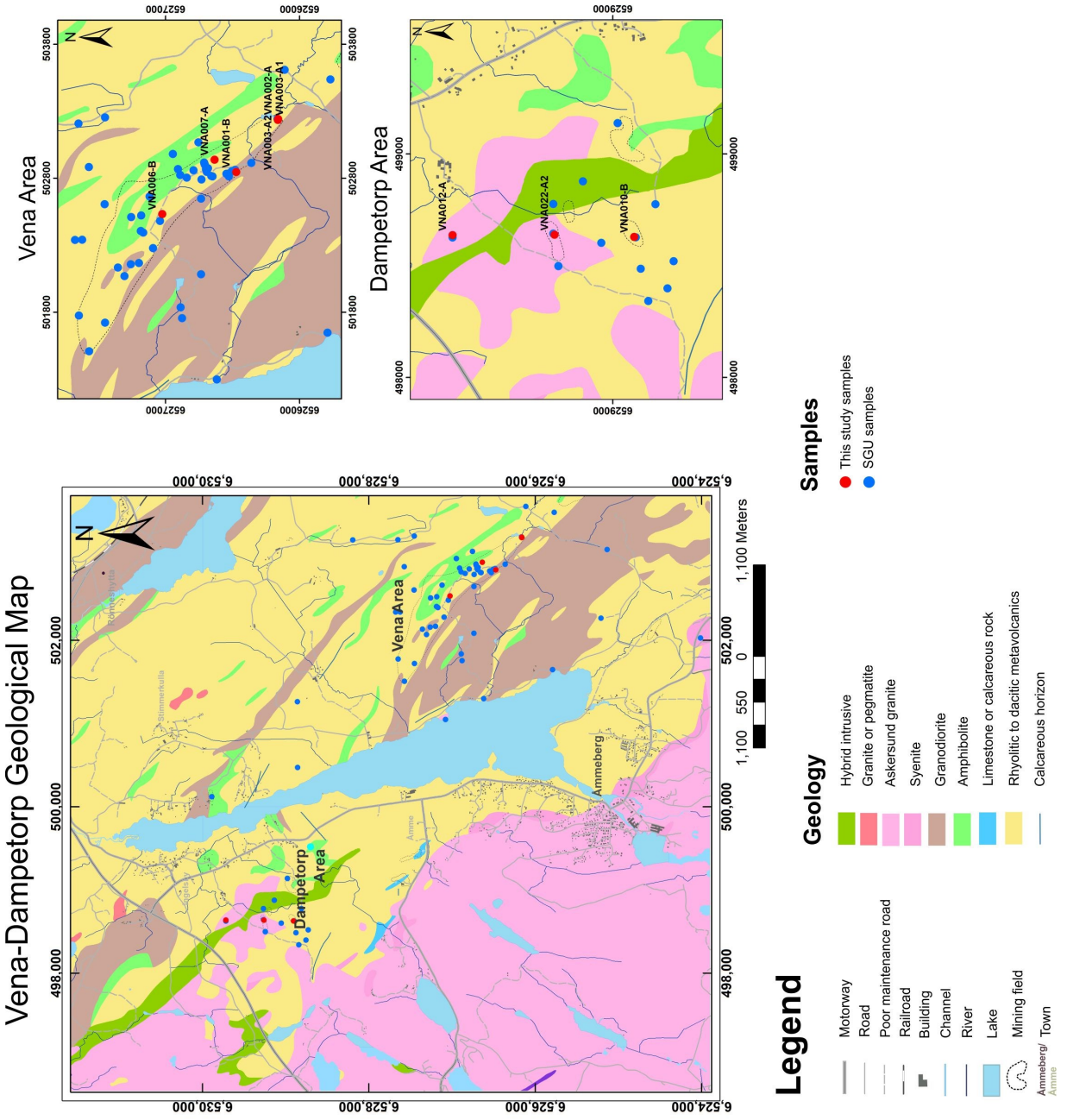


Figure 5. Simplified Geological map of the area of study. Based on geographical and geological data © *Lantmäteriet* and ©*SGU*.

Table 1. List of samples and their location together with the analyses performed on each sample. All coordinates in are in SWEDEREF 99TM.

| Sample | Coordinates | | Analyses | | | Sample | Coordinates | | Analyses | | |
|---|---|---|---|---|---|---|---|---|---|---|---|
| | North | East | Geochemistry | Petrography | SEM | | North | East | Geochemistry | Petrography | SEM |
| ALZ180002A | 6525791 | 501649 | ✓ | ✓ | × | EDB180026A | 6527257 | 502512 | ✓ | × | × |
| ALZ180006A | 6526546 | 502836 | ✓ | × | × | EDB180026B | 6527257 | 502512 | ✓ | × | × |
| ALZ180008A | 6528192 | 503209 | ✓ | ✓ | × | EDB180028A | 6527184 | 502409 | ✓ | × | × |
| ALZ180009A | 6525208 | 502268 | ✓ | × | × | EDB180031A | 6527094 | 502280 | ✓ | × | × |
| ALZ180033A | 6527650 | 503210 | ✓ | ✓ | × | EDB180031B | 6527094 | 502280 | ✓ | × | × |
| ALZ180034A | 6527452 | 503256 | ✓ | ✓ | × | EDB180034A | 6527198 | 502170 | ✓ | × | ✓ |
| ALZ180035A | 6527647 | 501777 | ✓ | ✓ | × | EDB180036A | 6527355 | 502135 | ✓ | × | × |
| ALZ180036A | 6526506 | 502854 | ✓ | × | × | EDB180039A | 6527623 | 502343 | ✓ | × | × |
| ALZ180037A | 6526481 | 502864 | ✓ | ✓ | ✓ | EDB180040A | 6527676 | 502342 | ✓ | × | × |
| ALZ180051A | 6526527 | 502816 | ✓ | × | × | EDB180050A | 6527042 | 502484 | ✓ | × | × |
| ALZ180052A | 6526692 | 502849 | ✓ | × | × | EDB180060A | 6527119 | 502667 | ✓ | × | × |
| ALZ180052B | 6526683 | 502876 | ✓ | ✓ | ✓ | EDB180071A | 6527306 | 502071 | ✓ | × | × |
| ALZ180053A | 6526842 | 502807 | ✓ | × | × | EDB180072A | 6527451 | 501724 | ✓ | × | ✓ |
| ALZ180059A | 6526792 | 502861 | ✓ | ✓ | × | EDB190001A | 6526754 | 503071 | ✓ | × | × |
| ALZ180062A | 6526732 | 502793 | ✓ | × | × | EDB190002A | 6526712 | 502920 | ✓ | × | × |
| ALZ180067A | 6526735 | 502649 | × | ✓ | ✓ | EDB190003A | 6526710 | 502914 | ✓ | × | × |
| ALZ180068A | 6526890 | 502826 | ✓ | × | × | EDB190004A | 6526710 | 502914 | ✓ | × | × |
| ALZ180071A | 6526907 | 502871 | ✓ | × | × | EDB190005A | 6526708 | 502906 | ✓ | × | × |
| ALZ180072A | 6526946 | 502984 | ✓ | ✓ | ✓ | EDB190006A | 6526708 | 502905 | ✓ | × | × |
| ALZ180076A | 6524013 | 502029 | ✓ | ✓ | ✓ | EDB190007A | 6526708 | 502905 | ✓ | × | × |
| ALZ180085A | 6526617 | 501300 | ✓ | ✓ | × | EDB190008A | 6526707 | 502904 | ✓ | × | × |
| ALZ180087A | 6527078 | 501051 | ✓ | ✓ | × | EDB190010A | 6527182 | 502525 | ✓ | × | × |
| ALZ180089A-1 | 6526650 | 502816 | ✓ | ✓ | ✓ | EDB190011A | 6526699 | 502875 | ✓ | × | × |
| ALZ180089A-2 | 6526650 | 502816 | × | ✓ | ✓ | EDB190012A | 6526699 | 502875 | ✓ | × | × |
| ALZ180089A-3 | 6526650 | 502816 | × | ✓ | ✓ | EDB190013A | 6526699 | 502874 | ✓ | × | × |
| ALZ190012A | 6528875 | 498487 | ✓ | ✓ | × | EDB190014A | 6526699 | 502873 | ✓ | × | × |
| ALZ190013A | 6528728 | 498521 | ✓ | × | ✓ | EDB190015A | 6526699 | 502872 | ✓ | × | × |
| ALZ190014A | 6529243 | 498499 | ✓ | × | × | EDB190016A | 6526698 | 502872 | ✓ | × | × |
| ALZ190015A | 6529243 | 498499 | ✓ | ✓ | × | EDB190017A | 6526698 | 502871 | ✓ | × | × |
| ALZ190016A | 6529243 | 498499 | ✓ | × | × | EDB190018A | 6526698 | 502870 | ✓ | × | × |
| ALZ190019A | 6528978 | 499139 | ✓ | × | × | EDB190019A | 6526698 | 502869 | ✓ | × | × |
| ALZ190019B | 6528978 | 499139 | ✓ | × | × | EDB190020A | 6526698 | 502869 | ✓ | × | × |
| ALZ190029A | 6528897 | 498628 | ✓ | × | × | EDB190021A | 6526697 | 502868 | ✓ | × | × |
| ALZ190030A | 6529266 | 498644 | ✓ | × | × | EDB190022A | 6526697 | 502867 | ✓ | × | × |
| ALZ190031A | 6528841 | 498343 | ✓ | × | × | EDB190023A | 6526697 | 502866 | ✓ | × | × |
| ALZ190032A | 6525488 | 503809 | ✓ | × | × | EDB190023B | 6526658 | 502819 | ✓ | × | ✓ |
| ALZ190033A | 6525770 | 503540 | ✓ | × | × | EDB190028A | 6527572 | 502886 | ✓ | × | × |
| ALZ190034A | 6526164 | 503246 | ✓ | ✓ | ✓ | EDB190031A | 6529717 | 498627 | ✓ | × | × |
| ALZ190036A | 6527260 | 502160 | ✓ | × | × | EDB190032A | 6529266 | 498777 | ✓ | × | × |
| ALZ190037A | 6529885 | 500122 | ✓ | ✓ | ✓ | EDB190035A | 6528755 | 498399 | ✓ | × | ✓ |
| ALZ190040A | 6528809 | 498776 | ✓ | × | × | EDB190037A | 6528858 | 501264 | ✓ | × | × |
| ALZ190065A | 6529051 | 498603 | ✓ | × | × | EDB190040A | 6528854 | 500472 | ✓ | × | × |
| ALZ190067A | 6529134 | 498878 | ✓ | × | × | EDB190043A | 6527571 | 501510 | ✓ | × | × |
| ALZ190087A | 6526946 | 502984 | × | ✓ | ✓ | VNA001-B | 6526473 | 502850 | × | ✓ | × |
| ALZ190088A-1 | 6527455 | 502608 | × | ✓ | × | VNA002-A | 6526160 | 503244 | × | ✓ | ✓ |
| ALZ190088A-2 | 6527455 | 502608 | × | ✓ | ✓ | VNA002-B2 | 6526160 | 503244 | × | ✓ | ✓ |
| EDB180001A | 6525135 | 503092 | ✓ | × | × | VNA003-A1 | 6526162 | 503238 | × | ✓ | ✓ |
| EDB180002A | 6526360 | 502917 | ✓ | × | × | VNA003-A2 | 6526162 | 503238 | × | ✓ | × |
| EDB180003A | 6526111 | 503611 | ✓ | × | × | VNA006-B | 6527024 | 502535 | × | ✓ | × |
| EDB180005A | 6526877 | 501757 | ✓ | × | × | VNA007-A | 6526635 | 502941 | × | ✓ | × |
| EDB180016A | 6526887 | 501838 | ✓ | × | × | VNA010-B | 6528904 | 498630 | × | ✓ | × |
| EDB180020A | 6526735 | 502086 | ✓ | × | × | VNA022-A2 | 6529261 | 498640 | × | ✓ | ✓ |
| EDB180024A | 6527167 | 502397 | ✓ | × | × | VNA012-A | 6529717 | 498638 | × | ✓ | ✓ |

ing the method of Droop (1987) for minerals without site vacancies. For chlorite and biotite-like minerals, all Fe was assumed to be $Fe^{2+}$. These minerals were named using the classifications of Zane & Weiss (1998) and Deer et al. (1992), respectively. Halogen estimations and corrections were performed in apatite and biotite crystals, following the method 1 of Ketcham (2015). In comparison, sulphide minerals were classified based on the optical properties and chemical analysis, as no crystallographic analyses were performed (e.g. no distinction between monoclinic or hexagonal pyrrhotite). Compositions were determined based primarily on the moles of S, except elsewhere stated.

## 4.4 Whole-Rock Geochemistry

In order to determine the metal distribution, chemical alterations and origin of the rocks, the whole rock geochemistry database of the SGU was used for this study. This database comprises a total of 98 samples from the area. The ALS laboratories in Piteå, Sweden performed the multi-elemental geochemical analysis for the SGU, whereby major elements were determined using Inductive Coupled Plasma with Atomic Absorption Spectroscopy (ICP-AES), trace elements with Inductive Coupled Plasma with Mass Spectrometry (ICP-MS), all on lithium metaborate fused whole rock powder, as well as volatile phases with Combustion on Ignition (CI). Additionally, most trace ele-

Table 2. Samples from drill-cores analysed.

| Sample | Core | From [m] | To [m] |
|---|---|---|---|
| ALZ190012A-1 | DAP002 | 3.75 | 5.8 |
| ALZ190015A-1 | DAP004 | 29.2 | 29.6 |
| ALZ190088A-1 | 9004 | 567.4 | 567.65 |
| ALZ190088A-2 | 9004 | 567.4 | 567.65 |

ments and ore-forming elements were analysed using four acid and aqua regia digestion which gives better accuracy for sulphide-bound components and used for identification of ore grades. In a further step, elemental plots were generated using GdcKit software.

Both the ICP-MS and the ICP-AES create a plasma source by either dissolving the sample in acid or by laser ablation of the metaborate-fused samples, which is nebulized into a stream of argon that is later turned into a plasma by passage through a high voltage coil. In the case of the atomic absorption spectroscopy, the plasma goes through a diffraction grating that separates the plasma light emission into different wavelengths which are later collected to measure their intensities. Each specific wavelength corresponds with an element, while the intensity is proportional to the element concentration. In comparison, the mass spectrometry accelerates the plasma ions by a magnetic field that pushes them through a mass analyser. The mass analyser uses a magnetic field through a curved tube to separate the ions according to their masses. The separated ions then hit a detector, where their position and intensity correlate with the element and the abundance, respectively (Pavia et al. 2009).

The CI method involves heating a sample in a furnace under high oxygen conditions and trapping the resulting gases using different substances. The only measurable elements through this method are C, H, O, N, and S (i.e. $CO_2$, $H_2O$, NO or $NO_2$, and $SO_2$), and their proportions are determined by stoichiometry (Pavia et al. 2009).

## 4.5 Sphalerite Barometry

The sphalerite barometer of Barton and Toulmin (1966) was used to estimate the pressure of the sulphide assemblages. This estimate is based on the association pyrite + pyrrhotite + sphalerite. Equilibrium is assumed where the sphalerite grains are in contact with pyrite and pyrrhotite, or if equilibrium can be inferred from other textures in the rock. Similarly, the method excludes grains that have impurities of other elements (except for Cd) or grains with numerous chalcopyrite inclusions, following the recommendations by Hutchinson and Scott (1981). The FeS mol% was calculated for each grain and plotted against temperature, the latter determined by stability fields in the Fe-Co-Ni-As and Fe-Co-Ni-S systems (Klemm 1965; Kaneda et al. 1986). Pressure values were then obtained from the pressure curves of Scott (1976) and Toulmin et al. (1991).

## 4.6 U-Pb Dating of Titanite

In order to constrain the timing of metamorphism, titanite dates were obtained by using Laser Ablation Inductively Coupled Plasma Mass Spectrometer (LA-ICP-MS) U-Pb dating. In total four thin sections (ALZ1800089A-1, 2, 3 and VNA007) were selected based on the presence of metamorphic titanite grains of at least 30 µm width. A total of 94 titanite grains were analysed within the four samples. BSE images were used to detect compositional zonation and overgrow patterns in the titanite grains.

U-Pb dating was performed at the LA-ICP-MS Laboratory at Lund University, using a Bruker Aurora Elite ICP-MS analyser coupled with a Teledyne Photon Machines G2 laser. A total of 107 spots were measured using a laser acceleration voltage of 1.26 kV and a square spot with a size of 25X25µm for sample ALZ180089A-1 and 30X30µm for the other samples. Calibration was performed using the natural titanite MKED1 (Spandler et al. 2016) as main reference material and the ONT2 natural titanite (Spencer et al. 2013) as secondary standard for quality check. The laser was operated with 300 shots at 10 Hz with a fluence of 1.5 J/cm$^2$ for the analyses. A step-forward-approach was used to subtract the baseline composition, which were measured for 30 seconds before each measurement. Common Pb was monitored by measuring $^{202}$Hg and mass 204 ($^{204}$Hg+$^{204}$Pb), baseline levels on mass 204 was around 440 cps with a standard error (SE) around 20 CPS (ca. 5-6 %). Data reduction was done with Iolite using the X_U_Pb_Geochron4 DSR (Paton et al. 2010; 2011) and the common Pb correction was done using the VizualAge DRS (Petrus and Kamber 2012).

# 5 Results

## 5.1 Field relations and petrography

The studied area is dominated by a metavolcanic succession (Figure 5) with limestone lenses and minor semi-conformable amphibolitic and granodioritic bodies. Late unconformable intrusions of varying compositions affect the succession, particularly towards the south of the Vena mining field and in the Dampetorp area.

The classification of the metavolcanic rocks is based on their dominant composition (e.g. rhyodacitic or dacitic), which is based on their mineralogical characteristics, and the presence of specific minerals such as cordierite, orthopyroxene or orthoamphibole. However, it must be noted that each rock type might show variations in compositions (e.g. the rhyodacitic metavolcanics also include slightly dacitic compositions; see section 5.2). Table 3 presents a summary of the mineral contents of the different rock types.

### 5.1.1 Rhyodacitic metavolcanics

Rhyodacitic metavolcanics are one of the most common rocks in the studied area, outcropping in most of the Dampetorp and Vena areas. These rocks are composed of fine-grained quartz, K-feldspar, plagioclase and biotite. They are foliated and sometimes banded with biotite rich domains. Locally they are migmatitic with leucosomes that vary in composition from Qz+Kfs- to Qz+Kfs+Pl- or Qz+Pl-rich (mineral abbre-

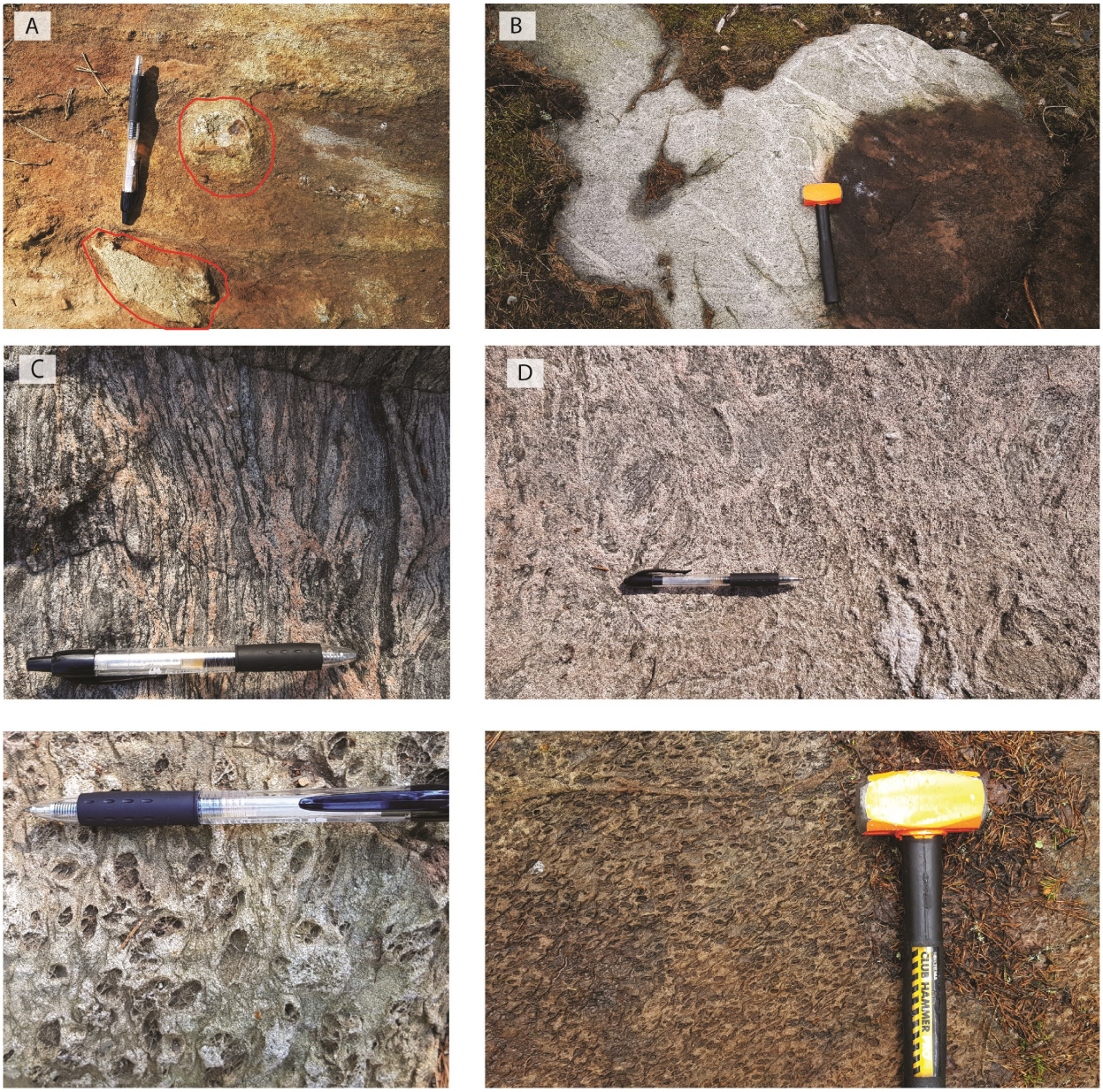


Figure 6. Volcanic and migmatitic structures in the rhyodacitic and cordierite bearing metavolcanic rocks. a) Silicified relict volcanic clasts. b) migmatitic metavolcanic rocks with Qz+Pl leucosome. c) Migmatitic metavolcanic rock in the Dampetorp area with Kfs+Qz leucosome. d) Migmatitic metavolcanic rocks with folded leucosome. e) Relict pumice lapilli structures. f) Pumice lapilli structures in the metavolcanic rocks.

viations in Appendix 1; Figure 6b-d). The rocks in the Dampetorp area are typically more migmatitic and their leucosomes are richer in K-feldspar (Figure 6c). Predominantly in the Vena area but also in the Dampetorp region, the metavolcanics show relict volcanic structures including lapilli and deformed pumice clasts (Figure 6a, e, f), which have been replaced by quartz ± plagioclase; the foliation usually wraps around these silicified clasts.

Most samples show various signs of deformation (Figure 7a-d), from serrated edges and subgrain rotations to preferential elongation of grains (Figure 7c-d), up to mylonitic textures (Figure 7a-b). However, strain intensity varies locally, with some domains being considerably less deformed than the surrounding rock. Regardless of the strain state, most rocks are typically composed of granoblastic quartz, K-feldspar and lesser amounts of plagioclase. Biotite is usually reddish-brown (Ti-rich) and forms elongate laths oriented along the foliation. Many samples are finely banded with alternating biotite-rich and Qz+Kfs+Pl bands. Small muscovite grains can be found as inclusions within K-feldspar and quartz crystals. Late chlorite can be seen replacing partially some of the biotite crystals. Some samples also have stretched and rounded finer-grained biotite domains (Figure 8a-b) that replace previous structures in the rock. Zircon is a common accessory mineral and forms rounded crystals that occur as inclusions and is easily recognized within biotite.

Occasionally, the rhyodacitic metavolcanic rocks contain pale green amphibole (Figure 8c) and

Table 3. Summary of minerals present in the samples. Abbreviations can be found in Appendix 2.

| Lithology | Qz | Pl | Kfs | Bt | Ms | En | Cpx | Ath | Cam | Zo | Czo | Chl | Ttn | Grt | Srp | Cal | Crd | And | Rt | Tur | Zrn | Ap |
|---|---|---|---|---|---|---|---|---|---|---|---|---|---|---|---|---|---|---|---|---|---|---|
| Rhyolitic metavolcanics | X | / | X | X | / | | / | | / | / | / | / | / | | | / | | | / | | X | / |
| Dacitic metavolcanics | X | X | | X | | | | | | X | X | X | | | | / | | | | | | |
| Cordierite-bearing metavolcanics | X | X | X | X | X | / | | / | | | | X | | | | | X | | | | | |
| Enstatite-anthophyllite metavolcanics | X | X | X | / | / | X | / | X | / | / | / | X | / | / | X | | / | X | | X | / | / |
| Limestone and calcareous skarns | X | | | | | | / | | / | / | / | | X | X | | X | | | | | | / |
| Amphibolite | X | X | | | | | | | X | | | | X | | | | | | X | | | |
| Granodiorite | X | X | X | X | X | | | | | | | X | | X | | | | | | | | |
| Post orogenic granitoids | | | | | | | | | | | | | | | | | | | | | | |
| Syenite | | | X | | | | | | | | | X | | | | | | | | | | |
| Pegmatites | X | X | X | / | | | | | | | | / | | | | | | | | | | |
| Diabase | X | X | | | | | X | | | | | | | | | | | | X | | | |

X=present in all samples

/= present in some of the samples

Blank=not present

titanite. In these rocks, amphibole is mostly euhedral to anhedral poikiloblasts with numerous rounded to sub-rounded inclusions of quartz, plagioclase and K-feldspar. However, in certain rocks, amphiboles occur as finer grained irregular crystals. Similarly, titanite is present as millimetre long, rounded or irregular crystals, or as smaller euhedral crystals. Amphibole and the titanite appear associated as they commonly form amphibole-rich bands in the metavolcanic rocks, alternating with the amphibole-poor domains (Figure 8c-d).

### 5.1.2 Dacitic metavolcanics

In contrast to the rhyodacitic metavolcanics, the dacitic rocks are dominated by plagioclase and quartz with rare K-feldspar. The extent of these rocks is unknown but observations from drill cores suggest that they are intercalated with the rhyolitic metavolcanics, and observations on the surface suggest that they outcrop preferentially in the NE Vena area.

Under the microscope, the dacitic rocks are fine grained and composed of granoblastic plagioclase, quartz with serrated grain boundaries, abundant chlorite, and subhedral to euhedral crystals of clinozoisite (Figure 9). Chlorite occurs in bands that are oriented along the foliation, and locally appears to be part of small-scale folding together with opaque veinlets (Figure 9a-b). Two types of chlorite can be found. The first type forms laths with perfect cleavage (Chl-1; Figure 8a-b), and the second (Chl-2) replaces partially epidote crystals or form fine-grained globular aggregates (Figure 9).

### 5.1.3 Cordierite-bearing metavolcanics

Cordierite-bearing metavolcanic rocks have compositions similar to the rhyodacitic volcanics but contain cordierite and other Mg- and Al-rich phases. These rocks have been found in the Vena area only and are characterized by abundant pumice lapilli structures. (Figure 6e-f). Lapilli clasts are typically oriented and slightly elongate with the foliation, and their size varies throughout the unit. These clasts have commonly been pseudomorphed by quartz and/or plagioclase aggregates. Locally, these rocks are migmatitic with plagioclase-quartz rich leucosome. In general, this type of metavolcanic rocks form localized, relatively thin units, both in outcrop and in the drill cores.

Under the microscope, this type of rock shows abundant microcline poikiloblasts in a matrix of quartz, K-feldspar and biotite. Biotite forms elongate laths in aggregates that define a coarse foliation. Cordierite occurs as relict porphyroblasts that are often replaced by needle-like aggregates of chlorite and muscovite ("pinnitization"; Figure 10a-b). Andalusite forms square-shaped porphyroblasts that are usually in contact with or surrounded by biotite crystals (Figure 10a-b). In many cases, late chlorite has replaced partially or totally the biotite crystals. Scarce minute garnet crystals as well as subhedral to euhedral greenish tourmaline crystals are occasionally found in these rocks (Figure 10c-d).

### 5.1.4 Anthophyllite-bearing metavolcanics

Metavolcanic rocks that contain anthophyllite look similar to the rhyodacitic metavolcanics in hand specimen and in outcrop. They are both fine grained and rich in quartz, feldspars and biotite; however, the anthophyllite-bearing rocks also contain Mg-rich minerals such as anthophyllite and enstatite. These rocks have been recognized in the Vena area only, but their presence in the Dampetorp mining field cannot be discarded.

In thin section, the anthophyllite-bearing rocks are composed of fine-grained quartz, different proportions of plagioclase and K-feldspar, and biotite orient-

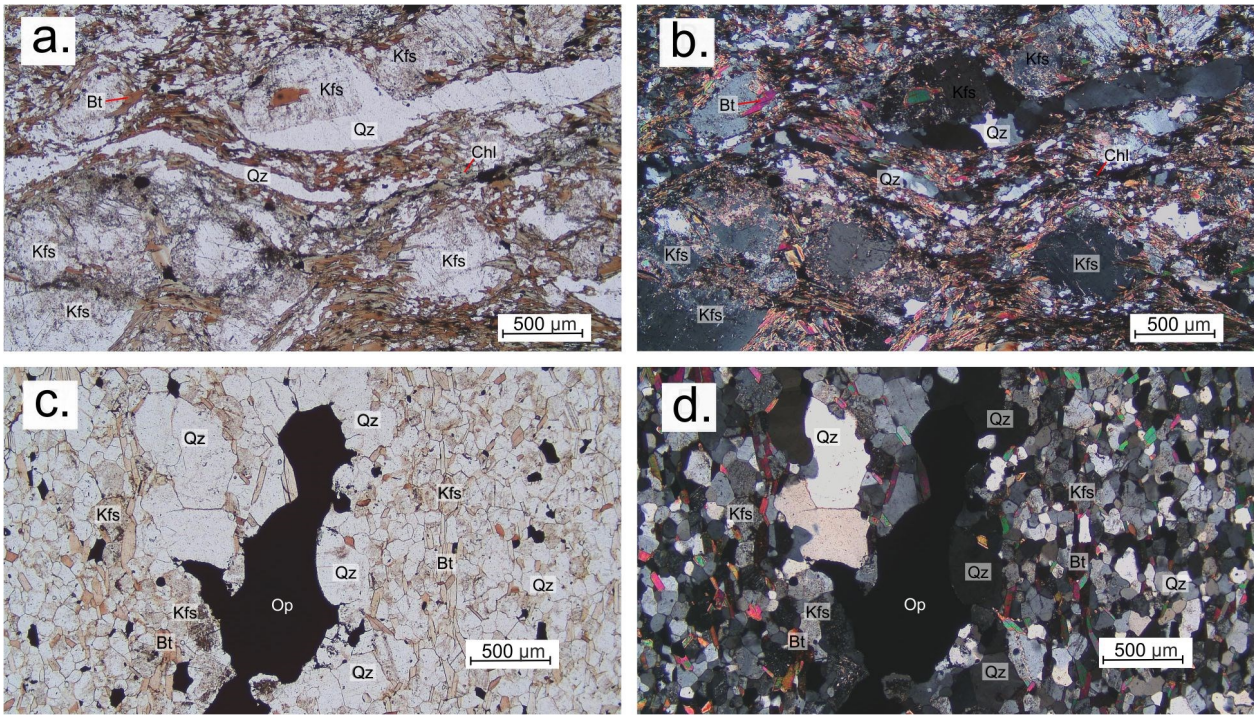


Figure 7. Photomicrographs of rhyodacitic rocks (a) and (c) under PPL; (b) and (d) the same textures under XPL a & b) Mylonitic texture with Kfs porphyroclasts, wrapped by quartz ribbons and biotite bands. Minor and partial replacement of biotite by chlorite (sample ALZ190012A-1). c & d) Rhyodacite showing aligned biotite crystals and slightly elongated quartz grains (sample ALZ190034A-1).

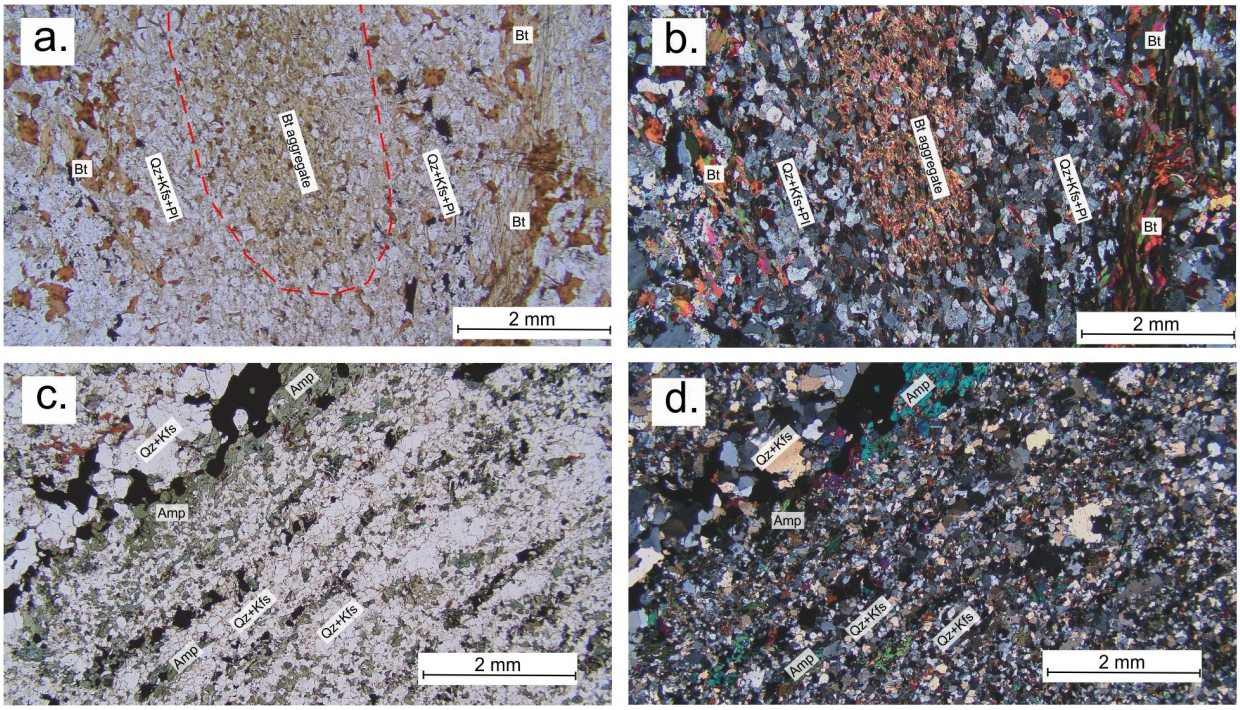


Figure 8. Photomicrographs of the compositional banding in rhyodacitic metavolcanic rocks showing (a) elongated biotite-rich domains and (c) amphibolitic banding both in PPL; (b) and (d) show the same textures under XPL respectively.

ed along the foliation. A main characteristic is the presence of porphyroblasts of enstatite surrounded by poikiloblastic anthophyllite that encloses rounded inclusions of feldspar and quartz (Figure 11a-b). Anthophyllite poikiloblasts are also found without enstatite, enclosing quartz, plagioclase and K-feldspar (Figure 11c-f). Both enstatite and anthophyllite are affected by low-grade partial serpentinization and chloritization. Muscovite occurs as small crystals within feldspars or in partial replacements of anthophyllite poikiloblasts (Figure 11e-f). Some samples also contain cordierite, partly replaced by a muscovite and chlorite. The accessory minerals in these rocks include zircon, apatite and rutile, of which the latter is present as coronas around ilmenite crystals.

In a similar fashion to the rhyolitic metavolcanics, some anthophyllite-bearing rocks have bands with greenish amphibole and titanite. Where present, amphibole also forms poikiloblasts with quartz, plagioclase and K-feldspar inclusions, and is typically associated with both irregular and euhedral grains of titanite. In rare cases the rocks are affected by a late vein filling of chlorite, muscovite, and calcite. Such veinlets crosscut the foliation and form irregular interconnected networks.

### 5.1.5 Limestone and calcareous skarn

In the area of study, no major outcrop of limestone or calcareous skarn was found; however, in the drill cores from the Vena area, limestone and calcareous skarn thin intervals can be recognized. There they form thin lenticular bodies intercalated with the metavolcanics. Most calcareous intercalations have been altered and form different types of skarn or calc-silicate rocks. Calcareous skarns vary significantly in composition, from amphibole-garnet and pyroxene-garnet-epidote skarns to vesuvianite-bearing skarns.

Only one sample (ALZ180089A-1) of a skarn association was investigated. This sample consists of sub-parallel bands of subhedral to euhedral garnet-clinozoisite, with minor zoisite and amphibole intergrowths with interstitial anhedral carbonate (Figure 12). Amphibole is finer grained than zoisite and tends to be surrounded by the latter. Minor clinopyroxene is associated with amphibole; both minerals are concentrated in bands surrounding the garnet-zoisite aggregates. Discontinuous bands or veinlets of quartz crosscut the skarn subparallel to its banding. The quartz veinlets seem to have crystallized late as they surround euhedral to subhedral garnet crystals (Figure 12a-b); however, quartz is also found as inclusions within the garnet crystals. Within these quartz bands, tiny euhedral titanite crystals occur in small aggregates. Titanite occurs as coarser and more irregular crystals in the skarn bands.

### 5.1.6 Amphibolite

Outcrops of amphibolite can be found in both the Vena and Dampetorp areas as bodies subparallel to the folia-

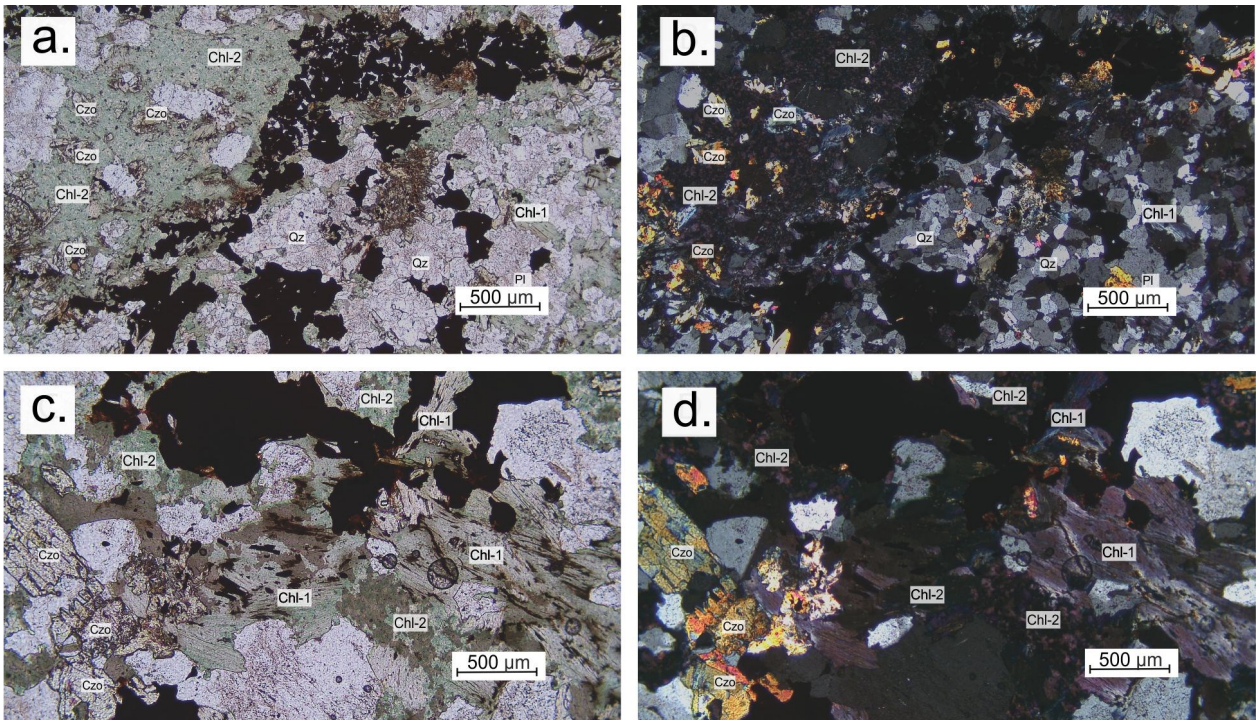


Figure 9. Photomicrographs of dacitic rocks. a) Typical assemblage in sample ALZ180072A-1 with clinozoisite (Czo) porphyroblasts, fine-grained aggregates of chlorite (Chl-2) and minor tabular chlorite crystals (Chl-1) in PPL; (b) show the same assemblage in XPL. c) Tabular laths of chlorite (Chl-1) associated with finer grained chlorite (Chl-2) and minor clinozoisite porphyroblasts in PPL; (d) the same textures under XPL.

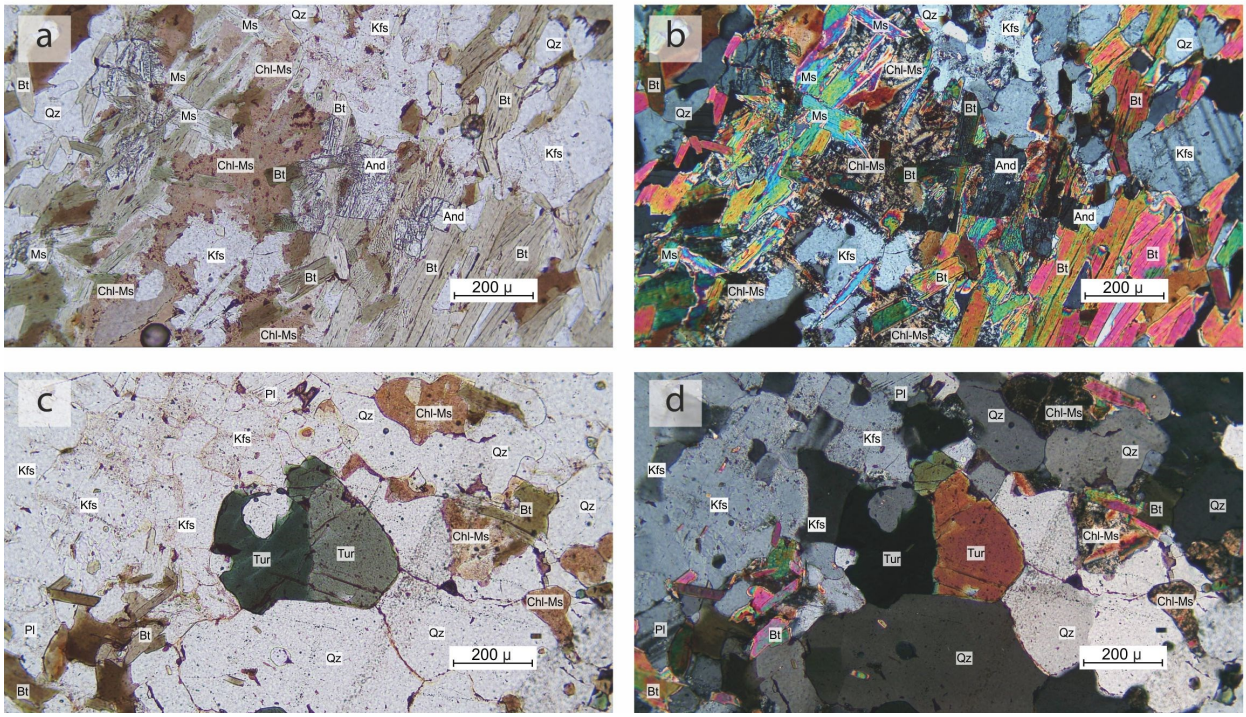


Figure 10. Textures of the cordierite-bearing sample, (a) and (c) under PPL; (b) and (d) the same textures under XPL. a & b) sub -rectangular andalusite (And) porphyroblasts surrounded by chlorite-muscovite (Chl-Ms) aggregates that pseudomorph cordierite crystals. c & d) Tourmaline porphyroblast within a quartz-K-feldspar matrix along with minor Chl-Ms pseudomorphs after cordierite.

tion. In comparison to the metavolcanic rocks, amphibolite outcrops seem absent of migmatitic structures. Sometimes pegmatite or quartz veins are present along the contacts of amphibolitic bodies and the surrounding metavolcanic rocks.

In thin section, most amphibolites are composed of mm to cm sized porphyroblasts of green to bluish-green amphibole, and finer grained plagioclase and quartz (Figure 13). Amphibole porphyroblasts have a preferred orientation and define a coarse foliation. Fine-grained titanite crystals occur, either as rounded anhedral crystals or as well-defined euhedral crystals. Plagioclase- and quartz-rich bands alternate with amphibole-rich domains, where in the plagioclase rich areas, amphibole forms disseminated small sub-rounded crystals (Figure 13c-d).

### 5.1.7 Granodiorite

Sub-volcanic granodioritic intrusions can be found in the study area, crosscutting both the amphibolites and the metavolcanic rocks. A coarser grain size distinguishes them from the metavolcanic rocks. They are composed of quartz, plagioclase, K-feldspar, biotite and scarce garnet, locally with feldspar phenocrysts up to 5 cm.

In thin section, granodiorite samples have microcline phenocrysts with plagioclase and minor anhedral quartz crystals (Figure 14). They show evidence of deformation such as quartz crystals with serrated edges and subgrain rotation. Biotite forms aggregates in which individual grains are randomly oriented; biotite is locally partially replaced by chlorite (Figure 14a-b). Anhedral muscovite grains are enclosed by K-feldspar. Most of the plagioclase and K-feldspar crystals are moderately sericitized. Myrmekitic quartz-feldspar and biotite-quartz are also present. Small rounded crystals of ilmenite are surrounded by coronas of rutile and enclosed by biotite crystals.

Rounded porphyroblasts of pinkish garnet are present locally (Figure 14c-d). They commonly have fractures filled with chlorite and when in contact with K-feldspar, tiny crystals of chlorite nucleate on their borders towards the feldspar crystal. Garnet hosts inclusions of quartz, biotite and K-feldspar. Abundant sub-rounded zircon crystals can be found as inclusions, especially within biotite crystals.

### 5.1.8 Post-orogenic granitoids

Post-orogenic granitoids include the Askersund granite (Persson & Wikström 1993), associated pegmatites, syenitic intrusions, and bimodal (felsic-mafic) intrusions (Figure 15A). The Askersund granite intrudes the southern part of the Vena area and outcrops in the northern-central and western parts of the Dampetorp area.

The bimodal intrusive rock (also referred as hybrid intrusion by Wikström & Karis 1991) forms a composite intrusion aligned in a NW-SE direction, that only outcrops in the Dampetorp area. This intrusion varies in character from a mafic rock veined by granitic pegmatite to a granite veined by mafic material. A single syenitic intrusion is found towards the west part of the Vena area, next to the Åmmelången lake. Pegmatitic intrusions (Figure 15b) are common throughout the whole area of study, but especially in the Dampetorp area, where they are in contact with miner-

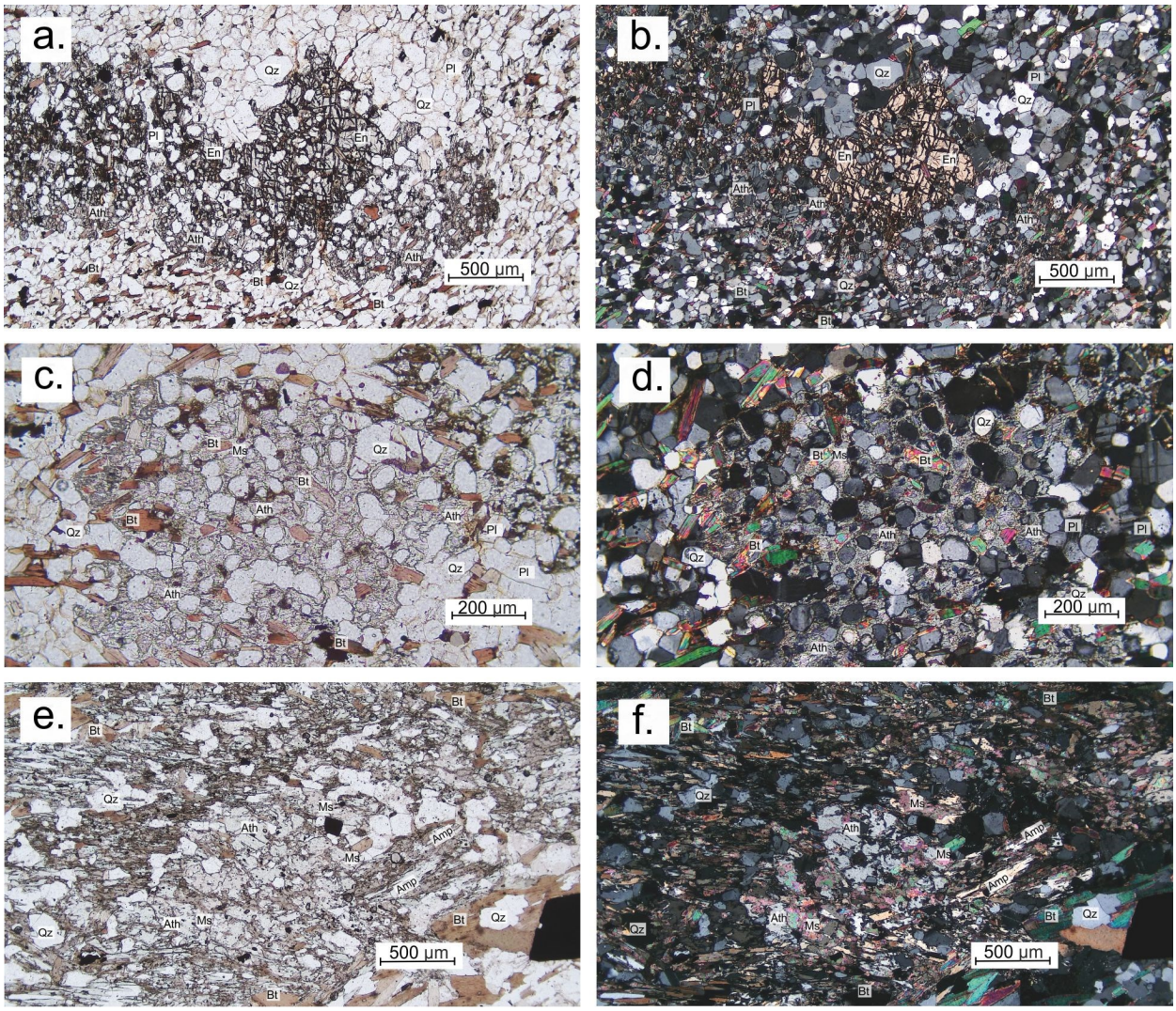


Figure 11. Photomicrographs of the textures and minerals assemblages of anthophyllite-bearing metavolcanics, (a), (c) and (e) under PPL; (b), (d) and (f) the same textures under XPL. a & b) enstatite (En) poikiloblast surrounded by anthophyllite (Ath), and overgrowing quartz and plagioclase crystals in a metavolcanic rock (Sample ALZ180067A-1).c & d) Ath poikiloblast with Qz and Pl inclusions (Sample ALZ180067A-1). e & f) PPL image of an Ath poikiloblast being partially replaced or overgrown by muscovite (Ms) (Sample ALZ180037A-1).

alized areas. Additionally, it is typical for the intrusives to include country rock inliers. For instance, the Nickelgruvan mine is hosted within a metavolcanic block within the Askersund granite in the Dampetorp area.

Only the syenite and a micro-pegmatite have been investigated. Under the microscope (Figure 15c-d), the syenite is composed of perthitic K-feldspar with serrated edges, abundant subgrains, and undulose extinction. Plagioclase occurs as angular inclusions within the potassic feldspar. Disseminated aggregates of chlorite occur throughout the rock, commonly having relict biotite cleavage and sometimes opaque inclusions. Subhedral epidote crystals can be found disseminated in the sample and is frequently associated with the chlorite.

The pegmatites are essentially made up of K-feldspar, quartz, biotite and minor plagioclase phenocrystals. The observed pegmatite intrudes relatively parallel to the foliation of the metavolcanic rocks. The contacts of the pegmatite are diffuse and finer-grained than the central parts. Around the pegmatite there is evidence of recrystallization in the metavolcanic rock. Local deformation associated to the pegmatite intrusion can be recognized within the metavolcanic rock as small-scale folding or bending of the metavolcanic layers.

### 5.1.9 Diabase

Late diabase dikes intrude the whole sequence southwest of the Vena area. The dikes are undeformed and unmetamorphosed. Commonly, they are fine grained and mainly composed of elongated plagioclase crystals that locally show flow-aligned texture (Figure 15e-f). These crystals are in an extremely fine-grained matrix of clinopyroxene with abundant disseminated opaques. The rock has yellowish alteration around opaque phenocrysts. A complex micro-symplectitic growth occurs between the opaques and the plagioclase crystals, also containing isolated anhedral crystals of rutile within

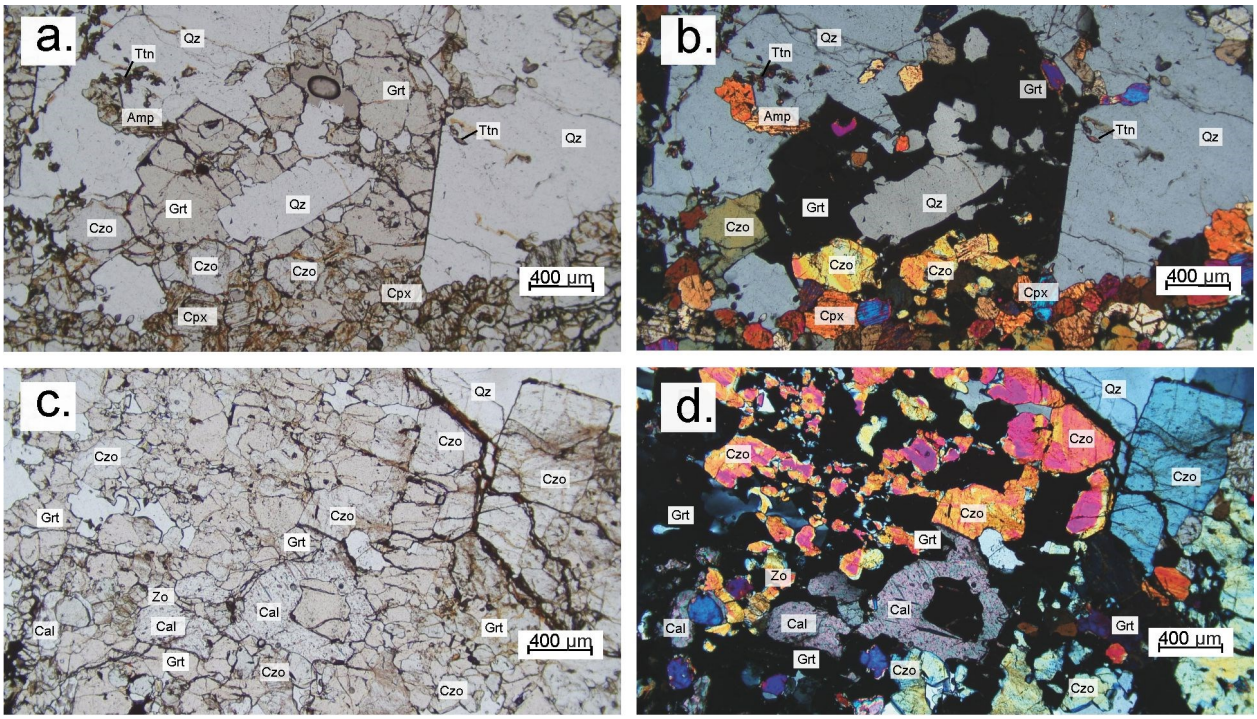


Figure 12. Photomicrographs of skarn textures of sample ALZ180089A-1, (a) and (c) under PPL; (b) and (d) the same textures under XPL. a &b) garnet (Grt) porphyroblast growing from clinopyroxene (Cpx), clinozoisite (Czo) aggregate into a quartz band; minor titanite (Ttn) crystals grow on this band. c & d) garnet and clinozoisite subhedral aggregates with interstitial calcite.

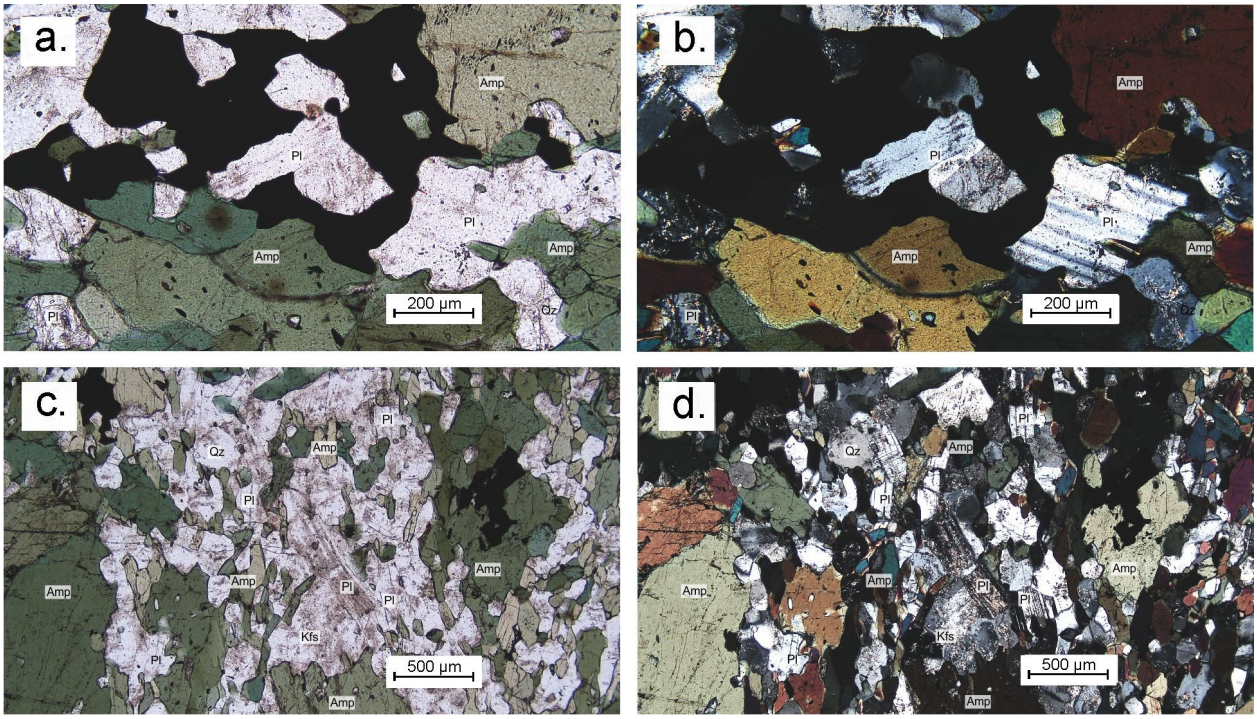


Figure 13. Photomicrographs of amphibolite textures in sample ALZ180033A-1, (a) and (c) under PPL; (b) and (d) the same textures under XPL. a & b) amphibole (Amp) porphyroblasts with subhedral plagioclase (Pl) crystals and interstitial mineralization. c & d) subrounded Amp in quartz- and plagioclase-rich bands.

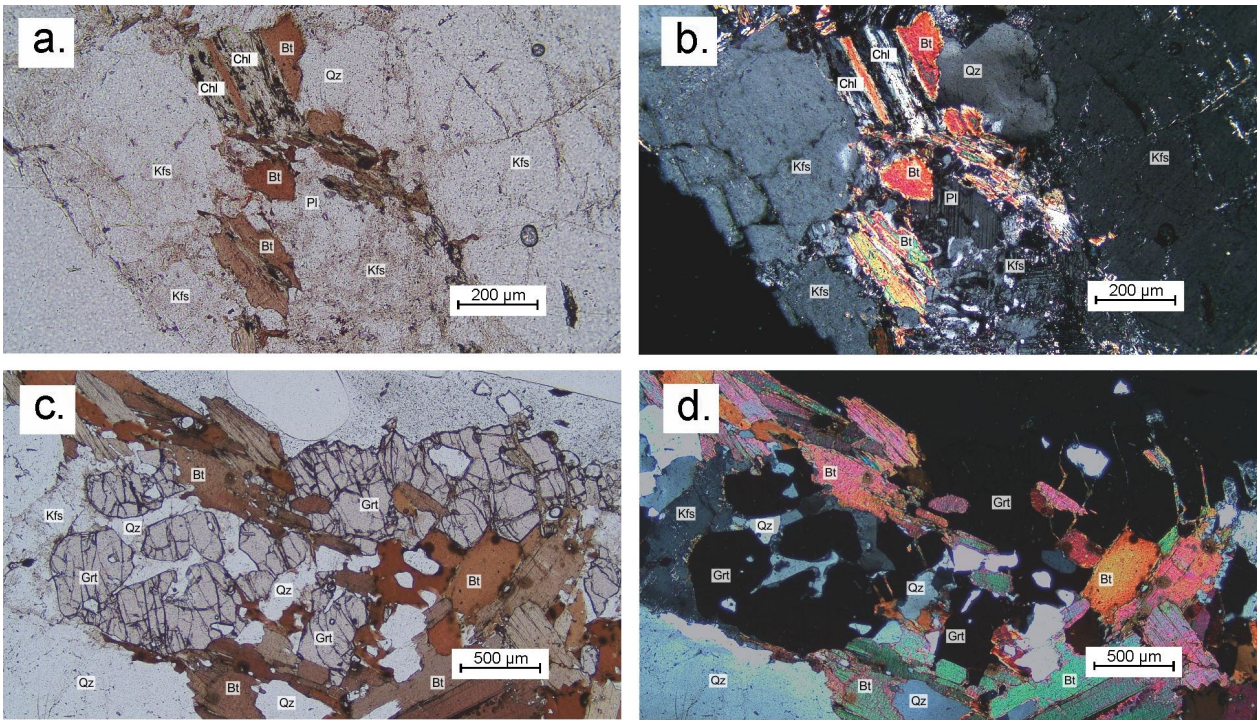


Figure 14. Photomicrographs of textures in the granodiorite sample, (a) and (c) under PPL; (b) and(d) the same textures under XPL. a & b) a biotite (Bt) crystal being partially replaced by chlorite (Chl), with myrmekitic Kfs-Qz crystal growths underneath the Bt. c & d) PPL image of pinkish garnet (Grt) porphyroblasts in the granodiorite.

the yellowish alteration. Veinlets filled with coarser quartz, plagioclase with minor biotite and some relict plagioclase crystals that have been completely replaced by the symplectitic assemblage can be found.

## 5.2 Geochemistry

SGU analyses of chemical compositions for 98 samples include samples from outcrops, waste piles, and drill-cores, both mineralized and unmineralized. The samples classified as mineralized contain different quantities of ore-minerals, from traces to a strong pervasive mineralization. In general, the metavolcanic rocks show a range of compositions from rhyolitic to andesitic (Figure 16a), with some samples falling in the alkali-rich series between trachytes and trachybasalts. In comparison, amphibolites range from andesitic to basaltic compositions with samples within the trachytic series. However, when plotted in the igneous spectrum diagram of Hughes (1973), most of the volcanic rocks fall outside of the igneous spectrum (Figure 17a), being predominantly K-enriched. Therefore, the immobile element classification of Winchester and Floyd (1977) is more appropriate for identifying the original compositions of the rocks. In this scheme (Figure 17b), most of the metavolcanics have a rhyodacitic composition but cover and spectrum from rhyolite to andesite. It must be noted that on average the metavolcanics with iron oxide mineralization show the most mafic compositions from the whole set of metavolcanic rocks. Conversely, amphibolite is mostly composed of andesite-basalt with a few samples within dacitic compositions.

The Svecofennian intrusives have a predominantly granodioritic composition (Figure 16b). In contrast, late orogenic intrusives show compositions ranging from syenites to granites. The hybrid intrusive rock has a granitic composition on its felsic end member and a gabbroic composition on its mafic end member.

In terms of rare earth element (REE) distribution the metavolcanic rocks, are enriched in light rare earth elements (LREE) compared to heavy rare earth elements (HREE) with a strong negative Eu anomaly (Figure 19a). However, in unmineralized samples the Eu anomaly is less pronounced. Similarly, the syn-orogenic granodiorites (Figure 19e) have an analogous enrichment in LREE in contrast with HREE with a comparable Eu negative anomaly. In opposition, most of the granites show little to no Eu anomaly.

The amphibolites have a moderate enrichment of LREE in comparison with HREE and an Eu negative anomaly (Figure 19c) which is more noticeable in mineralized amphibolites. The diabase sample shows a similar enrichment pattern, only that it lacks the Eu anomaly and has a more pronounced enrichment of LREE in contrast to HREE. The Fe-oxide skarns and metavolcanics are enriched in LREE, where the Fe-skarns are significantly more enriched in these and have positive Eu anomalies. On the contrary, calcareous skarns display only a moderate LREE enrichment compared to HREE and have a negative Eu anomaly.

MORB normalized patterns for most rocks (Figure 19b, d and f) show an enrichment of K, Rb, Ba, Th and LREE. However, the metavolcanics, granodiorite and granite have marked P and Ti negative anomalies with a minor Ta anomaly. In contrast, the amphibolite lacks the P anomaly, but has a more pronounced Ta anomaly. In terms of Ti, only unmineralized amphibolite show a negative anomaly.

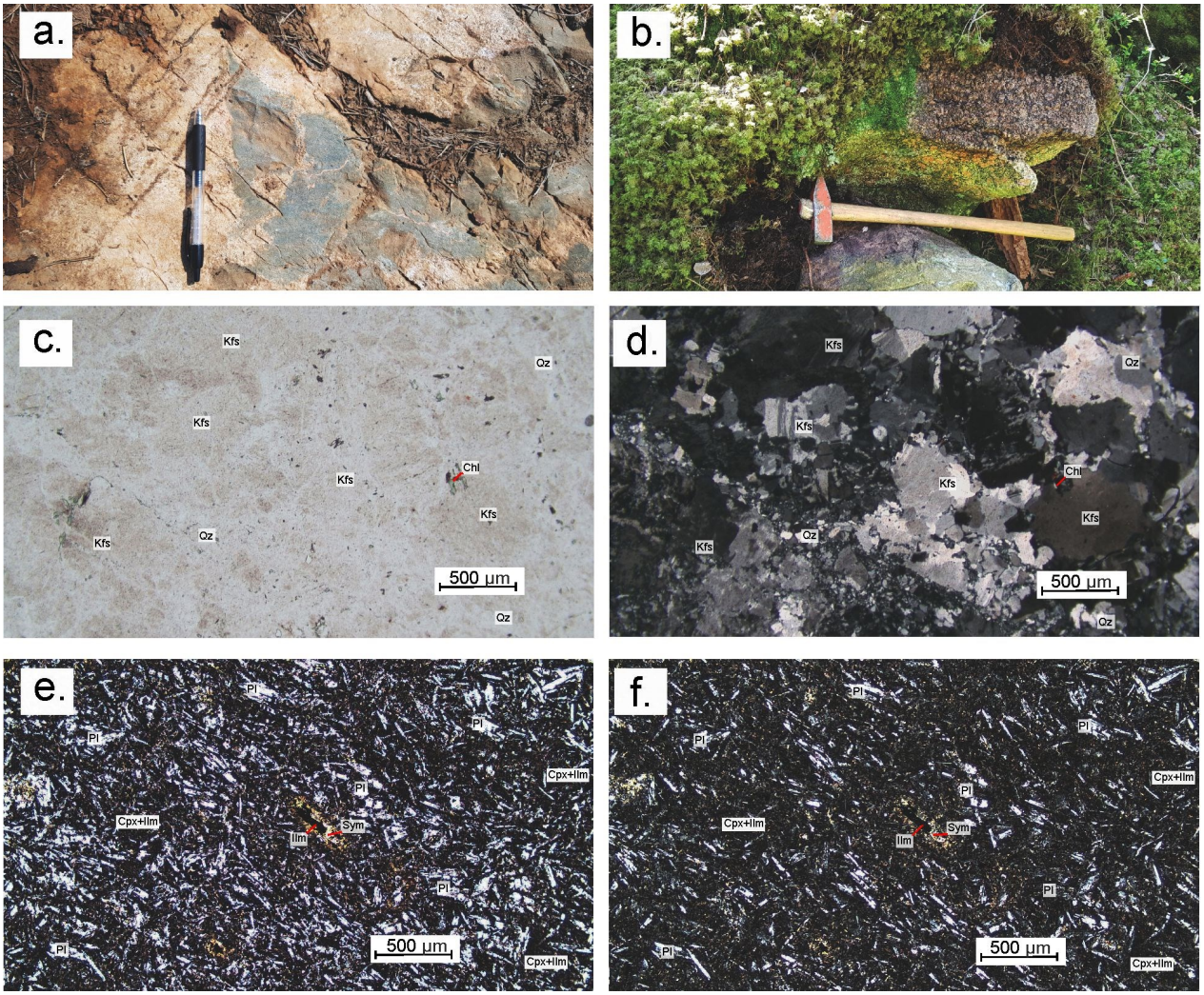


Figure 14. Field and textural relationships of late-orogenic intrusives. a) Mafic intrusive fragment in a felsic intrusion. b) contact between a pegmatite (upper part) and the metavolcanics (lower part). c)syenite showing a predominance of Kfs phenocrystals, with minor chlorite aggregates in sample ALZ180087A-1 under PPL; (d) same textures under XPL. e) typical texture in the diabase of plagioclase (Pl) crystals, in a Cpx+Ilm matrix under PPL (Sample ALZ180002A-1); (f) same textures under XPL.

## 5.3 Mineral chemical compositions

The results of the EDS-SEM studies of non-ore minerals are presented below. Mineral analytical data are provided as Tables 1-14 in Appendix 3.

### 5.3.1 Feldspar

Plagioclase and K-feldspar are major constituents of the studied rocks. A total of four plagioclase and four K-feldspar grains were analysed. Most plagioclase crystals have a predominant albitic composition, but the albite-content varies from 51 mol% to 98 mol%. In general, the Fe-oxide sample contains the more anorthite rich plagioclase, whereas the dacitic metavolcanics have the higher albitic components In contrast to the plagioclase crystals, are mostly pure except for one analysis that show a minor albitic component (5 mol%) which could represent minor solid-solution or a mixed analysis. Minor trace quantities of Fe are occasionally found within plagioclase and K-feldspar which is assumed to be $Fe^{3+}$.

### 5.3.2 Amphibole

Optically two types of amphibole crystals can be found in the metavolcanic rocks. The first type is green to greenish blue poikilo- and porphyroblasts of clinoamphibole. The second type is low birefringence poikiloblasts of orthoamphibole. The analysis of 9 grains of orthoamphibole reveal a Mg-rich composition close to anthophyllite. However, is part of the solid solution anthophyllite-gedrite and contain up to 30 mol% of the Fe end-member. In comparison, the two analysis of the greenish amphibole reveal that they have composition close to actinolite. Similarly, to the orthoamphibole the clinoamphiboles form a solid solution between ferro-actinolite (Fe-rich) and tremolite (Mg- rich), being slightly richer in the Mg end-member (53 mol%). The petrographic and chemical observations suggest that both, anthophyllite and actinolite can coexist within the same sample.

### 5.3.3 Pyroxene

The anthophyllite-bearing rocks host the majority of the orthopyroxene occurrences. In comparison, clino-

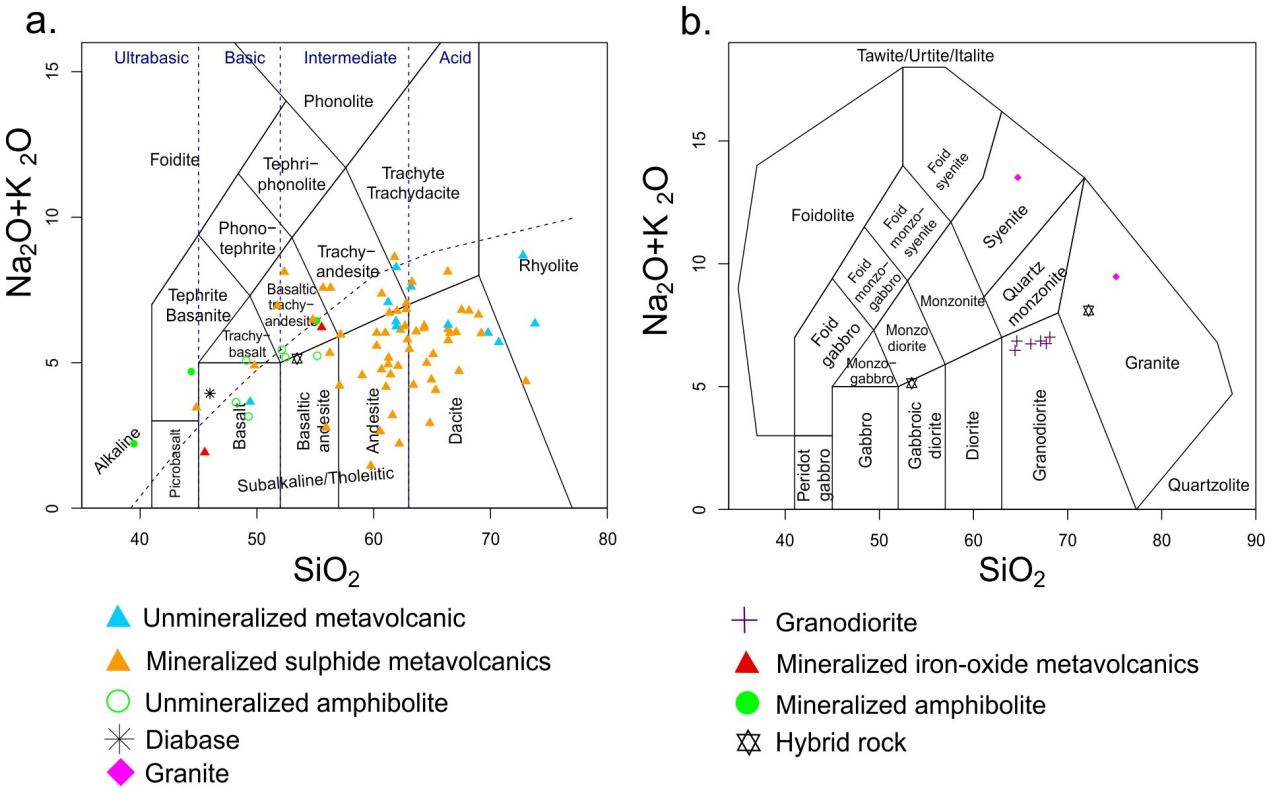


Figure 16. Major element rock classification plots for volcanic and plutonic rocks. a) TAS plot for classification of volcanic rocks metavolcanic and amphibolitic rock (after Le Bas 1983). b) TAS plot for the classification of plutonic rocks (after Middlemost 1994).

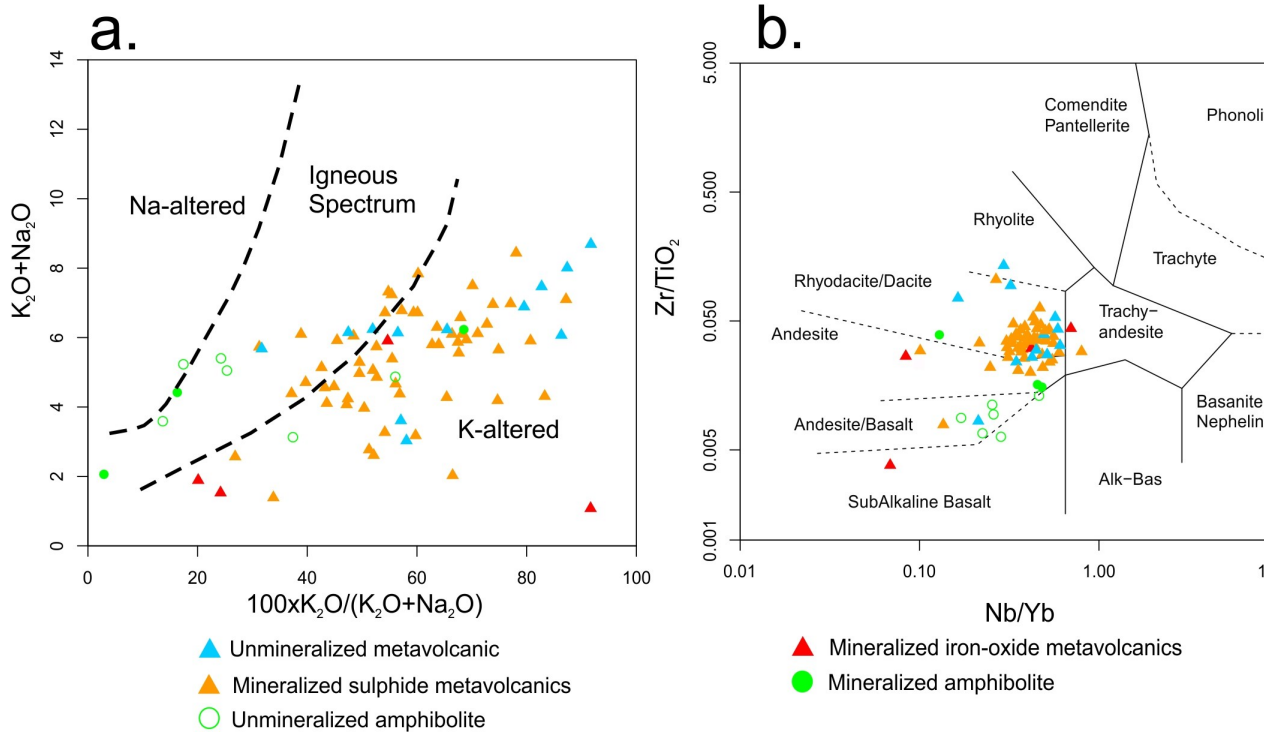


Figure 17. Elemental plots of K-Na alteration and immobile element classification for igneous rocks. a) Metavolcanics and amphibolites plotting in the right of the igneous spectrum at the Na-K alteration plot (after Hughes 1973). b) Rock classification diagram using immobile elements (After Winchester & Floyd 1977).

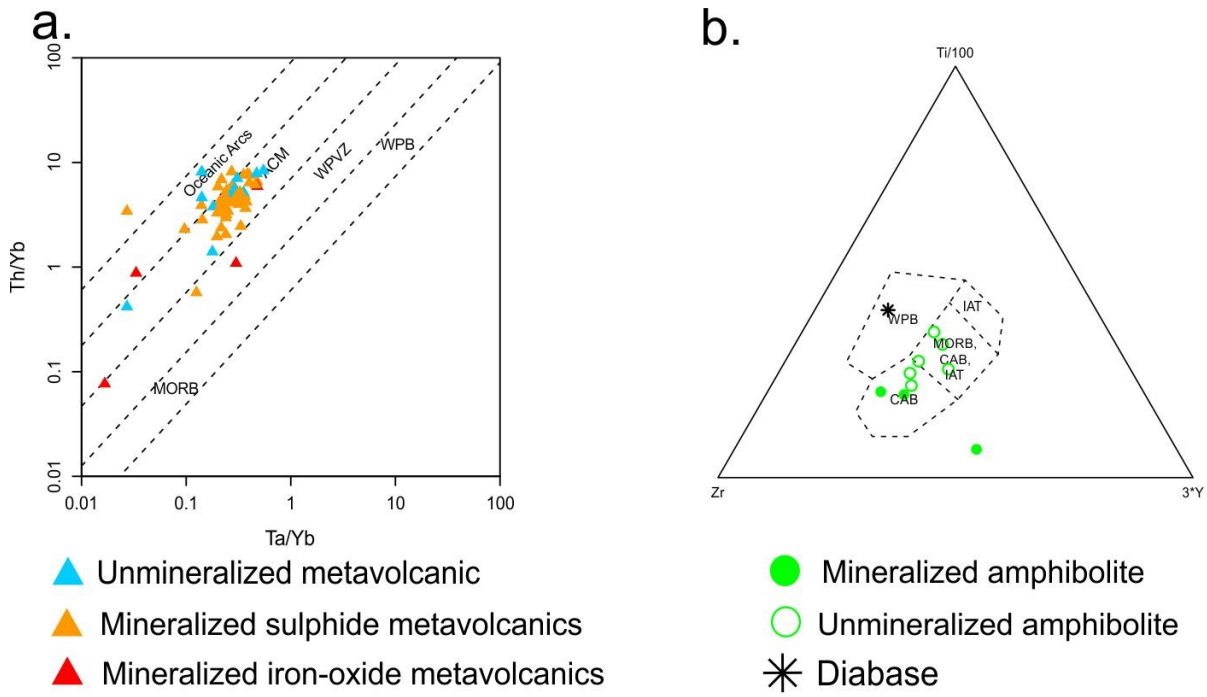


Figure 18. Geotectonic classification plots for felsic and mafic igneous rocks. a) Geotectonic affinity plot for felsic igneous rocks. ACM= active continental margin, WPVZ= within plate volcanic zones, WPB=within plate basalt, MORB=mid-ocean ridge basalt (after Schandl & Gorton 2002) b) Geotectonic affinity plot for mafic rocks. CAB= continental arc basalt, IAT= island arc tholeiite (after Pearce & Cann 1973).

pyroxenes are found sporadically in other metavolcanic samples and calcareous skarns. In total, one pyroxene crystal in an anthophyllite-bearing metavolcanic rock, five clinopyroxene crystals in calcareous skarn, and two clinopyroxene grains in another metavolcanic sample, were analysed. The enstatite grain is surrounded by anthophyllite and partially replaced by fine-grained serpentine and chlorite. The analysis of this pyroxene is close to enstatite-ferrosilite in composition with Mg/(Mg+Fe) = 0.58, and small amounts of Ca (0.02 atoms per 6 oxygens). However, the stoichiometry of this analysis is not ideal due to either analytical problems or microscopic replacement of the pyroxene by orthoamphibole. In comparison pyroxene in other samples vary in composition from diopside to hedenbergite (Mg/(Mg+Fe) = 0.40-0.84). In the calcareous skarn sample, pyroxenes form a solid solution between hedenbergite and diopside with Mg numbers between 0.41 and 0.52. In the metavolcanic samples, clinopyroxene is more enriched in the diopside component with an average Mg number of 0.82.

### 5.3.4 Garnet

Garnet is a main component in some of the calcareous skarns, an accessory mineral in granodiorite, and in rare cases also found in the metavolcanic rocks. A total of six garnet grains of the calcareous skarn were analysed. Garnet is grossular-rich in the skarn, with minor andradite, almandine and spessartine components Transects and elemental maps of garnet (Figure 20) in the skarn show no compositional zoning, and all analysed garnet grains have similar compositions with an average of 76 mole% grossular, 17 mol% andradite, 5 mol% almandine, and 1 mol of spessartine. In comparison, garnet in the granodiorite garnet is almost pure almandine (94 mol %) with minor pyrope (6 mol %).

### 5.3.5 Clinozoisite

A total of eight clinozoisite grains were analysed within the skarn sample (ALZ180089A-1), and clinozoisite grains in different metavolcanic rock samples. All the grains within the skarn sample are clinozoisite with minor Fe contents, varying from 4.92 to 8.81 wt% of $Fe_2O_3$. Zoisite was only analysed in sample ALZ180089A-2, where it is devoid of Fe and slightly poorer in Al in comparison to clinozoisite. Although, they were not analysed, zoisite is also present in the

Figure 19. Chondrite and MORB normalized REE plots for the rocks in the area of study. a) Chondrite normalized REE plot of mineralized and unmineralized metavolcanic rocks (after Boynton 1984). b) MORB normalized REE plot of mineralized and unmineralized metavolcanic rocks (after Pearce 1983). c) Chondrite normalized REE plot of mineralized and unmineralized amphibolites and the diabase (after Boyton 1984). d) MORB normalized REE plot of mineralized and unmineralized amphibolites and the diabase (after Pearce 1983). e) Chondrite normalized REE plot of granodioritic rocks and post-orogenic granitoids (after Boynton 1984). f) MORB normalized REE plot of granodioritic rocks and post-orogenic granitoids (after Pearce 1983). g) Chondrite normalized REE plot of iron oxide metavolcanics and skarns. Note the Eu positive anomaly in skarns (after Boynton 1984). h) Chondrite normalized REE plot of calcareous skarns (after Boynton 1984).

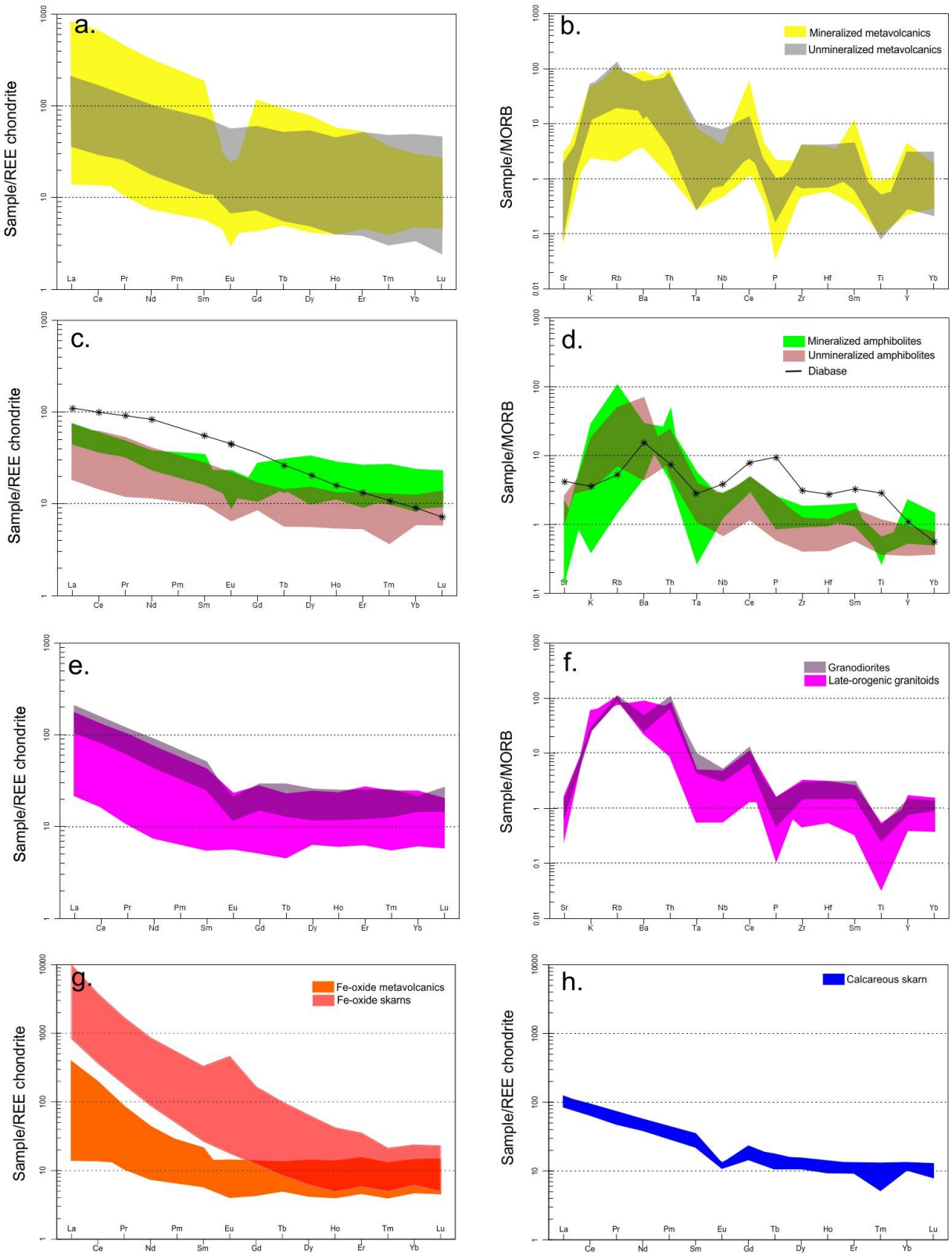
a.
Sample/REE chondrite
La Ce Pr Nd Pm Sm Eu Gd Tb Dy Ho Er Tm Yb Lu
b.
Mineralized metavolcanics
Unmineralized metavolcanics
Sample/MORB
Sr K Rb Ba Th Ta Nb Ce P Zr Hf Sm Ti Y Yb
c.
Sample/REE chondrite
d.
Mineralized amphibolites
Unmineralized amphibolites
Diabase
Sample/MORB
e.
Sample/REE chondrite
f.
Granodiorites
Late-orogenic granitoids
Sample/MORB
g.
Fe-oxide metavolcanics
Fe-oxide skarns
Sample/REE chondrite
h.
Calcareous skarn
Sample/REE chondrite

skarn and in the dacitic metavolcanics where it coexists with clinozoisite.

### 5.3.6 Hydrous phases

Chlorite and biotite, together with clay minerals and muscovite constitute the main hydrous silicate phases; however, the latter two were not analysed. A total of seven chlorite crystals in five different samples were analysed. The analysed chlorites occur in different settings, such as biotite replacements, veinlets crosscutting sulphides or needle-like aggregates around ore minerals. Three essential types of chlorite species were discovered: Mg-rich or clinochlore chlorite was found primarily as replacement of biotite. In contrast, Fe-rich chlorite (chamosite and Al-Fe-rich chlorites) occurs associated with sulfides and iron oxides, either as needle-like aggregates that surround the iron oxides or as veinlets that crosscut them.

Only two of the performed analyses on biotite crystals were deemed suitable for interpretation. They come from different samples (VNA002A and ALZ180037A-1). Both grains contain Ti within their structure, however, they differ greatly in their Fe content, where biotite in the anthophyllite-bearing sample has higher #Fe than the in rhyolitic sample. Based on their Fe content and on the classification scheme of Deer et al. (1992), the biotites are enriched in phlogopitic and annitic components, for the rhyolitic and the anthophyllite bearing-metavolcanics, respectively.

### 5.3.7 Cordierite

All total of four cordierite grains were analysed from

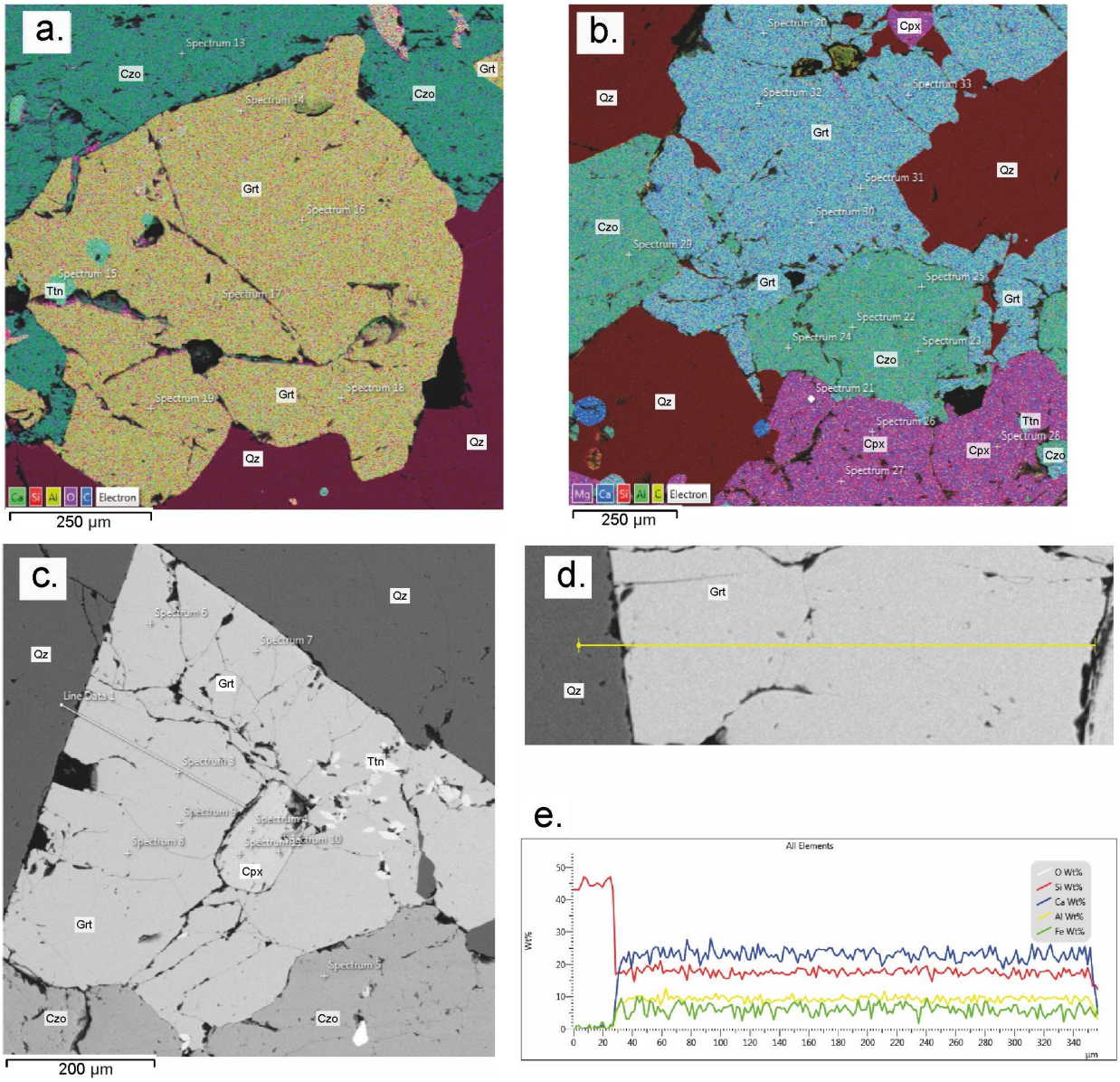


Figure 20. Elemental maps and chemical profiles of garnets associated to calcareous skarns. a) Garnet porphyroblasts surrounded by clinozoisite. b) garnet porphyroblasts associated with clinozoisite and clinopyroxene. c) subhedral garnet porphyroblasts with a clinopyroxene inclusion. The LineData1 shows the location of the profile of (d) and (e). d) Profile across the garnet crystal. e) Elemental variation across the garnet profile. Note the constant contents of Ca and Fe.

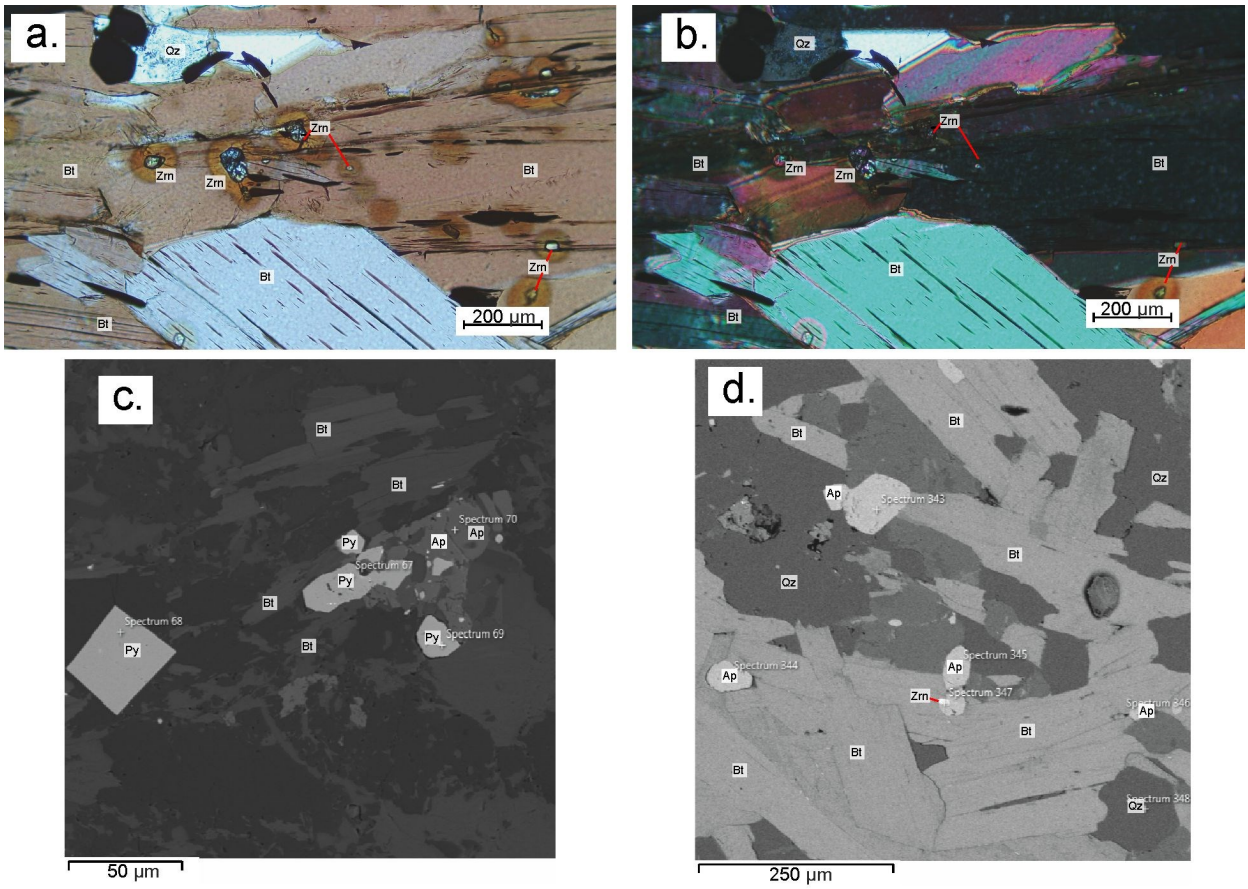


Figure 21. Photomicrographs and EDS-images of the textural relationships of zircon and apatite in the metavolcanic rocks in general. a) Rounded zircon inclusions in biotite from sample VNA002A under PPL and (b) the same textures under XPL. c) EDS-image of an apatite crystal associated with biotite and pyrite crystals in sample ALZ190015A-1. d) EDS-image of small rounded apatite crystals that occur as inclusions in biotite or within the matrix, occasionally associated with minute zircon crystals.

sample ALZ180076A-1., which consistently yielded wt% totals above 130 wt%. These results were used for composition calculation as no other cordierite analysis gave a lower total wt% (see methods). The cordierite weight percentages were normalized in order to calculate their composition. After the normalization, their composition gives a nearly stochiometric proportion with almost identical compositions of 80-82 mol% of the Mg-end member.

### 5.3.8 Accessory minerals

Accessory minerals in the samples include apatite, zircon, titanite, rutile and REE-minerals. The compositions of the REE-minerals are reviewed in section 5.5.6. Apatite is a common accessory mineral in the metavolcanic rocks, often found as minute subhedral to anhedral crystals disseminated in the matrix (Figure 21c-d) and commonly associated with REE-minerals. According to the calculations, most of the apatite crystals have a fluorapatite composition with minor OH components. The only identified fluor-oxy-apatite (AP-1) is within the carbonate skarn. It should be noted that apatite crystals are mostly absent of impurities, with a composition close to the stochiometric.

Zircon crystals are also present in most metavolcanic rocks, mainly as small inclusions preferentially within biotite crystals (Figure 21a-b). Four grains were analysed within four different samples. These samples give a composition close to the one of stochiometric zircon with Zr slightly above the stochiometric proportion. Two samples, VNA002A and ALZ180037, contain a trace amount of Hf (between 1.21 and 1.32 wt%) with Zr/Hf ratios of 55.36 and 49.82, respectively. These ratios are above the modal average for granitic derived magmas (Wang et. al. 2010). The compositions of 16 different titanite grains within four different samples were analysed. In general, regardless if they are anhedral or euhedral, titanites frequently show a defined irregular core surrounded by a second growth; this is discussed further in the section 5.7. The $TiO_2$ contents vary between 34.95 wt% and 40.08 wt%. Some of the grains also have minor Fe contents, up to 0.98 wt% of FeO. Similar to zircon, rutile only occurs as minute inclusion in metavolcanic rocks or as coronas around ilmenite crystals. Only two grains of rutile where analysed. They are consistent in their composition and have trace quantities of V and Nb.

## 5.4 Overview of the mineralization

The metavolcanic rock succession hosts most of the mineralization, however, the amphibolites and some

pegmatites are also locally mineralized. Two main types of mineralization are recognized in the area. The first type is composed primarily of sulphides, whereas the second type is dominated by Fe-oxides ± REE minerals with minor contents of sulphides. The sulphide mineralization (SM) is characterized by a Cu-Zn-Pb-Co association with variable grades. In contrast, the iron-oxide mineralization (IOM) is composed of a Fe-Mn-REE-Cu association.

The SM style of mineralization is mainly composed of disseminated pyrrhotite-pyrite-chalcopyrite-sphalerite aggregates, that can also occur as veinlet filling or as part of bigger mineralized patches in the rocks. Other accessory minerals include arsenopyrite, cobaltite, galena, native Bi, magnetite, hematite, carrolite, willyamite-ullmannite and molybdenite. Additionally, veins of chalcopyrite-pyrrhotite-arsenopyrite can be found. Table 4 shows a summary of the ore minerals contained in each sample. Of all the observed mineralized samples, pyrrhotite-pyrite is present in most of them, followed by chalcopyrite and sphalerite.

### 5.4.1 Metal ratios

#### *Sulphide Mineralization (SM)*

The relationship between common metals and REE are summarized in table 5 and figures 22 and 23. The most abundant base metal in the SM is Cu, which shows strong correlations with Co and Mo, and positive trends with Zn, Fe and REE (Figure 22a, b, d, f and g). However, in the case of Cu and Mo, two trends are discernible between the two elements (Figure 22f). A shallower correlation pattern is present for most samples, whereas a steep trend characterizes the Cu- and Mo- richer samples. This Mo anomaly can also be identified in its relationship to Pb and Zn (Figure 23d and h), but instead of being associated to higher Zn and Pb concentrations, the anomaly forms a linear pattern that separates from the normal trend around 300 and 10 ppm of Zn and Pb respectively.

In contrast to other metals, Co shows strong positive correlations with Mo and Cu (Figure 22d and k), while its relationship with Zn and Pb is more ambiguous. When compared to Zn (Figure 22i), Co concentrations around 80 ppm show Zn quantities that arrange themselves along a steep linear trend, however

Table 4. Distribution of ore minerals per sample. Abbreviations in appendix 2.

| SAMPLE ID | TYPE OF ROCK | Sulphides and Bi-phases | | | | | | | | | | | | | | | | | Oxides | | REE minerals | | | |
|---|---|---|---|---|---|---|---|---|---|---|---|---|---|---|---|---|---|---|---|---|---|---|---|---|
| | | Po | Py | Cpy | Sph | Gal | Asp | Cob | Car | Wil | Ull | Co-Py | Mol | Bth | Bi | Cat | Pen | Mag | Hem | Mnz | Xen | Par | All |
| ALZ180002A-1 | Diabase | | | | | | | | | | | | | | | | | | | | | | |
| ALZ180008A-1 | Rhyodacitic metavolcanic | | X | | | | | | | | | | | | | | | | | | | | |
| ALZ180033A-1 | Amphibolite | X | X | X | X | | | | | | | | | | | | | | | | | | |
| ALZ180034A-1 | Rhyodacitic metavolcanic | | | | | | | | | | | | | | | | | | | | | | |
| ALZ180035A-1 | Anthophyllite-bearing metavolcanic | | X | X | | | | | | | | | | | | | | | | | | | |
| ALZ180037A-1 | Anthophyllite-bearing metavolcanic | | X | X | X | X | X | X | | | | | | X | | X | | | | X | | X | |
| ALZ180052B-1 | Rhyodacitic metavolcanic | X | X | X | X | | | | | | | | | | | | | | | | | | |
| ALZ180059A-1 | Rhyodacitic metavolcanic | X | | X | X | | | | | | | | | | | | | | | | | | |
| ALZ180067A-1 | Anthophyllite-bearing metavolcanic | X | | X | X | | | | | | | | | | | | | | | | | | |
| ALZ180072A-1 | Dacitic metavolcanic | | | X | | | | X | X | | | | X | | | | | | | | | | |
| ALZ180076A-1 | Cordierite-bearing metavolcanic | X | X | X | | | | | | | | | | | | | | | | | X | | |
| ALZ180085A-1 | Granodiorite | | | | | | | | | | | | | | | | | | | | | | |
| ALZ180087A-1 | Syenite | | | | | | | | | | | | | | | | | | | | | | |
| ALZ180089A-1 | Calcareous skarn | | X | X | | | | | | | | | | | | | | | | | | | |
| ALZ180089A-2 | silicate skarn | | X | | | X | | | | X | | | | | | | | | X | | | | |
| ALZ180089A-3 | Anthophyllite-bearing metavolcanic | X | | X | | X | | | | X | | X | | | | | | | | | | | |
| ALZ190012A | Anthophyllite-bearing metavolcanic | X | X | X | X | | | | | | | | | | | | | | | | | | |
| ALZ190015A | Rhyodacitic metavolcanic | X | X | X | X | X | | | | | | X | | | | | | | | X | | | |
| ALZ190034A | Rhyodacitic metavolcanic | X | X | X | X | | | | | | | | | | | | | X | | | | | |
| ALZ190037A-1 | Fe-oxide skarn | | X | X | | | | | | | | | | | | | | X | X | X | | X | X |
| ALZ190087A | Anthophyllite-bearing metavolcanic | | X | X | X | | | | | | | X | | | | | | | | | | | |
| ALZ190088A-1 | Rhyodacitic metavolcanic | X | | X | | | | | | | | X | | | | | X | | | | | | |
| ALZ190088A-2 | Rhyodacitic metavolcanic | X | | X | | | | | | | | X | | | | | X | | | | | | |
| EBD180034A-1 | Rhyodacitic metavolcanic | X | X | X | | | X | | | | | | | | | | | | | | | | |
| EBD190023B1 | Rhyodacitic metavolcanic | X | X | | X | | | | | X | | | | | | | | | | | | | |
| VNA001-B | Rhyodacitic metavolcanic | X | X | X | X | | | | | | | | | | | | | | | | | | |
| VNA002-A | Rhyodacitic metavolcanic | X | X | X | | X | X | X | | | | | X | X | X | | | | | X | X | | |
| VNA002-B2 | Rhyodacitic metavolcanic | | X | X | X | X | | | | X | X | X | | X | X | | | | | X | | | |
| VNA003-A1 | Rhyodacitic metavolcanic | X | X | X | X | | X | X | | X | | X | X | X | X | | | | | X | | | |
| VNA003-A2 | Rhyodacitic metavolcanic | X | X | X | X | | X | | | | | X | | | X | | | | | | | | |
| VNA006-B | Rhyodacitic metavolcanic | | X | X | X | | | | | | | | | | | | X | | | | | | |
| VNA007-A | Rhyodacitic metavolcanic | X | X | X | X | | | | | | | | | | | | | | | | | | |
| VNA010-B | Rhyodacitic metavolcanic | X | X | X | X | | | | | | | X | | | | | | | | | | | |
| VNA011-A1 | Rhyodacitic metavolcanic | X | X | X | | | | | | | | X | X | | | | | | | | | | |
| VNA012-A | Rhyodacitic metavolcanic | X | X | X | | | | | | | | | | | | | | | | | | | |

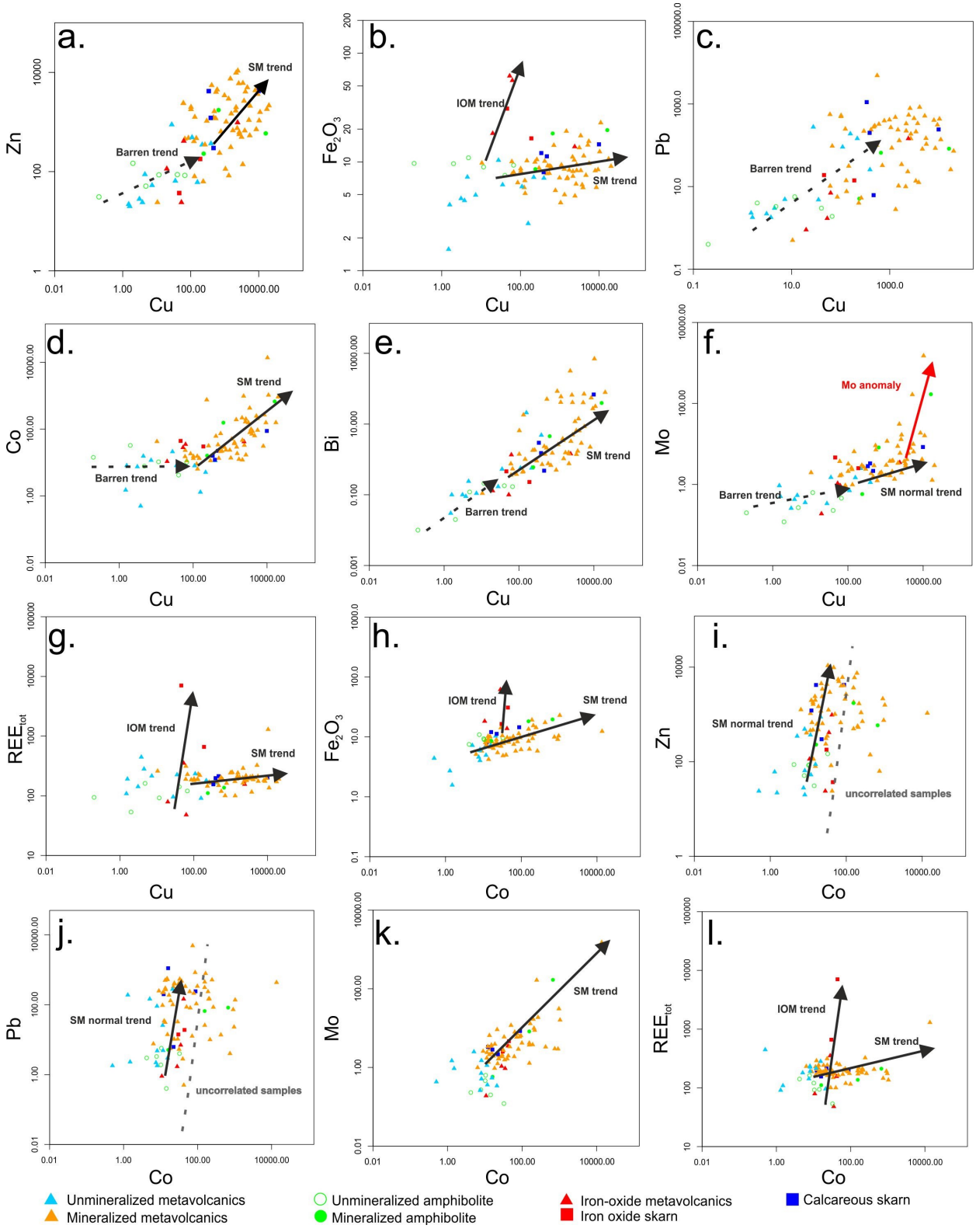


Figure 22. Log-log scatterplots showing the relationships between Cu and Co with other elements and oxides. a) Cu-Zn plot showing a rough correlation. b) Cu-$Fe_2O_3$ plot denoting two different trends for the SM and IOM. c) Cu-Pb plot with no correlation for mineralized samples. d) Cu-Co plot showing a positive trend between both elements. e) Cu-Bi plot indicating a rough positive between the two. f) Cu-Mo plot denotes a clear positive trend and the presence of a Mo anomaly. g) Cu-REE plot show two trends for the IOM and SM. h) Co-$Fe_2O_3$ plot indicating different trends for the IOM and SM. i) Co-Zn plot with a positive trend before the dashed line. j) Co-Pb plot with a steep positive correlation before the dashed line. k) Co-Mo plot with a clear positive correlation l) Co-REE plot showing two trends for the IOM and the SM.

after 100 ppm of Co, Zn has no correlation with Co. A similar behaviour is observed between Co and Pb with a high scattering in the plot after 100 ppm of Co (Figure 22j).

In general, Fe and the REE concentrations are positively correlated with the other metals in the SM (Figures 22b, g, h, l; and 23i). However, Fe shows no distinct correlation with Bi, Mo or the REE (Table 5.). Comparatively, the REE shares a flat trend with Pb and a weakly negative pattern when compared to Zn (Figure 23e and i).

*Iron-oxide mineralization (IOM)*

In comparison to the SM the IOM has only week positive trends correlations between the major metals associated to sulphides (i.e. Cu, Zn, Pb and Mo; Table 6.) only Bi seems to have positive trends with Zn and Pb (Figure 23c and g), whereas Co and Mo show a similar positive correlation between each other in IOM as in the SM (Figure 22k). Nonetheless, Fe and REE show clear positive trends between each other and with Co (Figure 22h and l), which presents as steep positive pattern with both. In contrast, Zn has negative correlations with Fe and REE, where particularly with REE has a strong negative pattern (Figure 23a and e).

Comparatively, for Cu, Co, Pb, Bi and Mo, have steep positive correlations with the REE (Figures 22g, l; and 23i), in which the samples of the IOM form

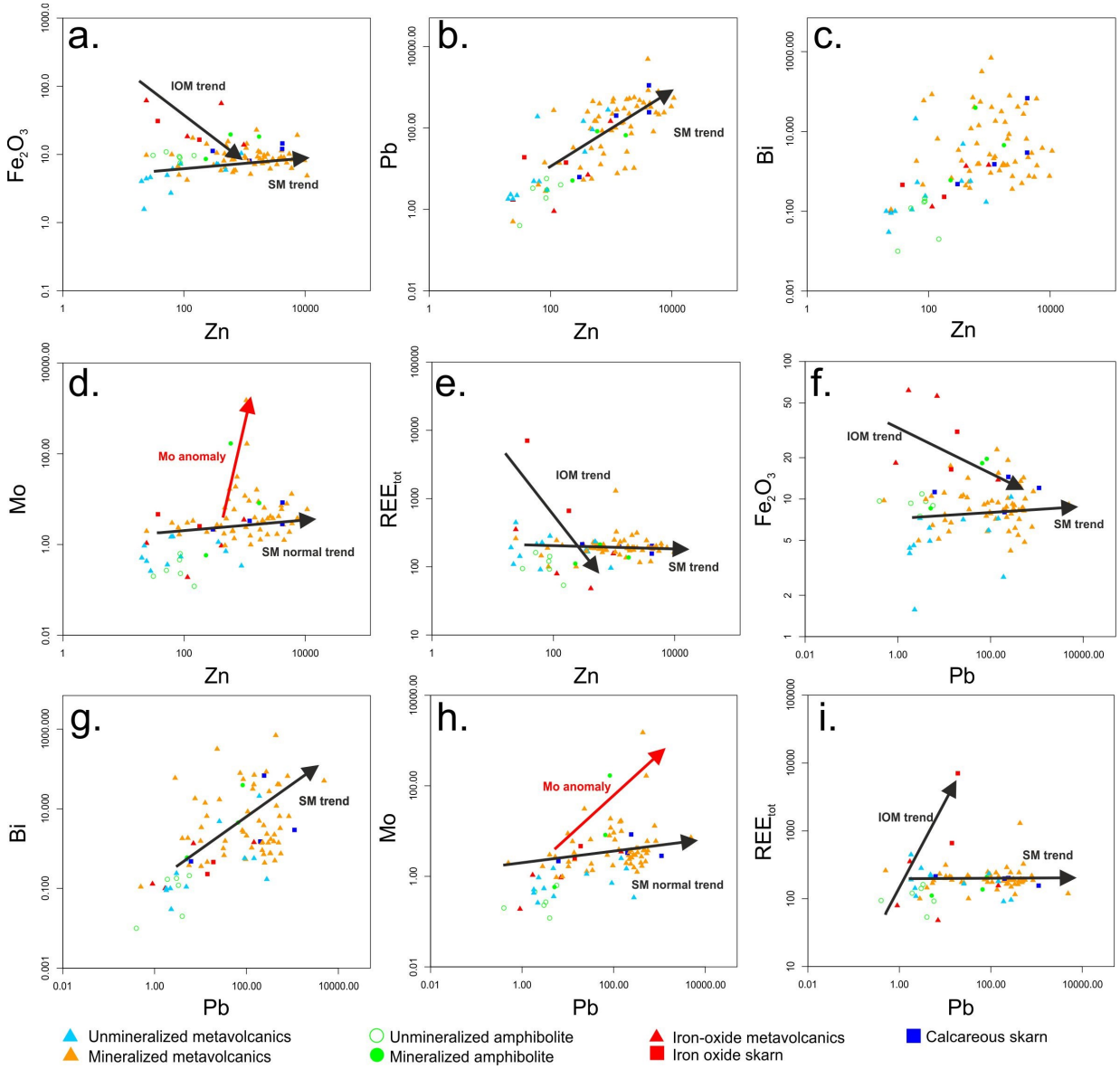


Figure 23. Log-log scatterplots showing the relationships between Zn and Pb with other elements and oxides. a) Zn- $Fe_2O_3$ plot recording a negative relationship for the IOM. b) Zn-Pb plot with a roughly positive trend. c) Zn-Bi plot showing no correlation. d) Zn-Mo plot with noticeable Mo anomaly. e) Zn-REE plot denoting two different trends for the IOM and the SM. f) Pb- $Fe_2O_3$ plot with a negative trend for the IOM. g) Pb-Bi plot showing a rough correlation h) Pb-Mo plot indicating a positive correlation with a district Mo anomaly. i) Pb-REE plot that exhibit different trends for the SM and the IOM

Table 5. Metal correlations for the SM.

| | Cu | Zn | Pb | Co | Bi | Mo | Fe | REE tot |
|---|---|---|---|---|---|---|---|---|
| Cu | | + | X | ++ | ≈+ | +/++ | + | + |
| Zn | + | | + | ++/X | X | +/++ | + | ≈- |
| Pb | X | + | | X | +/X | +/++ | + | X |
| Co | ++ | ++/X | X | | ≈+ | ++ | + | + |
| Bi | ≈+ | X | +/X | ≈+ | | + | X | + |
| Mo | +/++ | +/++ | +/++ | ++ | + | | X | ++ |
| Fe | + | + | + | + | X | X | | X |
| REE tot | + | ≈- | X | + | + | ++ | X | |

+: positive correlation
-: negative correlation
++: strongly positive correlation
--: strongly negative correlation
≈+: moderate positive correlation
≈-: moderate negative correlation
X: no correlation

trends that decouple from the main SM trend at relatively low metal concentrations. Similar patterns are found with Fe, which shows steep correlations with Cu and Co (Figure 21b and h), whereas Pb has a negative trend with Fe (Figure 23f) .

### 5.4.2 Subsurface mineralization

Whereas most of the samples that can be obtained today from the Vena and Dampetorp fields, only offer an indirect way of studying the mineralization (i.e. waste pile sampling), previous exploration campaigns in the area resulted in the drilling of four long (>500 m) and seven shorter (<200 m) bore holes. The four longer bore holes dissect the Vena mining field on its northern, central and southern parts (Figure 24). The cores form the four main boreholes and their alterations are described below. The lithological and alteration logs of these cores can be found in Appendix 5.

#### *BH 8903*

The core BH8903 is the longest core available from the Vena area. It mainly cuts through the metavolcanic succession along with minor granodioritic and granitic intrusions, amphibolite and limestone horizons. Mineralization is scarce, composed mainly of traces of chalcopyrite, pyrite and pyrrhotite in the metavolcanic rocks. The normal zonation of the mineralization consists of an area of chalcopyrite-pyrite-pyrrhotite that grades into pyrite-pyrrhotite or pyrrhotitic zones outwards. Chalcopyritic zones also have sharper contacts with unmineralized areas. In addition, the mineralized areas seem to be localized in the proximity of granitic intrusions, although, they also occur distal to them.

Table 6. Metal correlations for the IOM.

| | Cu | Zn | Pb | Co | Bi | Mo | Fe | REE tot |
|---|---|---|---|---|---|---|---|---|
| Cu | | X | X | X | X | X | ++ | ++ |
| Zn | X | | X | ≈+ | + | ≈+ | - | -- |
| Pb | X | X | | ≈+ | + | ≈+ | - | - |
| Co | X | ≈+ | ≈+ | | ≈+ | + | ++ | ++ |
| Bi | X | + | + | ≈+ | | ≈+ | X | ++ |
| Mo | X | ≈+ | ≈+ | + | ≈+ | | X | + |
| Fe | ++ | - | - | ++ | X | X | | + |
| REE tot | ++ | -- | - | ++ | ++ | + | + | |

+: positive correlation
-: negative correlation
++: strongly positive correlation
--: strongly negative correlation
≈+: moderate positive correlation
≈-: moderate negative correlation
X: no correlation

Metasomatic alteration is common throughout the core affecting the limestone and the metavolcanics, by giving a greenish colour to the latter. This alteration is commonly associated with mineralized areas and can further be found surrounding some granitic intrusions. Other types of alteration in the core include oxidation (hematitic staining), silicification, chloritization and minor Mg-alteration. Chloritization is only found affecting the amphibolite bodies, whereas silicification and Mg-alteration occur in the metavolcanic rocks and close to mineralized areas.

*BH 9002*

Located towards the NE of the Vena are, the BH 9002 has sulphide mineralization throughout, with discrete intervals of strong mineralization. The core itself cuts through the metavolcanic sequence with a granodioritic intrusion towards the shallower levels and a granitic intrusion towards the deeper sections. Mineralization is hosted by the metavolcanic sequence with traces of pyrite and pyrrhotite in the granodiorite. The samples taken from the core show a maximum grade of 0.98% Zn, 0.79% Cu and 0.02% Co (averages of 0.29% Zn, 0.15% Cu and 0.004% Co).

The ore minerals in this core, in order of abundance, are pyrrhotite, pyrite, chalcopyrite, cobaltite and arsenopyrite. Pyrite and pyrrhotite are ubiquitous as disseminations in the metavolcanic rocks but can also occur concentrated in bands and in veinlets or stockworks with chalcopyrite. Together with these stockworks some disseminated cobaltite crystals can be found. Chalcopyrite also occurs in bands that follow the foliation direction. The granodioritic interval has Po-Py-Cpy aggregates disseminated or in bands like metavolcanic rocks; they, too, are affected by minor Po+Cpy±Cob veinlets. Most of the cobalt mineralization can be found relatively close to the magmatic intrusions. In contrast with the core BH 8903, the mineralization in this core shows no clear zonation pattern. For example, chalcopyrite rich zones can alternate with cobaltite rich areas as well as have sharp transitions to unmineralized rocks.

Metasomatism or skarn alteration is a common feature in the metavolcanic rocks and is closely associated with mineralized areas. Other alterations include "biotite alteration" and Mg-alteration. The biotite alteration is characterized by a local abundance of biotite in the rock, possibly related to clay rich zones predating metamorphism. While biotite alteration in commonly associated with mineralized intervals, Mg-alteration is normally found directly in contact with mineralized section, but not within them.

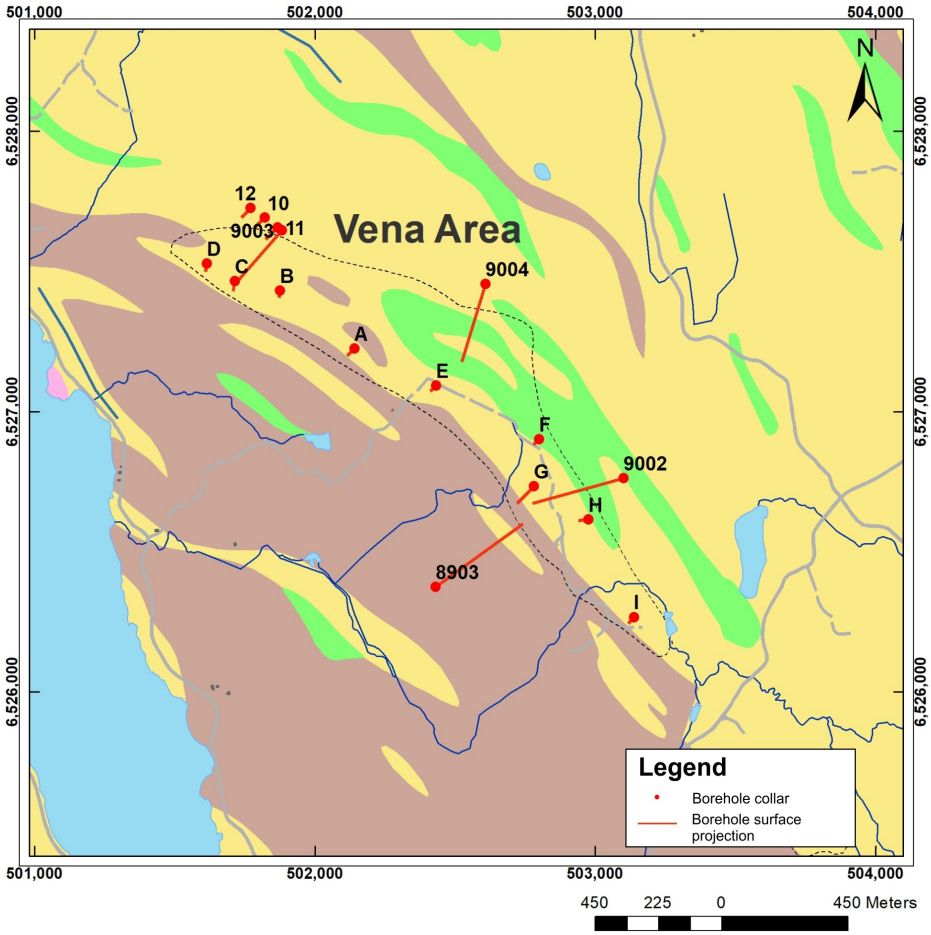


Figure 24. Map of the Vena area showing the location and orientation of exploration boreholes. For bedrock symbology see figure 4.

*BH 9003*

The BH 9003 drill core was drilled in the NW part of the Vena mining field. It cuts mainly the metavolcanic sequence along with minor limestone or skarn horizons. In addition, granitic and pegmatitic intrusions are found towards the deeper parts of the core. Most of the core show signs of mineralization with sulphides hosted by the metavolcanic sequence and locally in some pegmatites. In contrast, the limestone and skarn horizons seem devoid of ore minerals.

The mineralization is composed of chalcopyrite, sphalerite, pyrite and pyrrhotite associations with occasional cobaltite. There is a clear zoning in the mineralization characterized by cobaltite bearing intervals surrounded by Cpy+Po+Py±Sph that grade out into Po-Py zones. Metasomatism is the most common alteration, usually associated with mineralized and limestone intervals. Minor chloritization and silicification occur along discrete intervals of the core without any specific pattern.

*BH 9004*

The drill-hole 9004 crosses the middle part of the Vena mining field in a SW direction. Most of the core comprises metavolcanic rocks that alternate between rhyolitic and dacitic compositions. Thin pegmatitic intrusions can be found in the core, as well as some amphibolite intervals in the shallower levels and thin limestone horizons towards the deeper sections. Only one granitic intrusion occurs at the middle of the drilled interval.

The most common type of alteration is metasomatism that is commonly associated to mineralized intervals. Chloritization is widely spread but limited to the amphibolite sections and to dacitic metavolcanics. Oxidation, biotite and Mg-alteration can be found towards the shallower sections of the core. Mg-altered zones seem to be devoid of mineralization, whereas biotite-altered areas are relatively rich in mineralization. Between 298 and 327 m along the core, a granitic intrusion is heavily altered with an epidote replacement of the matrix. This altered zone is located below one metavolcanic interval rich in mineralization that contains cobaltite.

In the metavolcanic intervals pyrite and pyrrhotite are the most common phases, occurring as disseminations or fine-grained bands that follow the foliation. In comparison, chalcopyrite is usually found in irregular patches that crosscut the foliation or within the same fine Py-Po bands. Similarly, veinlets of Cpy+Co-Py, Asp+Cpy, Po+Co-Py+Cpy and Qz+Py+Cpy occur locally, in some cases as a micro-stockwork network. Cobaltite is usually found in localized areas and in bands that follow the foliation. In contrast, the amphibolite intervals have pyrite, pyrrhotite and chalcopyrite, either as disseminations or as veinlets that crosscut the foliation.

## 5.5 Ore mineral assemblages

The mineralization is divided into eight different assemblages based on the genetical relationship of the ore minerals. However, these associations are not mutually exclusive, as two or more of them can occur in the same sample. Furthermore, a single assemblage can have more than one mode of occurrence, e.g. disseminations or veinlets. This subdivision is meant for simplification and generalization of common characteristics between the ore minerals.

### 5.5.1 Pyrrhotite-Pyrite (Po-Py)

The most abundant ore mineral is pyrrhotite, which is present in most of the analysed samples, including amphibolites, metavolcanic rocks and some pegmatites. It occurs as disseminations of anhedral crystals (Figure 25c), as fine veinlets that follow the gangue crystals faces (Figure 25b), or within biotite cleavage planes. Regardless of its mode of occurrence, most pyrrhotite crystals have been partially to totally replaced by marcasite lamellae along borders and fractures (Figure 25e-f). Pyrite is often associated with pyrrhotite and occurs as subhedral to anhedral aggregates (Figure 25a), however, it is not uncommon to find it as disseminated subhedral crystals within the metavolcanic and amphibolitic rocks. Together with pyrrhotite, pyrite sometimes forms fine bands that follow the foliation direction (Figure 25d). These bands are typically related with amphibole- or biotite-rich areas.

### 5.5.2 Pyrrhotite-Pyrite-Chalcopyrite-Sphalerite (Po-Py-Cpy-Sph)

The second most common association found, both in the metavolcanic and amphibolite rocks, is pyrrhotite-chalcopyrite-sphalerite. These three minerals form aggregates (Figure 26a-d) in different combinations (e.g. Po, Po-Cpy, Po-Cpy-Sph, Po-Sph, etc). Even though pyrite is not always present, it is often found as either part of this aggregates or as disseminated crystals within the matrix of the rocks. The Po-Py-Cpy-Sph assemblages occur as disseminations, or in biotite-rich bands where chalcopyrite and pyrrhotite are commonly emplaced in between cleavage planes of biotite crystals (Figure 26d). In addition, these aggregates can be found as veinlets or micro-stockworks (Figure 26e-f).

When in contact with chalcopyrite, the sphalerite crystals have irregular or aligned to each other, chalcopyrite inclusions ("chalcopyrite disease") (Figure 27a). In contrast, when sphalerite is found only in contact with pyrrhotite, it can present pyrrhotite inclusions or exsolutions (Figure 27). Both chalcopyrite and pyrite occur as inclusions emplaced in the cleavage planes of biotite. Similar to the Po-Py assemblage, pyrrhotite in this association is often partially to fully replaced by marcasite along borders and fractures.

### 5.5.2 Galena and Bi-minerals (Gal-Bi)

Galena and native bismuth can be found as minute inclusions in chalcopyrite or sphalerite, or as part of complex aggregates with other Bi-bearing sulphides (Figure 28). The aggregates can be associated with chalcopyrite or other sulphides, either as coarse-grained aggregates or as fine aggregates that nucleate at sulphides crystal borders (Figure 28c). The aggregates themselves are a complex mixture of galena, native Bi, bismuthinite, cosalite and other rarer phases (see section 5.5.2). Within these aggregates subhedral to anhedral crystals of costibite and willyamite-

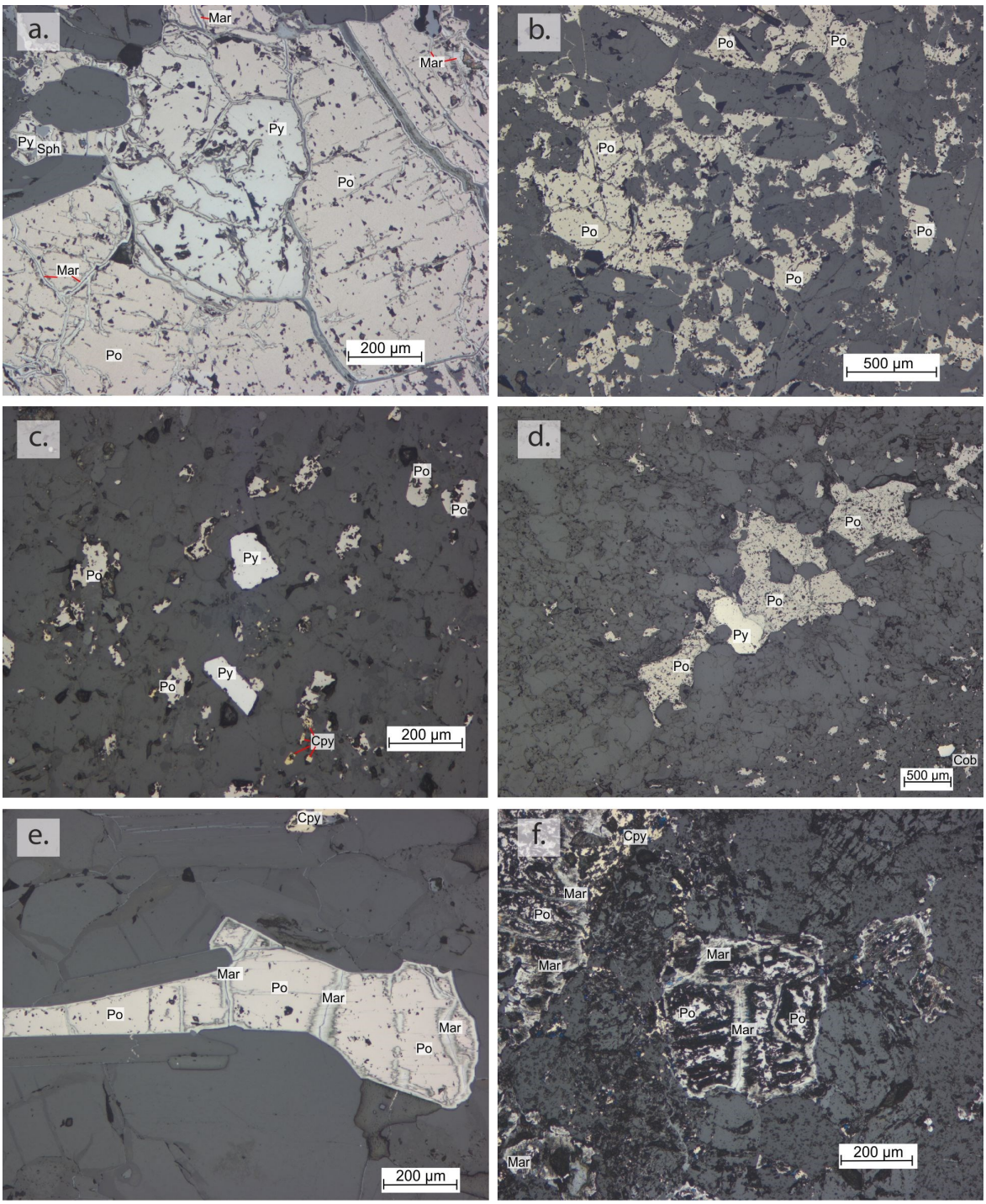


Figure 25. Photomicrographs under reflected polarized light (RPL) showing the textural relationships of pyrite and pyrrhotite. a) Anhedral crystal of pyrite (Py) included in an anhedral aggregate of pyrrhotite (Po). The pyrrhotite is breaking down into marcasite (Mar) along borders and fractures (sample ALZ180089A-3). b) micro stockwork of pyrrhotite (sample ALZ180089A-3). c) dissemination of pyrite and pyrrhotite (Sample ALZ180052B-1). d) anhedral pyrite within a band of pyrrhotite (sample VNA0012A). e) Pyrrhotite crystal partially replaced by marcasite along fractures (Sample VNA002A) f). Relict pyrrhotite, replaced by marcasite (sample ALZ180089A-2).

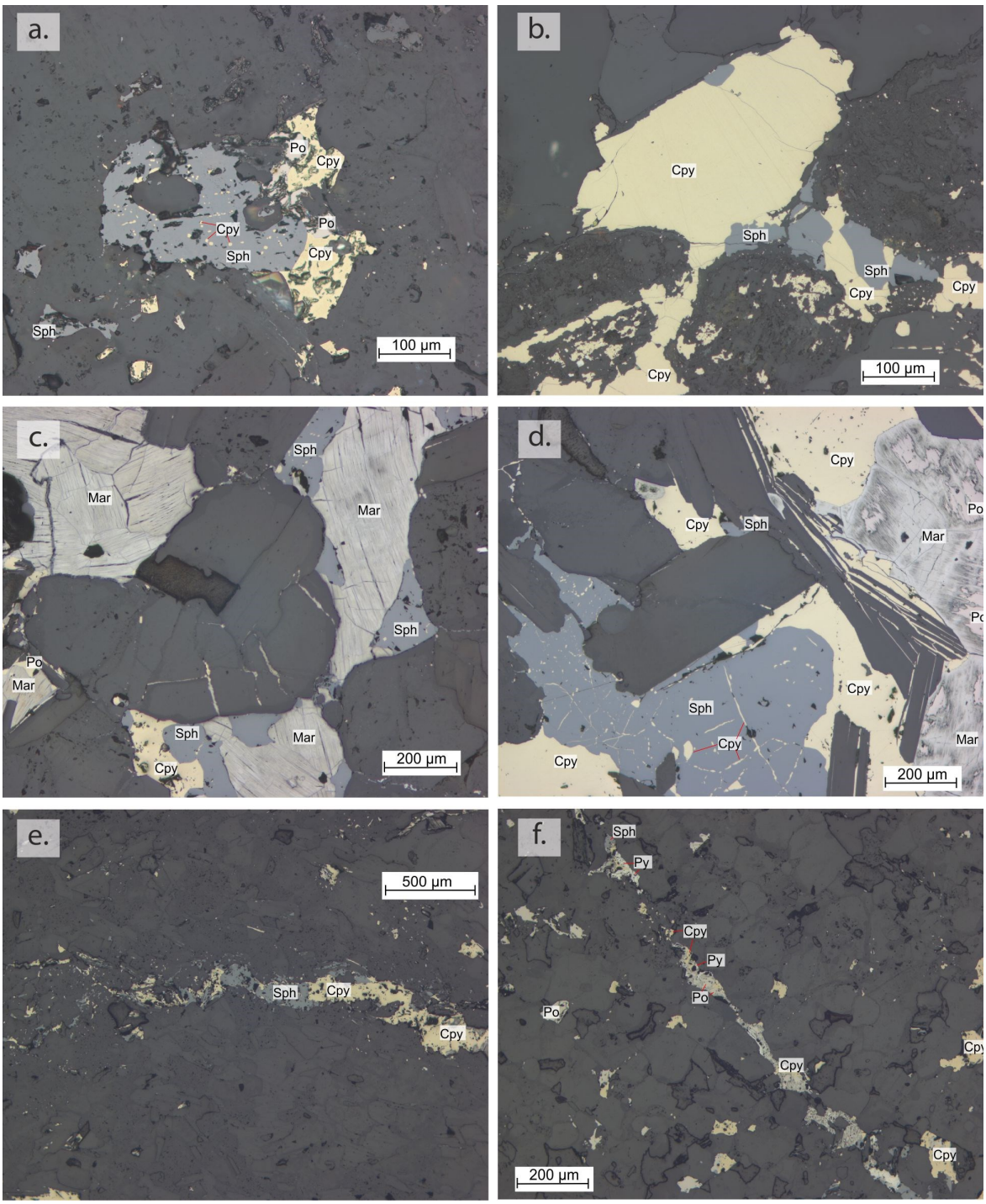


Figure 26. Photomicrographs under RPL of common types of Cpy-Po-Sph aggregates and veinlets. a) Sph-Cpy-Po aggregate, the Sph crystal has Cpy inclusions (sample ALZ180050A-1). b) Sph-Cpy aggregate, the Sph crystals are free from Cpy inclusions (sample VN001A). c) Po-Sph-Cpy. Pyrrhotite has been completely replaced by marcasite (Mar; sample VNA003A1). d) Cpy-Sph-Po aggregate, where some of the chalcopyrite crystalizes along the cleavage planes of biotite crystals (sample VNA003A1). e) Cpy-Sph veinlet (Sample VNA006B). f) Cpy-Po-Sph-Py veinlet with partial breakdown of the Po into Mar (sample VNA0010B).

ullmannite are common (Figure 28d). Galena is also found independently from Bi phases as small discontinuous veinlets inside sulphide crystals.

### 5.5.3 Arsenopyrite-Cobaltite-Skutterudite-Chalcopyrite-Molybdenite (Asp-Cob)

This assemblage is only present in samples ALZ18037A-1 and VNA002-A. Arsenopyrite occurs as mm-sized euhedral crystals along biotite-rich areas and commonly has cores of cobaltite or skutterudite, and/or rounded cobaltite inclusions (Figure 29). However, some cobaltite occurs independently of arsenopyrite as anhedral to subhedral crystals, disseminated within the biotite-rich areas. Fine-grained, elongate laths of molybdenite can also be found within these biotite-rich areas or included within the As-bearing phases. It is often deformed and folded and locally wraps around arsenopyrite crystals.

In addition to the As-rich mineral phases, anhedral Cpy+Py±Sph±Py aggregates can be found in these samples, either associated with the As-bearing minerals or as individual aggregates. When in contact with arsenopyrite crystals, these aggregates have nucleated and crystallized around them (Figure 28e-f). Pyrite can also form tiny veinlets or occur within biotite cleavage planes. Later complex minute aggregates of galena and Bi minerals grow around both the chalcopyrite and arsenopyrite crystals, although, minute native bismuth and galena inclusions are also present inside arsenopyrite crystals.

Subrounded monazite crystals are common within the biotite crystals or as inclusions within the arsenopyrite crystals. Where found within the arsenopyrite, radial fracturing affects the arsenopyrite crystals, starting from the monazite crystals and expanding outwards. Regular fracturing is also common in cobaltite and arsenopyrite crystals, but not in skutterudite. When present, fractures have oblique angle with the foliation, suggesting a left shearing direction (Figure 29d).

### 5.5.4 Chalcopyrite-Cobaltite-Carrolite-Molybdenite (Cpy-Car)

The occurrence of carrolite is restricted to sample ALZ180079A-1, which is the only examined dacitic metavolcanic rock. Fine-grained, elongate molybdenite laths occur in chlorite-rich areas, often deformed and folded. Carrolite and cobaltite crystals are found as subhedral to anhedral crystals either disseminated or within deformed veinlets (Figure 30c-d), often associated with anhedral chalcopyrite that fills in the spaces between them or occurs as inclusions or veinlets in the cobalt-bearing phases (Figure 30). Chalcopyrite is also present as disseminations in the rock. Small and complex galena-Bi-phase aggregates can be found nucleating at the edges of Cpy-Car-Cob aggregates or as inclusions within the sulphides.

Both carrolite and cobaltite crystals show fracturing, however, carrolite is more affected than cobaltite (Figure 30a-b). In comparison, chalcopyrite seems to behave in a ductile manner without any visible fracturing. Fracturing of the bigger grains show a preferential direction oblique to the foliation, that would be in accordance to a left sense of shearing (Figure 30a).

### 5.5.5 Pyrrhotite-Pyrite (Co)-Pentlandite (Co) - Chalcopyrite (Po-Py(Co))

This assemblage was only found in samples ALZ190088A-1 and 2, taken from the core 9004, and sample VNA006-B. The samples from the core were taken from a vein like structure that crosscut one of the lower metavolcanic intervals of the core. In thin section the mineralization is composed of anhedral pyrrhotite aggregates that occur in biotite-rich areas, commonly either surrounding the biotite crystals or within their cleavage planes (Figure 31a-b). Inside the pyrrhotite aggregates, subhedral to euhedral cobaltoan pyrite crystals are present. The euhedral pyrite-(Co) crystals are also found disseminated in the matrix. Occasionally, anhedral chalcopyrite is associated with the pyrrhotitic aggregates or occurs as minute inclusions within pyrite-(Co) crystals.

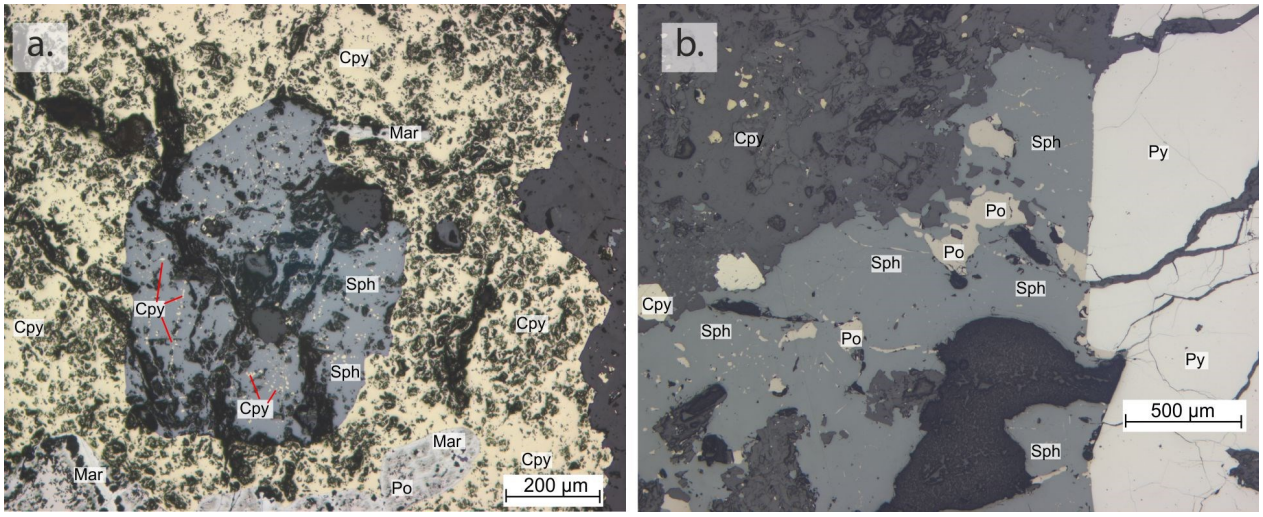


Figure 27. Photomicrographs under RPL of common types of inclusions in sphalerite crystals. a) Chalcopyrite (Cpy) inclusions within sphalerite (Sample ALZ190087A-1). b) Inclusions of pyrrhotite (Po) in Sphalerite crystal associate to pyrite (Py). Notice how some Po crystals nucleate at the border of the pyrite (Sample VNA010B).

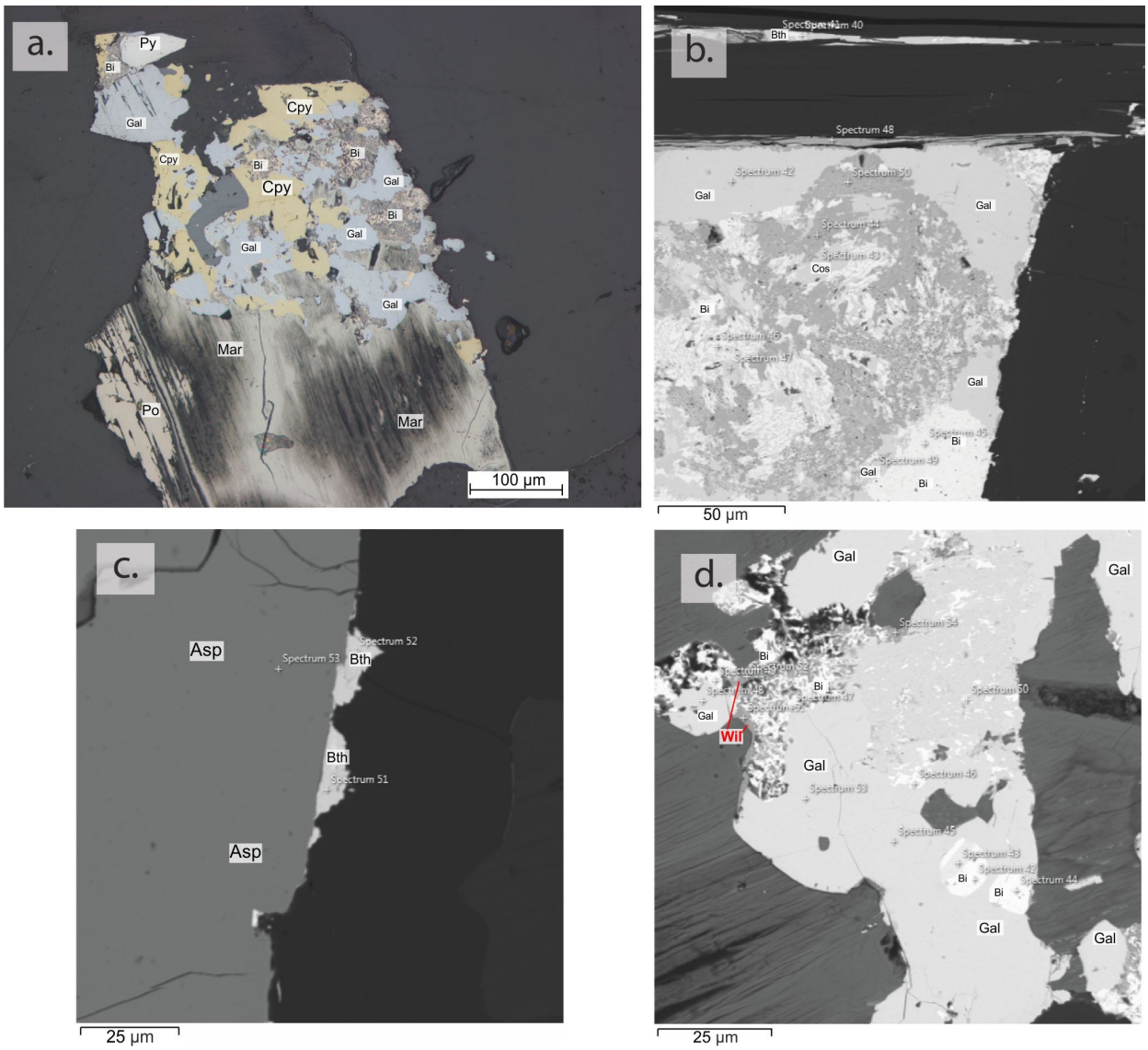


Figure 28. Photomicrographs under RPL and EDS images of galena and Bi-minerals aggregates. a) Cpy-Po-Py aggregate intergrowth with galena (Gal) and Bi-minerals (Bi) (Sample VNA002B2). b) EDS image of a complex galena (Gal), Cosalite (Cos), native bismuth (Bi) and other Bi-mineral pashas aggregate (sample VNA002A). c) EDS image of bismuthinite crystals nucleating on the border of an arsenopyrite crystal (sample VNA002A). d) EDS image of complex aggregate containing galena (Gal), native bismuth (Bi) and willyamite (Wil) (sample VNA002B2).

In comparison, the sample VNA006-B is more abundant in chalcopyrite and pyrite-(Co) is scarcer, with the latter only found as solitary disseminations and rarely within the pyrrhotite aggregates. Instead, sphalerite forms part of the Cpy-Po association and occurs together in large aggregates and within veinlets throughout the sample.

Flame-like exsolutions of cobalt pentlandite, up to 0.06 mm long, are found in both drill core and waste pile samples These exsolutions typically nucleate along the borders of pyrrhotite crystals and grow inwards the aggregates (Figure 31e). Commonly, the exsolution are aligned along horizontal and vertical planes within the pyrrhotite crystals (Figure 31c-f). From sample VNA006A (Figure 31d), it can be inferred that exsolution of pentlandite occurred before the breakdown of pyrrhotite into pyrite.

### 5.5.6 REE minerals

Whereas most of the REE minerals occur in the IOM, they are common in the SM as well. In general, the most abundant phases are monazite and allanite, but other minerals include parisite and xenotime. In the SM, REE minerals are present as tiny inclusions within biotite crystals and other metamorphic minerals and sometimes associated with apatite crystals around which they nucleate. In the case of monazite, it is also found included within arsenopyrite crystals (Figure 32d). Parisite is a rarer phase that occurs as an alteration product of monazite (Figure 32f). Xenotime is only found scarcely as minute inclusions within monazite crystals (Figure 32d) or as disseminated fine-grained crystals (Figure 32e).

In the IOM, REE minerals form irregular aggregates of allanite with chalcopyrite, pyrite and magnetite (Figure 32a-c). Magnetite and pyrite crystals within

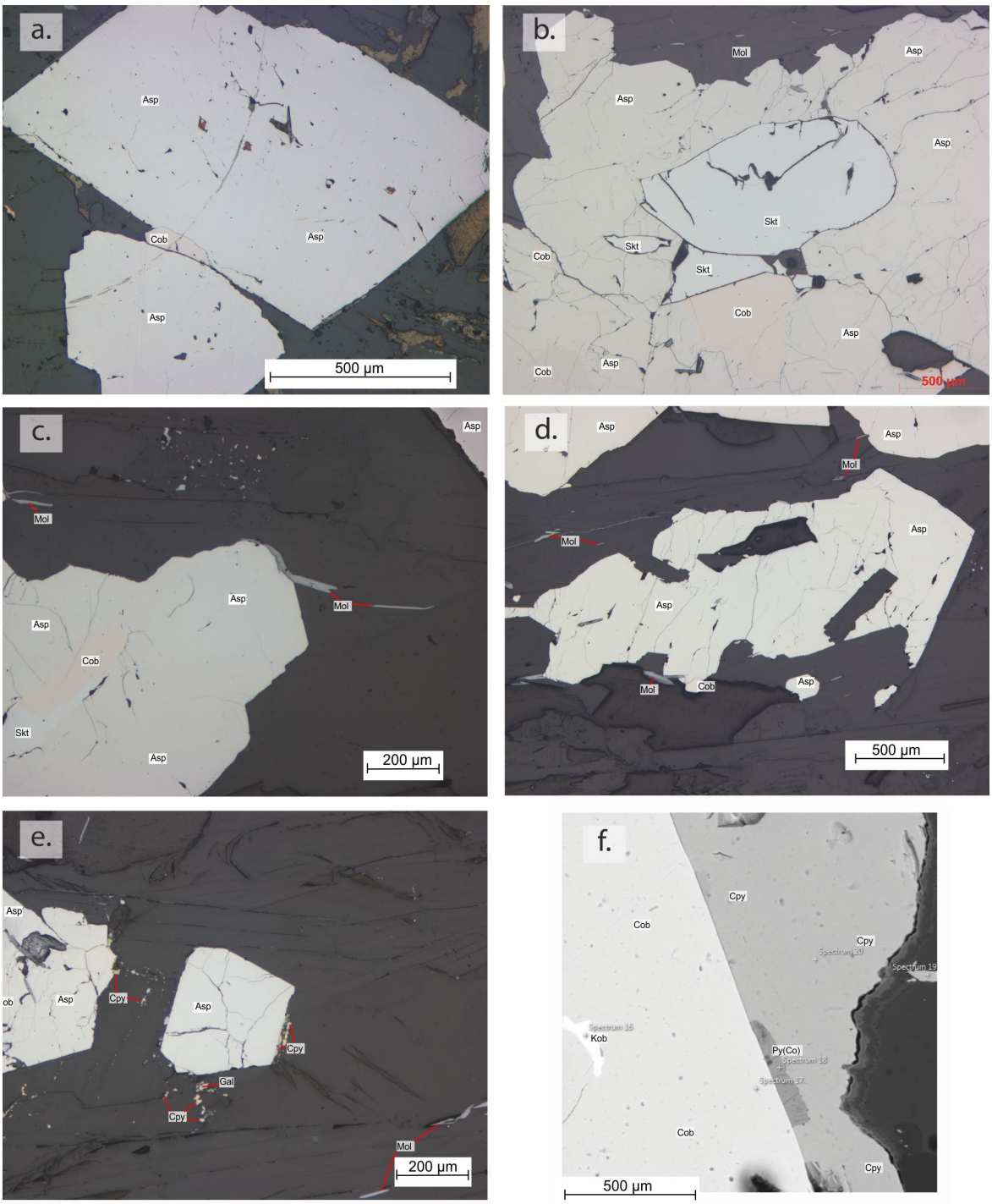


Figure 29. Photomicrographs under RPL and EDS images of arsenopyrite, cobaltite and skutterudite mineral relationships. a) Euhedral and subhedral arsenopyrite (Asp) crystals with an anhedral pinkish cobaltite (Cob) crystal sandwiched between them under reflected light. b) Arsenopyrite crystal with a skutterudite (Skt) core and pinkish cobaltite inclusions and minor molybdenite (Mol) in the matrix under reflected light. c) Arsenopyrite subhedral crystal with a cobaltite-skutterudite core with deformed molybdenite laths wrapping around the crystal. d) Arsenopyrite crystal with minor cobaltite inclusions. Note the oblique fracturing in the crystal with respect to the foliation. E) Euhedral arsenopyrite crystals with cobaltite inclusions and chalcopyrite (Cpy) and galena (Gal) aggregates that nucleate on the arsenopyrite crystal faces. f) EDS image showing Cpy and cobalt bearing pyrite (Py(Co)) nucleating along the borders of a cobaltite crystal. The cobaltite crystal has a small kobellite (Kob) inclusion.

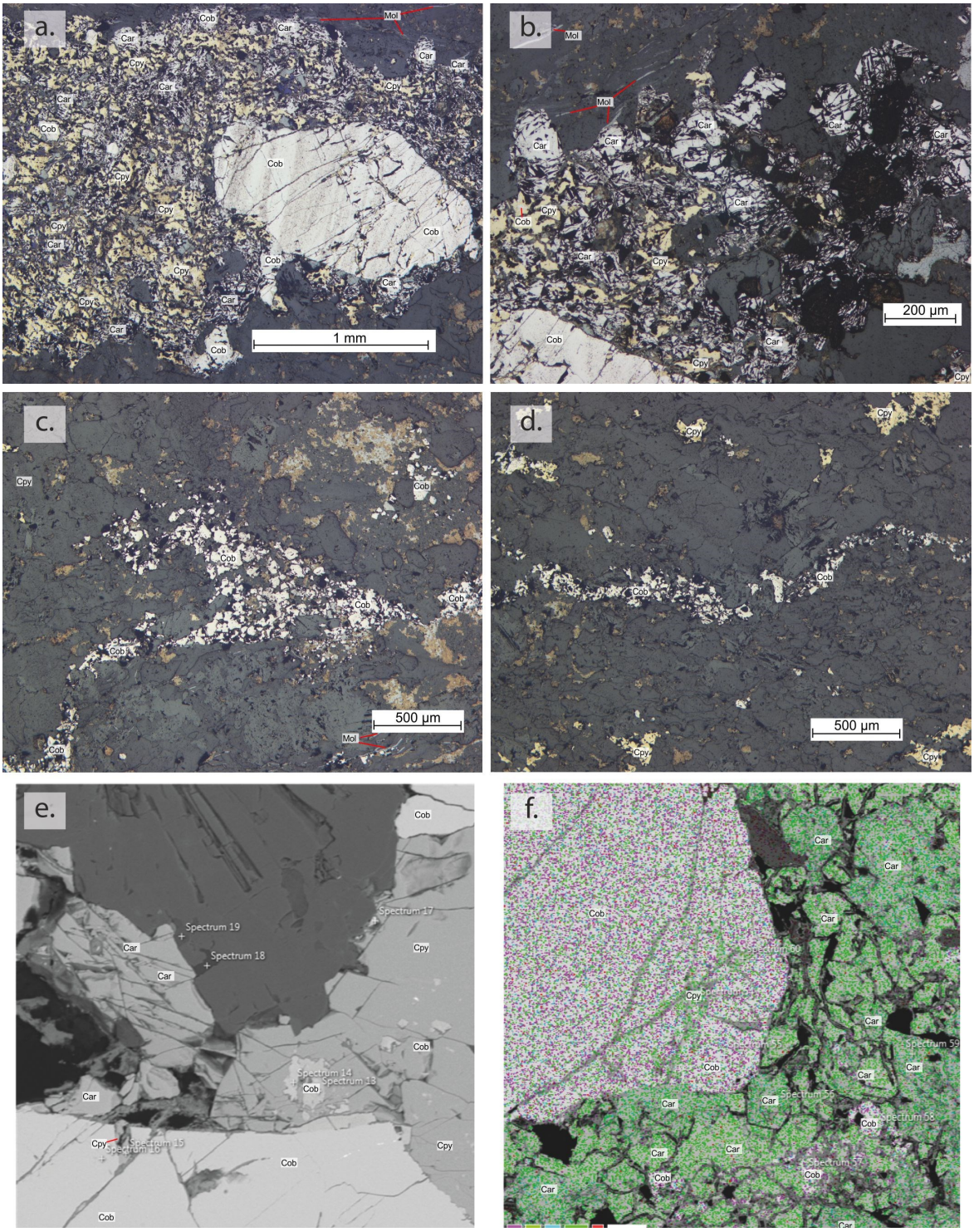


Figure 30. Photomicrographs under RPL, EDS images and elemental maps of typical textures and relationships in carrolite-bearing assemblages. a) Chalcopyrite (Cpy), cobaltite (Cob) and carrolite (Car) aggregate under reflected light. Note the oblique fracturing in the Cob phenocryst. b) Close up of the Cpy-Cob-Car aggregate; note the fracturing in the carrolite crystals. c) Cobaltite veinlet that shows deformation. d) Cobaltite veinlet with minor deformation and Cpy disseminations. e) EDS image of a Cpy-Cob-Cpy aggregate, where the Cpy crystals have irregular inclusions of cobaltite. f) Elemental map of As (magenta), Cu (light-green), Co (cyan), Fe (green), S (green) and Si (red) a Cpy-Cob -Car aggregate. Note the Cpy veins in the cobaltite crystals along fractures.

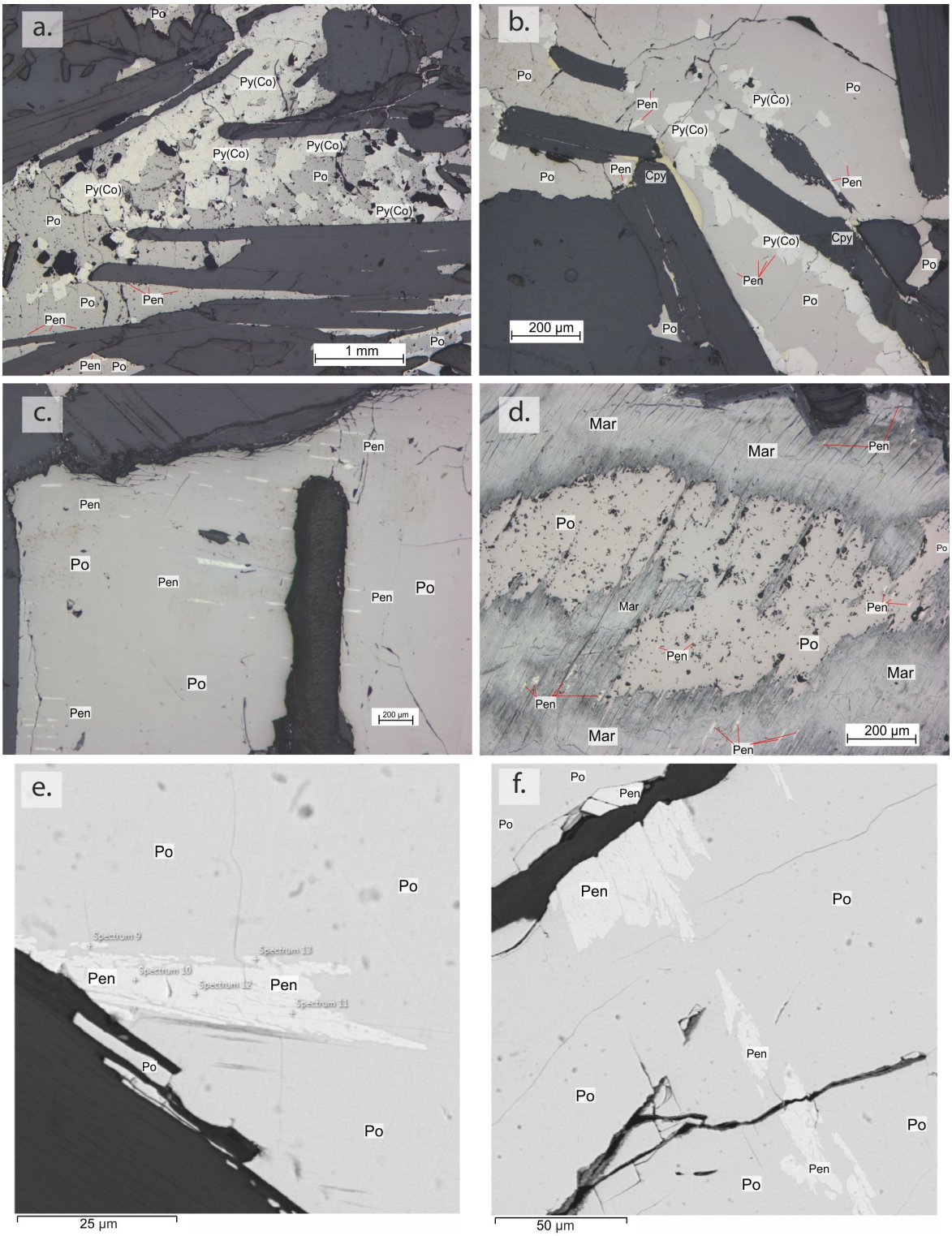


Figure 31. Photomicrographs under RPL and EDS images of typical textures associated to pentlandite-bearing pyrrhotite assemblages a) Sub- to euhedral cobaltoan pyrite crystals (Py(Co)) in anhedral pyrrhotite (Po) with pentlandite (Pen) exsolutions under reflected light. The aggregates occur in in between biotite crystals. (sample ALZ190088A-1). b) Aggregate of Py(Co)-Cpy-Po with Pen exsolutions emplace around biotite crystals (sample ALZ190088A-2). c) Close-up of a Po crystal with aligned "flame-like" exsolutions of Pen (sample ALZ190088A-2). d) Pyrrhotite crystal with pentlandite exsolutions partially breaking down into marcasite (Mar; sample VNA006B). e) EDS image of a "flame-like exsolution of pentlandite nucleating at the border of a Po crystal (sample ALZ190088A-2). f) EDS image of a series of aligned Pen exsolutions within a Po crystal.

this association are surrounded by later hematite coronas. Locally, monazite is found included within allanite crystals (Figure 32b). Parisite occurs as either fibrous aggregates that grow between Mag-Py-Cpy-All aggregates (Figure 32a-b) or as an extremely fine-grained alteration of allanite.

## 5.6 Chemical variation in ore minerals

The results of the EDS-SEM analysis of ore minerals from the studied samples are summarized in the section below, together with descriptions of chemical variability and common elemental substitutions. Detailed compositions for each mineral phase can be found in Appendix 4.

### 5.6.1 Pyrrhotite

Pyrrhotite chemical composition varies between $Fe_{0.91}S$ to $Fe_{0.84}S$, with an average composition of $Fe_{0.87}S$. The contents of Fe vary among different grains in the same sample, and even within a single crystal it can vary considerably. However, pyrrhotite crystals with Co-pentlandite exsolutions generally show a higher Fe content (Figure 33a). In addition to the differences in Fe, the Po crystals within the Po-Py (Co) assemblage show no traces of O, while the pyrrhotite from other assemblages have O contents varying between 0.00 and 7.52 at%. The presence of O is responsible for the group of scattered Fe-S contents in figure 32. Otherwise, pyrrhotite crystals free of O plot a linear negative correlation line between Fe and S.

### 5.6.2 Pyrite-Marcasite

As mentioned in previous sections, the $FeS_2$ is present in one of three main forms: (1) as isolated pyrite crystals or aggregates associated with Cpy-Po, (2) as a marcasite lamella replacing pyrrhotite, or (3) as a recrystallization of marcasite in pyrite coronas. Both the recrystallized pyrite mixture and the marcasite formed from pyrrhotite breakdown show significant contents of oxygen (up to 14.57 at% in the case of marcasite), whereas the primary pyrite only show traces of it (Figure 33b). This is possibly related to the texture of the breakdown-related marcasite, as it is an irregular surface the analyses might include oxygen trapped within the crevasses. Alternatively, part of the breakdown might include an oxidized Fe-phase (e.g. hematite or magnetite). In a similar fashion, Fe and S contents vary throughout the different pyrite crystals, where they define two groups correlated to the presence or absence (higher contents of Fe and S) of O. Figure 32 shows that the breakdown marcasite is more variable in terms of Fe-S contents and relatively lower in Fe.

Pyrite crystals can also have trace quantities of Co and As within its structure. Cobalt and As-bearing pyrites are often found in samples devoid of other major Co-As phases (e.g. cobaltite or arsenopyrite). Most pyrite grains contain either Co or As, but in rare cases, they can have trace quantities of both elements. Additionally, variable O and rare Zn contents are present. The average content of As-bearing grains is 0.23 at% As. In comparison, Co-bearing pyrites show a more variable concentration of Co (0.38 to 4.49 at%, average 1.26 at%). Elemental mapping of Co-bearing grains reveals that Co is randomly distributed along the whole pyrite structure, with no discernible zonation (Figure 34). Figure 33c shows that most Co-bearing pyrite crystals fall within a well-defined range both for S and Fe, the outliers to the main grouping are due to the variable contents of oxygen. In comparison Co and Fe in Co-bearing pyrite crystals have a negative correlation (Figure 33d) as expected for Co-Fe substitution in pyrite.

Co-bearing pyrites from sample ALZ190088A-2 show the highest Co contents, and samples VNA002A and VNA002A2 show the lowest concentrations (Figure 323), which implies that the average Co content in cobaltoan-pyrite is higher when associated with pyrrhotite-pentlandite assemblages than in other assemblages.

### 5.6.3 Chalcopyrite

The composition of chalcopyrite crystals is close to stochiometric in most cases, where Cu contents vary from 27.98 to 23.55 at% and Fe concentration from 26.04 to 23.32 at%. Comparison of the Cu and Fe contents indicates two groups of chalcopyrite, where one has slightly higher Fe contents (Figure 35a). Oxygen impurities were found in some crystals, which might be attributed to either errors in the analysis or a minor oxide component. Similarly, trace amounts of Zn up to 2.20 at% are present in some chalcopyrite crystals; however, all these crystals are inclusions within sphalerite crystals.

### 5.6.4 Sphalerite

In general, all sphalerite crystals are Fe-poor with a maximum content of 8 at% Fe. Some crystals within sample ALZ190015A-1 are almost devoid of Fe, with contents as low as 2.15 at%. Figure 35b shows three main groups of sphalerite, in terms of their Fe and Zn contents. The first group is extremely Fe-poor sphalerite, only found in sample ALZ190015A-1. The second group contains most of the analysed sphalerite grains, which have a Fe-poor composition varying between 4.12 to 6.31 at% Fe. The last group is an outlier with a Fe-richer composition, which is interestingly found within the same sample as the extremely Fe-poor sphalerite.

Minor impurities, such as Cu or Cd, are common within sphalerite grains, with concentrations up to 6.50 at% Cu in sphalerites with “chalcopyrite disease”. Cadmium, on the other hand, shows no correlation with Cu, Zn or Fe contents in sphalerite, and does not exceeds 0.63 at% where present. Most of the performed analyses show minor O impurities (up to 3.07 at%), possibly related to the quality of the analysis itself rather than to the presence of oxide phases.

### 5.6.5 Galena

Most galena crystals are found as part of complex aggregates with Bi-bearing minerals; however, galena is also found as tiny disseminated crystals, inclusions within other ore minerals, or as part of later veins that cut the sulphides. Chemically, the disseminated single crystals seem to be the most diverse, with trace amounts Fe in their structures. Fe content is higher in the crystals nucleated along pyrite crystals. In a similar

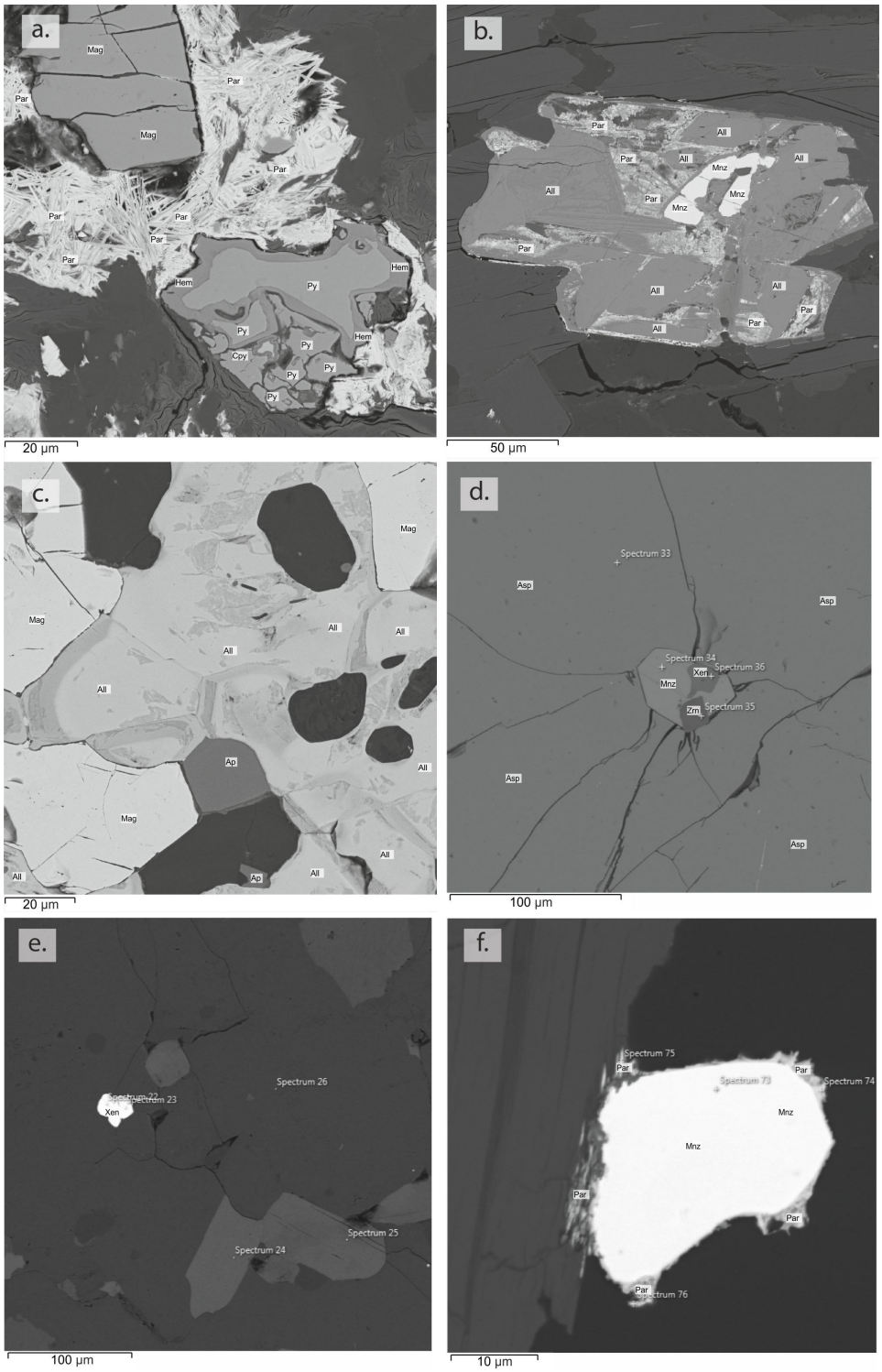


Figure 32. EDS images of textures and associations of REE-minerals a) pyrite (Py) and magnetite (Mag) crystals, hematite (Hem) surrounds the Py and a late needle-like parisite (Par) aggregates in between the Mag and Py crystals (Sample ALZ190037A-1). b) allanite (All) crystal with a monazite (Mnz) inclusion. The allanite is altered to fine grained Par (sample ALZ190037A-1). c) Allanite aggregate in between Mag and apatite (Ap) crystals (sample ALZ190037A-1). d) Monazite (Mnz) inclusion in an arsenopyrite (Asp) crystal. The Mnz crystal has inclusions of zircon (Zrn) and xenotime (Xen) (sample VNA002A). e) Fine-grained xenotime inclusion (sample ALZ180076A-1). f) Monazite (Mnz) crystal surrounded by needle like parisite (sample ALZ190015A-1).

way, galena within aggregates in contact with chalcopyrite have traces of Cu. In galena found in late veins, traces of Er were found. All three types of galena have O in their analysis, which is most likely mistakenly detected by the analysis. Thus, the analysis with higher O decouple from the negative trend between Pb and S (Figure 35c). Similarly, the trace amount contents of Fe present a negative correlation with Pb (Figure 35d). However, Fe concentrations are not dependant of the type of crystal where they occur.

### 5.6.6 Bismuthinite

Bismuthinite shows great compositional variation and often include minor quantities of other elements such as Fe, Co, Ni, Cu, As, Tc and Sb, which can account for up to 12.61 at% of the composition. Similarly, most analyses show significant quantities of oxygen, related to either the presence of oxide phases or to the quality of the analysis. Since bismuthinite occurs as part of complex fine-grained aggregates, it cannot be discarded that most results represent mix analysis.

### 5.6.7 Native bismuth

Native bismuth is found either as tiny inclusions within arsenopyrite or chalcopyrite crystals, or as part of aggregates with other Bi-bearing minerals and galena. Compositionally, it includes small quantities of Fe, Zn and Sb, probably due to mixed analysis with the surrounding minerals. In a large share of the analysis, Bi was overestimated giving high wt%, consequently these analyses were not considered as reliable for quantitative comparisons. Similarly, most analyses show an average content of 22.21 at% O that is either due to an oxidized component or the analytical methods.

### 5.6.8 Molybdenite

Molybdenite crystals contain trace quantities of Fe, Co, As and W, although none of them higher than 1 at%. Both S and Mo vary between the crystals in response to the content of O (less S and Mo in higher O contents) (Figure 36a). However, when ignoring the O content and normalizing the S and Mo, the elements show a negative correlation. In normalized values the concentration of Mo varies from 31.06 to 33.44 at%, with S varying in a similar proportion defining an inverse correlation between S and Mo (Figure 36a).

### 5.6.9 Cobaltite

Cobaltite occurs within two assemblages, either associated with arsenopyrite or with carrolite. In both assemblages, cobaltite is Ni-poor with concentrations that range from 0.0 to 2.39 at%. Moreover, the quantities of Ni vary within a single crystal, without any discernible zonation. On average, the highest contents of Ni were found in cobaltite inclusions within the Cob-Asp assemblage, whereas the inclusions of cobaltite in the Cpy-Car-Cob association present the lowest contents (Figure 36b). In comparison, average Co contents are higher in the single crystals than in the inclusions found within the Cob-Asp assemblage. The opposite pattern can be seen for the Cpy-Car-Cob assem-

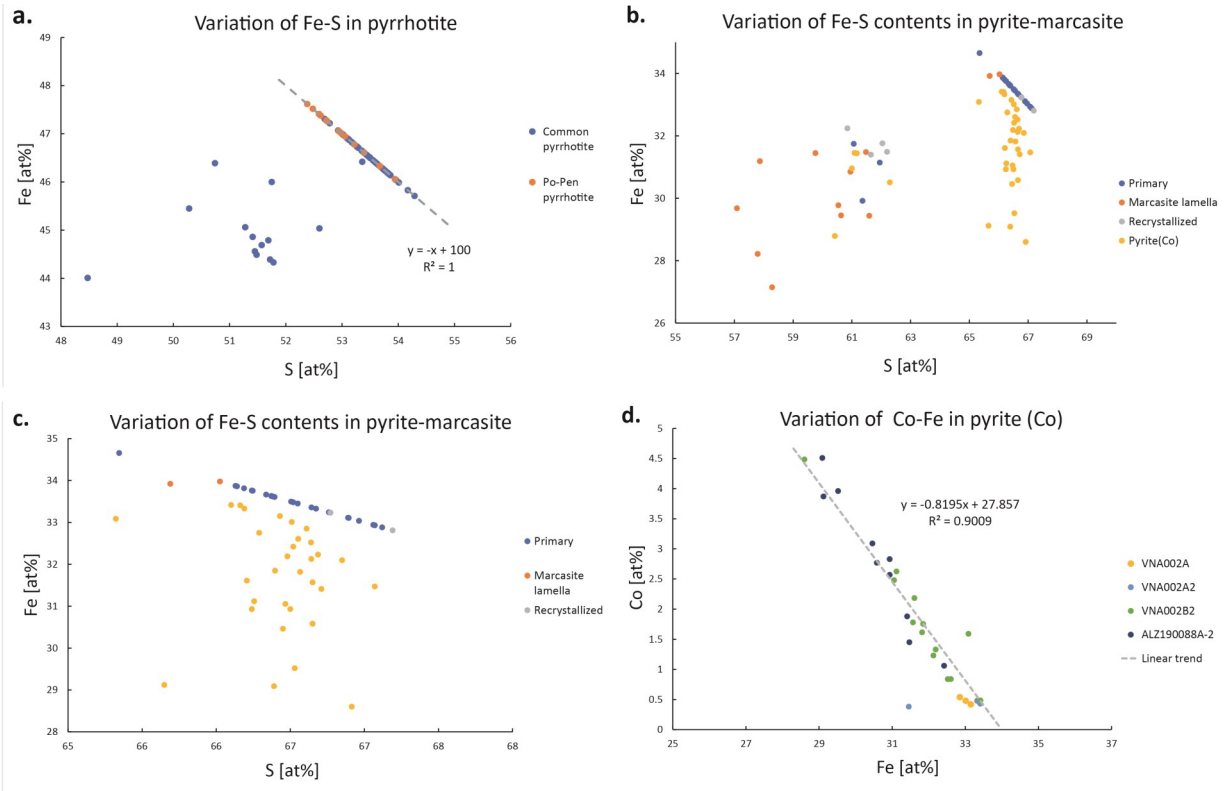


Figure 33. Scatter plots of selected elements for pyrite and pyrrhotite in at%. a) Variation of Fe and S in pyrrhotite. b) Atomic percentages of S and Fe in pyrite and marcasite. c) Scatter plot of Fe and S excluding O rich compositions; note how the Co bearing pyrite decouples from the negative correlation of other types of pyrite. d) Variation of Co and Fe contents in Co-bearing pyrite.

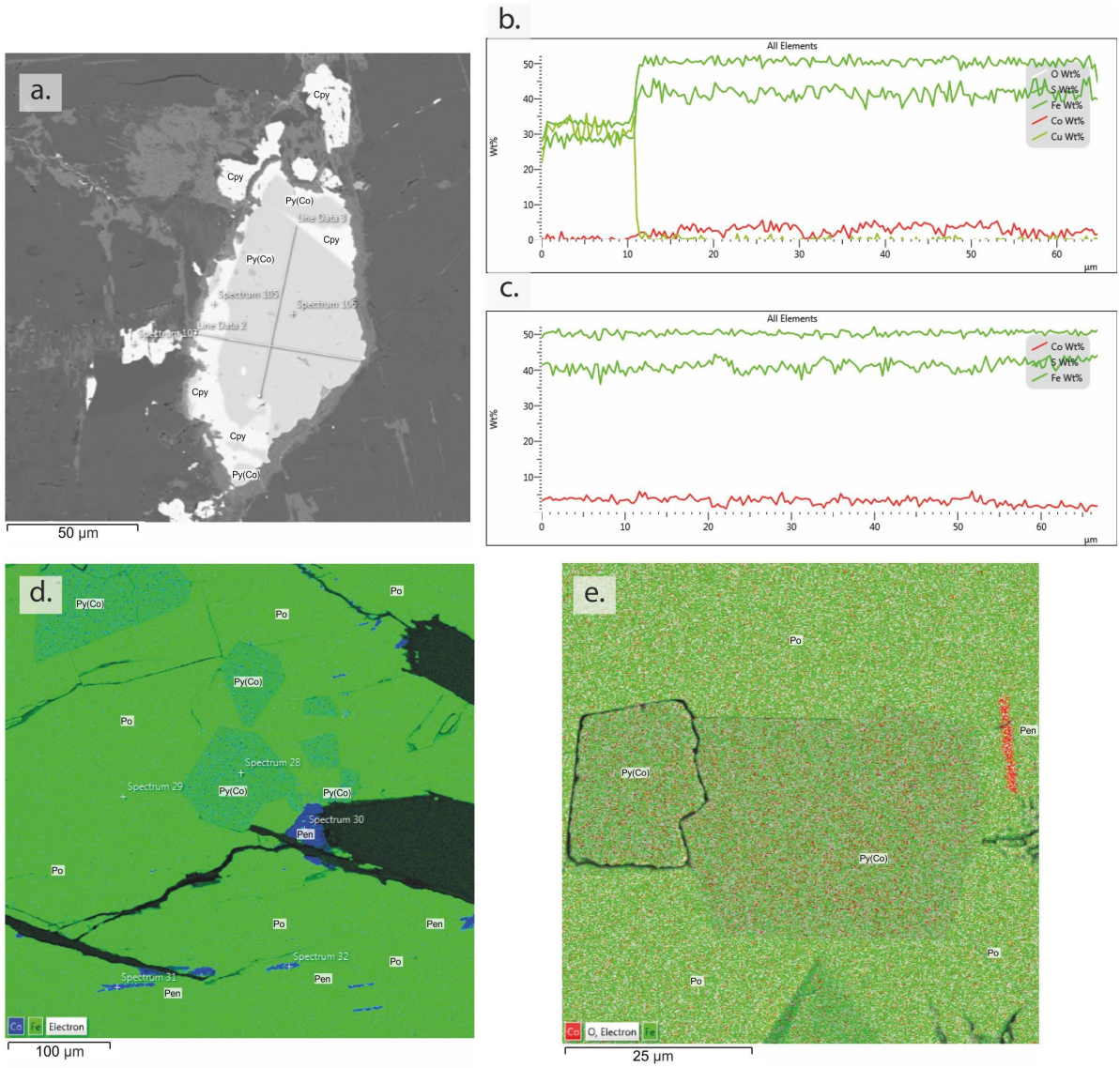


Figure 34. Elemental maps and chemical cross-sections of cobaltoan-pyrite. a) EDS image of a cobaltoan pyrite (Py(Co)) surrounded by chalcopyrite (Cpy). b) Wt% contents of Co, Fe, Cu, S and O in the Line Data 2 transect. c) Wt% contents of Co, Fe, Cu, S and O in the Line Data 3 transect. d) Elemental map of Co (Blue) and Fe (Green) in a Py(Co)-Po-Pen association. Note how the cobalt is concentrated in pentlandite and it is irregularly distributed in the Py(Co). e) Elemental map of Co (Red) and Fe (Green) in a Py(Co) crystal. Note the lack of zonation in the Co concentration.

blage, where Co is higher within the inclusions.

All the cobaltite crystals are Fe-poor, however, from Figure 36b three groups can be identified: (1) extremely Fe-poor cobaltite, (2) Low-Fe cobaltite, and (3) Fe-rich cobaltite. While groups one and two are found within both assemblages, the Fe-richer group 3, with up to 4.58 at% of Fe, only occur within the chalcopyrite-carrolite-cobaltite association.

### 5.6.10 Arsenopyrite

Arsenopyrite crystals are only present together with cobaltite crystals. All the crystals analysed in the three samples containing arsenopyrite have moderate contents of Co between 6.11 and 9.46 at%. Figure 36c shows the relationship between Co and Fe in the arsenopyrite crystals from the different samples. The crystals in sample ALZ180037A-1 are, on average, Co-richer than arsenopyrite grains in the other two samples. Additionally, whereas Co contents vary greatly between crystals of the same sample, variation within single crystals is minimal (<1 at%). All the arsenopyrite crystals that show the higher concentrations of Co, contain inclusions or are in direct contact with other Co-phases (cobaltite or skutterudite). A chemical profile across an arsenopyrite crystal (Figure 37) shows that Co content varies in small proportion without any discernible zonation, and that it differs proportionally to the variation in As content.

In all crystals Co and As show a positive correlation ( Figure 36d), and the arsenopyrites in sample ALZ180037A-1 are the richest in As. Conversely, Fe and Co show a negative correlation (Figure 36c), which is expected as they substitute for each other in the arsenopyrite structure. It is important to note that in contrast to cobaltite, arsenopyrite does not present

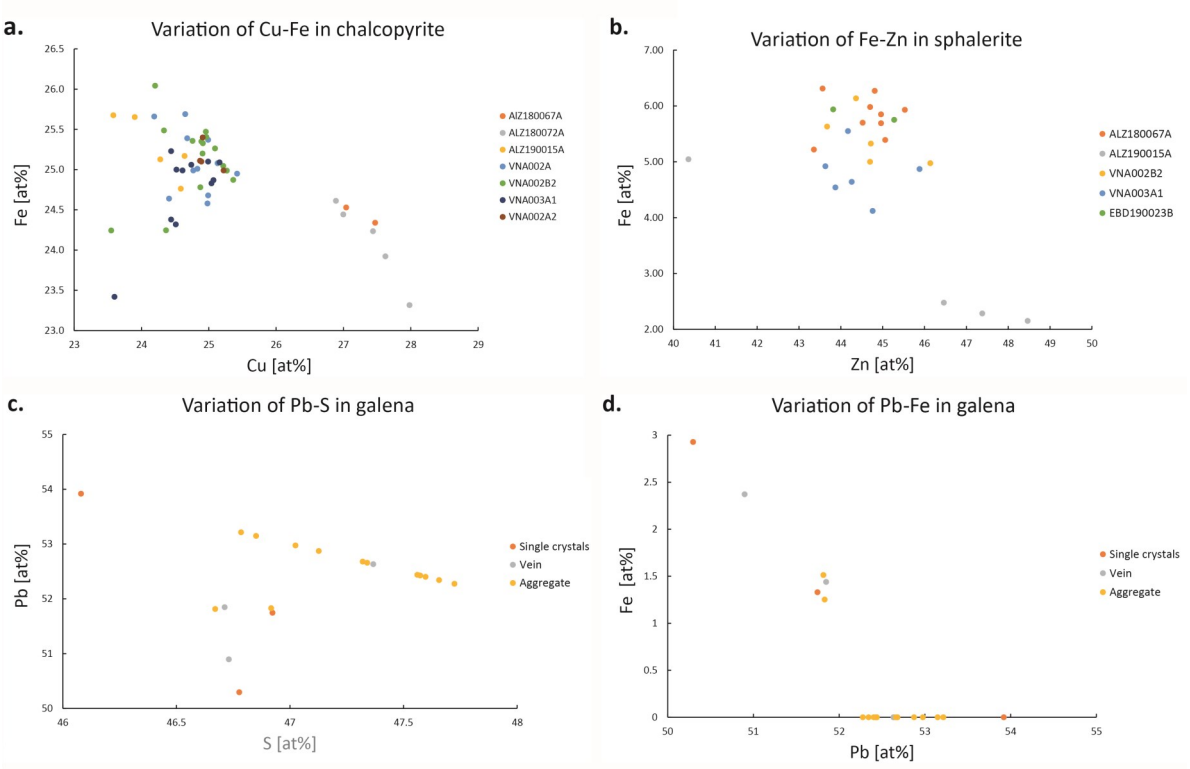


Figure 35. Scatter plots of selected elements for chalcopyrite, sphalerite and galena in at%. a) Atomic percentages of Fe and Cu in chalcopyrite. b) Contents of Fe against Zn in sphalerite. c) Variation of Pb and S in galena. d) Atomic percentages of Pb and Fe in galena.

any Ni content, which implies solid solution only between cobaltite and arsenopyrite and not with gersdorffite.

### 5.6.11 Skutterudite

Skutterudite is only found in sample VNA002A, where it forms part of the cores of arsenopyrite crystals. All the analysed grains show a consistent composition (24.25 at% Fe, 74.44 at% As). Similarly, all crystals have trace quantities of S and Fe that are not greater than 1 at%. Profiles through different skutterudite crystals have a constant Co and As content across the crystals with no visible zonation (Figure 37.). Cobalt and arsenic show a poorly defined inverse correlation (Figure 38a). As has a negative trend against S, likewise Fe against Co (Figure 38b-c).

### 5.6.12 Costibite-Willyamite-Ullmannite

Willyamite and ullmannite form a solid solution as subgroup of the cobaltite group in the system NiSbS-CoSbS. Costibite and paracostibite are the orthorhombic polymorphs of the Co-end member (CoSbS; Dobbe 1991). Four of the observed samples contain minerals within these compositions, as part of different assemblages (Cob-Asp, Po-Py(Co), or Po-Py-Cpy-Sph). Without further X-ray diffraction analysis is impossible to differentiate Co-rich willyamite from costibite with minor Ni contents. However, following the classification of Dobbe (1991) all compositions with Co/(Co+Ni) values between 0.87 and 0.5 are classified as willyamite, where anything outside of that range, is referred as ullmannite (Ni-rich) or costibite (Co-rich). Based on this classification, costibite and Fe-costibite are present in all samples, apart from sample VNA002B2, either as euhedral to subhedral crystals surrounded by chalcopyrite or pyrrhotite, or within galena and native Bi aggregates. Nonetheless, Ni contents in costibite vary within the same sample. In contrast, willyamite and ullmannite crystals are only found in Gal-Bi aggregates in sample VNA002B2, either separately or coexisting within the same aggregate.

Figure 39a shows that the contents of Ni vary greatly within each sample and association for costibite, which can contain up to 3.16 at% Ni, where the Ni and Sb contents are not correlated. In contrast Ni contents in willyamite range between 8.98 and 10.17 at%. For the willyamite crystals a linear negative correlation is observed between Sb and Ni contents.

### 5.6.13 Carrolite

Carrolite is only found in dacitic metavolcanics where it occurs as part of veinlets and disseminations associated with chalcopyrite and cobaltite. Some impurities within the crystals include Fe up to 1.23 at% and Ni up to 1.17 at%. Whereas Co-rich cobaltite crystals have an almost constant Cu content around 15 at% (Figure 39b), Co-poorer grains exhibit higher Cu contents. Lower concentrations of Co are also associated to small contents of either Fe or Ni. Thus, minor Fe-Ni substitution of Co (Wagner & Cook, 1999) is responsible for proportional higher Cu carrolite crystals.

### 5.6.14 Pentlandite

Pentlandite only occur as flame-like exsolutions within pyrrhotite aggregates. They are commonly Co-rich (average 44.49 at% Co), and therefore classified as Co-pentlandite. In contrast, Fe and Ni contents are low, averaging 5.29 and 2.79 at% respectively. Within a single crystal, Fe content can vary as much as 3.73 at% with no discernible zonation. In comparison, Ni variation is lower than 0.6 at% within the same grain.

Figure 39c shows the variation of both elements against Co concentrations. In the case of Fe versus Co, they have a strong negative correlation as Fe substitutes for the latter. In comparison, Ni has a flatter pattern which gives an almost constant Ni content. It is noteworthy that the behaviour of Fe and Ni varies independently from each other in the analysis.

### 5.6.15 REE minerals

#### *Sulfide Mineralization (SM)*

In the SM, the most common REE mineral is monazite. The main REE contained in monazite are Ce, La and Nd, however, different quantities of Y, Pr, Sm and Gd are also present. In addition to REE, traces of Th, U, Ca, Pb and Ag locally detected within the crystals. The average La# (La/(La+Ce)) of 0.33 shows that all monazites are Ce-rich.

Parisite was only found in sample ALZ190015A-1, as part of REE mineral aggregates, usually growing close by to apatite crystals. Most analyses have low wt% totals, which is due to the inability of the EDS to measure $CO_2$ contents due to the carbon sample coating. It was not possible to calculate the empirical formulas for parisite crystals since no X-ray diffraction analysis was performed, $H_2O$ contents were not measured and there was a probable loss of F during analysis. However, a parisite composition is assigned due to the contents and relations of Ce, La, F, Ca and low total wt%. Compositionally, all parisite crystals of the SM are rich in Ce as evidenced by their low La# (0.34 on average). In addition to Ce and La, parisite also contains variable amounts of Y, Pr, Nd, Sm and Gd. Moreover, Nd is the third most enriched element in their composition, after La.

In comparison, xenotime is a less abundant REE mineral that is only found locally as minute inclusions in the metavolcanic rocks of the SM. Only three analyses of xenotime crystals were obtained and two of them (XEN-01, XEN-02) have totals above 117 wt%. Nonetheless, they maintain the elemental proportions and give an almost stochiometric xenotime composition when normalized. Chemically, xenotime crystals are enriched in Y, and contain other REEs such as Gd, Dy, Er, Yb, and traces of U.

#### *Iron-Oxide Mineralization (IOM)*

In contrast to the SM, the most abundant REE mineral in this type of mineralization is allanite. Allanite crystals are Fe-rich with minor Mg substitution. They contain La, Ce and trace quantities of Nd. Lanthanum and cerium are equally concentrated in most samples or show a slight La enrichment (La# between 0.50 and 0.54). Monazite crystals in the IOM show a minor La enrichment over Ce (La# = 0.53), but in contrast to the monazite grains from the SM they show less variety of REE, with only minor quantities of Nd.

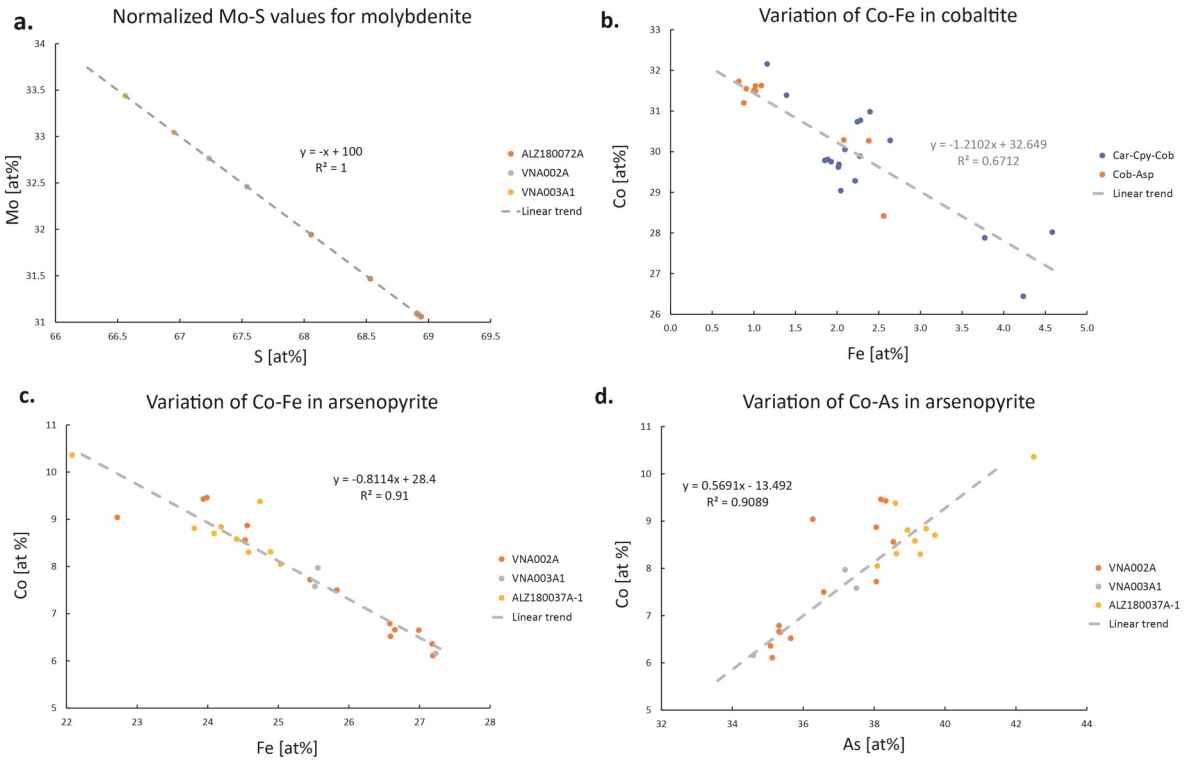


Figure 36. Scatter plots of selected elements for molybdenite, cobaltite and arsenopyrite in at%. a) Normalized atomic percentages of Mo and S in molybdenite. b) Atomic percentages of Fe and Co in cobaltite. c) Variation of Fe and Co in arsenopyrite. b) Concentrations of Co and As in arsenopyrite.

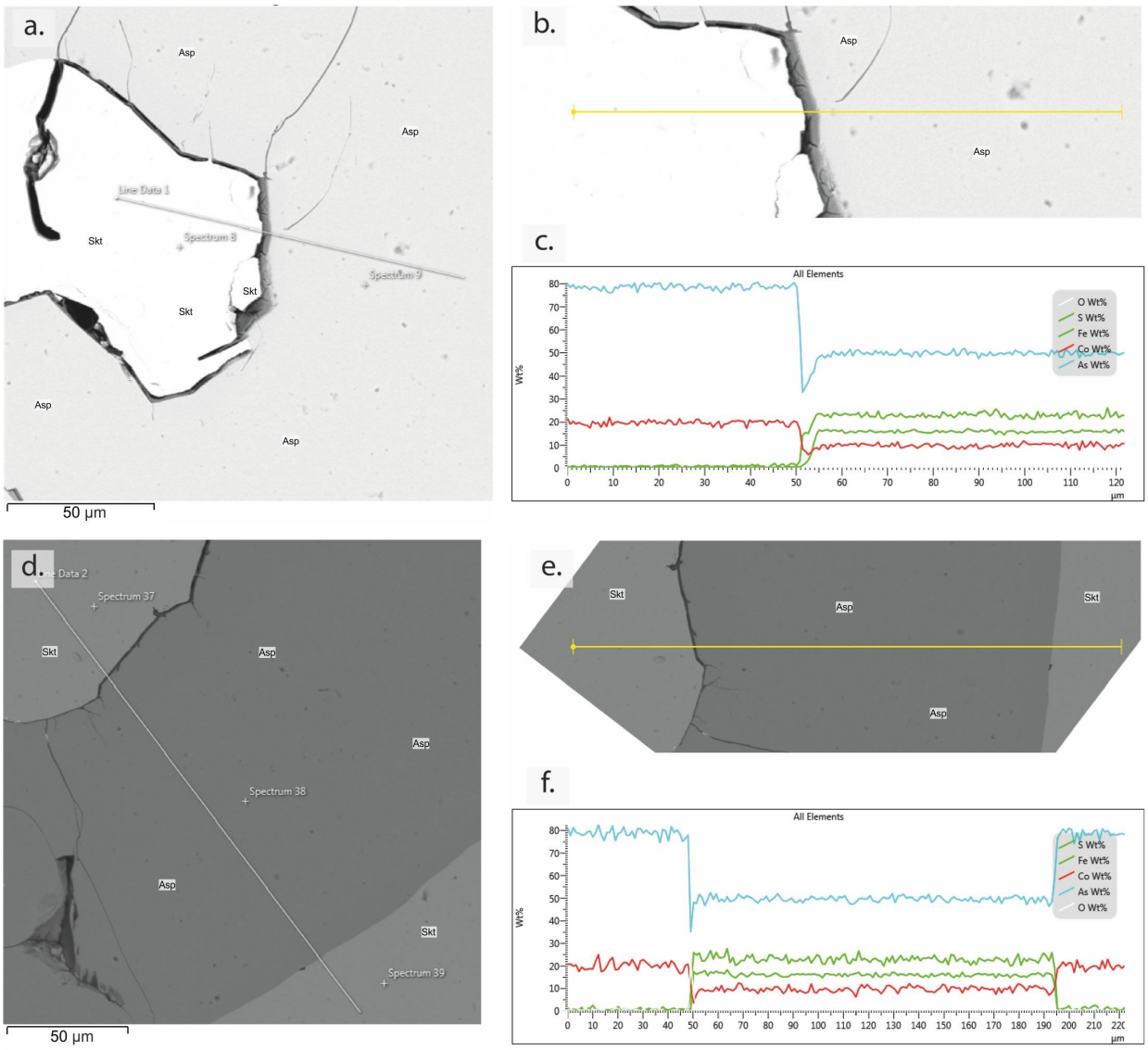


Figure 37. Chemical cross-sections of arsenopyrite and skutterudite crystals. a) EDS image of an arsenopyrite (Asp) crystals with a skutterudite (Skt) core. b) Detailed view of the transect across the Skt and Asp crystals. c) Wt% variations of As, Co, Fe, S and O across the transect in b. d) EDS image showing the transect across an Asp sandwiched between 2 Skt crystals. e) Detailed view of the transect. f) Wt% variations of As, Co, Fe, S and O across the transect in e.

Parisite crystals are found as alteration products around allanite crystals in the IOM. In comparison to the parisite found in the SM, these crystals are more enriched in La (La# between 0.52 and 0.60). This La/Ce relationship in parisite is similar to the other REE minerals observed within the IOM. Another difference compared to the SM, is that in the IOM parisite has a significantly lower content of Nd (average of 3.40 wt% in comparison to 10.46 wt% in the SM).

### 4.6.16 Minor minerals

Rare and exotic Co- and Bi-bearing phases are locally found as inclusions within other ore minerals, particularly inside Gal-Bi aggregates. The section below discusses their compositions.

#### *Cosalite*

A mineral similar in composition to cosalite was found in sample VNA002A, as part of the complex Gal-Bi aggregates. The composition is close to cosalite apart from deficiencies of Bi and S, which can be a consequence of the analysis being mixed with another phase or due to the O and Al impurities.

#### *Kobellite*

Kobellite is found in sample VNA003A1, as an inclusion within a cobaltite crystal (Figure 29f). The composition of the grain fits the composition of kobellite for the most part; however, traces of O and a considerable content of cobalt differ from the stochiometric composition. The empirical formula based on 69 sulphur moles (ignoring O) would be $Pb_{22.93}Co_{5.27}Cu_{3.33}Bi_{23.62}Sb_{8.56}S_{69}$. The content of Co might indicate that this is another mineral, a variety of kobellite or a mixed analysis.

#### *Co-Ni-pyrite*

A Co-Ni bearing pyrite was found in sample

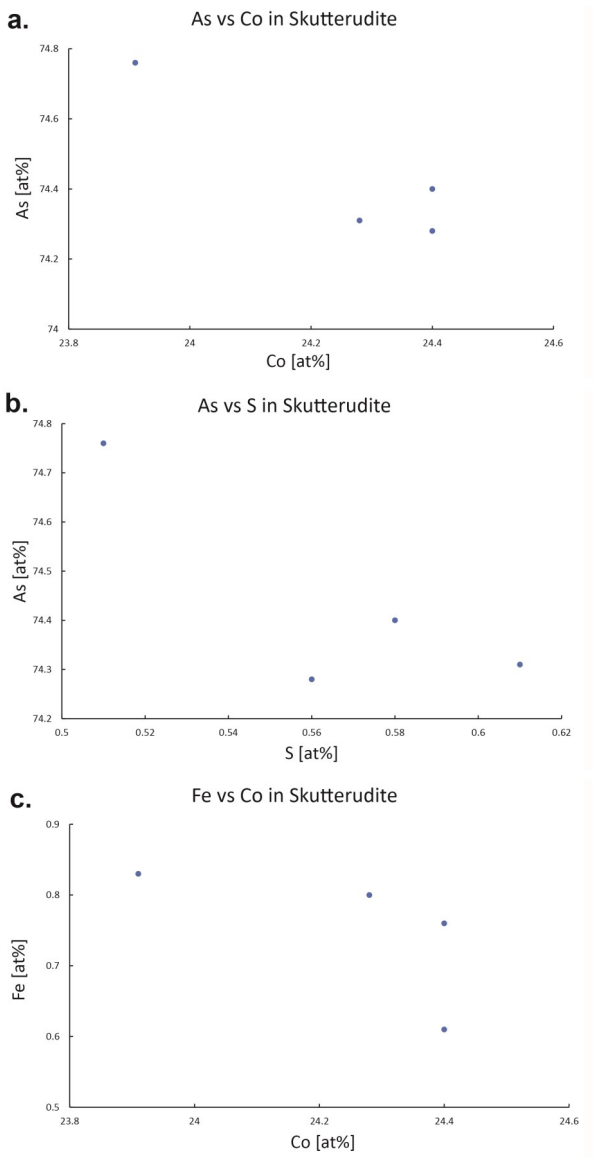


Figure 38. Scatter plots of selected elements for skutterudite in at%. a) Variation of Co and As. b) Concentrations of As and S. c) Atomic percentages of Fe and Co.

VNA002B2, where it is present as a tiny crystal surrounding a monazite crystal in association with a pyrite-(Co). This crystal is different from the other Co-bearing pyrites in that it is heavily enriched in Co, whereas the average Co-bearing pyrite has 1.21 at% of Co this crystal has 12.23 at%. In addition to being more enriched in Co this crystal contains Ni, which is completely absent in any of the other types of pyrites.

### *Unknown phases*

One unknown mineral was found in sample VNA002B2 that is similar in composition to ullmannite; however, it has Fe and Bi in its structure, which deviates from the typical ullmannite composition (NiSbS). The crystal occurs within a Gal-Bi aggregate and yields an empirical formula of $Ni_{0.95}Fe_{50.04}Bi_{0.29}Sb_{0.75}S$. Based on this composition, the mineral could either be a so far unidentified species or a Ni-Bi variety of ullmannite.

## 5.7 U-Pb dating

LA-ICP-MS U-Pb measurements are summarized in table 6 and Tera-Wasserburg diagrams can be found in figures 41 to 45.

### 5.7.1 Sample ALZ180089A-1

The sample is a garnet-zoisite calcareous skarn, made up of skarn bands alternated by quartz veinlets or bands, with a pyrrhotite-pyrite-chalcopyrite mineralization. The skarn assemblages show little to no deformation, thus interpreted as syn-metamorphic. In general, two types of titanite crystals can be found. The first type is related to the skarn band and has subhedral to anhedral crystals with a wide range of morphologies and locally containing different sorts of inclusions, these titanite crystals range from 0.05 to 0.4 mm in size. The second type of crystals are found within the

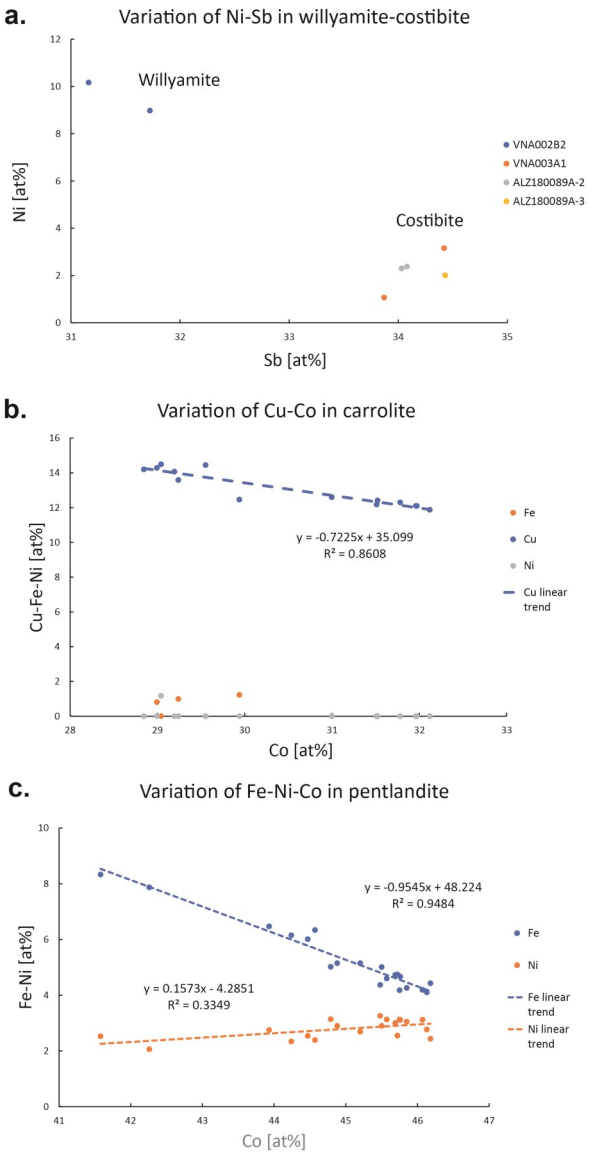


Figure 39. Scatter plots of selected elements for willyamite, carrolite and pentlandite in at%. Concentrations of Ni and Sb per sample in the willyamite grains. b) Variation of Fe and Ni against Co in carrolite. c) Atomic percentages of Ni and Fe against Co concentrations in pentlandite.

quartz veinlets, they are significantly smaller (from 0.01 to 0.15 mm) and are usually euhedral with rhombohedral shapes.

The inside structure of the titanite grains associated to the skarn bands is complex (Figure 40c-d), often having more than one core and several inclusions of quartz or apatite. In comparison, titanite crystals related to the quartz veins show a simpler internal structure, but also contain complexities such as individual cores and growth zoning patterns.

A total of 28 U-Pb analyses were performed on 22 grains of titanite within both quartz veins and skarn bands, of these seven analyses are from titanite rims and 21 from cores. Since the results from rims show variable amounts of common Pb coupled with low radiogenic U contents, they are discarded for age estimations. Additional filtering criteria include to consider only results with over 86% concordance, and to discard analyses that were performed on textural complex grains or that might have included more than one domain within the grains. From the filtered data, only two analyses (Figure 41) give a concordant date with the other four being slightly discordant using common Pb uncorrected data. The concordant analyses are from the core of a complex grain in the Grt-Czo bands (Figure 41a) and from a euhedral crystal within the quartz-bands (Figure 41b), respectively. The mean $^{207}Pb/^{206}Pb$ date is 1929±47 Ma for the filtered analyses, and 1882±16 Ma for the concordant results.

### 5.7.2 Sample ALZ180089A-2

This sample is a metavolcanic rock with abundant amphibole poikiloblasts, with a pyrrhotite-pyrite-chalcopyrite mineralization. Titanite is commonly associated with the amphibole crystals or can be found as single crystals in the rock matrix. Morphologies of the titanites range between euhedral to subhedral crystals with scarce anhedral and irregular grains. The crystals' sizes are between 0.035 to 0.25 mm. It is typical for some of the crystals to present rounded shapes.

All titanite grains have an overgrowth or partial recrystallization that surrounds a rounded to subrounded core. Nonetheless, a smaller portion of the grains contain complex cores, represented by either complex multigeneration cores or by two or more rounded to subrounded cores. The proportion of core to rim varies greatly among the grains, with most crystals presenting a minor overgrowth, whereas in some extreme cases the crystals may only have a minimal core (Figure 40e-f).

A total of 23 grains where analysed including 23 cores and five rims. Titanite rims and cores were treated separately. Analyses of texturally complex grains that included more than two different domains were excluded to avoid the use of mixed data. Data calculations were made using common Pb uncorrected data. Although no concordant date was attained, the cores have a lower intercept date (Figure 42) of 1851±77 Ma (MSWD=9.0) and, likewise, the rims (Figure 43) give a more loosely constrained lower intercept date of 1881±150 (MSWD=8.3).

### 5.7.3 Sample ALZ180089A-3

Similar to sample ALZ180089A-2, these rocks are metavolcanic rocks with amphibole poikiloblasts and pyrrhotite-pyrite-chalcopyrite-sphalerite mineralization. The titanite grains are either associated with the amphibole, as single grains in the matrix or as groups of titanite crystals. Sizes range from 0.03 to 0.6 mm,

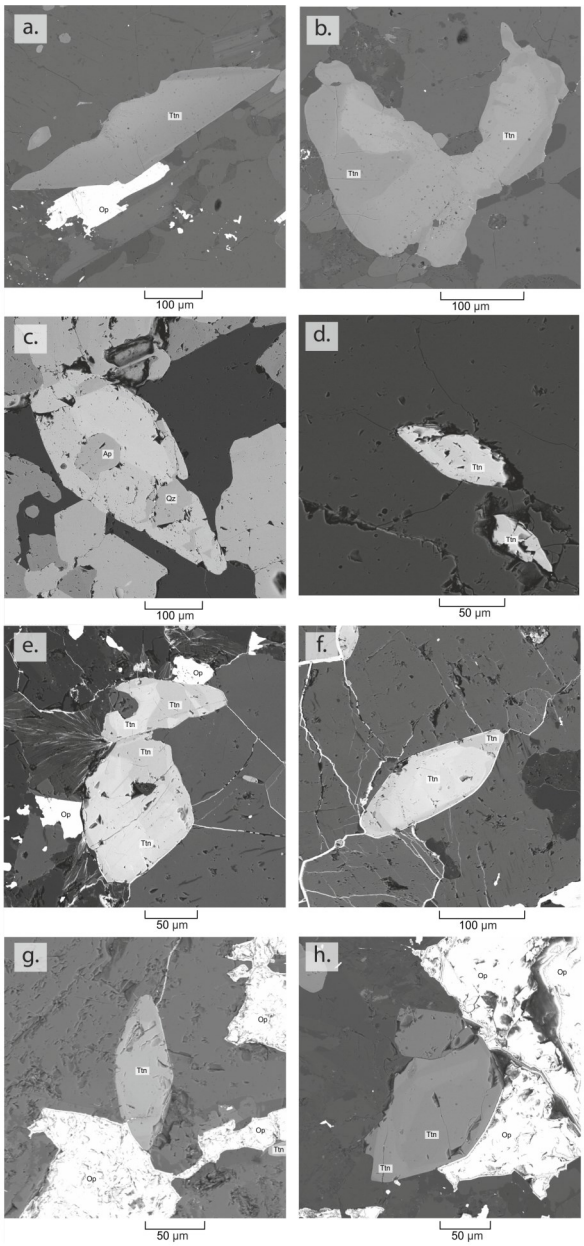


Figure 40. Back-scattered electron (BSE) images of representative titanite grains for each sample analysed. a) Euhedral grain (sample VNA007) with minor overgrowth. b) Complex irregular titanite crystal with an irregular core (sample VNA007). c) Complex euhedral titanite with euhedral core and apatite inclusions (sample ALZ180089A-1). d) Euhedral crystal with a partial overgrowth (sample ALZ180089A-1). e) Irregular crystals with complex irregular cores (sample ALZ180089A-2). f) Euhedral overgrowth around subrounded titanite core (sample ALZ180089A-2). g) Euhedral titanite crystal with a homogeneous core and minor overgrowth (sample ALZ180089A-3). h) Titanite crystal with a core and irregular overgrowth (sample ALZ180089A-3).

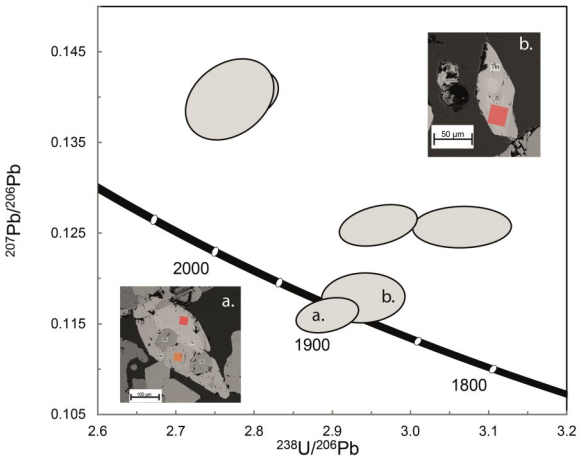


Figure 41. U-Pb Tera-Wasserburg Concordia diagram for cores from sample ALZ180089A-1. a) titanite grain that yields the concordant age (a). The concordant analysis is marked in red, while another analysis performed in the same grain is marked in orange. b) Spot (red) in the titanite grain that corresponds to the concordant age of (b).

and morphologies vary from perfect euhedral rhombohedral crystals to anhedral higher irregular grains (Figure 40g-h). The anhedral crystals are usually bigger than the euhedral ones. Internally, most grains present a sub-rounded core with a minor overgrowth. Complex cores are only present in the bigger and more irregular titanite crystals. Inclusions of apatite, quartz or sulphides are not uncommon within the titanite grains.

A total of 25 cores and four rims were analysed. Rims and analyses that included two domains within the titanite crystals were excluded from the age calculations. All the results from the selected cores are discordant (Figure 44) with a lower intercept date of 1843±56 (MSWD=1.15) based on 14 analyses , without common Pb corrections. In contrast core data show highly discordant and scattered dates yielding a lower intercept of 1933±350 (MSWD=23).

### 5.7.4 Sample VNA007A

This is the only in-situ sample, collected from the wall of the pit of the Långgruvan mine. It is a rhyolitic metavolcanic rock with green amphibole bands and pyrrhotite + pyrite ± chalcopyrite mineralization associated to these bands. These titanite and amphibole bands are parallel to the general foliation of the rock.
Titanite crystals range in morphology from perfectly rhombohedral euhedral crystals to irregular anhedral crystals. The irregular crystals are between 0.1 and 0.3 mm in length, whereas the euhedral crystals tend to be smaller with sizes between 0.05 and 0.2 mm.
The more rhombohedral crystals usually have a core with a minor overgrowth or partial recrystallization around it, however, some of them show a zoned overgrowth (Figure 40a-b). The larger and more irregular grains have complex internal structures including multiple and irregular cores, often with inclusions of quartz, apatite or sulphides.

Date results for this sample were obtained from a total of 22 analyses that included 17 cores and five rims using common Pb uncorrected data. Analyses that included two or more domains within the titanite crystals and texturally complex grains were excluded to avoid mixed data. Rims and cores were treated separately, cores (Figure 45) show discordant results with a lower intercept date of 1889±70 (MSWD=7.1). Similarly, the rims (Figure 46) show scattered results with a lower intercept date of 1857±180 (MSWD=10.1).

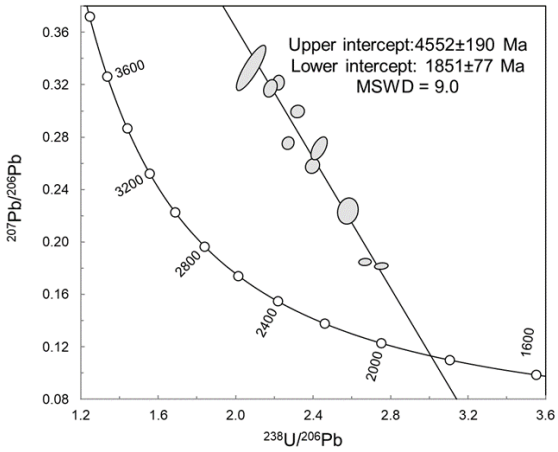


Figure 42. U-Pb Tera-Wasserburg Concordia diagram for cores from sample ALZ180089A-2, uncorrected for common Pb.

# 6 Discussion

## 6.1 Petrography and Metamorphic conditions

### 6.1.1 Rhyodacitic metavolcanics

The rhyodacitic metavolcanics show rhyodacitic and dacitic compositions based on immobile trace elements; however, mineralogically the abundance of quartz and K-feldspar would suggest more rhyolitic compositions. According to the alteration diagram of

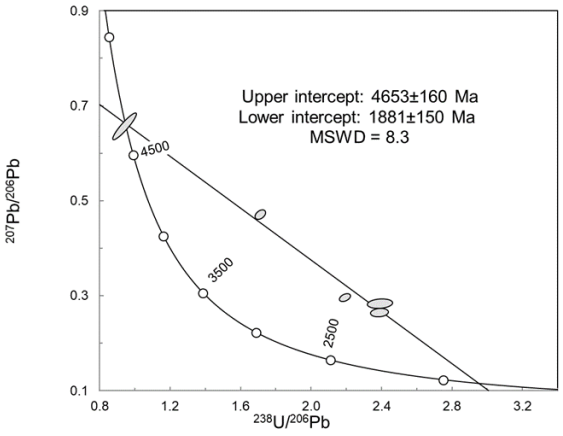


Figure 43. U-Pb Tera-Wasserburg Concordia diagram for rims from sample ALZ180089A-2, uncorrected for common Pb.

Table 7. LA-ICP-MS U-Pb data.

| Sample | Spot | Th/U[c] | $^{206}Pb/^{204}Pb$[a] | Isotope ratios, uncorrected for common-Pb | | | | | | | Age data (Ma), uncorrected for common-Pb | | | | | | |
|---|---|---|---|---|---|---|---|---|---|---|---|---|---|---|---|---|---|
| | | | | $^{207}Pb/^{235}U$[b] | 2σ [%][e] | $^{206}Pb/^{238}U$ | 2σ [%][e] | rho[d] | $^{207}Pb/^{206}Pb$ | 2σ [%][e] | $^{207}Pb/^{235}U$ | 2σ[e] | $^{206}Pb/^{238}U$ | 2σ[e] | $^{207}Pb/^{206}Pb$ | 2σ[e] | Conc% |
| ***ALZ180089A-1*** | | | | | | | | | | | | | | | | | |
| *Cores* | | | | | | | | | | | | | | | | | |
| | ALZ180089A1-15 | 0.08 | 1411 | 5.529 | 1.593 | 0.346 | 1.129 | 0.467 | 0.12 | 1.36 | 1905 | 21 | 1914 | 19 | 1895 | 24 | 100 |
| | ALZ180089A1-19 | 0.08 | 477 | 5.655 | 2.344 | 0.326 | 1.682 | 0.763 | 0.13 | 1.49 | 1925 | 30 | 1820 | 27 | 2039 | 26 | 95 |
| | ALZ180089A1-21 | 0.10 | 1062 | 5.532 | 2.405 | 0.340 | 1.477 | 0.575 | 0.12 | 1.91 | 1906 | 31 | 1888 | 24 | 1925 | 34 | 99 |
| | ALZ180089A1-25 | 0.13 | 441 | 6.964 | 3.495 | 0.361 | 1.664 | 0.691 | 0.14 | 2.61 | 2107 | 46 | 1988 | 28 | 2225 | 45 | 94 |
| | ALZ180089A1-6 | 0.79 | 653 | 5.869 | 1.764 | 0.338 | 1.373 | 0.524 | 0.13 | 1.49 | 1957 | 23 | 1878 | 22 | 2041 | 26 | 96 |
| | ALZ180089A1-9 | 0.08 | 341 | 6.933 | 2.258 | 0.358 | 1.172 | 0.699 | 0.14 | 1.62 | 2103 | 30 | 1975 | 20 | 2231 | 28 | 94 |
| ***ALZ180089A-2*** | | | | | | | | | | | | | | | | | |
| *Cores* | | | | | | | | | | | | | | | | | |
| | ALZ180089A2-11 | 1.56 | 196 | 19.990 | 1.730 | 0.450 | 1.075 | 0.535 | 0.32 | 1.41 | 3091 | 25 | 2397 | 22 | 3579 | 22 | 78 |
| | ALZ180089A2-12 | 1.04 | 139 | 16.740 | 1.870 | 0.441 | 1.112 | 0.628 | 0.28 | 1.42 | 2920 | 27 | 2354 | 22 | 3338 | 22 | 81 |
| | ALZ180089A2-13 | 1.49 | 172 | 17.824 | 1.855 | 0.431 | 1.214 | 0.670 | 0.30 | 1.34 | 2980 | 27 | 2311 | 24 | 3469 | 21 | 78 |
| | ALZ180089A2-15 | 1.33 | 187 | 20.109 | 2.421 | 0.459 | 1.331 | 0.714 | 0.32 | 1.73 | 3097 | 35 | 2436 | 27 | 3558 | 27 | 79 |
| | ALZ180089A2-21 | 1.13 | 238 | 11.967 | 3.828 | 0.388 | 1.661 | 0.307 | 0.22 | 3.63 | 2602 | 54 | 2113 | 30 | 3008 | 58 | 81 |
| | ALZ180089A2-22 | 1.55 | 436 | 22.085 | 6.872 | 0.481 | 2.959 | 0.945 | 0.33 | 4.22 | 3187 | 99 | 2532 | 62 | 3631 | 65 | 79 |
| | ALZ180089A2-23 | 0.85 | 215 | 14.863 | 2.295 | 0.417 | 1.246 | 0.626 | 0.26 | 1.77 | 2807 | 33 | 2249 | 24 | 3236 | 28 | 80 |
| | ALZ180089A2-5 | 1.13 | 271 | 15.419 | 3.584 | 0.412 | 1.394 | 0.781 | 0.27 | 2.67 | 2842 | 51 | 2222 | 26 | 3316 | 42 | 78 |
| | ALZ180089A2-6 | 1.24 | 269 | 9.112 | 1.432 | 0.363 | 1.030 | 0.542 | 0.18 | 1.15 | 2349 | 20 | 1999 | 18 | 2669 | 19 | 85 |
| | ALZ180089A2-7 | 1.21 | 253 | 9.565 | 1.502 | 0.375 | 1.007 | 0.562 | 0.19 | 1.18 | 2394 | 21 | 2052 | 18 | 2699 | 19 | 86 |
| *Rims* | | | | | | | | | | | | | | | | | |
| | ALZ180089A2-10 | 1.34 | 36 | 37.932 | 2.600 | 0.583 | 1.425 | 0.797 | 0.47 | 1.71 | 3718 | 38 | 2961 | 34 | 4155 | 25 | 80 |
| | ALZ180089A2-16 | 1.42 | 77 | 16.374 | 4.033 | 0.418 | 2.451 | 0.717 | 0.28 | 2.83 | 2899 | 58 | 2251 | 47 | 3386 | 44 | 78 |
| | ALZ180089A2-4 | 0.04 | 72 | 18.632 | 2.841 | 0.456 | 1.181 | 0.709 | 0.30 | 2.18 | 3023 | 41 | 2420 | 24 | 3453 | 34 | 80 |
| ***ALZ180089A-3*** | | | | | | | | | | | | | | | | | |
| *Cores* | | | | | | | | | | | | | | | | | |
| | ALZ180089A3-11 | 3.16 | 75 | 17.034 | 1.825 | 0.436 | 1.182 | 0.570 | 0.28 | 1.45 | 2937 | 26 | 2335 | 23 | 3380 | 23 | 79 |
| | ALZ180089A3-13 | 4.00 | 80 | 19.865 | 3.747 | 0.464 | 2.430 | 0.776 | 0.31 | 2.41 | 3085 | 54 | 2457 | 50 | 3523 | 37 | 80 |
| | ALZ180089A3-14 | 2.96 | 83 | 15.440 | 1.784 | 0.423 | 1.212 | 0.586 | 0.26 | 1.40 | 2843 | 25 | 2274 | 23 | 3275 | 22 | 80 |
| | ALZ180089A3-15 | 3.23 | 81 | 17.652 | 1.912 | 0.443 | 1.352 | 0.666 | 0.29 | 1.39 | 2971 | 27 | 2364 | 27 | 3412 | 22 | 80 |
| | ALZ180089A3-19 | 2.92 | 89 | 16.832 | 1.826 | 0.438 | 1.261 | 0.612 | 0.28 | 1.40 | 2925 | 26 | 2340 | 25 | 3357 | 22 | 80 |
| | ALZ180089A3-2 | 2.94 | 88 | 16.282 | 1.771 | 0.430 | 1.237 | 0.562 | 0.27 | 1.42 | 2894 | 25 | 2307 | 24 | 3332 | 22 | 80 |
| | ALZ180089A3-20 | 3.89 | 74 | 16.522 | 2.006 | 0.439 | 1.300 | 0.665 | 0.27 | 1.46 | 2907 | 29 | 2344 | 26 | 3324 | 23 | 81 |
| | ALZ180089A3-23 | 3.00 | 79 | 15.274 | 1.744 | 0.425 | 1.062 | 0.601 | 0.26 | 1.34 | 2833 | 25 | 2284 | 20 | 3250 | 21 | 81 |
| | ALZ180089A3-24 | 1.16 | 116 | 14.898 | 1.972 | 0.419 | 1.243 | 0.618 | 0.26 | 1.51 | 2809 | 28 | 2255 | 24 | 3235 | 24 | 80 |
| | ALZ180089A3-25 | 2.96 | 71 | 18.283 | 2.037 | 0.452 | 1.209 | 0.664 | 0.29 | 1.50 | 3005 | 29 | 2403 | 24 | 3436 | 23 | 80 |
| | ALZ180089A3-26 | 3.55 | 78 | 16.998 | 1.838 | 0.443 | 1.187 | 0.587 | 0.28 | 1.44 | 2935 | 26 | 2365 | 24 | 3352 | 22 | 81 |
| | ALZ180089A3-27 | 1.23 | 146 | 12.445 | 1.877 | 0.398 | 1.320 | 0.550 | 0.23 | 1.53 | 2639 | 26 | 2159 | 24 | 3030 | 25 | 82 |
| | ALZ180089A3-28 | 1.26 | 128 | 18.055 | 1.930 | 0.449 | 1.296 | 0.639 | 0.29 | 1.44 | 2993 | 28 | 2390 | 26 | 3427 | 22 | 80 |
| | ALZ180089A3-29 | 0.44 | 177 | 17.211 | 1.675 | 0.441 | 1.191 | 0.611 | 0.28 | 1.28 | 2947 | 24 | 2357 | 24 | 3378 | 20 | 80 |

Table 7(cont.). LA-ICP-MS U-Pb data.

| Sample | Spot | Th/U[c] | $^{206}Pb/^{204}Pb$[a] | Isotope ratios, uncorrected for common-Pb | | | | | | | Age data (Ma), uncorrected for common-Pb | | | | | | |
|---|---|---|---|---|---|---|---|---|---|---|---|---|---|---|---|---|---|
| | | | | $^{207}Pb/^{235}U$[b] | 2σ [%][e] | $^{206}Pb/^{238}U$ | 2σ [%][e] | rho[d] | $^{207}Pb/^{206}Pb$ | 2σ [%][e] | $^{207}Pb/^{235}U$ | 2σ[e] | $^{206}Pb/^{238}U$ | 2σ[e] | $^{207}Pb/^{206}Pb$ | 2σ[e] | Conc% |
| ***VNA007A*** | | | | | | | | | | | | | | | | | |
| *Cores* | | | | | | | | | | | | | | | | | |
| | VNA007A10 | 1.23 | 146 | 10.377 | 1.894 | 0.378 | 1.351 | 0.586 | 0.199 | 1.32 | 2469 | 26 | 2067 | 24 | 2819 | 22 | 84 |
| | VNA007A12 | 1.26 | 128 | 11.930 | 2.152 | 0.395 | 1.324 | 0.509 | 0.219 | 1.65 | 2599 | 30 | 2146 | 24 | 2973 | 27 | 83 |
| | VNA007A13 | 0.44 | 177 | 9.232 | 1.920 | 0.363 | 1.358 | 0.610 | 0.184 | 1.31 | 2361 | 26 | 1997 | 23 | 2693 | 22 | 85 |
| | VNA007A14 | 1.18 | 156 | 10.362 | 1.660 | 0.384 | 1.395 | 0.563 | 0.196 | 1.14 | 2468 | 23 | 2095 | 25 | 2791 | 19 | 85 |
| | VNA007A15 | 1.71 | 119 | 12.286 | 2.317 | 0.397 | 1.482 | 0.684 | 0.224 | 1.57 | 2627 | 33 | 2156 | 27 | 3013 | 25 | 82 |
| | VNA007A17 | 1.51 | 145 | 10.991 | 2.176 | 0.386 | 1.605 | 0.504 | 0.206 | 1.71 | 2522 | 30 | 2106 | 29 | 2877 | 28 | 83 |
| | VNA007A19 | 0.90 | 183 | 9.848 | 1.706 | 0.384 | 1.396 | 0.451 | 0.186 | 1.30 | 2421 | 24 | 2093 | 25 | 2709 | 21 | 86 |
| | VNA007A2 | 1.88 | 82 | 15.392 | 1.786 | 0.406 | 1.376 | 0.560 | 0.275 | 1.25 | 2840 | 25 | 2194 | 26 | 3336 | 20 | 77 |
| | VNA007A20 | 1.55 | 110 | 13.316 | 2.535 | 0.404 | 1.823 | 0.525 | 0.239 | 2.02 | 2702 | 36 | 2188 | 34 | 3113 | 32 | 81 |
| | VNA007A21 | 1.63 | 76 | 18.011 | 2.509 | 0.447 | 1.408 | 0.627 | 0.293 | 1.85 | 2990 | 36 | 2380 | 28 | 3431 | 29 | 80 |
| | VNA007A22 | 1.32 | 152 | 10.808 | 1.916 | 0.387 | 1.484 | 0.657 | 0.203 | 1.25 | 2507 | 27 | 2108 | 27 | 2847 | 20 | 84 |
| | VNA007A23 | 1.41 | 156 | 10.583 | 1.579 | 0.381 | 1.328 | 0.454 | 0.201 | 1.16 | 2487 | 22 | 2081 | 24 | 2838 | 19 | 84 |
| | VNA007A3 | 2.38 | 98 | 13.873 | 2.427 | 0.399 | 1.478 | 0.600 | 0.252 | 1.79 | 2741 | 34 | 2165 | 27 | 3198 | 28 | 79 |
| | VNA007A5 | 1.99 | 114 | 12.740 | 1.743 | 0.395 | 1.448 | 0.538 | 0.234 | 1.25 | 2661 | 25 | 2147 | 26 | 3078 | 20 | 81 |
| | VNA007A6 | 1.86 | 122 | 12.245 | 2.046 | 0.391 | 1.329 | 0.627 | 0.227 | 1.42 | 2623 | 29 | 2129 | 24 | 3030 | 23 | 81 |
| | VNA007A7 | 2.04 | 111 | 12.398 | 1.902 | 0.387 | 1.389 | 0.603 | 0.232 | 1.30 | 2635 | 27 | 2111 | 25 | 3067 | 21 | 80 |
| *Rims* | | | | | | | | | | | | | | | | | |
| | VNA007A11 | 1.49 | 55 | 23.673 | 2.694 | 0.485 | 1.533 | 0.672 | 0.354 | 1.93 | 3255 | 39 | 2549 | 32 | 3724 | 29 | 78 |
| | VNA007A16 | 1.68 | 26 | 67.785 | 3.058 | 0.802 | 2.004 | 0.811 | 0.613 | 1.80 | 4296 | 46 | 3796 | 57 | 4539 | 26 | 88 |
| | VNA007A18 | 1.77 | 73 | 18.172 | 2.303 | 0.441 | 1.868 | 0.542 | 0.299 | 1.81 | 2999 | 33 | 2354 | 37 | 3465 | 28 | 79 |
| | VNA007A4 | 1.43 | 102 | 13.539 | 2.648 | 0.407 | 1.409 | 0.657 | 0.242 | 1.95 | 2718 | 37 | 2199 | 26 | 3130 | 31 | 81 |
| | VNA007A8 | 0.38 | 16 | 1289.178 | 11.693 | 11.000 | 11.859 | 0.958 | 0.850 | 3.42 | 7273 | 175 | 16019 | 704 | 5008 | 48 | 220 |

[a] Common Pb estimate based on background-corrected Pb ratios

[b] Corrected for background and within-run U-Pb fractionation and normalised to reference zircon MKED1; $^{207}Pb/^{235}U$ calculated using $(^{207}Pb/^{206}Pb)/(^{238}U/^{206}Pb * 1/137.88)$

[c] U and Pb concentrations and Th/U ratios are approximations calculated relative to MKED1 reference standard

[d] Rho is the error correlation defined as the quotient of the propagated errors of the $^{206}Pb/^{238}U$ and the $^{207}Pb/^{235}U$ ratio

[e] Quadratic addition of within-run errors (2 SDM) and daily reproducibility of MKED1 (2 SDM)

Hughes (1973), most rocks have a K enrichment or alteration which explains why most samples show a greater proportion of felsic minerals than expected from their original composition.

Moreover, a considerable amount of the rhyodacitic samples are overprinted by Ca-rich clinopyroxene, amphibole or titanite which is associated to the "skarn banding". Their textural relationships suggest that they crystalized during a metamorphic event. In addition, calcite occurs in minor quantities in some samples, both in pre-peak-metamorphic assemblages and as part of retrograde assemblages. Most likely, the presence of Ca-bearing minerals indicates the existence of variable quantities of carbonates in the pre-metamorphic assemblages.

Similarly, biotite-rich zones occur throughout the rhyodacitic metavolcanics. These are commonly mineralized with some of them showing traces of sulphide veinlets or micro-stockworks. The fact that they are often associated with mineralized areas points towards a hydrothermal origin where they would be metamorphosed sericitic or argillic alteration zones (Shanks III 2010). Finally, partial chloritization of biotite and amphiboles are interpreted as retrograde

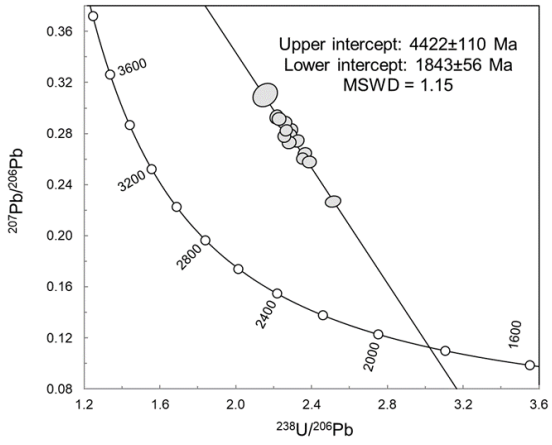


Figure 44. U-Pb Tera-Wasserburg Concordia diagram for cores from sample ALZ180089A-3, uccrrected for common-Pb.

metamorphic products associated to late fluid influx.

### 6.1.2 Cordierite-bearing metavolcanics

The presence of Mg-Al phases such as cordierite and andalusite (Figure 10) in this type of rocks indicate a pre-metamorphic enrichment of such elements. Similar cordierite assemblages have been recognized in other sulphide deposits in the Bergslagen region (e.g. Trägårdh 1991) and associated to pre-metamorphic Mg-enrichment (i.e. alteration) of metavolcanic rocks. Additionally, the presence of tourmaline suggests that B-rich fluids circulated through the volcanoclastic sequence (Jansson et al. 2017).

The stable metamorphic assemblage in the analysed sample (ALZ180076A-1) is cordierite-biotite-plagioclase-K-feldspar with andalusite hints at the start of a break-down as a result of partial melting. Muscovite relicts show the consumption of this phase to pro-

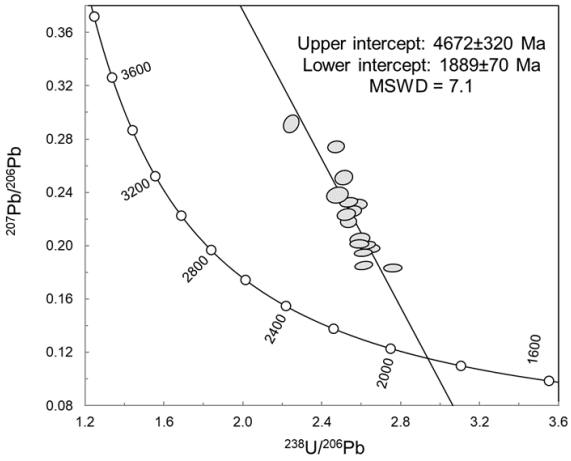


Figure 45. U-Pb Tera-Wasserburg Concordia diagram for cores from sample VNA007A, uncorrected for common-Pb.

duce K-feldspar. In addition, the presence of minute garnet crystals might suggest the metastability of garnet. Preliminary data by Lewerentz (unpublished data; 2020) tentatively show prograde- to peak-metamorphic conditions of 517-612°C and 1.3-3.5 kbar, based on the stable assemblage in a pseudosection model for the cordierite-bearing sample. These data imply that the peak of metamorphism took place under low P, middle amphibolite-facies. This is in accordance with the regional metamorphic conditions as was found by other authors (e.g. Stephens et al. 2009; Skelton et al. 2018).

### 6.1.3 Anthophyllite-bearing metavolcanics

The occurrence of anthophyllite poikiloblasts in this type of rock, by analogy to the cordierite-bearing metavolcanics, suggests a pre-metamorphic enrichment of Mg. Dobbe (1994) interprets this presence of anthophyllite within metamorphosed volcanics at the Tunaberg deposit as a result of metamorphism of a sub-sea floor altered volcanic sequence. Similar conclusions have been drawn from other deposits in the region (Weihed & Eilu 2005; Kampmann et al. 2018).

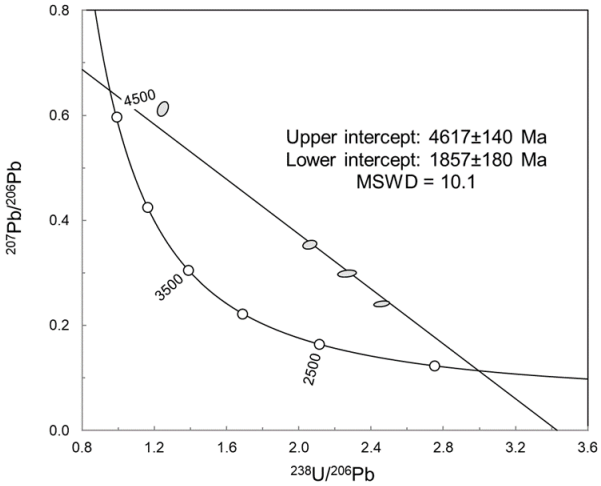


Figure 45. U-Pb Tera-Wasserburg Concordia diagram for rims from sample VNA007A, uncorrected for common-Pb.

In addition, scarce enstatite poikiloblasts associated with anthophyllite imply that at least locally metamorphism occurred at higher temperatures. The transition from anthophyllite to enstatite in the $MgO\text{-}SiO_2\text{-}H_2O$ system is represented by the dehydration reaction:

1) $$Ant = 7En + Qz + H_2O$$

Experimental studies (Hemley et al. 1977; Chernosky et al. 1985) show that this reaction occurs at a minimum temperature between 720 to 790 °C under low pressures (2.0 to 3.5 kbar). However, the presence of other components, like CaO in the case of the Vena area, can significantly alter the P-T conditions for the reactions. Furthermore, the existence of $H_2O$ in the system is also known to influence the temperature at which enstatite is stabilized; where higher $H_2O$ translate into lower temperatures at which enstatite can become stable (Chernosky et al. 1985). The occurrence of enstatite points towards peak-metamorphic temperatures in the upper part of the span estimated from cordierite-bearing rocks (Lewerentz, personal communication), or possibly even higher.

### 6.1.4 Dacitic metavolcanics

Although the dacitic metavolcanics show a similar composition to the mafic end members of the rhyodacitic metavolcanics, they do not share the same mineralogical characteristics. Dacitic metavolcanics are richer in chlorite and Ca-bearing minerals such as clinozoisite and plagioclase, while K-feldspar, quartz and biotite dominate the rhyodacitic samples.

Using the alteration box approach of Large et al. (2001), the dacitic sample shows (Figure 47) a hydrothermal trend to a carbonate-propylitic type of alteration which would explain both the abundant chlorite and epidote together with the low-Ca plagioclase. Two types of chlorite are thought to represent two distinct generations of chlorite. The first consists of thick foliated chlorite laths which most likely formed during hydrothermal alteration of the previous rock, later recrystallized and deformed during metamorphism. The second type is made up of fine-grained chlorite aggregates that are commonly found pseudomorphing epidote crystals, indicating that they probably represent a second generation that occurred during retrograde influx of fluids.

### 6.1.5 Amphibolite

The geochemical data show that amphibolites have compositions between andesite and basalt. These, together with the mineralogy and the contact relationships with the metavolcanics, suggest that they represent mafic intrusions, emplaced before regional metamorphism. Extensive modelling of metabasite assemblages during metamorphism by Palin et al. (2016) demonstrates that under low pressure conditions, the minimum possible temperature to initiate partial melting is 680°C for the more dacitic compositions, whereas in more mafic compositions at least 720°C are required for melt generation. It can be inferred that low-pressure conditions have operated at the deposit based current local and regional metamorphic pressure estimates (Skelton et al. 2016; Lewerentz 2020; unpublished data). The lack of major migmatitic structures in the amphibolite rocks at the deposit it is likely that amphibolites attained temperatures below 680°C.

### 6.1.6 Granodiorite

Field observations in this study suggest that at least in the Vena area, granodioritic bodies intruded the metavolcanic sequence either before or during early deformation and metamorphism. This is supported by conformable contacts and a foliation parallel to the regional deformation, together with the presence of garnet porphyroblasts. Although garnet can crystalize from peraluminous magmas at low pressures, their textural relations (i.e. foliated garnets) and the low $Fe_2O_3$ contents (<7 wt%) are strong indicators for a metamorphic origin (Zhang et al. 2012).

The geochemistry of the granodiorites show that all samples have a moderately to strong peraluminous composition (Figure 48), characteristic of S-type granites (Chappell 1999). The S-type granitoid are widely assumed to be products of partial-melting of metasediments in the upper crust during orogenesis (Pearce et al. 1984; Chappell 1999). This agrees with the current interpretation of the genesis of some of the syn-orogenic intrusions of the GDC suite (Stephens et al. 2009; Stephens & Jansson 2020).

### 6.1.7 Tectonic environment and general metamorphic conditions

The general trace element distribution of all the metavolcanic rocks (Figure 18a) suggests that they were deposited near a continental margin. Amphibolite samples (Figure 18b) appear to be emplaced in either a volcanic arc, mid-ocean ridge or a continental subduction zone. Together, they are in general agreement with a continental back-arc setting as proposed by other authors (Nironen 1997; Hermansson et al. 2008; Johansson & Stephens 2017). Nevertheless, since most samples of both amphibolites and volcanics are pervasively altered (Figure 18), interpretations on the geotectonic environment should be taken with caution as the elements used for geotectonic interpretation could have been remobilised during alteration.

Both the granodioritic intrusions and the metavolcanic rocks show similar REE patterns. Additionally, their field relationships suggest that they were metamorphosed together. Thus, due to their spatial relationship and geochemical signature they are interpreted as subvolcanic intrusions that were emplaced shortly after the volcanoclastic rocks and before metamorphism. Lewerentz et al. (2019) had previously suggested this, and several examples of granodioritic bodies occurring as subvolcanic intrusions have been documented in the Bergslagen Province (Stephens & Jansson 2020).

Most metavolcanic rocks show signs of hydrothermal alteration before regional metamorphism. The rhyodacitic metavolcanics are commonly K-altered, whereas the anthophyllite- and cordierite-bearing rocks show different degrees of Mg alteration. In comparison, dacitic volcanics were subjected, to a certain degree, to carbonate propylitic alteration.

Based on the data from cordierite-bearing metavolcanics, the peak metamorphic temperatures in

the area are assumed to have reached up to 612°C. However, the presence of enstatite porphyroblasts in anthophyllite-bearing rocks suggest together with the lack of partial melting in the amphibolite suggest that peak metamorphic temperatures probably were higher than 612°C, somewhere between 612-680 °C. In comparison, pressures, as determined by the cordierite assemblage, remained low with a maximum pressure below 3.5 kbar. Both temperature and pressure determinations agree with regional metamorphic conditions (Skelton et al. 2018; Stephens & Jansson 2020).

## 6.2 Titanite geochronology

All the U-Pb dates obtained from rim analyses show variable amounts of Pb loss coupled with low quantities of radiogenic U and highly scattered data. Thus, they were disregarded for age calculations. Similarly, due to the scatter in the data, the results of samples ALZ180089A-2 and VNA007A precludes any age interpretations. Therefore, the two concordant dates of sample ALZ180089A-1 (weighted average mean $^{207}Pb/^{206}Pb$ date of 1882±16 Ma) and the lower intercept age of sample ALZ180089A-3 (1843±56 Ma and MSWD=1.15) represent the only suitable results for age interpretations due to their concordance and low MSWD value, respectively. These two dates are, including their error, within the crystallization age (1884±8 Ma; unpublished data; Lewerentz 2020) of the metavolcanics in the Vena area, which could lead to the interpretation that these cores are inherited igneous cores with a metamorphic overgrowth or recrystallization.

In order to evaluate whether the cores are of metamorphic or igneous origin, the contents of Al and Fe were used according to the method of Aleinikoff et al. (2002). From figure 49, it can be observed that most of the cores in sample ALZ180089A-1 fall within the metamorphic range and only one analysis shows a possible igneous character. Additionally, Frost et al. (2002) suggest that higher Fe contents can be present at high-T metamorphic titanites. Thus, it is interpreted that the titanites from the calcareous skarn, despite variations in size, morphology and mode of occurrence, are metamorphic. Unfortunately, no chemical data is available for the titanite crystals of the other metavolcanic sample (ALZ180089A-3), however,

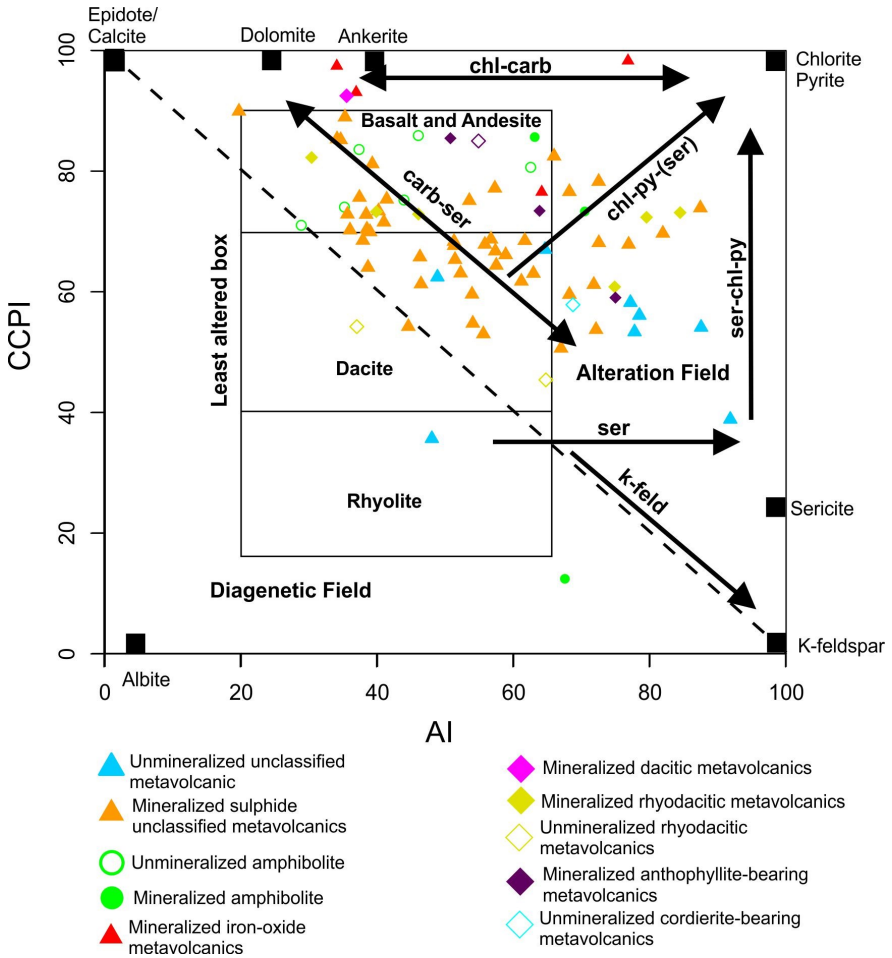


Figure 47. Alteration box plot and common alteration trends for the amphibolite and metavolcanic rocks in the Vena area, where the alteration index (AI) of Ishikawa et al. (1976) plotted against the chlorite–carbonate–pyrite index (CCPI and diagram after Large et al. 2001). ser=sericitization, carb= carbonatization, chl=chloritization, py=pyrite alteration, kfeld=K-feldspar alteration. *AI =100x(MgO+$K_2O$) /(MgO+$K_2O$+CaO+$Na_2O$) and CCPI= 100x(MgO+$Fe_2O_3$)/(MgO+$Fe_2O_3$+$Na_2O$+$K_2O$).*

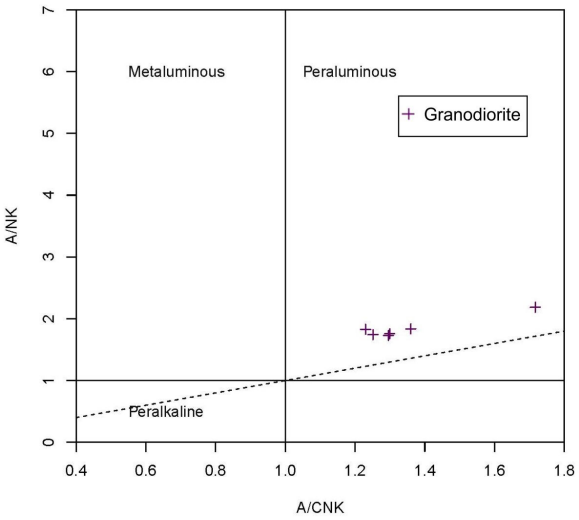


Figure 48. Granodiorite rocks plotted in the aluminium character diagram of Shand (1943). *A/NK = $Al_2O_3$ / ($Na_2O$ + $K_2O$), A/CNK = $Al_2O_3$/ ($CaO$ + $Na_2O$ + $K_2O$).*

their textural association with prograde metamorphic assemblages in the rocks suggest a similar metamorphic origin.

Regional metamorphism in the southern part of the Bergslagen Province was inferred to be two staged processes, where the first metamorphic event ($M_1$) occurred around 1.86 Ga and the second ($M_2$) between 1.84 and 1.80 Ga (Stephens & Jansson 2020). Conversely, intrusion of the GDG suite of rocks, to which the granodioritic intrusions at the study area relate, span a time period between 1.91 and 1.87 Ga (Stephens & Jansson 2020). Therefore, the results of this study overlap within error with both the $M_1$ metamorphic event and the granodiorite intrusion age. Thus, leading to three possible scenarios: 1) titanite cores represent a metasomatic event associated with the granodiorite intrusion, with negligible resetting of the U-Pb system during later metamorphism. 2) The crystal cores were generated during metamorphism and the dates represent either a prograde metamorphic or cooling age. 3) The titanite crystals formed due to metasomatism related to granodiorite emplacement and later regional metamorphism variably modified the U-Pb relations of the crystals.

The first scenario implies that the system maintained itself unaltered during high temperature metamorphism. Traditionally most authors have considered U-Pb ages to reflect cooling ages of metamorphism for high temperature systems (e.g. Frost et al. 2000), due to its closure temperatures between 660 and 700°C. In the Vena-Dampetorp area, peak metamorphic temperatures reached between 612 and 680°C. However, recent studies show that diffusion rates in titanite are slower than previously thought, implicating that U-Pb modifications in titanite can start at temperatures as high as 840°C (Hartnady et al. 2019). Consequently, there is a possibility that the titanite grains could have endured high-temperature metamorphism without fully resetting. Nonetheless, partial resetting cannot be discarded. However, textural relationships of the titanites suggest that they experienced little to no deformation, whereas the granodioritic intrusives show clear evidence of deformation, arguing against this scenario.

In comparison, the second case would imply that all titanite crystalized during metamorphism. Traditionally, titanite dates in Bergslagen have been considered cooling ages for metamorphism (e.g. Stephens & Jansson 2020). The above discussion about closure temperatures in U-Pb isotopic system and the metamorphic condition at the area of study which leaves open two possibilities in which the dates, could represent metamorphic or cooling ages. The mean $^{207}Pb/^{206}Pb$ date of 1882±16 Ma obtained from the calcareous skarn concordant analyses is slightly older than the current estimations of cooling ages from the $M_1$ metamorphic event in Bergslagen (1.86 Ga; Stephens & Jansson 2020). In contrast, the discordant lower intercept date (1843±56 Ma) from the metavolcanic sample ALZ180089A-3, within error spans both the metamorphic and the cooling ages.

Finally, the third case is a combination of both scenarios, where ages could represent either the age of intrusion related metasomatism or regional metamorphism. The data and textures of rims in most of the samples suggest that recrystallization took place after

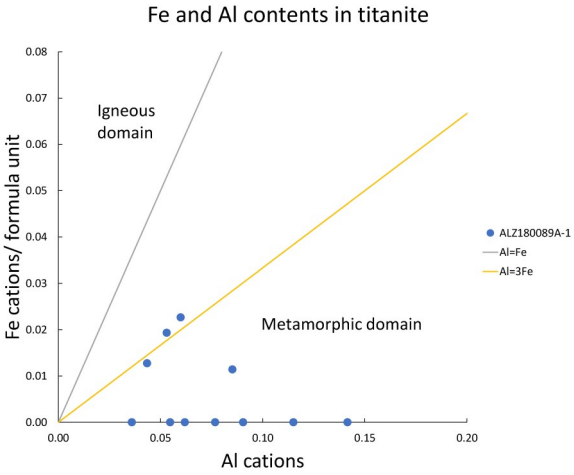


Figure 49. Al and Fe proportions within titanite crystals for sample ALZ180089A-1 (after Aleinikoff et al. 2002).

the core formation, effectively disrupting the U-Pb system in the rims. However, as with the first scenario, the lack of deformational features in the calcareous skarn, argue against a pre-metamorphic crystallization of the titanite and against this scenario.

In conclusion, the second scenario is preferred as it agrees with the field observation together with the current textural and chemical data. Therefore, the mean $^{207}Pb/^{206}Pb$ age of 1882±16 Ma for the skarn sample possibly represents the onset of metamorphism in the Vena-Dampetorp deposit. This is supported by their titanite textural relationship with the skarn prograde metamorphic assemblages. Unfortunately, in the case of the sample ALZ180089A-3 the resolution (i.e. the error) of the lower intercept 1843±56 Ma date obtained combined with the rapid geological evolution of the Bergslagen Province, result in a harder to interpret result. The most likely scenario is that it represents a cooling age where the U-Pb system was kept open during high temperature metamorphic conditions

causing variable Pb loss and thus, the lower intercept reflects the cooling age of the rock when temperatures dropped below the isotopic closure system. However, due to the large error of the dating the alternative scenario in which it also represents the age of the onset of metamorphism cannot be discarded. Therefore, the interpretation of this date most be taken with care.

Nonetheless, the mean $^{207}Pb/^{206}Pb$ metamorphic age of 1882±16 Ma obtained from the skarn sample suggests that metamorphism, at least of the calcareous horizons, occurred shortly after the deposition of the metavolcanic rocks (1884 ±8 ) as both ages overlap. Thus, vulcanism, mineralization and the amphibolite and granodiorite intrusion occurred rapidly within a time period of maximum 24 Ma.

## 6.3 Mineralization and ore distribution

The SM and the OIM differ in several aspects. In general, the IOM tends to be more mafic (andesitic to basaltic; based of immobile element classification), whereas the SM has slightly more felsic compositions (andesitic to rhyolitic). Additionally, they have distinct elemental behaviours where REE and Fe show strong positive correlations in the IOM, while some base metals like Zn show opposite trends. Similarly, there is a strong fractionation of Ce and La between both suites, with the SM being richer in Ce than its IOM counterpart. This indicates that, even though both deposits are spatially related, the mineralization processes that were responsible for each suite are different and possibly independent from each other.

The SM is the focus of this study and represents the majority of samples collected and analysed. The core data of the SM demonstrate that mineralized bodies usually show a normal zonation from Py to Py-Po in disseminations with a gradual transition to Cpy-Po-Py-Sph zones followed by discrete contents of Co-phases sharply in contact with Py disseminated zones. However, more complex ore bodies, like those observed in cores BH9002 and BH9004 zones, can overlap each other, thus, disrupting this pattern, which commonly results in Cpy-Po-Py-Sph in contact with Py disseminations or two Cpy bearing zones close grouped together. Furthermore, the overprinting of these zones by veining adds to the complexity and hinders original zonation.

Based on the current sampling, the Vena mineralization is spatially zoned from NW to SE. Base metals such as Cu and Zn are concentrated in the middle section of the deposit, while Pb, Bi and Sb appear enriched in the NW zone, and As, Co and Mo are more abundant towards the SE section. In comparison, in the Dampetorp area, most elements concentrate in the SW part of the deposit, with Co, Cu and Zn also concentrated towards the SE side.

The elemental distribution also controls the mineralogical phases within the deposit. For example, even though significant Co concentrations can be found across both Vena and Dampetorp areas, cobaltite and skutterudite are only found in the As-rich areas in the Vena SE section. Similarly, carrolite is only discovered in Cu- and Co-rich areas towards the mafic intrusions (i.e. amphibolite) but is absent in Co-rich but Cu-poorer areas. Thus, the different assemblages are controlled both by the metal distribution and zonation of the deposit.

## 6.4 Variability of ore minerals

A common feature in most of the analysed sulphides is the presence of variable amounts of O. For most cases, the main explanation is an analytically false estimation of the element. Elemental analysis using the EMPA are sensitive to sample roughness and the background noise can sometimes be confused with O signature (Egerton 2005). For example, in the case of marcasite as a result from pyrrhotite breakdown, the lamellae create crevasses and valleys that most likely are responsible for higher oxygen content in comparison with primary pyrites. An alternative explanation for this phenomenon is that some results represent mixed analyses and therefore they contain oxidized phases. However, this is only probable in the case of the Bi-Gal aggregates, where the fine-grained intergrowth could include minute inclusions of oxygen bearing minerals.

In contrast, sphalerite, cobaltite, arsenopyrite, costibite-ullmannite, pentlandite and pyrite, have compositional variations of which the amount of Fe is thought to reflect the pressure conditions of the deposit (e.g. Barton & Toulmin 1966). This is further discussed in section 6.5.3. Sphalerite and cobaltite are generally Fe-poor. In contrast, arsenopyrite is Co-rich, where Co and Fe substitute for each other and their compositions reflect temperature conditions of formation (e.g. Klemm 1965; see section 6.5.1). In addition to arsenopyrite and cobaltite, Co-rich pentlandite exsolutions within pyrrhotite have compositional fluctuation between Fe-richer and Co-richer varieties. In comparison with other deposits in the Bergslagen area, for instance Zinkgruvan (Bjärnborg 2009), the pentlandite crystals in the studied area are significantly Ni-poorer. Low Ni contents are also a characteristic of other Ni bearing minerals like cobaltite, arsenopyrite and willyamite. Thus, Ni seems to be only concentrated in a few minerals that occur as rare inclusions within other sulphides such as ullmannite. Low Ni concentrations throughout the deposit probably reflect a low Ni/Co relationship of the mineralizing hydrothermal fluids or a pre-mineralization Ni deficiency in the host rocks.

The occurrence of ullmannite-willyamite has been previously reported in other Co deposits in Bergslagen (e.g. *Hällefors*; Zakrzewski et al. 1980 or *Tunaberg*; Dobbe 1991), where coexistence of Co-free ullmannite with willyamite has been interpreted as a result of a miscibility gap in the CoSbS-NiSbS system at low temperatures (Dobbe 1991). In the Vena area, Co-free ullmannite and willyamite coexist with a Co/Ni+Co ratio of 0.66 on average within the same aggregate. This, together with the observed textures, agrees with the miscibility gap and crystallization mechanism proposed by Dobbe (1991), implying that ullmannite crystalized before willyamite. The fact that ullmannite is scarcer links to the deposit-wide depletion of Ni and to the phase relationships of the CoSbS-NiSbS system that has a peritectic reaction for the latter. This means that in Co-richer compositions, as is the case of the deposit, ullmannite is consumed.

Cobalt-bearing pyrites occur within sulphide veins associated with pyrrhotite and pentlandite or as

single disseminated crystals. They have variable contents of Co that partially substitute Fe in the pyrite structure, as suggested by their negative correlation. The concentration of Co in these pyrites does not have any discernible pattern, with contents independently varying between each crystal. However, crystals within veins have on average the highest cobalt values, possibly indicating Co re-mobilisation (see section 6.6).

## 6.5 Sulphide Thermobarometry

Sulphides and sulphide assemblages have been widely used as geothermometers and geobarometers in order to constrain the P-T conditions of sulfide deposits, especially when fluid inclusion thermobarometry is not available (e.g. Fanlo et al. 2004; Andersson et al. 2016). Whereas arsenopyrite has been used as a geothermometer for metamorphosed sulfide deposits (e.g. Andersson et al. 2016), previous authors (Kretschmar & Scott 1976; Sundblad et al. 1984; Sharp et al. 1985) have suggested the caveats of the method, especially in cases where impurities such as Co exceed 1 wt%. The analysed arsenopyrite crystals have on average 8.10 wt% Co with a minimum value of 6.64 wt%. Therefore, constraining the temperatures using such method is not viable. Instead, this study uses the stability fields of the systems Fe-Ni-Co-S and Fe-Ni-Co-As to broadly constrain the formation temperatures of the distinct assemblages. In order to determine the possible formation pressures, the sphalerite geobarometer of Barton & Toulmin (1966) was used.

### 6.5.1 Fe-Ni-Co-As system

Arsenopyrite and cobaltite are minerals within the present Fe-Ni-Co-As system. Figure 50 shows the composition of cobaltite and arsenopyrite crystals plotted against the temperature curves of Klemm (1965). Although the cobaltite crystals suggest formation temperatures below 400°C, some arsenopyrite crystals fall within the range of 650 to 600°C, with the limitation that most of them plot within the immiscibility gap.

Such high temperatures can be due to the fact that the geothermometer of Klemm (1965) does not consider the As-S substitution within the system, as suggested by Misra & Fleet (1975). Thus, the model is only applicable to As/S ratios lower than one (Fanlo et al. 2004). Figure 51 shows that all of the arsenopyrite grains and most cobaltite crystals have As/S ratios greater than one (1.08-1.69 and 0.84-1.05 respectively). Therefore, it is likely that most of the arsenopyrite and cobaltite temperatures yield false values. Nonetheless, considering the grains with As/S below 1, cobaltite temperatures for the Cob-Car-Cpy assemblage plot between 300 and 400°C. Only one grain with As/S ratio below 1 was found for the Asp-Cob assemblage, plotting between the 300 and 400°C curves.

Therefore, current estimations suggest that at least the Cob-Car-Cpy assemblage formed between 300 and 400°C. These results include estimations from single crystals and inclusions of cobaltite within other phases. The latter show the lowest temperatures (300°C). Considering that As/S ratios in single crystals are higher and approximately one, there is a possibility that single crystals started to re-equilibrate during metamorphism, explaining the higher temperatures, while the inclusions remained shielded from re-equilibration. Whilst these conclusions might be applied to the Asp-Cob assemblage, the temperature of formation should be taken with care, since only one grain was used for the calculations,.

### 6.5.2 Fe-Ni-Co-S system

Pentlandite crystals can be found in samples ALZ190088A-1 and 2, and in sample VNA006B. They are present as subhedral exsolutions or "flames" that commonly grow from the borders of pyrrhotite crystals, and towards the inside of pyrrhotite. Further, they can occur as exsolutions aligned in planes within the pyrrhotite crystals. Flame-like exsolutions of pentlandite are relatively common and have been recognized in several deposits around the world (e.g. Duran et al. 2016; Badiya et al. 2018), ranging from magmatic to hydrothermal.

It is widely accepted that flame-like pentlandite crystals in pyrrhotite exsolve during the cooling of the Fe-S mono-sulfide solution (mss) at lower temperature. In most deposits, pentlandite crystals tend to be Ni- and Fe-rich. In the Fe-Ni-S system pentlandite forms a solid solution with mss from 900°C to 270°C (Kelly & Vaughan 1983). However, recent studies (e.g. Mansur et al. 2019) show that exsolution of pentlandite first occurs below 650°C.

The pentlandite crystals found in Vena are Co-rich, thus can be classified as Co-pentlandite and outside the full scope of the Fe-Ni-S system. The effect of cobalt in the solid solution of Co-pentlandite were studied by Kaneda et al. (1986) who defined these temperature ranges between 600 and 200°C. Figure 52 depicts the pentlandite crystals of Vena in terms of the mol% of each end member in the Fe-Ni-Co-S system, against the fields of solid solution according to the temperature. The compositions of pentlandite indicate that most crystals exsolved from the mss at the minimum temperatures of 200°C. Only one analysis gives temperatures between 300°C and 400°C. These results imply that exsolution of pentlandite occurred either below 400 or 200°C, depending on the analysis considered.

Georgatou and Chiaradia (2020; based on the studies of Craig & Scott, 1974), demonstrate that the pyrite-chalcopyrite-pyrrhotite or intermediate solid solution (iss) is only stable at 200°C in the Cu-Fe-S system in the absence of cubanite. In the sample ALZ190088A-1 and 2, chalcopyrite occurs together with the pyrrhotite and Co-bearing pyrite crystals. Their textural relationships indicate that the chalcopyrite and the pyrrhotite crystalized coevally. By correlation and together with the pentlandite data, it can be inferred that this assemblage crystalized below 200°C.

### 6.5.3 Sphalerite barometry

Sphalerite crystals that are associated with pyrite and pyrrhotite and in equilibrium with such phases were selected for geobarometry. Grains with impurities (except Cd) or with chalcopyrite inclusions ("chalcopyrite disease") were excluded as well (cf. Hutchinson & Scott 1981). A total of 13 grains were analysed, yielding an average of 11.46 mol% of FeS in

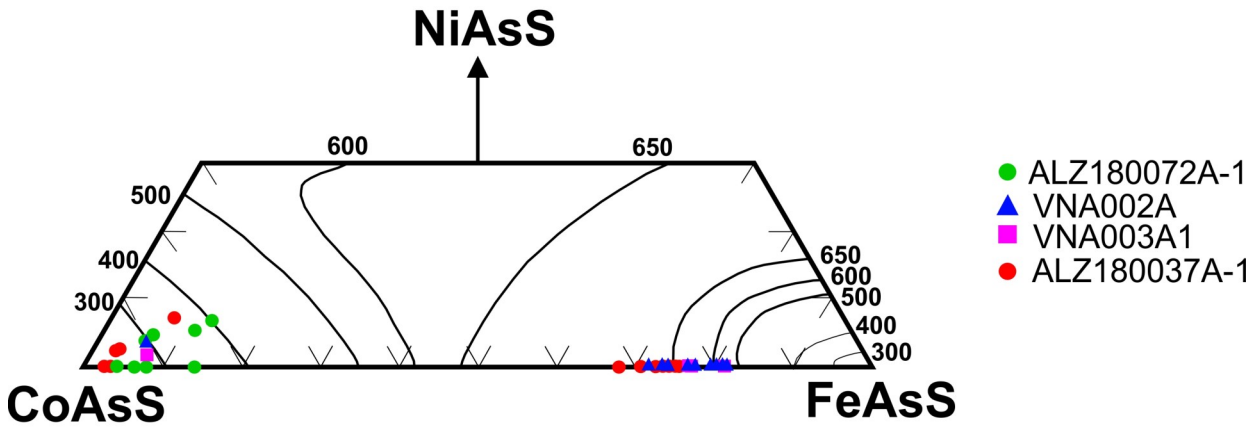


Figure 50. Arsenopyrite and cobaltite compositions plotted in the Co-Ni-Fe diagram with the formation temperature curves (After Klemm 1965).

the sphalerites with the range of 10.06 to 12.65 mol%. Because temperature results show variations from 200 to 300°C, these temperatures were used as the lower and upper limits to plot mol% of Fe in the sphalerite against these temperatures (Figure 53). When compared to the experimental isobars, most sphalerites have pressures between 700 and 1000 MPa with a few grains below and above these values. In contrast, when using the calculated isobars, pressure is significantly lower, where the upper intercept yields pressures between 500 and 700 MPa and the lower intercept implies pressures between 500 and 375 MPa. The pressures for the upper intercept are unreasonably high for a hydrothermal system and do not agree with metamorphic conditions that suggest pressures below 350 MPa. In comparison, the lower intercept pressures are closer to the expected metamorphic pressures, but still higher than expected.

Jamieson & Craw (1987) demonstrated that the sphalerite barometer can show anomalously high pressures due to re-equilibration during metamorphism from temperature above 350°C. Resetting of sphalerite during metamorphism and failure to re-equilibrate during retrograde conditions is the most likely explanation for the low FeS contents in sphalerite and consequently the high obtained pressures. Even though it is not possible to obtain mineralization pressures through the sphalerite barometer, the results suggest that all the analysed sphalerite grains are pre-metamorphic crystals.

## 6.6 Sulphide deformation and re-mobilisation

The area is clearly deformed with at least three deformation episodes that have resulted in open and isoclinal folding (Wikström & Karis 1991; Lewerentz et al. 2019). In massive sulphide deposits and other basin related ore deposits, deformation and re-mobilisation is a common and important feature that can operate during metamorphism (Marshall et al. 2000; Tomkins 2007).

In general, three main mechanisms are responsible for re-mobilisation of sulphides during metamorphism (Marshall et al. 2000; Tomkins 2007): 1) mechanical re-mobilisation, 2) hydrothermal metamorphic re-mobilisation, and 3) melt assisted re-mobilisation. The evidence for each type of re-mobilisation and their significance in the Dampetorp-Vena deposit are discussed below.

### 6.6.1 Mechanical re-mobilisation

Mechanical re-mobilisation means that different mechanisms control the flow of sulfides during solid state transfer, including cataclasis, granular and dislocation flow, and diffusive mass transfer (Marshall et al. 2000; Tomkins 2007). The different mechanical properties in a heterogenous mix of sulphides imply that several mechanisms can be active at the same time during deformation (Tomkins 2007), thus different sulphides will experience ductile or brittle deformation at given metamorphic and deformational conditions.

In the investigated area, folded veins and crystals (i.e. molybdenite) constitute evidence that at least part of the mineralization was emplaced before deformation. Furthermore, the sulphides of the Vena-Dampetorp area record different mechanical behaviours. For example, within the Cpy-Car-Cob assemblage, cobaltite and carrolite show signs of brittle deformation, such as fracturing corresponding with the shearing direction and cataclastic flow that results in a decrease of grain size. However, the chalcopyrite from the same assemblage behaved ductile, with intergranular flow between the other sulphides and partitioning the strain causing variation in the fracturing. Sample

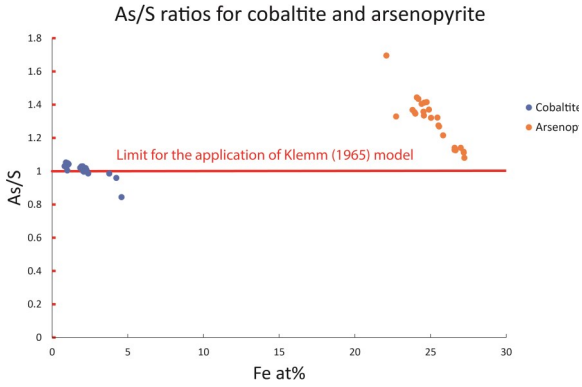


Figure 51. As/S ratios for cobaltite and arsenopyrite.

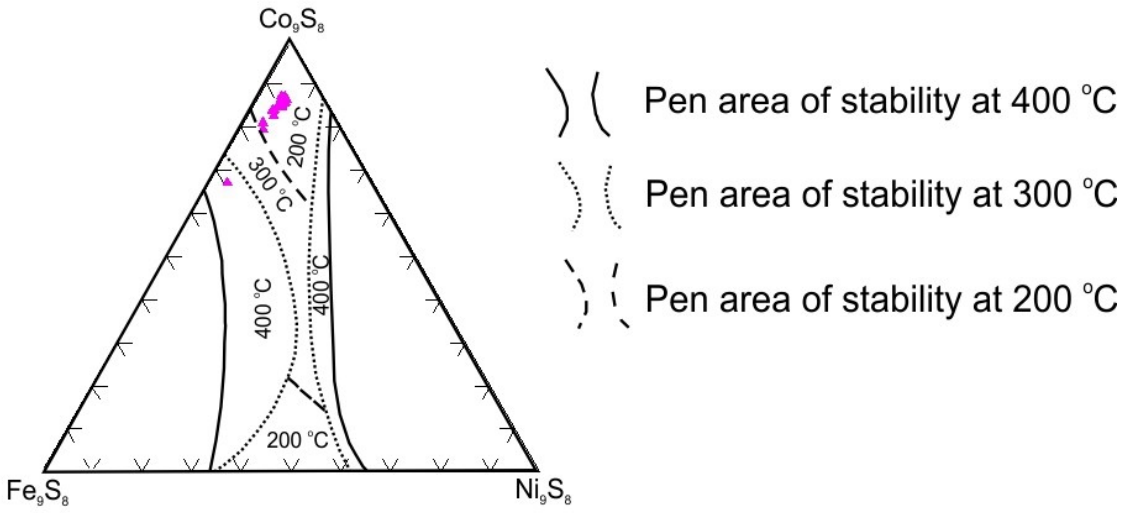


Figure 52. Arsenopyrite and cobaltite compositions plotted in the Co-Ni-Fe diagram with the formation temperature curves (After Klemm 1965).

ALZ190015A shows another example of mechanical re-mobilisation where folded pyrite-chalcopyrite veinlets show thickening towards the fold nose and shortening at the limbs as well as sulphide migration to feldspar porphyroclast pressure shadows, which are all common features of sulphide mechanical re-mobilisation (cf. Tomkins 2007). In addition, the emplacement of pyrrhotite and chalcopyrite along cleavage planes in biotite laths is a common feature in the deposit that also indicates the ductile deformation of both mineral phases.

Most of the disseminated crystals show little to no evidence of deformation or flow. However, as Tomkins (2007) notes, strain partitioning makes the re-mobilisation of massive sulphides effective while being highly ineffective for disseminations. Thus, in the Vena-Dampetorp deposit, it is probable that re-mobilisation only operated within areas with high sulphide contents or where it was aided by local structures.

### 6.6.2 Hydrothermal metamorphic re-mobilisation

Hydrothermal metamorphic re-mobilisation implies solution-aided mass-transfer of metals during metamorphism. This can occur either with fluid interaction during prograde metamorphism or during the retrograde fluid influx (Marshall et al. 2000; Tomkins 2007). Prograde metamorphism at lower amphibolite facies involves fluid generation through the breakdown of chlorite. Moreover, prograde metamorphic conditions promote the breakdown of pyrite in the desulphidation reaction:

2) $2FeS_2 = 2FeS + S_2$

The breakdown of chlorite and pyrite are responsible for the re-mobilisation of metals during prograde metamorphism as sulphur-based complexes (Tomkins 2007). Though sulphur-based ligands are important for the transport of Au, Ag, Sb and As, they are not relevant for the mobility of other base metals (Seward et al. 2013). In comparison, retrograde metamorphism typically involves the influx of an external fluid which commonly contains chloride complexes and usually is responsible for pyrite crystallization (Tomkins 2007).

Re-mobilisation during prograde metamorphism, often involves the generation of hydrothermal alteration areas that transform Fe-rich amphibole-pyrite assemblages to pyrrhotite-tremolite-anthophyllite and phlogopite (Tomkins 2007). In the Vena-Dampetorp area, Mg-altered rocks are commonly associated with the mineralization, however, so far there is no significant textural or field evidence that suggests that this alteration overprints the metamorphic textures. Additionally, metamorphism of Mg-altered rocks related to the original mineralization event can also yield similar assemblages (Tomkins 2007). Nonetheless, observations suggest that pyrite is slightly depleted in more mineralized samples where pyrrhotite is dominant. Pyrite depletion can be explained by desulfidation reactions (reaction 3) or simply by primary variations of the sulphur fugacity (Tomkins et al. 2007). Other possible evidences of prograde re-mobilisation include late Pb-Bi sulphosalt veins in sulphides which have also been recognized in other deposits in Bergslagen as signs of metamorphic re-mobilisation (e.g. Falun; Kampmann et al. 2018).

In contrast to the described evidence for prograde re-mobilisation, evidence of retrograde re-mobilisation at the deposit is limited. Veined-controlled retrograde chloritization is only related to minor pyrite crystallization with most of the retrograde silicate assemblages texturally preceding the sulphide minerals.

### 6.6.3 Sulphide melting and re-mobilisation

Both the metamorphic assemblages (section 6.1) and the thermobarometry (section 6.5) results show that the mineralization experienced high temperature (~600°C) during peak metamorphism. Under high S fugacity conditions, sulphide assemblages can initiate partial melting at temperatures as low as 300°C (Frost et al. 2002). Arsenopyrite-rich deposits are prone to melt due to the reaction:

3) $FeS_2 + FeAsS = As\text{-}S_{melt} + FeS$

According to this equation, arsenopyrite reacts with pyrite at 490°C to produce melt and pyrrhotite (Frost et al. 2002; Tomkins et al. 2007). The progression of this reaction consumes galena, but normally the excess of galena in the system allows for some proportion of it to remain solid while the melt becomes saturated in it. Sulphide melts are enriched in low-melting point chalcophile elements (LMPCE) such as Bi and Sb due to their partition coefficients (Frost et al. 2002; Tomkins 2007; Tomkins et al. 2007). This process then creates a precious metal and sulphosalt rich melt, leaving an Zn, Fe, Cu enriched restite (Tomkins 2007). Finally, migration of sulphide melts is induced by their low viscosity and ability to partition stress and move into dilatational structures (Frost et al. 2002; Tomkins 2007).

In the Vena-Dampetorp area, Gal-Bi-phases aggregates are common. These are conformed in approximate abundance order of: galena, native Bi, bismuthinite, willyamite, ullmannite, cosalite, and other complex Bi-Pb-Sb mineral phases. Textures between the Bi-bearing minerals in these aggregates resemble the textures found in other deposits that experienced sulphide melting, such as Montauban Zn-Pb-Au-Ag (e.g. Tomkins 2007). Galena and native Bi also occur as inclusions within other sulphide minerals within the Vena-Dampetorp deposit. Usually, LMPCE minerals and galena do not melt when shielded inside other sulphides but the generation of an arsenopyrite melt can contribute to rapid intracrystalline diffusion of such elements as they partition strongly in sulphide melts. Therefore, the most likely scenario is that inclusions of native Bi and galena, along with other minor inclusions in pre-existent pyrite or arsenopyrite, melted during prograde metamorphism, thereby generating galena- and sulphosalt-rich sulphide melts that migrated towards dilatational structures and along crystal interphases (Figure 28c). The fact that galena and Bi-bearing mineral veins occur within other sulphides is a strong evidence for sulphide melting and remobilisation in the Vena-Dampetorp deposit.

Additionally, arsenopyrite melting would explain the lack of arsenopyrite for most part of the deposit, however, this might also have been controlled by the location and availability of As, which would mean that Asp-Py melting was an isolated process. Notwithstanding, the Gal-Bi aggregates occur through the deposit, meaning that two scenarios are possible for arsenopyrite absent areas with melts: 1) melts migrated to those areas from arsenopyrite richer zones, or 2) arsenopyrite was consumed completely leaving only the Pb-Bi-Sb melts. The first scenario is more probable because if all arsenopyrite was consumed, As would be expected to be redistributed in other phases which cannot be observed in the samples at hand.

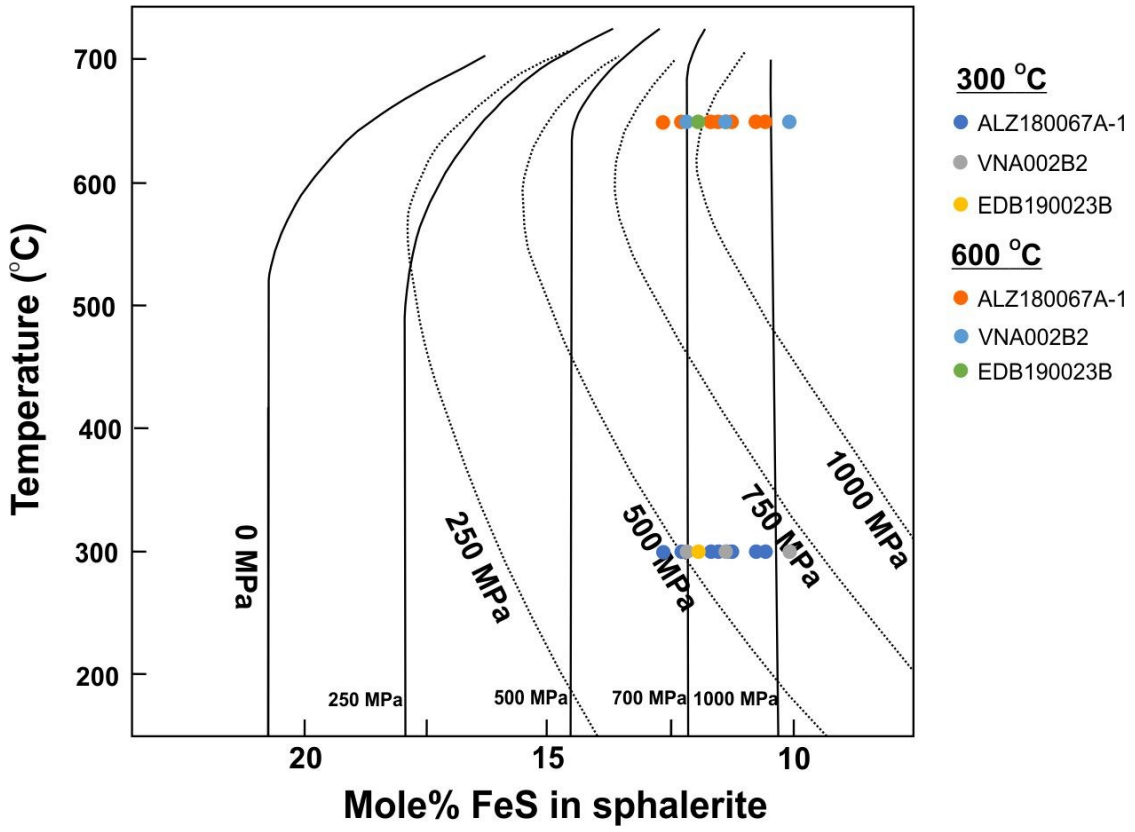


Figure 53. Mol% FeS against temperature in sphalerite grains from the Vena area. Calculated isobars are dashed (Toulmin et al. 1991) and experimental isobars are solid black (Scott 1976).

## 6.7 Processes and genesis of the mineralization

Traditionally, sulphide deposits in the Bergslagen province have been classified into either SVALS or SAS types (e.g. Allen et al. 1996). Although these two types of deposits share certain characteristics with each other, they have major differences in terms of alteration, style of mineralization and genesis (Jansson et al. 2017). The Zinkgruvan deposit, the best-known example of a SAS type deposit, is located roughly within 10 km of the Vena mining field. SVALS type mineralization includes deposits such as Falun, Garpenberg and Sala (e.g. Allen et al 1996; Kampmann et al. 2017). Table 8 summarizes and compares key characteristics of the Zinkgruvan deposit, as a typical example of an SAS mineralization, the SVALS deposits in general, and the Vena-Dampetorp mineralized area.

In the Zinkgruvan deposit, ore minerals occur in three distinct but related modes. Most of the deposit occurs within stratiform Zn-Pb-Ag massive sulphide bodies hosted by metatuffite and minor calcareous horizons. A minor proportion of the mineralization is hosted within the Burkland ore body, a marble hosted Cu-Zn-(Co-Ni) sulphide disseminated to massive mineralization (Jansson et al. 2017). Lastly, disseminated to massive magnetite hosted in calc-silicate skarn or dolomitic rocks is often found near a discontinuity in the Burkland ore body, as well as in other calcareous horizons around the deposit (Jansson et al. 2017; Ivarsson 2019). Like Zinkgruvan, the Vena-Dampetorp deposit is hosted mainly in a felsic metavolcanic sequence. However, whereas the first one is found within the Zinkgruvan Formation, a metatuffite sequence (Jansson, et al. 2017), the current observations suggest that the Vena-Dampetorp deposit is hosted by the Mariedamm unit, although some authors (Ivarsson 2019), have suggested that the Zinkgruvan Formation might extend towards the southern portions of the Vena and Dampetorp areas.

In contrast, the main characteristic of SVALS deposits is that sulphides are mainly hosted within calcareous horizons (Allen et al. 1996; Jansson & Allen 2011; Kampmann et al. 2017), although some deposits might be partially hosted within metamorphosed volcanic sequences (Kampmann et al. 2017). Even though most of the mineralization occurs outside calcareous horizons, the Zinkgruvan mineralization is closely related to marble occurrences (Jansson et al. 2017). In this aspect, the Vena-Dampetorp deposit has a striking contrast as limestone horizons tend to be scarcer, thinner, and mineralized to a lesser extent than

Table 8. Comparison of key characteristics between the Vena-Dampetorp, Zinkgruvan an SVALS deposits in general.

| | Vena-Dampetorp | Zinkgruvan (SAS type)[1] | SVALS type[2] |
|---|---|---|---|
| Main host rock | Metavolcanics | Metavolcanoclastics | Limestone |
| Carbonate rocks associated | Occasionally | Yes | Yes |
| Associated mineralizations | REE-bearing Fe-oxide skarn | BIF, Fe-Si rich exhalites, REE-Fe-oxide skarn | Some deposits have REE-bearing Fe-oxide skarn |
| Within fine grained, deep-water sedimentary or volcanosedimentary facies | Minor sedimentary component | Yes | Not all deposits |
| Association with mafic intrusions | Yes | Yes | Yes |
| Pervasive wallrock K-feldspar alteration | Yes | Yes | Yes |
| Mg-altered originally quartzofeldspathic rocks (sediments or volcanics) common | Yes | No | Yes |
| Mn-enrichment halo to stratiform ore | No | Yes | Not all deposits |
| Metal content of entire ore body: Zn/Pb > 1.5 | Yes | Yes | Yes |
| Average Ag/Pb | 0.064 | ≥15 | 0.0072 |
| Average Zn/Cu | 1.69 | 11.65 | 66 |
| Py > (Sph, Gal) in significant parts of massive sulfide mineralization | Yes | No | Yes |
| Cu-Co association in proximal/feeder zone | Yes | Yes | No |
| Type of mineralizing fluid | Possibly acidic, but not constrained | Oxidized and near-neutral | Reduced and acidic |
| Eu anomalies in ore zone and/or associated exhalites (e.g. iron formations) | Positive in the IOM skarns/ Negative for the SM | Positive | Positive in marble mineralization |

[1]Based on data by Jansson et al 2017.

[2]Based on data by Vivallo 1985; Jansson & Allen 2011; Kampmann et al. 2017; Högnäs 2018.

the volcanic sequence.

The association with other types of deposits, namely BIF and REE-bearing iron-oxide skarns, seems to be a common characteristic of most sulphide deposits in the Bergslagen region (Jansson & Allen 2005; Kampmann et al. 2017; Jansson et al. 2017; Ivarsson 2019), where the Vena-Dampetorp deposit is not an exception as REE-bearing iron oxide skarns (IOM) occur in close spatial relationship with the main sulphide mineralization (SM). This relationship is discussed further in section 6.7.2.

At Zinkgruvan, the most important alteration in the footwall is a pervasive K-enrichment or potassic alteration attributed to oxidized metal-bearing brines that were canalized through a synsedimentary structure and vented into a reduced ocean causing the deposition of massive stratiform Zn-Pb-Ag (Janssen et al. 2017). In contrast, SVALS deposits, like the Falun mineralization, show important Mg-alterations coupled with silicification, sericitization (K-alteration) and, in some cases, Na-alteration; which have been associated to acidic reduced hydrothermal fluids (Kampmann et al. 2017). Like SVALS types, the sulphide mineralization at Vena has an important Mg-alteration as demonstrated by the cordierite- and anthophyllite-bearing metavolcanics. However, it also possesses a widespread and localized K-alteration in most metavolcanic rocks as suggested by the K-enrichment in rocks and discrete biotite-rich zones, which resembles the alteration at Zinkgruvan. Another, common feature in Zinkgruvan is a Mn enrichment halo around the mineralization (Janssen et al. 2017), which is also shared by some of the SVALS deposits (e.g. Falun; Kampmann et al. 2017). This is completely absent in the Vena-Dampetorp mineralization, where average MnO concentrations are below 0.08 wt%.

Whereas most sulphide deposits in Bergslagen show similar REE patterns, marked by positive Eu anomalies (e.g. Jansson et al. 2017; Kampmann et al. 2017), the Vena-Dampetorp mineralized rocks have consistently marked negative anomalies. Only skarn samples from the IOM have positive Eu anomalies. Although, the negative Eu anomalies at Vena might be partially inherited from the host rocks, the Eu/Eu* anomalies for mineralized rocks show consistently to be lower than unmineralized rocks (Figure 54). This may be explained by the sericitization, as the breakdown of plagioclase in a hydrothermal system is effective in removing the $Eu^{+2}$, while sericite can only accommodate a fraction of the Eu (Genna et al. 2014).

Perhaps the most contrasting characteristic of the studied deposits is its metal contents. Unlike, other sulphide deposits in the Bergslagen region which are highly enriched in Zn in contrast to Cu, Vena-Dampetorp has, on average, a slightly higher proportion of Cu. Furthermore, the enrichment of Co represents an anomaly with respect of most deposits. Nonetheless, the Burkland ore body of the Zinkgruvan mine show similar characteristics to Vena-Dampetorp, which include: 1) Zn/Cu ratios below 1 (Jansson et al 2017). 2) Presence of Co and similar Co-bearing phases (Bjärnborg 2009). 3) Areas with impregnation style mineralization (Bjänborg 2009; Jansson et al. 2017). 4) Spatially associated Fe-skarns (Jansson et al. 2017). Further, the Burkland ore body is hosted in a marble unit, unlike Vena where most of the Cu-Co ore minerals occur within the metavolcanics. Additionally, at Zinkgruvan the Co mineralization is richer in Ni, as shown by presence of Ni minerals and generally higher contents of Ni in phases such as pentlandite, whereas Ni minerals are rare and pentlandite exsolutions are Ni-poor in the area of study. In summary, the Vena-Dampetorp shares similar host rock and metal association with SAS type deposits, but it is closer to SVALS types in terms of alterations and mineralogy.

### 6.7.1 Cobalt distribution and origin

Comparable Cu-Co deposits within Bergslagen have been documented in at least three other locations: Tunaberg, Håkansboda and Hällefors (Johannsson 1919; Dobbe 1994; Wagner et al. 2005; Tillberg 2014). These ore deposits show similar features that include anomalous high Cu and Co contents, metavolcanic host rocks (in most cases), spatial association with limestone horizons and mafic intrusions, K- and Mg-altered horizons and re-mobilisation of ores during metamorphism (Dobbe 1991; Dobbe 1994; Wagner et al. 2005; Tillberg 2014).

In the Vena-Dampetorp deposit, cobalt occurs mainly as cobaltite or as traces within pyrite crystals. However, it is also present in other mineral phases such as arsenopyrite, pentlandite or in rarer phases such as willyamite or costibite. Regardless of the host mineral, Co is found in assemblages where more than one cobalt phase occurs (e.g. Asp-Cob or Cpy-Car-Cob). At deposit scale, cobalt is concentrated on the SE side of the Vena area where it occurs mostly as cobaltite. The distribution of cobaltite is controlled by availability of As because it is only found in areas with high As contents. However, Co itself is not restricted to As-rich areas, as Co-bearing phases occur also in As-poorer parts. In such areas, Co is present as part of the intracrystalline structure in pyrite or allocated to pentlandite.

Textural and chemical evidence suggest that Co

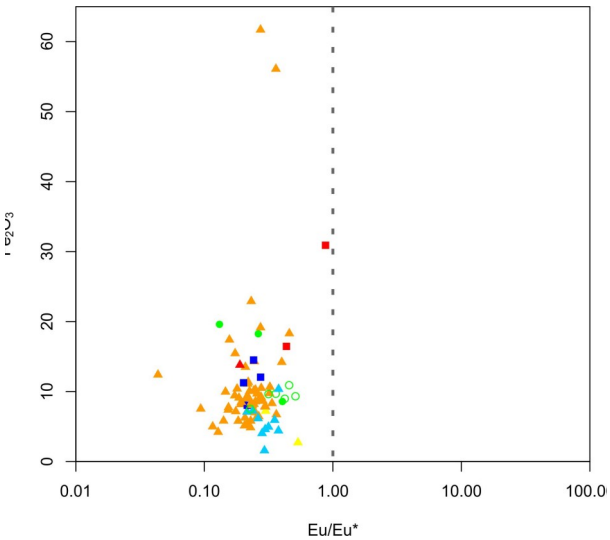


Figure 54. Plot of Eu/Eu* anomalies against $Fe_2O_3$. Eu/Eu*= $Eu_{SN}$ / ($Dy_{SN}$ x $Sm_{SN}$)$^{0.5}$ based post Archean Australian shale normalized values (PAAS) according to Taylor & McLennan (1985).

is located both in primary and re-mobilised sulphides. The presence of willyamite and costibite in sulphide melts indicates that, up to a certain degree, Co fractionated into the melts, possibly as part of arsenopyrite. Similarly, late veins that contain cobaltite and pyrite-(Co) suggest that hydrothermal re-mobilisation of Co was also in place during metamorphism. The extent of re-mobilisation and concentration cannot be determined, due to the limited sampling and exploration of the deposit. However, it is likely that hydrothermal re-mobilization was more effective at concentrating the Co, while melting and mechanical re-mobilization only had a local influence, unless aided by major shear zones or other structures.

Most of the primary Co mineralization is located along biotite rich areas. This "biotite alteration" is interpreted as metamorphosed sericitic alteration (Shanks III, 2010). Several authors (Carlon & Bleeker 1988; Jansson et al. 2016) have speculated that Cu-Co-rich mineralization, associated to localized zones with sericitic and chloritic alteration, represent feeder zones to major stratiform base metal massive sulphide deposits. Although, in the Vena-Dampetorp deposit, no major massive sulphide ore body has been found so far, the association and distribution of the alterations together with sulphide temperature estimates are congruent with high temperature Cu-Co feeder zone in a volcanic hosted hydrothermal system.

### 6.7.2 REE mineralization

Magnetite-REE silicate and calcareous skarn deposits are common across the Bergslagen district (Stephens et al. 2009; Sahlström 2014; Sahlström et al. 2019), most of these have been classified as Bastnäs-type deposits (e.g. Sahlström et al. 2019). Bastnäs-type deposits are characterized by skarn assemblages that host iron oxide and mainly LREE-rich silicate and phosphate minerals and possibly also include base metal sulfides. The best studied examples of these type of deposit are found in a small elongate area by some authors referred to as the "REE line" in the NW part of the Bergslagen region (Jonsson et al. 2014; Sahlström et al. 2019).

In addition to Bastnäs-type deposits, iron oxide deposits associated to sulphide mineralization include BIF, Fe-rich exhalites and non-magmatic magnetite skarns (Stephens et al. 2009; Jansson et al. 2017 ; Ivarsson 2019). The occurrence of magnetite-bearing skarns in Zinkgruvan, the southern part of the Dampetorp area, and southwest of the Vena area were studied by Ivarsson (2019). He observed some similarities between the magnetite skarns in the Burkland ore body and the southwestern parts of the Vena-Dampetorp deposit: 1) similar lithology and mineralogy, 2) magnetite as the main iron oxide, 3) Eu/Eu* (shale normalized) anomalies above 1.1, 4) MnO concentrations from 1-4 wt%, 5) high (>35% wt%) $Fe_2O_3$ contents of magnetite rich samples, and 6) shale normalized REE patterns with a relative enrichment of MREE and HREE with respect of LREE. Additionally, he interpreted that most of the magnetite formed either as part of skarn reactions between Fe-enriched limestone and silicate minerals or as retrograde alteration of olivine; where based on Eu/Eu* anomalies the northern-most samples represented distal parts to the vent system at the Zinkgruvan deposit.

However, the IOM at Vena, namely at the north-west of the Vena mining field, has several differences with the Zinkgruvan and the southwestern magnetite skarns. For instance, MnO contents are relatively low (<1 wt%). Furthermore, most shale normalized patterns for the IOM, have a LREE enrichment with only one metavolcanic sample (EBD190040A) showing the characteristic patter of Zinkgruvan magnetite skarns. Although most samples at Vena have Eu positive anomalies, especially the skarn-hosted IOM, their Eu/Eu* anomalies are comparatively low (< 1) in comparison to Zinkgruvan. While REE minerals are locally found in the magnetite skarns in the Burkland ore body (Ivarsson 2019), they are widespread within the Vena IOM.

In contrast, the IOM at Vena shares similar LREE enrichment patterns and mineralogy with Bastnäs-type deposits (e.g. Sahlström 2014). Thus, here a Bastnäs-style mineralization mechanism is preferred over a SEDEX-associated skarn generation. The most recent model by Sahlström et al. (2019) explains Bastnäs-type deposits as a result of the interaction between carbonate rocks and high temperature (>450 $^{o}$C) magmatic derived hydrothermal fluids, which experienced variable amount of mixing with oceanic waters.

In comparison to the IOM, the SM has little in common with the Bastnäs-type deposits, however, it has anomalous amounts of REE minerals. In the SM, the main REE mineral is monazite with scarcer xenotime. The fact that monazite can be found nucleating around apatite crystals suggest that REE-bearing hydrothermal fluids interacted with the primary apatite in the metavolcanic rocks either scavenging phosphate or just nucleating by affinity to them. Textural evidence indicates that monazite predates most of the sulphide mineralization. Xenotime could either formed even earlier than monazite or is coeval, as inclusions of it were found within monazite. Parisite was found in both types of mineralization (IOM and SM) as aggregates replacing REE minerals. This implies that, possibly during retrograde metamorphism as the textural evidence suggests, $CO_2$- and F-rich fluids interacted with the REE assemblages to form parisite.

### 6.7.3 Genesis and timing of the mineralization

There is a clear spatial relationship between the IOM and the SM at Vena-Dampetorp. Several sulphide deposits in Bergslagen are associated with Fe-oxide skarn mineralization. The majority of these deposits can be explained as metamorphic products of Fe-exhalates in carbonate horizons (Jansson et al. 2017; Jansson et al. 2018; Frank et al. 2019; Ivarsson 2019), while others have been associated to later Fe-metasomatism (Jansson & Allen 2015). This study, as discussed in the previous section, suggests that the Vena-Dampetorp IOM is a Bastnäs type mineralization. Although the stratigraphic relationships of the IOM and the SM remain poorly constrained due to the lack of detailed mapping and underground exploration, no textural evidence of the IOM overprinting the SM has been found yet. Thus, the IOM is interpreted to be slightly younger than the SM.

Since Bastnäs-type mineralization requires temperatures above 450 $^{o}$C (Sahlström et al. 2019) and the

temperature estimates suggest that the Vena-Dampetorp sulphide mineralization precipitated below 350 °C, a model is proposed where the two styles of mineralization represent the evolution of a single hydrothermal system. The SM and the IOM would then represent different stages, where hot magmatic fluids initial deposited the Fe-oxides and REE-minerals of the IOM. Later cooling of the hydrothermal system led to the establishment of an exhalative-like hydrothermal cell that was responsible for the precipitation of base metal sulphides in the volcanoclastic rocks. In this scenario Cu-Co-rich mineralized areas represent the hotter and more proximal parts of the system. REE-minerals then possibly where remobilized from the IOM by the same mineralizing fluids that precipitated the sulphides. This would explain the lower La contents in the SM with respect to Ce, since Ce is more mobile is hydrothermal systems (Torres-Alvarado et al. 2010).

Conversely, rather than the product of an evolving hydrothermal system, the SM might represent a distal part of the same hydrothermal system, which would account for the La distribution and lower temperatures. However, either scenario is speculative and further research is needed to constrain the relationship between both styles of mineralization. Regardless, the textural, chemical and thermobarometric observations in the SM suggest that it occurred shortly after the deposition of the metavolcanics (1.89 Ga) and the intrusion of mafic dikes (amphibolite). This involved the precipitation of pyrite, pyrrhotite, chalcopyrite, sphalerite, cobaltite, carrolite, galena, arsenopyrite, skutterudite, molybdenite and minor REE minerals, from a hydrothermal solution. The original distribution of elements and assemblages was most likely controlled by evolution of the hydrothermal fluid as it moved away from the source, as well as by the lithology (i.e. felsic or mafic) which determined the availability of elements and the interactions with the fluid.

After this, the sulphide assemblage was subjected, along with their host rocks, to high temperature and low pressure Svecokarelian metamorphism around 1.88 Ga or shortly thereafter (see discussion at section 6.2). Granodioritic intrusions were emplaced slightly before or at the early stages of metamorphism as the regional and local interpretations suggest (e.g. Stephens & Jansson, 2020). Prograde metamorphism led to a re-mobilisation stage, where mechanical, hydrothermal and melt-assisted re-mobilisation of the sulphides took place. In this stage, arsenopyrite, pyrite, galena, and Bi-Sb-phases were partially to completely removed from their original sulphide associations and redistributed along the deposit. In contrast, retrograde metamorphism had little contribution to re-mobilising the mineralization. Retrograde hydrothermal fluids mostly precipitated pyrite with a pyrite-chlorite-calcite alteration associated to them. The effects of re-mobilisation in the IOM assemblage are hindered by the lack of sufficient sampling and remain speculative.

The late- to post-orogenic intrusion of granites and pegmatites might have contributed with local heat fluxes along with fluids that may have inflicted discrete localized re-mobilisations along the intrusions. They, however, assimilated and possibly partially melted sulphides as they intruded the mineralized metavolcanics. This is particularly evidenced by chalcopyrite and pyrrhotite inclusions in pegmatite-related quartz and feldspar crystals.

Supergene alteration of exposed samples (waste pile samples) was ultimately responsible for the hydrated and low temperature alteration assemblages such as Fe -hydroxides, Fe-sulphates, and the generalized pyrrhotite inversion to marcasite.

# 7. Conclusions

Most of the Vena-Dampetorp mineralization is hosted within a rhyolitic to dacitic metavolcanic succession, with local variation in composition and mineralogical assemblages. The majority of these assemblages can be explained as metamorphic products of variably K- and Mg-altered horizons associated with sulphide deposition in a volcanoclastic subsea-floor environment in a back-arc setting. Where sericitic alterations resulted in biotite-rich intervals, chlorotic alterations produced anthophyllite or cordierite bearing assemblages. In comparison, Ca-alteration is either related to hydrothermal fluid alteration during metamorphism, or to magmatic metasomatism induced by the intrusion of the granodiorites.

The U-Pb dating of metamorphic titanite grains only yields significant results for two samples out of the four analysed. The mean $^{207}Pb/^{206}Pb$ metamorphic age of 1882±16 Ma based on two concordant analyses within the skarn sample is interpreted as the age of the onset of metamorphism in the study area. In comparison the discordant lower intercept date of 1884 ±8 Ma, obtained from 14 titanite grain analyses withing the metavolcanic sample (ALZ180089A-3), is harder to interpret due to the associated uncertainty. Therefore, this date could represent either a metamorphic or cooling age. The textural relationships of the titanite with the SM minerals, together with field observations show that the mineralization and granodiorite intrusion occurred in a period of maximum 24 Ma between the deposition of the volcanic sequence (1884±8 Ma) and the titanite growth (1882±16 Ma); denoting a fast geological evolution of the area. Variable Pb loss is present in all the samples which is understood as post-metamorphic modifications of the Pb system in the titanite possibly by later metamorphic events.

Two types of ore deposits are recognized in the Vena-Dampetorp area, a base metal sulphide deposit (SM) and an iron-oxide skarn hosted mineralization (IOM). The SM mineralization consists of disseminations and veinlets of pyrrhotite, pyrite, chalcopyrite and sphalerite with minor cobaltite or arsenopyrite associated to them. Ore bodies are zoned with a transition from pyrite-pyrrhotite areas to pyrrhotite-pyrite-chalcopyrite-sphalerite zones with localized cores of Cu-Co bearing minerals. However, overlap in the zoning is common. At deposit scale, metal zoning is present where melt mobile elements (Pb, Bi, and Sb) concentrate to the NW parts of the Vena deposit, whereas the middle part is dominated by Cu and Zn, with Co and As present in the south-eastern segment. The Dampetorp lacks a zoning as clear as the one seen on the Vena side. This metal distribution across the deposit also controls the mineralogy (e.g. cobaltite concentrated in the SE As-rich areas).

Most of the ore minerals show relatively constant compositions except for Co-bearing phases and sphalerite, which are interpreted as a result of their genetic conditions or their re-equilibration during metamorphism. Further, a low Ni/Co relationship characterizes the deposit with most mineral phases that can accommodate Ni in their structure being Ni-poor. This differs from comparable mineral occurrences in the area that show Ni-richer compositions.

The thermometric estimates for the assemblages in the Fe-Ni-Co-As suggest that cobaltite from the chalcopyrite-cobaltite-carrolite assemblage crystalized at temperatures around 300 ºC. The high As/S make results for other cobaltite- or arsenopyrite-bearing assemblages unreliable. Similarly, the cobalt pentlandite exsolutions within re-mobilised veins of pyrite-(Co), pyrrhotite and chalcopyrite suggest that these crystallized below 200 ºC. In contrast, sphalerite barometry shows anomalously high pressures, which are interpreted as a result of failure to re-equilibrate during high temperature metamorphism.

Metamorphism and deformation affected the sulphide mineralization through three mechanisms: 1) mechanical re-mobilisation, 2) hydrothermal metamorphic re-mobilisation, and 3) melt assisted re-mobilisation. Mechanical re-mobilisation, in both ductile or fragile way, was responsible for local migration of sulphides to dilatation structures, fracture and grain down-size of sulphide crystals. Hydrothermal re-mobilisation that were induced by desulfidation reactions involving pyrite, were an important mechanism for the concentration of certain elements like Co in secondary veins throughout the deposit. However, the extent of this process remains unknown due to the lack of widespread alteration mapping. Likewise, high temperature, low pressure metamorphic conditions were responsible for inducing sulphide anatexis. Partial melting of the sulphides partitioned low melting point elements (Bi, Pb, Sb) and elements with sulphide melt affinity. Most of these elements were inside arsenopyrite and pyrite as inclusions or within their structures. Sulphide melt migration was limited, probably in the scale of mm to cm within the rocks, where they crystalized in sulphide interfaces or dilatational structures (e.g. factures within other sulphides). Complex native Bi, Bi-bearing minerals, galena and willyamite-ullmannite crystalized from these sulphosalt rich melts. The presence of willyamite and costibite suggests that Co was partially partitioned into the melt.

The IOM is a Bastnäs-type deposit that was emplaced shortly after the deposition of the metavolcanics, as a result of the interaction of hot (>450ºC) REE-bearing magmatic fluids with calcareous horizons. In comparison, cooler fluids, which either evolved through time from the same hydrothermal system responsible for the IOM or developed as a separated hydrothermal cell, precipitated the minerals of the SM. Specifically, the Cu-Co rich areas of the SM developed in a high temperature (300 to 400ºC) feeder-like system of a volcanic hosted sub-seafloor exhalative hydrothermal system. The coeval intrusion of mafic magmas probably contributed with heat and metals such as Co and Cu for the SM, while adding heat to the system. Metamorphism then re-mobilised and concentrated the cobalt and other metals locally.

# 8. Acknowledgments

This study would not have been possible without all the contributions and support I received. I would specially like to thank my supervisor Charlotte Möller at Lund University for helping me start this project and for her valuable observations along the way. In the same way thank goes to my supervisor at SGU Alex Lewerentz who provided me with thin sections and data for this study and was key in making this whole project happen. His guidance and input were essential for the culmination of this project.

A special thanks goes to the SGU letting me be part of such and interesting project and providing funding and information for it. Similarly, thank goes to Zinkgruvan AB for providing access and permission to use the cores of the Vena are for this study.

I wish to thank Tomas Næraa for his insight and help with LA-ICP-MS analyses. Additionally, I would like to thank my examiner Ulf Söderlund for his valuable comments and suggestions. Similar thanks goes to my student opponent Stylianos Karastergios for his useful observations.

I would also like to thank my family for their unconditional support. A special mention goes to Leonie Beckmann for her invaluable support and help. Lastly, I would like to extend a thank you to all my fellow colleagues and friends at Lund University for their optimism and constant support.

# References

Aleinikoff, J.N., Wintsch, R.P., Fanning, C.M. & Dorais, M.J., 2002: U–Pb geochronology of zircon and polygenetic titanite from the Glastonbury Complex, Connecticut, USA: an integrated SEM, EMPA, TIMS, and SHRIMP study. *Chemical Geology 188(1-2),* 125-147.

Allen, R., Ripa, M. & Jansson, N., 2008: Palaeoproterozoic volcanic- and limestone- hosted Zn-Pb-Ag- (Cu-Au) massive sulphide deposits and Fe oxide deposits in Bergslagen, Sweden. *In 33 excursion No 12 guide*, pp. 78.

Allen, R.L., Lundström, I., Ripa, M., Simeonov, A. & Christofferson, H., 1996: Facies analysis of a 1.9 Ga, continental margin, back-arc, felsic caldera province with diverse Zn-Pb-Ag-(Cu-Au) sulfide and iron oxide deposits, Bergslagen region, Sweden. *Economic Geology 91*, 979−1008.

Andersson, S., Jonsson, E. & Högdahl, K., 2016: Metamorphism and deformation of a Palaeoproterozoic polymetallic sulphide–oxide mineralisation: Hornkullen, Bergslagen, Sweden, *GFF*, 138:3, 410-423,

Andersson, U.B., 1991: Granitoid episodes and mafic-felsic magma interaction in the Svecofennian of the Fennoscandian Shield, with main emphasis on the ≈ 1.8 Ga plutonics. *Precambrian Research 51*, 127−139.

Andersson, U.B., 2005: Age and P-T paths of metamorphism in Bergslagen region, southern Swe-

den. *FoU-seminarium vid SGU, At Uppsala, Volume: SGU-rapport 2005:7,* 22-24.

Andersson, U.B., Högdahl, K., Sjöström, H. & Bergman, S., 2006: Multistage growth and reworking of the Palaeoproterozoic crust in the Bergslagen area, southern Sweden: evidence from U-Pb geochronology. *Geological Magazine 143,* 679–697.

Baidya, A.S., Sen, A. & Pal, D.C., 2018: Textures and compositions of cobalt pentlandite and cobaltian mackinawite from the Madan-Kudan copper deposit, Khetri Copper Belt, Rajasthan, India. *Journal of Earth System Science 127(4),* 56.

Baker, J.H. & de Groot, P.A., 1983: Proterozoic seawater–felsic volcanics interaction W. Bergslagen, Sweden. Evidence for high REE mobility and implications for 1.8 Ga seawater compositions. *Contributions to Mineralogy and Petrology 82*, 119−130.

Baker, J.H. & de Groot, P.A., 1992: High element mobility in 1.9-1.86 Ga hydrothermal alteration zones, Bergslagen, central Sweden: relationships with exhalative Fe-ore mineralizations. *Precambrian Research 54(2–4),* 109–130.

Barton, P.B. & Toulmin, P., 1966: Phase relations involving sphalerite in the Fe-Zn-S system. *Economic Geology 61(5),* 815-849.

*Boynton, W. V., 1984: Cosmochemistry of the rare earth elements: meteorite studies. In Developments in geochemistry (Vol. 2, pp. 63 -114). Elsevier.*

Bergman, S., Högdahl, K., Nironen, M., Ogenhall, E., Sjöström, H., Lundqvist, L. & Lahtinen, R., 2008: Timing of Palaeoproterozoic intraorogenic sedimentation in the central Fennoscandian Shield; evidence from detrital zircon in metasandstone. *Precambrian Research 161,* 231-249.

Beunk, F. & Kuipers, G., 2012: The Bergslagen ore province, Sweden: Review and updated of an accreted orocline 1.9-18 Ga BP. *Precambrian Research 216-219*, 95-119.

Bjärnborg, K., 2009: *The copper sulphide mineralization of the Zinkgruvan deposit, Bergslagen, Sweden*. Dissertations in Geology at Lund University.:

Carlon, C. J., & Bleeker, W., 1988 The geology and structural setting of the Håkansboda Cu-Co-As-Sb-Bi-Au deposit and associated Pb-Zn-Cu-Ag-Sb mineralisation, Bergslagen, central Sweden. *Geologie en mijnbouw*, *67*(2-4), 279-292.

Chappell, B.W., 1999: Aluminium saturation in I-and S-type granites and the characterization of fractionated haplogranites. *Lithos 46(3),* 535-551.

Chernosky, J.V., Day, H.W. & Caruso, L.J., 1985: Equilibria in the system MgO–SiO2–H2O: experimental determination of the stability of Mg-anthophyllite. *American Mineralogist 70(3-4),* 223-236.

Craig, J.R. & Scott, S.D., 1974: Sulfide phase equilibria, in: *Sulfide Mineralogy – Short Course Notes, 1,* edited by: Ribbe, P. H., Mineralogical Society of America, Southern Printing Co., Blacksburg, Virginia, CS1–110.

Dahlin, P., 2014: *Stratigraphy and Geochemistry of the Palaeoproterozoic Dannemora inlier, northeastern Bergslagen region, central Sweden* (Doctoral dissertation, Acta Universitatis Upsaliensis).

de Groot, P.A., 1990: A model for the formation of potassic and sodic alteration phases during hydrothermal processes: application of thermodynamic models to natural systems. *Geologiska Föreningens I Stockholm Förhandlingar 112*, 180-183.

Deer W.A., Howie A. & Sussman J., 1992: An interdiction to rock- forming minerals.17th. *Longman Ltd,* 528p.

Dobbe, R.T.M., 1991: Tellurides, selenides and associated minerals in the Tunaberg copper deposits, SE Bergslagen, Central Sweden. *Mineralogy and Petrology 44(1-2),* 89-106.

Dobbe, R.T.M., 1994: Geochemistry of cordierite-anthophyllite rocks, Tunaberg, Bergslagen, Sweden. *Economic Geology 89(4),* 919-930.

Droop, G.T.R., 1987: A general equation for estimating Fe 3+ concentrations in ferromagnesian silicates and oxides from microprobe analyses, using stoichiometric criteria. *Mineralogical magazine 51*(361), 431-435.

Duran, C.J., Barnes, S.J. & Corkery, J.T., 2016: Trace element distribution in primary sulfides and Fe–Ti oxides from the sulfide-rich pods of the Lac des Iles Pd deposits, Western Ontario, Canada: constraints on processes controlling the composition of the ore and the use of pentlandite compositions in exploration. *Journal of Geochemical Exploration 166*, 45-63.

Egerton, R.F., 2005: *Physical principles of electron microscopy* (Vol. 56). New York: Springer. 125-175.

Fanlo, I., Subías, I., Gervilla, F., Paniagua, A. & García, B., 2004: The composition of Co–Ni–Fe sulfarsenides, diarsenides and triarsenides from the San Juan de Plan deposit, central Pyrenees, Spain. *The Canadian Mineralogist 42(4),* 1221-1240.

Frank, K. S., Spry, P. G., Raat, H., Allen, R. L., Jansson, N. F., & Ripa, M., 2019: Variability in the Geologic, Mineralogical, and Geochemical Characteristics of Base Metal Sulfide Deposits in the Stollberg Ore Field, Bergslagen District, Sweden. *Economic Geology*, *114*(3), 473-512.

Frost, B.R., Chamberlain, K.R. & Schumacher, J.C.,

2001: Sphene (titanite): phase relations and role as a geochronometer. *Chemical geology 172(1-2),* 131-148.

Frost, B.R., Mavrogenes, J.A. & Tomkins, A.G., 2002: Partial melting of sulfide ore deposits during medium-and high-grade metamorphism. *The Canadian Mineralogist 40*(1), 1-18.

Gaál, G. & Gorbatschev, R., 1987: An outline of the Precambrian evolution of the Baltic Shield. *Precambrian Research 35*, 15–52.

Geijer, P., 1917: Falutraktens berggrund och malmfyndigheter. *Sveriges geologiska undersökning C 275*, 319 pp.

Genna, D., & Gaboury, D., 2015: Deciphering the hydrothermal evolution of a VMS system by LA-ICP-MS using trace elements in pyrite: an example from the Bracemac-McLeod deposits, Abitibi, Canada, and implications for exploration. *Economic Geology*, *110*(8), 2087-2108.

Georgatou, A.A. & Chiaradia, M., 2020: Magmatic sulfides in high-potassium calc-alkaline to shoshonitic and alkaline rocks. *Solid Earth 11(1),* 1-21.

Gorbatschev, R., 1969: A study of Svecofennian supracrustal rocks in central Sweden: lithological association, stratigraphy, and petrology in the northwestern part of the Malaren-Hjalmaren basin. *Geologiska Föreningens i Stockholm Förhandlingar 91*, 479-535.

Hartnady, M.I., Kirkland, C.L., Clark, C., Spaggiari, C.V., Smithies, R.H., Evans, N.J. & McDonald, B.J., 2019: Titanite dates crystallization: Slow Pb diffusion during super-solidus re-equilibration. *Journal of Metamorphic Geology 37(6*), 823-838.

Hedström, P., Simeonov, A., Malmström, L., 1989: The Zinkgruvan ore deposit, south-central Sweden: A Proterozoic, proximal Zn-Pb-Ag deposit in distal volcanic facies. *Economic Geology 84*, 1235-1261.

Hellingwerf, R.H., 1987: Formation of sulfide deposits and its relation to sodic and potassic alteration of Proterozoic metabasites in the Sax» rift basin, Bergslagen, Sweden. *Mineralium Deposita 22 (1),* 53–63.

Helmers, H., 1984: Stages of granite intrusion and regional metamorphism in the Proterozoic rocks of western Bergslagen, C. Sweden, as exemplified in the Grangen area. *Neues Jahrbuch für Mineralogie 150*, 307-324.

Hemley, J.J., Montoya, J.W., Shaw, D.R. & Luce, R.W., 1977: Mineral equilibria in the $MgO$-$SiO_2$-$H_2O$ system; II, Talc-antigorite-forsterite-anthophyllite-enstatite stability relations and some geologic implications in the system. *American Journal of Science 277(4),* 353-383.

Henriques, Å., 1957: Protokoll från kärnkarteringar, Venafältet, kbh A-I. Vieille-Montagne, Zinkgruvan.

Henriques, A., 1964: Geology and ores of the Ammeberg district (Zinkgruvan) Sweden. *Arkiv för Mineralogi och Geologi 4*, 246 pp.

Henriques, Å., 1979: Protokoll från kärnkarteringar, Silvergruvan, kbh 10-12. Vieille-Montagne, Zinkgruvan.

Hermansson, T., Stephens, M.B., Corfu, F., Page, L.M., Andersson, J., 2008: Migratory tectonic switching, western Svecofennian orogen, central Sweden: Constraints from U/Pb zircon and titanite geochronology. *Precambrian Research 161*, 250-278.

Hietanen, A., 1975: Generation of potassium-poor magmas in the northern Sierra Nevada and the Svecofennian of Finland. *U.S. Geological Survey Journal of Research 3*, 631-645.

Hughes, C.J., 1973: Spilites, keratophyres. and the igneous spectrum. *Geological Magazine 109,* 513-527.

Hutchinson, M.N. & Scott, S.D., 1981: Sphalerite geobarometry in the Cu-Fe-Zn-S system. *Economic Geology 76(143),* 53.

Högnäs, J., 2018: Garpenberg Boliden Summary Report, Resources and Reserves. Retrieved from Boliden AB website: https://www.boliden.com/globalassets/operations/exploration/mineral-resources-and-mineral-reserves-pdf/resources-and-reserves-garpenberg-2018-12-31.pdf

Högdahl, K. & Sjöström, H., 2001: Evidence for 1.82 Ga transpressive shearing in a 1.85 Ga granitoid in central Sweden: implications for the regional evolution. *Precambrian Research 105,* 37−56.

Högdahl, K., Andersson, U.B. & Eklund, O. (eds.), 2004: The Transcandinavian Igneous Belt (TIB) in Sweden: a review of its character and evolution. *Geological Survey of Finland Special Paper 37*, 125 pp.

Högdahl, K., Sjöström, H. & Bergman, S., 2009: Ductile shear zones related to crustal shortening and domain boundary evolution in the central Fennoscandian Shield. *Tectonics 28*, 18 pp.

Högdahl, K., Sjöström, H., Andersson, U.B. & Ahl, M., 2008: Continental margin magmatism and migmatisation in the west-central Fennoscandian Shield. *Lithos 102*, 435−459.

Ishikawa, Y., Sawaguchi, T., Ywaya, S., and Horiuchi, M., 1976: Delineation of prospecting targets for Kuroko deposits based on modes of volcanism of underlying dacite and alteration halos. *Mining Geology, 26*: 105–117.

Jamieson, R.A. & Craw, D., 1987: Sphalerite geobarometry in metamorphic terranes: an appraisal with implications for metamorphic pressure in the Otago Schist. *Journal of metamorphic geology 5(1),* 87-99.

Jansson, N.F. & Allen, R.L, 2015: Multistage ore formation at the Ryllshyttan marble and skarn-hosted Zn–Pb–Ag–(Cu)+ magnetite deposit, Bergslagen, Sweden. *Ore Geology Reviews 69*, 217-242.

Jansson, N.F. & Allen, R.L., 2011: Timing of volcanism, hydrothermal alteration and ore formation at Garpenberg, Bergslagen, Sweden. *Gff 133(1–2),* 3–18.

Jansson, N.F., Zetterqvist, A., Allen, R.L., Billström, K. & Malmström, L., 2017: Genesis of the Zinkgruvan stratiform Zn-Pb-Ag deposit and associated dolomite-hosted Cu ore, Bergslagen, Sweden. *Ore Geology Reviews 82*, 285-308.

Jansson, N. F., Sädbom, S., Allen, R. L., Billström, K., & Spry, P. G., 2018: The Lovisa stratiform Zn-Pb deposit, Bergslagen, Sweden: structure, stratigraphy, and ore genesis. *Economic Geology*, *113*(3), 699-739.

Jansson, N.F., Zetterqvist, A., Allen, R.L. & Malmström, L., 2018: Geochemical vectors for stratiform Zn-Pb-Ag sulfide and associated dolomite-hosted Cu mineralization at Zinkgruvan, Bergslagen, Sweden. *Journal of Geochemical Exploration 190*, 207-228.

Johansson, Å. & Stephens, M.B., 2017: Timing of magmatism and migmatization in the 2.0-1.8 Ga accretionary Svecokarelian orogen, south-central Sweden. *International Journal of Earth Sciences 106*, 783-810.

Johansson, H.E., 1919: Om Tunabergs kopparmalmsfalt.*Sveriges geologiska undersökning C 221*, 19 pp.

Jonsson, E., Högdahl, K., Sahlström, F., Nysten, P. & Sadeghi, M., 2014: The Palaeoproterozoic skarn -hosted REE mineralisations of Bastnäs-type: overview and mineralogical-geological character. In *ERES2014: 1st European Rare Earth Resources Conference, Milos–Book of abstracts* (pp. 382-390).

Kampmann, T.C., Jansson, N.F., Stephens, M.B., Majka, J. & Lasskogen, J., 2017: Systematics of hydrothermal alteration at the Falun base metal sulfide deposit and implications for ore genesis and exploration, Bergslagen ore district, Fennoscandian Shield, Sweden. *Economic Geology 112*(5), 1111-1152.

Kampmann, T.C., Jansson, N.F., Stephens, M.B., Olin, P.H., Gilbert, S. & Wanhainen, C., 2018: Syntectonic sulphide remobilization and trace element redistribution at the Falun pyritic Zn-Pb-Cu-(Au-Ag) sulphide deposit, Bergslagen, Sweden. *Ore Geology Reviews 96*, 48-71.

Kaneda, H., Takenouchi, S. & Shoji, T., 1986: Stability of pentlandite in the Fe-Ni-Co-S system. *Mineralium Deposita 21(3),* 169-180.

Kelly, D.P. & Vaughan, D.J., 1983: Pyrrhotine-pentlandite ore textures: a mechanistic approach. *Mineralogical Magazine 47(345),* 453-463.

Ketcham, R.A., 2015: Calculation of stoichiometry from EMP data for apatite and other phases with mixing on monovalent anion sites. *American Mineralogist 100*(7), 1620-1623.

Klemm, D.D., 1966: Synthesen und Analysen in den Dreickdiagrammen FeAsS-CoAsS-NiAsS und FeS2-CoS2-NiS2. *Neues Jahrb. Mineral. Abh. 103*, 205-255.

Kumpulainen, R. A., Mansfeld, J., Sundblad, K., Neymark, L., & Bergman, T., 1996: Stratigraphy, age, and Sm-Nd isotope systematics of the country rocks to Zn-Pb sulfide deposits, Ammeberg District, Sweden. *Economic Geology*, *91*(6), 1009-1021.

Korja, A., Lahtinen, R. & Nironen, M., 2006: The Svecofennian orogen: a collage of microcontinents and island arcs. *Geological Society, London, Memoirs 32*, 561-578.

Kretschmar, U. & Scott, S.D., 1976: Phase relations involving arsenopyrite in the system Fe-As-S and their application. *Canadian mineralogist 14 (3),* 364-386.

Kumpulainen, R.A., Mansfeld, J., Sundblad, K., Neymark, L. & Bergman, T., 1996: Stratigraphy, age and Sm-Nd isotope systematics of the country rocks to Zn-Pb sulphide deposits, Ammeberg district, Sweden. *Economic Geology 91*, 1009-1021.

Lahtinen, R., Garde, A.A. & Melezhik, V.A., 2008, Paleoproterozoic evolution of Fennoscandia and *Greenland. Episodes 31*, 20−28.

Lahtinen, R., Korja, A., Nironen, M., 2005: *Paleoproterozoic tectonic evolution*. In: Lehtinen, M., Nurmi, P.A., Rämö, O.T. (Eds.), Precambrian Geology of Finland-Key to the Evolution of the Fennoscandian Shield. Elsevier B.V., Amsterdam, 481-532.

Lahtinen, R., Korja, A., Nironen, M., Heikkinen, P., 2009: Paleoproterozoic accretionary processes in Fennoscandia. *Geological Society, London, Special Publications 318*, 237-256.

Large, R.R., Gemmell, J.B., Paulick, H. & Huston, D.L., 2001: The alteration box plot: A simple approach to understanding the relationship between alteration mineralogy and lithogeochemistry associated with volcanic-hosted massive sulfide deposits. *Economic geology 96(5),* 957-971.

Lewerentz, A., Bakker, E., Hedin, P., 2019: *"Undersökning av Vena gruvfält: preliminära resultat från fältarbeten 2018". SGU-rapport 2019:08, [Geological Survey of Sweden report no 2019:08; in Swedish with a summary in English], Uppsala, Sweden*. 25pp.

Lewerentz, 2020: *Undersökning av Vena gruvfält*,

unpublished data.
Lundstrom, I., 1985: Beskrivning till berggrundskartan Lindesberg NV. *Sveriges geologiska Undersökning Af 140*, 131 pp.
Lundström, I., Allen, R.L., Persson, P.-O. & Ripa, M., 1998: Stratigraphies and depositional ages of Svecofennian, Paleoproterozoic metavolcanic rocks in E. Svealand and Bergslagen, south central Sweden. *GFF 120*, 315−320.
Magnusson, N.H., 1953: *Malmgeologi*. Jernkontoret, Stockholm, 439 pp.
Mansur, E.T., Barnes, S.J. & Duran, C.J., 2019: Textural and compositional evidence for the formation of pentlandite via peritectic reaction: Implications for the distribution of highly siderophile elements. *Geology 47(4),* 351-354.
Marshall, B., Vokes, F.M. & Larocque, A.C.L., 2000: Regional metamorphic remobilization: upgrading and formation of ore deposits. *Reviews in Economic Geology 11*(1), 19-38.
Middlemost, E. A., 1994: Naming materials in the magma/igneous rock system. *Earth-Science Reviews*, *37*(3-4), 215-224.
Misra, K.C. & Fleet, M.E., 1975: Textural and compositional variations in a Ni-Co-As assemblage. *The Canadian Mineralogist 13(1),* 8-14.
Nironen, M., 1997: The Svecofennian orogen: a tectonic model. *Precambrian Research 86*, 21−44.
Oen, I.S., 1987: Rift-related igneous activity and metallogenesis in SW Bergslagen, Sweden. *Precambrian Research 35*, 367-382.
Oen, I.S., Helmers, H., Verschure, R.H. & Wiklander, U., 1982: Ore deposition in a proterozoic incipient rift zone environment: a tentative model for the Filipstad-Grythyttan-Hjulsjö region, Bergslagen, Sweden. *Geologische Rundschau 71(1),* 182–194.
Palin, R.M., White, R. W., Green, E.C., Diener, J.F., Powell, R. & Holland, T.J., 2016: High-grade metamorphism and partial melting of basic and intermediate rocks. *Journal of Metamorphic Geology 34(9),* 871-892.
Paton, C., Hellstrom, J., Paul, B., Woodhead, J. & Hergt, J., 2011: Iolite: Freeware for the visualisation and processing of mass spectrometric data. *Journal of Analytical Atomic Spectrometry 26,* 2508-2518.
Paton, C., Woodhead, J., Hellstrom, J., Hergt, J., Greig, A. & Maas, R., 2010: Improved laser ablation U-Pb zircon geochronology through robust down-hole fractionation correction. *Geochemistry Geophysics Geosystems. 11,* 1-36.
Pavia, D.L., Lampman, G.M., Kriz, G.S. & Vyvyan, J.A., 2008: *Introduction to spectroscopy*. Cengage Learning. p. 1-12, 381-413, 418-441.
Pearce, J. A., 1983: Role of the sub-continental lithosphere in magma genesis at active continental margins.
Pearce, J. A., & Cann, J. R., 1973: Tectonic setting of basic volcanic rocks determined using trace element analyses. *Earth and planetary science letters*, *19*(2), 290-300.
Pearce, J.A., Harris, N.B. & Tindle, A.G., 1984: Trace element discrimination diagrams for the tectonic interpretation of granitic rocks. *Journal of petrology 25(4),* 956-983.
Persson, K.S., Sjöström, H., 2002: *Fold and shear accommodated convergence in eastern Bergslagen, central Sweden*. *In* K.S. Persson: *Deformation zones in models and nature*. Ph.D. thesis, University of Uppsala, Uppsala, Sweden, 23 pp.
Persson, P.O., Wikström, A., 1993: A U-Pb dating of the Askersund granite and its marginal augen gneiss. *Geologiska Föreningens i Stockholm Förhandlingar 115*, 321-329.
Petrus, J.A. & Kamber, B.S., 2012: VizualAge: A novel approach to laser ablation ICP-MS U-Pb geochronology data reduction. *Geostandards and Geoanalytical Research 36*(3), 247-270.
Ripa, M., 1994: The mineral chemistry of hydrothermally altered and metamorphosed wall-rocks at the Stollberg Fe-Pb-Zn-Mn(-Ag) deposit, Bergslagen, Sweden. *Mineralium Deposita 29*, 180-188.
Sahlström F., 2014: *Stable isotope systematics of skarn-hosted REE-silicate - magnetite mineralisations in central Bergslagen, Sweden*. (Examensarbete vid Institutionen för geovetenskaper).
Sahlström, F., Jonsson, E., Högdahl, K., Troll, V.R., Harris, C., Jolis, E.M. & Weis, F., 2019: interaction between high-temperature magmatic fluids and limestone explains 'Bastnäs-type' REE deposits in central Sweden. *Scientific reports 9*(1), 1-9.
Schandl, E. S., & Gorton, M. P., 2002: Application of high field strength elements to discriminate tectonic settings in VMS environments. *Economic geology*, *97*(3), 629-642.
Scott, S.D., 1976: Application of the sphalerite geobarometer to regionally metamorphosed terrains. *American Mineralogist 61*(7-8), 661-670.
Shand, S.J., 1943: *Eruptive rocks. Their genesis, composition, classification, and their relation to ore -deposits with a chapter on meteorite*, 2nd edition: New York, NY, John Wiley & Sons, p. 1–444.
Shanks III & W.C. Pat, 2012: Hydrothermal alteration in volcanogenic massive sulfide occurrence model: U.S. *Geological Survey Scientific Investigations Report 2010–5070 –C, chap. 11,* 12 p.
Sharp, Z.D., Essene, E.J. & Kelly, W.C., 1985: A re-examination of the arsenopyrite geothermometer; pressure considerations and applications to

natural assemblages. *The Canadian Mineralogist 23(4),* 517-534.
Simeonov, A., 1990: *Borrhålsprotokoll VENA8903*. Vieille-Montagne, Zinkgruvan, 13 p.
Skelton, A., Mansfeld, J., Ahlin, S., Lundqvist, T., Linde, J., Nilsson, J., 2018: A compilation of metamorphic pressure–temperature estimates from the Svecofennian province of eastern and central Sweden. *GFF 140:1*, 1-10
Söderlund, U., Jarl, L.G., Persson, P.O., Stephens, M.B. & Wahlgren, C.H., 1999: Protolith ages and timing of deformation in the eastern, marginal part of the Sveconorwegian orogen, southwestern Sweden. *Precambrian Research 94(1-2),* 29-48.
Spandler, C., Hammerli, J., Sha, P., Hilbert-Wolf, H., Hu, Y., Roberts, E. & Schmitz, M., 2016: MKED1: A new titanite standard for in situ analyses of Sm-Nd isotopes and U-Pb geochronology. *Chemical Geology 425,* 110–126.
Spencer, K.J., Haker, B.R., Kyander-Clark, A.R.C., Andersen, T.B., Cottle, J.M., Stearns, M.A., Poletti, J.E. & Seward, G.G.E., 2013: Campaign -style titanite U–Pb dating by laser-ablation ICP: Implications for crustal flow, phase transformations and titanite closure. *Chemical Geology 341*, 84–101.
Stephens, M.B. & Andersson, J., 2015: Migmatization related to mafic underplating and intra- or back-arc spreading above a subduction boundary in a 2.0–1.8 Ga accretionary orogen, Sweden. *Precambrian Research 264*, 235-257.
Stephens, M.B., Ripa, M., Lundström, I., Persson, L., Bergman, T., Ahl, M, Wahlgren, C.H., Persson, P.O. & Wickström, L., 2009: Synthesis of bedrock geology in the Bergslagen region, Fennoscandian Shield, south-central Sweden. *Ba 58*, *Sveriges geologiska undersökning*, 259 pp.
Stephens, M. B., & Jansson, N. F., 2020: Paleoproterozoic (1.9–1.8 Ga) syn-orogenic magmatism, sedimentation and mineralization in the Bergslagen lithotectonic unit, Svecokarelian orogen. *Geological Society, London, Memoirs*, *50* (1), 155-206.
Sundblad, K., Zachrisson, E., Smeds, S.A., Berglund, S. & Ålinder, C., 1984: Sphalerite Geobarometry and Arsenopyrite Geothermometry Applied to Metamorphosed Sulfide Ores in the Swedish Caledonides. *Economic Geology 79*, 1660-1668.
Sundblad, K., 1994: A genetic reinterpretation of the Falun and Åmmeberg ore types, Bergslagen, Sweden. *Mineralium Deposita 29*, 170–179.
Sundblad, K., Ahl, M. & Schöberg, H., 1993: Age and geochemistry of granites associated with Mo-mineralizations in western Bergslagen, Sweden. *Precambrian Research 64*, 319–335.
Sundblad, K., Zachrisson, E., Smeds, S.A., Berglund, S. & Ålinder, C., 1984: Sphalerite geobarometry and arsenopyrite geothermometry applied to metamorphosed sulfide ores in the Swedish Caledonides. *Economic Geology, 79(7*), 1660-1668.
Taylor, S.R. and McLennan, S.M., 1985: *The Continental Crust; Its composition and evolution; an examination of the geochemical record preserved in sedimentary rocks*. Blackwell, Oxford. 312 pp.
Tegengren, F.R., 1924: Sveriges ädlare malmer och bergverk. Sveriges geologiska undersökning Ca 17. 406 pp.
Tillberg, M., 2014: *Geochronology and sulphide-related assemblages of Håkansboda Cu-Co mineralization*. MSc Thesis. University of Gothenburg, Sweden. 55 pp.
Tomkins, A.G., 2007: Three mechanisms of ore remobilisation during amphibolite facies metamorphism at the Montauban Zn–Pb–Au–Ag deposit. *Mineralium Deposita 42*(6), 627-637.
Tomkins, A.G., Pattison, D.R. & Frost, B.R., 2007: On the initiation of metamorphic sulfide anatexis. *Journal of Petrology 48*(3), 511-535.
Toulmin, P., Barton, P.B. & Wiggins, L.B., 1991: Commentary on the sphalerite geobarometer. *American Mineralogist 76*(5-6), 1038-1051.
Torres-Alvarado, I. S., Pandarinath, K., Verma, S. P., & Dulski, P., 2018: Element Mobility Due to Hydrothermal Alteration in Los Azufres Geothermal Field, Mexico. *in Proceedings World Geothermal Congress 2010 Bali, Indonesia,* 25-29.
Trägårdh, J., 1988: Bergslagen, Sweden. *Geologie en Mijnbouw 67*, 397-409.
Trägårdh, J., 1991: Metamorphism of magnesium-altered felsic volcanic rocks from Bergslagen, central Sweden. A transition from Mg-chlorite to cordierite-rich rocks. *Ore Geology Reviews 6*, 485−497.
Valbracht, P.J., 1991: *The origin of the continental crust of the Baltic shield, as seen through Nd and Sr isotopic variations in 1.89−1.85 Ga old rocks from the western Bergslagen*, Sweden. Ph.D. thesis, University of Amsterdam, Amsterdam, Holland (GUA Papers of Geology Series 1, No. 29), 222 pp.
Valbracht, P.J., Oen, I.S. & Beunk, F.F., 1994: Sm-Nd isotope systematics of 1.9−1.8 Ga granites from western Bergslagen, Sweden: inferences on a 2.1−2.0 Ga crustal precursor. *Chemical Geology 112,* 21−37.
Vokes, F.M., 1969: A Review of the Metamorphism of Sulphide Deposits. *Earth Science Reviews 5*, 99-143.
Wagner, T., Jonsson, E. & Boyce, A.J., 2005: Metamorphic ore remobilization in the Hällefors district, Bergslagen, Sweden: constraints from min-

eralogical and small-scale sulphur isotope studies. *Mineralium Deposita 40*(1), 100-114.
Wasström, A., 1991a: *Borrhålsprotokoll VENA9002*. Vieille-Montagne, Zinkgruvan, 8 p.
Wasström, A., 1991b: *Borrhålsprotokoll VENA9003*. Vieille-Montagne, Zinkgruvan, 8 p.
Wasström, A., 1991c: *Borrhålsprotokoll VENA900*4. Vieille-Montagne, Zinkgruvan, 9 p.
Webster, J.D., Thomas, R., Rhede, D., Förster, H.J. & Seltmann, R., 1997: Melt inclusions in quartz from an evolved peraluminous pegmatite: Geochemical evidence for strong tin enrichment in fluorine-rich and phosphorus-rich residual liquids. *Geochimica et Cosmochimica Acta 61*(13), 2589-2604.
Weihed, P. & Eilu, P., 2005: 8-1: Fennoscandian shield–proterozoic VMS deposits. *Ore Geology Reviews, 27(1-4),* 324-325.
Weihed, P., Arndt, N., Billström, K., Duchesne, J. C., Eilu, P., Martinsson, O. & Lahtinen, R., 2005: Precambrian geodynamics and ore formation: The Fennoscandian Shield. *Ore Geology Reviews 27(1-4)*, 273-322.
Wikström, A. & Karis, L., 1991: Beskrivning till berggrundskartorna Finspang NO, SO, NV, SV. *Sveriges geologiska undersökning Af 162, 163, 164, 165*, 216 pp.
Winchester, J. A., & Floyd, P. A., 1976: Geochemical magma type discrimination: application to altered and metamorphosed basic igneous rocks. *Earth and Planetary Science Letters*, *28* (3), 459-469.
Zakrzewski, M.A. & Makovicky, E., 1986: Izoklakeite from Vena, Sweden and the Kobellite homologous series. *Canadian Mineralogist 24*, 7-18.
Zakrzewski, M.A., Burke, E.A.J. & Nugteren, H.W., 1980: Cobalt minerals in the Haellefors area, Bergslagen, Sweden; new occurrences of costibite, paracostibite, nisbite and cobaltian ullmannite. *The Canadian Mineralogist 18(2)*, 165-171.
Zane, A. & Weiss, Z., 1998: A procedure for classifying rock-forming chlorites based on microprobe data. *Rendiconti Lincei 9(1),* 51-56.
Zhang, J., Ma, C. & She, Z., 2012: An Early Cretaceous garnet-bearing metaluminous A-type granite intrusion in the East Qinling Orogen, central China: Petrological, mineralogical and geochemical constraints. *Geoscience Frontiers 3 (5),* 635-646.
Åberg, A., 1987: Protokoll över diamantborrhål Vena gruvfält: Vena DBH A, B, G, H, I samt Silvergruvan DBH 10 och 12. Vieille-Montagne, Zinkgruvan, 17 p.

# Appendix 1- Common mineral abbreviations

Summary of non-ore mineral abbreviations used in the text and images of this study.

| Abbreviation | Name |
|---|---|
| Amp | Amphibole |
| And | Andalusite |
| Ath | Anthophyllite |
| Ap | Apatite |
| Bar | Baryte |
| Bt | Biotite |
| Cal | Calcite |
| Chl | Chlorite |
| Cam | Clinoamphibole |
| Cpx | Clinopyroxene |
| Czo | Clinozoisite |
| Crd | Cordierite |
| En | Enstatite |
| Ep | Epidote |
| Grt | Garnet |
| Ilm | Ilmenite |
| Kfs | K-feldspar |
| Ms | Muscovite |
| Oam | Orthoamphibole |
| Op | Opaque |
| Opx | Orthopyroxene |
| Pl | Plagioclase |
| Qz | Quartz |
| Rt | Rutile |
| Ser | Sericite |
| Sid | Siderite |
| Ttn | Titanite |
| Tur | Tourmaline |
| Zrn | Zircon |
| Zo | Zoisite |

# Appendix 2- Summary table of ore minerals

Summary of compositions and abbreviations of the ore minerals found in this study.

| Name | Generalised Formula | Abbreviation |
|---|---|---|
| *Native Elements* | | |
| Bismuth | Bi | Bi |
| *Sulphides* | | |
| Bismuthinite | $Bi_2S_3$ | Bth |
| Carrolite | $Cu(Co,Ni)_2S_4$ | Car |
| Chalcopyrite | $CuFeS_2$ | Cpy |
| Cobaltoan Pyrite | $(Fe, Co)S_2$ | Py(Co) |
| Galena | $PbS_2$ | Gal |
| Marcasite | $FeS_2$ | Mar |
| Molybdenite | $MoS_2$ | Mol |
| Pentlandite | $(Co, Fe, Ni)_9S_8$ | Pen |
| Pyrite | $FeS_2$ | Py |
| Pyrrhotite | $Fe_{(1-x)}S$ (x=0-0.17) | Po |
| Sphalerite | (Zn, Fe)S | Sph |
| *Sulphantimonides* | | |
| Costibite | CoSbS | Csb |
| Kobellite | $Pb_{22}Cu_4(Bi, Sb)_{30}S_{69}$ | Kob |
| Ullmannite | NiSbS | Ull |
| Willyamite | (Co,Ni)SbS | Will |
| *Sulphabismuthinides* | | |
| Cosalite | $Pb_2Bi_2S_5$ | Cos |
| *Sulpharsenides* | | |
| Arsenopyrite | FeAsS | Asp |
| Cobaltite | CoAsS | Cob |
| *Arsenides* | | |
| Skutterudite | $(Co, Ni)As_3$ | Skt |
| *Oxides* | | |
| Hematite | $Fe_2O_3$ | Hem |
| Magnetite | $Fe_3O_4$ | Mag |
| *Y+REE minerals* | | |
| Allanite | $(Ce, La, Ca, REE)_2(Al, Fe^{3+})_3(SiO4)_3(OH)$ | All |
| Monazite | $(La, Ce, Nd, REE)\ PO_4$ | Mnz |
| Parisite | $Ca\ (Ce, La, REE)_2(CO3)_3F_2$ | Par |
| Xenotime-(Y) | $(Y, REE)PO_4$ | Xen |

# Appendix 3. Representative EDS analyses of non-ore minerals

The tables 1-13 below list wt% oxides and atoms per formula unit of different minerals. Rydc= rhyodacitic, Dac=dacitic, Ath=anthophyllite-bearing, Crd=cordierite-bearing and Calc=calcareous.

Table 1. Plagioclase.

| Sample | ALZ180067A-1 | ALZ180072A-1 | VNA002B2 | ALZ190037A |
|---|---|---|---|---|
| Lithology | Ath-metavolcanic | Dac-metavolcanic | Rydc-metavolcanic | Fe-skarn |
| Analysis | PL-1 | PL-4 | PL-5 | PL-8 |
| $SIO_2$ | 61.72 | 67.88 | 60.67 | 55.96 |
| $AL_2O_3$ | 24.43 | 19.67 | 24.98 | 28.97 |
| $Fe_2O_3$* | - | - | - | 0.67 |
| CaO | 8.51 | 0.36 | 6.16 | 10.33 |
| $Na_2O$ | 5.47 | 11.45 | 8.02 | 5.87 |
| $K_2O$ | - | - | 0.35 | - |
| Total | 100.13 | 99.36 | 100.18 | 101.79 |
| Formula based on: | | 8 oxygens | | |
| Si | 2.73 | 2.98 | 2.70 | 2.48 |
| Al | 1.27 | 1.02 | 1.31 | 1.51 |
| $Fe^{3+}$* | - | - | - | - |
| Ca | 0.26 | 0.02 | 0.29 | 0.49 |
| Na | 0.73 | 0.98 | 0.69 | 0.50 |
| K | - | - | 0.02 | - |
| Total | 5.00 | 4.99 | 5.01 | 4.98 |
| Ab % | 74% | 98% | 69% | 51% |
| An % | 26% | 2% | 29% | 49% |
| Kfs % | 0% | 0% | 2% | 0% |
| Name | plagioclase | plagioclase | plagioclase | plagioclase |

*All Fe is assumed to be $Fe^{3+}$

Ab=albite, An=anorthite and Kfs=K-feldspar

Table 2. K-feldspar.

| Sample | ALZ180089A-2 | ALZ180067A-1 | | ALZ190015A-1 |
|---|---|---|---|---|
| Lithology | Rydc-metavolcanic | Ath-metavolcanic | | Rydc-metavolcanic |
| Analysis | KF-1 | KF-3 | KF-4 | KF-5 |
| $SIO_2$ | 66.49 | 65.22 | 65.76 | 64.67 |
| $AL_2O_3$ | 19.03 | 18.86 | 18.69 | 18.40 |
| $Fe_2O_3$* | - | - | - | 0.92 |
| $Na_2O$ | 0.54 | - | - | - |
| $K_2O$ | 16.42 | 16.77 | 16.45 | 16.33 |
| Total | 102.47 | 100.85 | 100.90 | 100.32 |
| Formula based on: | | 8 oxygens | | |
| Si | 2.98 | 2.99 | 3.00 | 2.98 |
| Al | 1.01 | 1.02 | 1.01 | 1.00 |
| $Fe^{3+}$* | - | - | - | 0.03 |
| Na | 0.05 | - | - | - |
| K | 0.94 | 0.98 | 0.96 | 0.96 |
| Total | 4.97 | 4.99 | 4.97 | 4.97 |
| Ab % | 5% | 0% | 0% | 0% |
| An % | 0% | 0% | 0% | 0% |
| Kfs % | 95% | 100% | 100% | 100% |
| Name | K-feldspar | K-feldspar | K-feldspar | K-feldspar |

*All Fe is assumed to be $Fe^{3+}$

Table 3. Amphibole.

| Sample | ALZ180067A-1 | | | | | |
|---|---|---|---|---|---|---|
| Lithology | Ath-metavolcanic | | | | | |
| Analysis | AMP-1 | AMP-2 | AMP-3 | AMP-4 | AMP-5 | AMP-6 |
| $SiO_2$ | 54.45 | 52.31 | 54.06 | 54.04 | 54.77 | 54.25 |
| $TiO_2$ | - | - | - | - | - | - |
| $AL_2O_3$ | - | - | 0.87 | - | - | - |
| FeO | 15.78 | 25.70 | 22.48 | 22.08 | 22.20 | 22.59 |
| $Fe_3O_2$ | 7.33 | - | - | - | - | - |
| MgO | 18.71 | 20.11 | 18.59 | 18.57 | 18.61 | 18.67 |
| MnO | 0.83 | 1.06 | 0.83 | 1.01 | 1.01 | 0.96 |
| CaO | 0.27 | 0.27 | 0.29 | 0.34 | 0.24 | - |
| $Na_2O$ | - | - | - | - | - | - |
| $K_2O$ | - | - | - | - | - | - |
| Total | 97.35 | 99.45 | 97.11 | 96.03 | 96.82 | 96.47 |
| Formula based on: | 22.00 oxygens | | | | | |
| Si | 7.87 | 7.47 | 7.90 | 7.99 | 8.03 | 8.00 |
| Ti | - | - | - | - | - | - |
| Al | - | - | 0.15 | - | - | - |
| $Fe^{2+}$ | 1.91 | 2.02 | 2.70 | 2.72 | 2.72 | 2.77 |
| $Fe^{3+}$ | 0.80 | 1.05 | 0.04 | 0.01 | 0.00 | 0.01 |
| $Mn^{2+}$ | 0.10 | 0.13 | 0.10 | 0.13 | 0.13 | 0.12 |
| Mg | 5.62 | 6.12 | 5.90 | 5.92 | 5.85 | 5.98 |
| Ca | 0.04 | 0.04 | 0.05 | 0.05 | 0.04 | |
| Na | - | - | - | - | - | - |
| K | - | - | - | - | - | - |
| OH | 2.00 | 2.00 | 2.00 | 2.00 | 2.00 | 2.00 |
| Total | 18.33 | 18.83 | 18.85 | 18.82 | 18.76 | 18.88 |
| #Mg | 0.75 | 0.75 | 0.69 | 0.69 | # 0.68 | 0.68 |
| Name | anthophyllite | anthophyllite | anthophyllite | anthophyllite | anthophyllite | anthophyllite |

| Sample | ALZ180067A-1 | | | | VNA022A |
|---|---|---|---|---|---|
| Lithology | Ath-metavolcanic | | | | Rydc-metavolcanic |
| Analysis | AMP-7 | AMP-8 | AMP-9 | AMP-10 | AMP-11 |
| $SiO_2$ | 50.87 | 50.38 | 51.54 | 54.17 | 50.02 |
| $TiO_2$ | - | - | - | - | 0.35 |
| $AL_2O_3$ | 1.00 | 1.00 | 1.17 | 1.89 | 5.95 |
| FeO | 25.97 | 25.67 | 25.89 | 12.66 | 13.13 |
| $Fe_3O_2$ | - | - | 0.01 | - | 0.02 |
| MgO | 19.05 | 18.90 | 19.12 | 15.69 | 14.41 |
| MnO | 0.92 | 1.03 | 1.02 | 0.43 | 0.67 |
| CaO | 0.20 | 0.20 | 0.22 | 12.62 | 12.27 |
| $Na_2O$ | - | - | - | 0.00 | 0.70 |
| $K_2O$ | - | - | - | 0.00 | 0.63 |
| Total | 98.02 | 97.18 | 98.97 | 97.45 | 98.15 |
| Formula based on: | | | | | |
| Si | 7.40 | 7.39 | 7.42 | 7.79 | 7.22 |
| Ti | - | - | - | - | 0.04 |
| Al | 0.17 | 0.17 | 0.20 | 0.32 | 1.01 |
| $Fe^{2+}$ | 2.12 | 2.10 | 2.16 | 1.43 | 1.33 |
| $Fe^{3+}$ | 1.04 | 1.05 | 0.96 | 0.09 | 0.26 |
| $Mn^{2+}$ | 0.11 | 0.13 | 0.12 | 0.05 | 0.08 |
| Mg | 5.99 | 5.97 | 5.95 | 3.37 | 3.10 |
| Ca | 0.03 | 0.03 | 0.04 | 1.95 | 1.90 |
| Na | - | - | - | - | 0.20 |
| K | - | - | - | - | 0.12 |
| OH | 2.00 | 2.00 | 2.00 | 2.00 | 2.00 |
| Total | 18.86 | 18.84 | 18.84 | 17.00 | 17.26 |
| #Mg | 0.74 | 0.74 | 0.73 | 0.55 | # 0.52 |
| Name | anthophyllite | anthophyllite | anthophyllite | actinolite | actinolite |

Table 4. Garnet. $Fe^{3+}$ was calculated using the method of Droop (1987).

| Sample | ALZ180089A-1 | | | | | |
|---|---|---|---|---|---|---|
| Lithology | Calc-skarn | | | | | |
| Analysis | GRT-1 | GRT-2 | GRT-3 | GRT-4 | GRT-5 | GRT-6 |
| $SiO_2$ | 38.81 | 38.83 | 38.87 | 38.10 | 39.02 | 38.63 |
| $AL_2O_3$ | 17.93 | 18.31 | 17.84 | 17.70 | 18.08 | 18.06 |
| $Fe_2O_3$ | 6.04 | 5.86 | 6.54 | 6.56 | 6.68 | 6.28 |
| FeO | 2.99 | 3.55 | 2.39 | 2.28 | 2.36 | 2.65 |
| MnO | 0.59 | 0.72 | 0.65 | 0.65 | 0.76 | 0.56 |
| CaO | 33.44 | 34.13 | 34.00 | 33.40 | 34.01 | 33.61 |
| Total | 99.80 | 101.40 | 100.28 | 98.69 | 100.92 | 99.79 |
| Formula based on: | 12.00 oxygens | | | | | |
| Si | 3.05 | 3.00 | 3.05 | 3.03 | 3.04 | 3.04 |
| Al | 1.66 | 1.67 | 1.65 | 1.66 | 1.66 | 1.67 |
| $Fe^{3+}$ | 0.35 | 0.34 | 0.39 | 0.39 | 0.39 | 0.37 |
| $Fe^{2+}$ | 0.20 | 0.23 | 0.16 | 0.15 | 0.15 | 0.17 |
| $Mn^{2+}$ | 0.04 | 0.05 | 0.04 | 0.04 | 0.05 | 0.04 |
| Ca | 2.82 | 2.83 | 2.85 | 2.85 | 2.84 | 2.83 |
| Total | 8.12 | 8.12 | 8.13 | 8.13 | 8.13 | 8.13 |
| Grossular% | 76.03% | 75.57% | 76.03% | 75.95% | 75.71% | 76.31% |
| Almandine% | 6.17% | 6.98% | 4.82% | 4.69% | 4.76% | 5.41% |
| Spessartine% | 1.22% | 1.44% | 1.32% | 1.35% | 1.56% | 1.15% |
| Andradite% | 16.58% | 16.01% | 17.83% | 18.01% | 17.98% | 17.14% |
| Name | grossular | grossular | grossular | grossular | grossular | grossular |

| Sample | ALZ180089A-1 | | | | | |
|---|---|---|---|---|---|---|
| Lithology | Calc-skarn | | | | | |
| Analysis | GRT-7 | GRT-8 | GRT-9 | GRT-10 | GRT-11 | GRT-12 |
| $SiO_2$ | 38.29 | 38.12 | 37.71 | 38.01 | 39.77 | 38.72 |
| $AL_2O_3$ | 17.91 | 17.55 | 17.70 | 17.70 | 18.48 | 18.18 |
| $Fe_2O_3$ | 7.08 | 7.32 | 6.12 | 5.69 | 6.43 | 5.99 |
| FeO | 1.88 | 2.09 | 2.68 | 2.66 | 2.75 | 2.82 |
| MnO | 0.71 | 0.65 | 0.57 | 0.56 | 0.49 | 0.58 |
| CaO | 33.76 | 33.51 | 32.69 | 32.95 | 34.69 | 33.59 |
| Total | 99.63 | 99.23 | 97.47 | 97.58 | 102.60 | 99.88 |
| Formula based on: | 12.00 oxygens | | | | | |
| Si | 3.03 | 3.03 | 3.04 | 3.05 | 3.04 | 3.04 |
| Al | 1.67 | 1.64 | 1.68 | 1.67 | 1.67 | 1.68 |
| $Fe^{3+}$ | 0.42 | 0.44 | 0.37 | 0.34 | 0.37 | 0.35 |
| $Fe^{2+}$ | 0.12 | 0.14 | 0.18 | 0.18 | 0.18 | 0.19 |
| $Mn^{2+}$ | 0.05 | 0.04 | 0.04 | 0.04 | 0.03 | 0.04 |
| Ca | 2.86 | 2.85 | 2.82 | 2.83 | 2.84 | 2.82 |
| Total | 8.14 | 8.15 | 8.13 | 8.12 | 8.13 | 8.12 |
| Grossular% | 75.71% | 74.65% | 76.12% | 77.19% | 76.45% | 76.63% |
| Almandine% | 3.85% | 4.29% | 5.60% | 5.54% | 5.43% | 5.74% |
| Spessartine% | 1.48% | 1.34% | 1.20% | 1.17% | 0.98% | 1.20% |
| Andradite% | 18.96% | 19.72% | 17.08% | 16.10% | 17.13% | 16.43% |
| Name | grossular | grossular | grossular | grossular | grossular | grossular |

Table 4 (cont.). Garnet. $Fe^{3+}$ was calculated using the method of Droop (1987).

| Sample | ALZ180089A-1 | | | | |
|---|---|---|---|---|---|
| Lithology | Calc-skarn | | | | |
| Analysis | GRT-13 | GRT-14 | GRT-15 | GRT-16 | GRT-17 |
| $SiO_2$ | 39.64 | 38.33 | 37.78 | 39.08 | 39.17 |
| $AL_2O_3$ | 18.14 | 17.70 | 17.59 | 17.82 | 18.25 |
| $Fe_2O_3$ | 6.56 | 7.07 | 6.11 | 4.04 | 6.26 |
| FeO | 2.91 | 1.97 | 2.33 | 4.45 | 2.91 |
| MnO | 0.71 | 0.70 | 0.61 | 0.58 | 0.50 |
| CaO | 34.21 | 33.73 | 33.02 | 32.57 | 33.92 |
| Total | 102.17 | 99.50 | 97.43 | 98.55 | 101.01 |
| Formula based on: | 12.00 oxygens | | | | |
| Si | 3.05 | 3.03 | 3.04 | 3.09 | 3.04 |
| Al | 1.64 | 1.65 | 1.67 | 1.66 | 1.67 |
| $Fe^{3+}$ | 0.38 | 0.42 | 0.37 | 0.24 | 0.37 |
| $Fe^{2+}$ | 0.19 | 0.13 | 0.16 | 0.29 | 0.19 |
| $Mn^{2+}$ | 0.05 | 0.05 | 0.04 | 0.04 | 0.03 |
| Ca | 2.82 | 2.86 | 2.85 | 2.76 | 2.82 |
| Total | 8.13 | 8.14 | 8.13 | 8.08 | 8.12 |
| Grossular% | 75.16% | 75.45% | 76.75% | 77.65% | 76.16% |
| Almandine% | 5.77% | 4.02% | 4.85% | 9.08% | 5.85% |
| Spessartine% | 1.43% | 1.45% | 1.28% | 1.20% | 1.03% |
| Andradite% | 17.64% | 19.08% | 17.12% | 12.07% | 16.96% |
| Name | grossular | grossular | grossular | grossular | grossular |

Table 45 Pyroxene.

| Sample | ALZ180067A-1 | ALZ180089A-1 | | | | | ALZ180089A-3 | |
|---|---|---|---|---|---|---|---|---|
| Lithology | Ath-metavolcanic | Calc-skarn | | | | | Ath-metavolcanic | |
| Analysis | OPX-1 | CPX-1 | CPX-2 | CPX-3 | CPX-4 | CPX-5 | CPX-6 | CPX-7 |
| $SIO_2$ | 54.34 | 50.21 | 50.29 | 50.08 | 49.99 | 49.44 | 55.64 | 55.23 |
| $TiO_2$ | 1.10 | - | - | - | - | - | - | - |
| $AL_2O_3$ | - | - | - | - | 0.36 | 0.00 | - | - |
| FeO | 23.18 | 17.55 | 17.65 | 17.01 | 14.67 | 15.16 | 6.01 | 5.13 |
| $Fe_2O_3$ | 0.00 | 0.49 | 0.00 | 0.48 | 0.00 | 0.34 | 0.68 | 0.00 |
| MgO | 18.19 | 6.75 | 6.67 | 6.95 | 8.77 | 7.56 | 15.17 | 15.74 |
| MnO | 0.00 | 0.40 | 0.62 | 0.66 | 0.74 | 0.89 | 0.48 | - |
| CaO | 0.42 | 23.44 | 23.39 | 23.25 | 22.36 | 23.07 | 25.41 | 24.92 |
| Total | 97.23 | 98.83 | 98.62 | 98.43 | 96.89 | 96.46 | 103.39 | 101.02 |
| Formula based on: | 6 oxygens | | | | | | | |
| Si | 2.09 | 1.99 | 2.00 | 1.99 | 1.99 | 1.99 | 1.99 | 2.00 |
| Ti | 0.03 | - | - | - | - | - | - | - |
| Al | - | - | - | - | 0.02 | - | - | - |
| $Fe^{2+}$ | 0.76 | 0.58 | 0.59 | 0.57 | 0.49 | 0.51 | 0.19 | 0.16 |
| $Fe^{3+}$ | - | 0.01 | - | 0.01 | - | 0.01 | 0.02 | - |
| Mg | 1.04 | 0.40 | 0.39 | 0.41 | 0.52 | 0.45 | 0.81 | 0.85 |
| Mn | - | 0.01 | 0.02 | 0.02 | 0.02 | 0.03 | 0.01 | - |
| Ca | 0.02 | 1.00 | 1.00 | 0.99 | 0.96 | 1.00 | 0.97 | 0.99 |
| Total | 3.94 | 4.00 | 4.00 | 4.00 | 4.00 | 4.00 | 4.00 | 4.00 |
| #Mg | 0.58 | 0.41 | 0.40 | 0.42 | 0.52 | 0.47 | 0.81 | 0.84 |
| Name | enstatite-ferrosillite | hedenbergite | hedenbergite | hedenbergite | diopside | hedenbergite | diopside | diopside |

Table 6. Zoisite and clinozoisite.

| Sample | ALZ180089A-1 | | | | | |
|---|---|---|---|---|---|---|
| Lithology | Calc-skarn | | | | | |
| Analysis | CZ-1 | CZ-2 | CZ-3 | CZ-4 | CZ-5 | CZ-6 |
| $SIO_2$ | 38.51 | 37.80 | 38.18 | 38.78 | 38.51 | 37.80 |
| $AL_2O_3$ | 27.21 | 27.30 | 27.21 | 27.85 | 28.04 | 27.08 |
| $Fe_2O_3$* | 7.75 | 8.22 | 8.74 | 8.58 | 8.01 | 8.54 |
| $Cr_2O_3$ | 0.34 | - | - | - | - | - |
| MnO | - | - | - | - | - | 7.71 |
| CaO | 24.33 | 23.52 | 24.07 | 23.77 | 24.12 | 23.48 |
| Total | 98.13 | 96.84 | 98.20 | 98.99 | 98.67 | 104.60 |
| Formula based on: | 12.50 oxygens | | | | | |
| Si | 3.05 | 3.04 | 3.04 | 3.05 | 3.04 | 3.05 |
| Al | 2.54 | 2.59 | 2.56 | 2.58 | 2.61 | 2.57 |
| $Fe^{3+}$ | 0.46 | 0.50 | 0.52 | 0.51 | 0.48 | 0.52 |
| $Cr^{3+}$ | 0.02 | - | - | - | - | - |
| $Mn^{3+}$ | - | - | - | - | - | 0.53 |
| Ca | 2.06 | 2.03 | 2.06 | 2.01 | 2.04 | 2.03 |
| Total | 8.13 | 8.16 | 8.18 | 8.15 | 8.16 | 8.69 |
| Name | clinozoisite | clinozoisite | clinozoisite | clinozoisite | clinozoisite | clinozoisite |

| Sample | ALZ180089A-1 | | ALZ180089A-3 | | EDB190023B | ALZ180089A-2 |
|---|---|---|---|---|---|---|
| Lithology | Calc-skarn | | Ath-metavolcanic | | Rydc-metavolcanic | Rydc-metavolcanic |
| Analysis | CZ-7 | CZ-8 | CZ-9 | CZ-10 | CZ-11 | ZO-1 |
| $SIO_2$ | 38.70 | 39.68 | 40.05 | 40.07 | 39.47 | 45.67 |
| $AL_2O_3$ | 27.40 | 27.95 | 31.55 | 28.78 | 30.35 | 25.72 |
| $Fe_2O_3$* | 8.79 | 7.79 | 4.92 | 7.56 | 6.56 | - |
| $Cr_2O_3$ | - | - | - | - | - | - |
| MnO | - | - | - | - | - | - |
| CaO | 24.05 | 24.15 | 24.96 | 24.51 | 24.23 | 27.90 |
| Total | 98.94 | 99.57 | 101.48 | 100.92 | 100.61 | 99.29 |
| Formula based on: | 12.50 oxygens | | | | | |
| Si | 3.12 | 3.12 | 3.02 | 3.09 | 2.92 | 3.21 |
| Al | 2.60 | 2.59 | 2.80 | 2.62 | 2.65 | 2.13 |
| $Fe^{3+}$ | 0.53 | 0.46 | 0.28 | 0.44 | 0.37 | - |
| $Cr^{3+}$ | - | - | - | - | - | - |
| $Mn^{3+}$ | - | - | - | - | - | - |
| Ca | 2.08 | 2.03 | 2.02 | 2.03 | 1.92 | 2.10 |
| Total | 8.34 | 8.20 | 8.12 | 8.17 | 7.85 | 7.43 |
| Name | clinozoisite | clinozoisite | clinozoisite | clinozoisite | clinozoisite | zoisite |

*All Fe is assumed to be $Fe^{3+}$

Table 7. Chlorite.

| Sample | EDB190035A | EDB190023B | ALZ180089A-2 | ALZ190034A | | | ALZ190037A |
|---|---|---|---|---|---|---|---|
| Lithology | Rydc-metavolcanic | Rydc-metavolcanic | Rydc-metavolcanic | Rydc-metavolcanic | | | Fe-skarn |
| Analysis | CHL-01 | CHL-02 | CHL-03 | CHL-04 | CHL-05 | CHL-06 | CHL-07 |
| $SIO_2$ | 34.25 | 29.26 | 30.27 | 33.86 | 34.18 | 36.73 | 30.83 |
| $TiO_2$ | 0.67 | 0.00 | 0.00 | 0.00 | 0.00 | 0.00 | 0.00 |
| $AL_2O_3$ | 22.84 | 20.48 | 14.21 | 26.79 | 27.66 | 29.53 | 14.87 |
| FeO | 17.05 | 13.60 | 38.78 | 28.08 | 27.44 | 21.90 | 32.37 |
| MgO | 23.61 | 24.59 | 8.77 | 11.26 | 9.48 | 10.45 | 7.69 |
| MnO | 0.81 | 0.88 | 0.00 | 0.00 | 0.00 | 0.00 | 0.00 |
| CaO | 0.38 | 0.00 | 0.00 | 0.00 | 0.00 | 0.00 | 0.36 |
| K2O | 0.40 | 0.00 | 0.00 | 0.00 | 0.00 | 0.00 | 0.71 |
| Total | 100.01 | 88.81 | 92.03 | 100.00 | 98.77 | 98.61 | 86.83 |
| Formula based on: | | 28 oxygens | | | | | |
| Si | 5.97 | 4.72 | 5.48 | 6.10 | 6.09 | 6.32 | 5.41 |
| Al (VI) | 2.03 | 3.28 | 2.52 | 1.90 | 1.91 | 1.68 | 2.59 |
| $\Sigma_{tetra}$ | 4.00 | 4.00 | 4.00 | 4.00 | 4.00 | 8.00 | 4.00 |
| Al (IV) | 2.66 | 0.61 | 0.52 | 3.79 | 3.90 | 4.31 | 0.49 |
| $Fe^{2+}$* | 2.48 | 1.83 | 5.87 | 4.23 | 4.09 | 3.15 | 4.75 |
| Mg | 6.14 | 5.91 | 2.37 | 3.03 | 2.52 | 2.68 | 2.01 |
| Mn | 0.12 | 0.12 | 0.00 | 0.00 | 0.00 | 0.00 | 0.00 |
| $\Sigma_{octa}$ | 8.74 | 7.87 | 8.24 | 7.26 | 6.61 | 5.83 | 6.76 |
| Ca | 0.07 | 0.00 | 0.00 | 0.00 | 0.00 | 0.00 | 0.07 |
| K | 0.09 | 0.00 | 0.00 | 0.00 | 0.00 | 0.00 | 0.16 |
| Total | 32.30 | 28.35 | 29.00 | 30.31 | 29.12 | 31.98 | 26.24 |
| #Mg | 0.71 | 0.76 | 0.29 | 0.42 | 0.38 | 0.46 | 0.30 |
| Name [1] | clinochlore | clinochlore | chamosite | chamosite | Al-chlorite | Al-chlorite | Al-chlorite |

* All Fe assumed to be Fe2+ according to the method of Zane & Weiss (1998)

[1] Name determined using the method of Zane & Weiss (1998)

Table 8. Biotite.

| Sample | VNA002A | ALZ180037A-1 |
|---|---|---|
| Lithology | Rydc-metavolcanic | Ath-metavolcanic |
| Analysis | BT-01 | BT-02 |
| $SIO_2$ | 39.06 | 36.58 |
| $TiO_2$ | 1.15 | 1.23 |
| $AL_2O_3$ | 20.12 | 17.16 |
| FeO | 8.04 | 18.41 |
| MgO | 18.12 | 12.45 |
| $K_2O$ | 9.83 | 9.19 |
| Cl | - | 0.20 |
| Total | 96.33 | 95.03 |
| Formula based on: | 11 oxygens | |
| Si | 2.76 | 2.61 |
| Al (IV) | 1.24 | 1.39 |
| Ti | 0.06 | 0.07 |
| Al (IV) | 0.44 | 0.06 |
| $Fe^{2+}$ * | 0.48 | 1.10 |
| Mg | 1.91 | 1.33 |
| K | 0.89 | 0.84 |
| $Cl^1$ | - | 0.05 |
| $OH^1$ | 2.00 | 1.95 |
| Total | 7.78 | 7.39 |
| #Fe | 0.20 | 0.45 |
| Name [2] | phlogopite | annite |

* All Fe estimated to be Fe 2+

[1] Estimated/corrected based on the method by Ketcham (2015).

[2] Determined through the classification by Deer, et al. (1992).

Table 9. Cordierite.

| Sample | ALZ180076A-1 | | | |
|---|---|---|---|---|
| Lithology | Crd-metavolcanics | | | |
| Analysis | CRD-01 | CRD-02 | CRD-03 | CRD-04 |
| $SIO_2$ | 69.37 | 68.93 | 68.63 | 64.15 |
| $AL_2O_3$ | 48.37 | 46.16 | 46.97 | 44.61 |
| FeO | 6.61 | 6.38 | 6.03 | 6.32 |
| MgO | 14.91 | 14.59 | 15.11 | 13.90 |
| Total | 139.27 | 136.06 | 136.74 | 128.98 |
| Formula based on: | | 18 oxygens | | |
| Si | 4.96 | 5.00 | 5.00 | 4.95 |
| Al | 4.07 | 3.95 | 4.03 | 4.06 |
| $Fe^{2+}$ | 0.39 | 0.39 | 0.37 | 0.41 |
| Mg | 1.59 | 1.58 | 1.64 | 1.60 |
| Total | 11.01 | 10.92 | 11.04 | 11.02 |
| #Fe | 0.20 | 0.20 | 0.18 | 0.20 |
| Name | Cordierite | Cordierite | Cordierite | Cordierite |

Table 10. Apatite.

| Sample | ALZ180089A-1 | ALZ190015A-1 | | | ALZ180037A | | |
|---|---|---|---|---|---|---|---|
| Lithology | Calc-skarn | Rydc-metavolcanic | | | Ath-metavolcanic | | |
| Analysis | AP-1 | AP-2 | AP-3 | AP-4 | AP-5 | AP-6 | AP-7 |
| $SIO_2$ | - | - | 0.36 | - | - | - | - |
| CaO | 53.94 | 54.83 | 54.12 | 55.20 | 55.02 | 54.44 | 54.89 |
| $P_2O_5$ | 41.57 | 42.12 | 41.94 | 41.82 | 42.92 | 42.46 | 42.39 |
| F* | 1.31 | 2.48 | 2.71 | 2.98 | 1.81 | 1.62 | 1.75 |
| Cl* | - | - | - | - | - | - | - |
| OH* | 1.28 | - | - | - | 0.59 | 0.84 | 0.64 |
| Total | 98.10 | 99.43 | 99.13 | 100.00 | 100.34 | 99.37 | 99.68 |
| Formula based on: | Full (F,Cl, OH) | site | | | | | |
| Si | - | - | 0.06 | - | - | - | - |
| Ca | 9.91 | 9.93 | 9.83 | 10.01 | 9.84 | 9.84 | 9.90 |
| P | 6.04 | 6.03 | 6.02 | 5.99 | 6.06 | 6.06 | 6.04 |
| F* | 1.23 | 2.00 | 2.00 | 2.00 | 1.65 | 1.49 | 1.61 |
| Cl* | - | - | - | - | - | - | - |
| OH* | 0.77 | - | - | - | 0.35 | 0.51 | 0.39 |
| Total | 17.18 | 17.96 | 17.91 | 18.01 | 17.90 | 17.90 | 17.94 |
| Name | fluoroxyapatite | fluorapatite | fluorapatite | fluorapatite | fluorapatite | fluorapatite | fluorapatite |

| Sample | ALZ180037A | ALZ180089A-3 | | ALZ190037A | EDB180034A | | |
|---|---|---|---|---|---|---|---|
| Lithology | Ath-metavolcanic | Ath-metavolcanic | | Fe-skarn | Rydc-metavolcanic | | |
| Analysis | AP-8 | AP-9 | AP-10 | AP-11 | AP-12 | AP-13 | AP-14 |
| $SIO_2$ | - | - | - | - | - | - | - |
| CaO | 55.13 | 56.70 | 55.80 | 54.32 | 54.72 | 54.64 | 55.04 |
| $P_2O_5$ | 42.67 | 43.70 | 43.15 | 42.49 | 42.81 | 42.56 | 42.94 |
| F* | 1.86 | 2.16 | 1.85 | 2.06 | 2.43 | 1.75 | 1.85 |
| Cl* | - | - | - | - | - | - | - |
| OH* | 0.50 | 0.13 | 0.55 | 0.17 | 0.44 | 0.66 | 0.53 |
| Total | 100.16 | 102.68 | 101.35 | 99.03 | 100.40 | 99.60 | 100.37 |
| Formula based on: | Full (F,Cl, OH) | site | | | | | |
| Si | - | - | - | - | - | - | - |
| Ca | 9.89 | 9.91 | 9.89 | 9.82 | 9.82 | 9.85 | 9.84 |
| P | 6.05 | 6.04 | 6.04 | 6.07 | 6.07 | 6.06 | 6.06 |
| F* | 1.70 | 1.92 | 1.67 | 1.90 | 1.74 | 1.61 | 1.68 |
| Cl* | - | - | - | - | - | - | - |
| OH* | 0.30 | 0.08 | 0.33 | 0.10 | 0.26 | 0.39 | 0.32 |
| Total | 17.93 | 17.95 | 17.93 | 17.89 | 17.89 | 17.91 | 17.90 |
| Name | fluorapatite | fluorapatite | fluorapatite | fluorapatite | fluorapatite | fluorapatite | fluorapatite |

* Recalculated using the method of Ketcham (2015).

Table 11. Zircon. ND=not determined.

| Sample | VNA001B | VNA022A2 | EDB180034A | ALZ180037A |
|---|---|---|---|---|
| Lithology | Rydc-metavolcanic | Rydc-metavolcanic | Rydc-metavolcanic | Ath-metavolcanic |
| Analysis | ZR-1 | ZR-2 | ZR-3 | ZR-4 |
| $SIO_2$ | 31.00 | 30.65 | 31.45 | 30.78 |
| FeO | 0.55 | - | - | - |
| CaO | - | - | - | 0.62 |
| $Na_2O$ | - | - | - | - |
| $ZrO_2$ | 67.24 | 67.45 | 68.93 | 65.80 |
| $HfO_2$ | 1.21 | - | - | 1.32 |
| Total | 100.01 | 98.10 | 100.38 | 98.52 |
| Formula based on: | | 4 oxygens | | |
| Si | 1.06 | 0.96 | 1.07 | 1.00 |
| $Fe^{2+}$ | 0.02 | - | - | - |
| Ca | - | - | - | 0.02 |
| Zr | 1.12 | 1.04 | 1.14 | 1.04 |
| Hf | 0.01 | - | - | 0.01 |
| Zr/Hf | 55.36 | ND | ND | 49.82 |
| Total | 2.20 | 2.00 | 2.21 | 2.08 |
| Name | zircon | zircon | zircon | zircon |

Table 12. Titanite

| Sample | ALZ180089A-1 | | | | | | | |
|---|---|---|---|---|---|---|---|---|
| Lithology | Calc-skarn | | | | | | | |
| Analysis | TTN-1 | TTN-2 | TTN-4 | TTN-5 | TTN-6 | TTN-7 | TTN-8 | TTN-9 |
| $SiO_2$ | 30.46 | 31.21 | 31.13 | 30.83 | 31.90 | 31.13 | 31.40 | 33.24 |
| $TiO_2$ | 38.17 | 34.95 | 37.78 | 36.43 | 37.05 | 37.48 | 37.78 | 37.20 |
| $AL_2O_3$ | 1.47 | 3.76 | 1.15 | 1.40 | 2.25 | 1.98 | 1.38 | 1.70 |
| FeO | 0.78 | 0.00 | 0.48 | 0.00 | 0.42 | 0.00 | 0.71 | 0.00 |
| CaO | 28.33 | 28.54 | 28.32 | 27.77 | 27.94 | 28.10 | 27.89 | 27.86 |
| Total | 99.22 | 98.46 | 98.86 | 96.43 | 99.56 | 98.69 | 99.16 | 100.00 |
| Formula based on: | | 5 oxygens | | | | | | |
| Si | 1.05 | 1.00 | 1.00 | 1.03 | 1.03 | 1.02 | 1.02 | 1.03 |
| Ti | 0.99 | 0.84 | 0.91 | 0.91 | 0.90 | 0.93 | 0.93 | 0.87 |
| Al | 0.06 | 0.14 | 0.04 | 0.05 | 0.09 | 0.08 | 0.05 | 0.06 |
| $Fe^{2+}$ | 0.02 | 0.00 | 0.01 | 0.00 | 0.01 | 0.00 | 0.02 | 0.00 |
| Ca | 1.05 | 0.98 | 0.97 | 0.99 | 0.96 | 0.99 | 0.98 | 0.92 |
| Total | 3.17 | 2.96 | 2.94 | 2.98 | 2.98 | 3.01 | 3.00 | 2.88 |
| Name | titanite | titanite | titanite | titanite | titanite | titanite | titanite | titanite |

| Sample | ALZ180089A-1 | | ALZ180089A-2 | | | | EDB190035A |
|---|---|---|---|---|---|---|---|
| Lithology | Calc-skarn | | Rydc-metavolcanic | | | | Rydc-metavolcanic |
| Analysis | TTN-10 | TTN-11 | TTN-12 | TTN-13 | TTN-14 | TTN-15 | TTN-16 |
| $SiO_2$ | 31.96 | 31.10 | 33.39 | 31.21 | 30.98 | 31.49 | 32.58 |
| $TiO_2$ | 37.45 | 36.58 | 36.18 | 37.50 | 39.18 | 40.08 | 38.22 |
| $AL_2O_3$ | 2.38 | 2.97 | 3.53 | 1.55 | 1.10 | 1.38 | 1.38 |
| FeO | - | - | - | 0.80 | - | 0.98 | - |
| CaO | 29.13 | 28.87 | 27.42 | 26.04 | 28.57 | 28.39 | 27.82 |
| Total | 100.92 | 99.52 | 100.53 | 97.10 | 99.83 | 102.32 | 99.99 |
| Formula based on: | | 5 oxygens | | | | | |
| Si | 1.03 | 1.02 | 1.01 | 0.96 | 0.96 | 0.98 | 1.05 |
| Ti | 0.91 | 0.91 | 0.83 | 0.87 | 0.92 | 0.94 | 0.93 |
| Al | 0.09 | 0.12 | 0.13 | 0.06 | 0.04 | 0.05 | 0.05 |
| $Fe^{2+}$ | - | - | - | 0.02 | - | 0.03 | - |
| Ca | 1.01 | 1.02 | 0.89 | 0.86 | 0.95 | 0.95 | 0.96 |
| Total | 3.04 | 3.06 | 2.86 | 2.75 | 2.88 | 2.94 | 2.99 |
| Name | titanite | titanite | titanite | titanite | titanite | titanite | titanite |

Table 13. Rutile.

| Sample | AlZ190034A-1 | |
|---|---|---|
| Lithology | Rydc-metavolcanic | |
| Analysis | RT-01 | RT-02 |
| $TiO_2$ | 98.13 | 95.62 |
| $V_2O_5$ | - | 1.86 |
| $Nb_2O_5$ | 0.83 | 1.08 |
| Total | 98.96 | 98.56 |
| Formula based on: | 2 oxygens | |
| Ti | 0.98 | 0.95 |
| V | - | 0.02 |
| Nb | 0.01 | 0.01 |
| Total | 0.99 | 0.98 |
| Name | rutile | rutile |

# Appendix 4- Composition tables of ore minerals

The tables 1-20 below list the chemical compositions of ore minerals in at% and of REE minerals in wt%. Lithology abbreviations can be found in appendix 3.

Table 1. Pyrrhotite.

| Sample | O | Al | Si | S | Fe | Σ at% | Σ wt% |
|---|---|---|---|---|---|---|---|
| 1867-2-2 | 0.00 | 0.00 | 0.00 | 53.01 | 46.99 | 100.00 | 97.78 |
| 1867-2-5 | 2.87 | 0.00 | 0.00 | 50.74 | 46.39 | 100.00 | 96.98 |
| 1867-2-7 | 0.00 | 0.00 | 0.00 | 56.80 | 43.20 | 100.00 | 96.36 |
| 1867-2-8 | 0.00 | 0.00 | 0.00 | 52.94 | 47.06 | 100.00 | 98.79 |
| 1867-2-9 | 2.26 | 0.00 | 0.00 | 51.75 | 46.00 | 100.00 | 99.80 |
| 1867-2-11 | 0.00 | 0.00 | 0.00 | 52.93 | 47.07 | 100.00 | 99.16 |
| 1867-2-12 | 2.35 | 0.00 | 0.25 | 51.80 | 45.60 | 100.00 | 100.26 |
| 1867-3-22 | 0.00 | 0.00 | 0.00 | 53.04 | 46.96 | 100.00 | 99.00 |
| 1867-4-34 | 0.00 | 0.00 | 0.00 | 53.72 | 46.28 | 100.00 | 96.21 |
| 1867-4-40 | 0.00 | 0.00 | 0.00 | 53.13 | 46.87 | 100.00 | 99.31 |
| 1867-4-41 | 0.00 | 0.00 | 0.00 | 53.26 | 46.74 | 100.00 | 98.15 |
| 1867-5-42 | 0.00 | 0.00 | 0.00 | 52.78 | 47.22 | 100.00 | 97.53 |
| 1867-5-43 | 0.00 | 0.00 | 0.00 | 52.69 | 47.31 | 100.00 | 98.49 |
| 1867-5-44 | 0.00 | 0.00 | 0.00 | 52.59 | 47.41 | 100.00 | 98.83 |
| 1867-6-57 | 0.00 | 0.00 | 0.00 | 53.11 | 46.89 | 100.00 | 98.37 |
| 2B2-3-7 | 7.52 | 0.00 | 0.00 | 48.48 | 44.01 | 100.00 | 99.64 |
| 2B3-9-39 | 0.00 | 0.00 | 0.00 | 53.37 | 46.63 | 100.00 | 98.37 |
| 2B4-12-62 | 0.00 | 0.00 | 0.00 | 53.49 | 46.51 | 100.00 | 98.14 |
| 2B5-12-68 | 0.00 | 0.00 | 0.00 | 53.60 | 46.40 | 100.00 | 98.15 |
| 2B6-18-95 | 0.00 | 0.00 | 0.00 | 53.35 | 46.65 | 100.00 | 98.97 |
| 3A1-13-64 | 0.00 | 0.00 | 0.00 | 53.50 | 46.50 | 100.00 | 99.80 |
| 12A-2-2 | 0.00 | 0.00 | 0.00 | 53.11 | 46.89 | 100.00 | 99.92 |
| 12A-3-6 | 0.00 | 0.40 | 0.00 | 53.14 | 46.46 | 100.00 | 100.01 |
| 12A-3-7 | 0.00 | 0.45 | 0.00 | 53.06 | 46.49 | 100.00 | 99.23 |
| 12A-4-10 | 0.00 | 0.00 | 0.00 | 53.48 | 46.52 | 100.00 | 98.12 |
| 12A-5-16 | 0.00 | 0.00 | 0.00 | 53.40 | 46.60 | 100.00 | 99.52 |
| 12A-6-17 | 0.00 | 0.00 | 0.00 | 53.36 | 46.42 | 100.00 | 98.93 |
| 12A-7-19 | 0.00 | 0.00 | 0.00 | 53.45 | 46.55 | 100.00 | 99.22 |
| 12A-8-25 | 0.00 | 0.00 | 0.00 | 53.28 | 46.72 | 100.00 | 98.54 |
| 12A-8-26 | 0.00 | 0.00 | 0.00 | 53.02 | 46.98 | 100.00 | 98.24 |
| 12A-9-27 | 0.00 | 0.00 | 0.00 | 53.17 | 46.83 | 100.00 | 99.76 |
| 12A-9-30 | 0.00 | 0.00 | 0.00 | 53.55 | 46.45 | 100.00 | 99.06 |
| 12A-11-33 | 0.00 | 0.00 | 0.00 | 53.20 | 46.80 | 100.00 | 99.76 |

Table 1 (cont.). Pyrrhotite.

| Sample | O | Al | Si | S | Fe | Σ at% | Σ wt% |
|---|---|---|---|---|---|---|---|
| 12A-11-36 | 5.28 | 0.00 | 0.46 | 50.31 | 43.95 | 100.00 | 99.71 |
| 12A-11-39 | 0.00 | 0.00 | 0.00 | 53.82 | 46.18 | 100.00 | 98.04 |
| 22A2-1-2 | 0.00 | 0.00 | 0.00 | 53.39 | 46.61 | 100.00 | 98.29 |
| 22A3-2-7 | 0.00 | 0.00 | 0.00 | 53.29 | 46.71 | 100.00 | 98.89 |
| 22A4-3-18 | 0.00 | 0.00 | 0.32 | 53.43 | 46.24 | 100.00 | 99.45 |
| 22A5-5-23 | 0.00 | 0.00 | 0.00 | 53.27 | 46.73 | 100.00 | 98.72 |
| 22A6-5-24 | 0.00 | 0.00 | 0.00 | 53.68 | 46.32 | 100.00 | 98.58 |
| 22A7-5-25 | 0.00 | 0.00 | 0.00 | 53.95 | 46.05 | 100.00 | 98.64 |
| 22A8-10-44 | 0.00 | 0.00 | 0.00 | 53.21 | 46.79 | 100.00 | 98.67 |
| 22A9-11-48 | 0.00 | 0.00 | 0.00 | 53.09 | 46.91 | 100.00 | 98.81 |
| 22A10-11-49 | 0.00 | 0.00 | 0.00 | 53.80 | 46.20 | 100.00 | 97.86 |
| 1889A2-10-123 | 3.73 | 0.00 | 0.00 | 51.41 | 44.86 | 100.00 | 103.21 |
| 1889A2-4-84 | 3.52 | 0.00 | 0.00 | 51.69 | 44.79 | 100.00 | 102.60 |
| 1889A2-6-96 | 0.00 | 0.00 | 0.00 | 53.50 | 46.50 | 100.00 | 101.62 |
| 1889A2-9-113 | 0.00 | 0.00 | 0.00 | 53.39 | 46.61 | 100.00 | 102.02 |
| 1889A3-11-40 | 0.00 | 0.00 | 0.00 | 53.65 | 46.35 | 100.00 | 101.05 |
| 1889A3-12-49 | 0.00 | 0.00 | 0.00 | 54.01 | 45.99 | 100.00 | 101.18 |
| 1889A3-13-54 | 0.00 | 0.00 | 0.00 | 54.17 | 45.83 | 100.00 | 100.50 |
| 1889A3-13-56 | 0.00 | 0.00 | 0.00 | 53.58 | 46.42 | 100.00 | 102.73 |
| 1889A3-14-58 | 0.00 | 0.00 | 0.00 | 53.74 | 46.26 | 100.00 | 100.69 |
| 1889A3-4-4 | 0.00 | 0.00 | 0.00 | 53.44 | 46.56 | 100.00 | 102.17 |
| 1889A3-5-6 | 0.00 | 0.00 | 0.00 | 53.40 | 46.60 | 100.00 | 103.00 |
| 1889A3-7-19 | 3.99 | 0.00 | 0.00 | 51.45 | 44.56 | 100.00 | 103.03 |
| 1889A3-8-25 | 0.00 | 0.00 | 0.00 | 54.29 | 45.71 | 100.00 | 100.57 |
| 1889A3-9-27 | 0.00 | 0.00 | 0.00 | 53.82 | 46.18 | 100.00 | 101.31 |
| 1834A-1-279 | 0.00 | 0.00 | 0.00 | 53.74 | 46.26 | 100.00 | 102.77 |
| 1834A-1-281 | 0.00 | 0.15 | 0.00 | 53.64 | 46.20 | 100.00 | 97.64 |
| 1834A-1-285 | 0.00 | 0.00 | 0.00 | 53.83 | 46.17 | 100.00 | 97.90 |
| 3834A-3-292 | 4.03 | 0.00 | 0.00 | 51.48 | 44.49 | 100.00 | 99.97 |
| 3834A-3-293 | 3.88 | 0.00 | 0.00 | 51.72 | 44.39 | 100.00 | 100.27 |
| 3834A-3-294 | 0.00 | 0.00 | 0.24 | 53.76 | 46.00 | 100.00 | 97.75 |
| 4834A-4-300 | 3.89 | 0.00 | 0.00 | 51.78 | 44.33 | 100.00 | 98.07 |
| 4834A-4-301 | 4.27 | 0.00 | 0.00 | 50.28 | 45.45 | 100.00 | 96.71 |
| 5834A-5-306 | 0.00 | 0.00 | 0.00 | 53.96 | 46.04 | 100.00 | 98.16 |
| 6834A-6-309 | 0.00 | 0.00 | 0.00 | 53.86 | 46.14 | 100.00 | 96.91 |
| 6834A-6-312 | 0.00 | 0.00 | 0.00 | 53.74 | 46.26 | 100.00 | 98.64 |
| 6834A-6-313 | 3.74 | 0.00 | 0.00 | 51.57 | 44.69 | 100.00 | 102.02 |
| 6834A-6-314 | 0.00 | 0.00 | 0.00 | 53.38 | 46.62 | 100.00 | 102.21 |
| 1923B-1-87 | 0.00 | 0.00 | 0.00 | 53.10 | 46.90 | 100.00 | 98.47 |
| 2923B-2-92 | 3.66 | 0.00 | 0.00 | 51.28 | 45.06 | 100.00 | 98.69 |
| 2923B-2-94 | 2.37 | 0.00 | 0.00 | 52.60 | 45.04 | 100.00 | 101.93 |
| 2923B-2-95 | 0.00 | 0.00 | 0.00 | 53.77 | 46.23 | 100.00 | 99.10 |
| 2923B-2-96 | 0.00 | 0.00 | 0.00 | 53.62 | 46.38 | 100.00 | 96.34 |
| n= 76 | | | | | | | |
| Maximum value | 7.52 | 0.45 | 0.46 | 56.80 | 47.41 | 100.00 | 103.21 |
| Minimum value | 0.00 | 0.00 | 0.00 | 48.48 | 43.20 | 100.00 | 96.21 |
| Average | 0.75 | 0.01 | 0.02 | 53.04 | 46.17 | 100.00 | 99.39 |
| Standard deviation | 1.62 | 0.07 | 0.07 | 1.11 | 0.85 | 0.00 | 1.70 |
| 2σ | 0.52 | 0.02 | 0.02 | 0.36 | 0.27 | - | - |

Table 2. Pyrite-marcasite.

| Sample | O | Mg | Al | Si | K | Ca | Ti | S | Fe | Σ at% | Σ wt% |
|---|---|---|---|---|---|---|---|---|---|---|---|
| 1915A-1-2 | 0.00 | 0.00 | 0.00 | 0.00 | 0.00 | 0.00 | 0.00 | 66.89 | 33.11 | 100.00 | 98.03 |
| 1915A-3-10 | 8.70 | 0.00 | 0.83 | 2.12 | 0.00 | 0.00 | 0.00 | 59.41 | 28.94 | 100.00 | 98.67 |
| 1915A-5-15 | 0.00 | 0.00 | 0.00 | 0.00 | 0.00 | 0.00 | 0.00 | 66.51 | 33.49 | 100.00 | 97.78 |
| 1915A-6-20 | 6.57 | 0.00 | 0.29 | 0.00 | 0.00 | 0.00 | 0.00 | 62.14 | 31.00 | 100.00 | 101.54 |
| 1915A-7-21 | 7.10 | 0.00 | 0.30 | 0.00 | 0.00 | 0.00 | 0.00 | 61.53 | 31.07 | 100.00 | 102.82 |
| 1915A-18-66 | 0.00 | 0.00 | 0.00 | 0.00 | 0.00 | 0.00 | 0.00 | 66.96 | 33.04 | 100.00 | 97.74 |
| 1915A-19-67 | 8.72 | 0.00 | 0.00 | 0.64 | 0.00 | 0.00 | 0.00 | 60.15 | 30.48 | 100.00 | 100.69 |
| 1915A-19-68 | 0.00 | 0.00 | 0.00 | 0.00 | 0.00 | 0.00 | 0.00 | 66.67 | 33.33 | 100.00 | 97.68 |
| 1915A-20-72 | 0.00 | 0.00 | 0.28 | 0.00 | 0.00 | 0.00 | 0.00 | 66.39 | 33.33 | 100.00 | 98.97 |
| 1915A-22-77 | 6.91 | 0.00 | 0.00 | 0.00 | 0.00 | 0.00 | 0.00 | 61.95 | 31.15 | 100.00 | 101.39 |
| 1915A-22-78 | 0.00 | 0.00 | 0.00 | 0.00 | 0.00 | 0.00 | 0.00 | 66.64 | 33.36 | 100.00 | 98.36 |
| 2A-5-12 | 0.00 | 0.00 | 0.00 | 0.00 | 0.00 | 0.00 | 0.00 | 65.69 | 33.92 | 100.00 | 96.77 |
| 2A-16-64 | 0.00 | 0.00 | 0.00 | 0.00 | 0.00 | 0.00 | 0.00 | 66.14 | 33.86 | 100.00 | 100.5 |
| 2A-16-67 | 0.00 | 0.00 | 0.00 | 0.00 | 0.00 | 0.00 | 0.00 | 66.52 | 33.48 | 100.00 | 99.05 |
| 2B2-2-2 | 0.00 | 0.00 | 0.00 | 0.00 | 0.00 | 0.00 | 0.00 | 66.34 | 33.66 | 100.00 | 99.54 |
| 2B2-3-8 | 0.00 | 0.00 | 0.00 | 0.00 | 0.00 | 0.00 | 0.00 | 66.39 | 33.61 | 100.00 | 97.69 |
| 2B2-7-26 | 13.99 | 0.00 | 0.00 | 0.00 | 0.00 | 0.00 | 0.00 | 57.79 | 28.22 | 100.00 | 101.65 |
| 2B2-7-27 | 0.00 | 0.00 | 0.00 | 0.00 | 0.00 | 0.00 | 0.00 | 65.34 | 34.66 | 100.00 | 100.28 |
| 2B2-7-32 | 0.00 | 0.00 | 0.00 | 0.00 | 0.00 | 0.00 | 0.00 | 66.37 | 33.63 | 100.00 | 97.83 |
| 2B2-7-33 | 0.00 | 0.00 | 0.00 | 0.00 | 0.00 | 0.00 | 0.00 | 66.19 | 33.81 | 100.00 | 98.53 |
| 2B2-7-34 | 0.00 | 0.00 | 0.00 | 0.00 | 0.00 | 0.00 | 0.00 | 66.25 | 33.75 | 100.00 | 98.37 |
| 2B2-9-40 | 13.23 | 0.00 | 0.00 | 0.00 | 0.00 | 0.00 | 0.00 | 57.09 | 29.68 | 100.00 | 99.62 |
| 2B2-18-96 | 9.68 | 0.00 | 0.00 | 0.00 | 0.00 | 0.00 | 0.00 | 60.54 | 29.78 | 100.00 | 101.41 |
| 2B2-19-105 | 0.00 | 0.00 | 0.00 | 0.00 | 0.00 | 0.00 | 0.00 | 66.77 | 33.23 | 100.00 | 98.08 |
| 3A1-4-12 | 13.13 | 0.00 | 0.27 | 0.51 | 0.22 | 0.00 | 0.00 | 56.82 | 28.67 | 100.00 | 97.37 |
| 3A1-13-65 | 8.97 | 0.00 | 0.00 | 0.00 | 0.00 | 0.00 | 0.00 | 61.59 | 29.44 | 100.00 | 100.7 |
| 2A-2-5 | 12.89 | 0.00 | 0.00 | 0.33 | 0.00 | 0.00 | 0.00 | 55.99 | 30.59 | 100.00 | 98.5 |
| 2A-4-9 | 0.00 | 0.00 | 0.00 | 0.00 | 0.00 | 0.00 | 0.00 | 53.51 | 46.49 | 100.00 | 99.03 |
| 2A-4-14 | 7.04 | 0.00 | 0.00 | 0.00 | 0.00 | 0.00 | 0.00 | 61.48 | 31.48 | 100.00 | 102.85 |
| 2A-7-20 | 8.79 | 0.00 | 0.00 | 0.00 | 0.00 | 0.00 | 0.00 | 59.76 | 31.45 | 100.00 | 96.85 |
| 2A-9-30 | 0.00 | 0.00 | 0.00 | 0.00 | 0.00 | 0.00 | 0.00 | 66.13 | 33.87 | 100.00 | 99.07 |
| 2A-11-36 | 11.59 | 1.14 | 1.12 | 1.85 | 0.00 | 0.74 | 0.45 | 43.61 | 39.50 | 100.00 | 100.44 |
| 2A2-1-3 | 0.00 | 0.00 | 0.00 | 0.00 | 0.00 | 0.00 | 0.00 | 66.24 | 33.76 | 100.00 | 99.96 |
| 2A2-2-9 | 0.00 | 0.00 | 0.00 | 0.00 | 0.00 | 0.00 | 0.00 | 66.37 | 33.63 | 100.00 | 98.2 |
| 2A2-3-11 | 14.57 | 0.00 | 0.00 | 0.00 | 0.00 | 0.00 | 0.00 | 58.29 | 27.15 | 100.00 | 97.49 |
| 2A2-3-12 | 6.31 | 0.00 | 0.00 | 0.00 | 0.00 | 0.00 | 0.00 | 62.20 | 31.49 | 100.00 | 100.7 |
| 2A2-3-13 | 6.20 | 0.00 | 0.00 | 0.00 | 0.00 | 0.00 | 0.00 | 62.04 | 31.76 | 100.00 | 101.58 |
| 2A2-3-15 | 6.91 | 0.00 | 0.00 | 0.00 | 0.00 | 0.00 | 0.00 | 60.85 | 32.24 | 100.00 | 101.69 |
| 2A2-3-17 | 3.15 | 0.00 | 0.00 | 0.00 | 0.00 | 0.00 | 0.00 | 51.60 | 45.25 | 100.00 | 99.95 |
| 2A2-3-22 | 6.96 | 0.00 | 0.00 | 0.00 | 0.00 | 0.00 | 0.00 | 61.65 | 31.40 | 100.00 | 100.8 |
| 2A2-6-27 | 0.00 | 0.00 | 0.00 | 0.00 | 0.00 | 0.00 | 0.00 | 66.89 | 33.11 | 100.00 | 98.39 |
| 2A2-8-39 | 0.00 | 0.00 | 0.00 | 0.00 | 0.00 | 0.00 | 0.00 | 66.03 | 33.97 | 100.00 | 101.56 |
| 2A2-8-40 | 10.94 | 0.00 | 0.00 | 0.00 | 0.00 | 0.00 | 0.00 | 57.87 | 31.19 | 100.00 | 102.71 |
| 2A2-8-41 | 8.72 | 0.00 | 0.00 | 0.00 | 0.00 | 0.00 | 0.00 | 61.36 | 29.92 | 100.00 | 100.89 |
| 2A2-8-42 | 9.92 | 0.00 | 0.00 | 0.00 | 0.00 | 0.00 | 0.00 | 60.63 | 29.45 | 100.00 | 103.19 |
| 2A2-8-43 | 0.00 | 0.00 | 0.00 | 0.00 | 0.00 | 0.00 | 0.00 | 66.38 | 33.62 | 100.00 | 100.48 |
| 2A2-8-44 | 8.20 | 0.00 | 0.00 | 0.00 | 0.00 | 0.00 | 0.00 | 60.95 | 30.85 | 100.00 | 98.3 |
| 2A2-8-45 | 0.00 | 0.00 | 0.00 | 0.00 | 0.00 | 0.00 | 0.00 | 67.12 | 32.88 | 100.00 | 97.89 |
| 2A2-8-46 | 0.00 | 0.00 | 0.00 | 0.00 | 0.00 | 0.00 | 0.00 | 67.07 | 32.93 | 100.00 | 99.96 |
| 2A2-8-47 | 0.00 | 0.00 | 0.00 | 0.00 | 0.00 | 0.00 | 0.00 | 67.06 | 32.94 | 100.00 | 100.01 |
| 2A2-8-48 | 0.00 | 0.00 | 0.00 | 0.00 | 0.00 | 0.00 | 0.00 | 66.76 | 33.24 | 100.00 | 101.36 |
| 2A2-8-49 | 0.00 | 0.00 | 0.00 | 0.00 | 0.00 | 0.00 | 0.00 | 66.55 | 33.45 | 100.00 | 98.99 |
| 2A2-8-50 | 0.00 | 0.00 | 0.00 | 0.00 | 0.00 | 0.00 | 0.00 | 67.19 | 32.81 | 100.00 | 96.7 |
| 2A2-8-51 | 0.00 | 0.00 | 0.00 | 0.00 | 0.00 | 0.00 | 0.00 | 66.77 | 33.23 | 100.00 | 98.45 |
| 2A2-8-51 | 7.19 | 0.00 | 0.00 | 0.00 | 0.00 | 0.00 | 0.00 | 61.06 | 31.74 | 100.00 | 102.59 |
| n=55 | | | | | | | | | | | |
| Maximum value | 14.57 | 1.14 | 1.12 | 2.12 | 0.22 | 0.74 | 0.45 | 67.19 | 46.49 | 100.00 | 103.19 |
| Minimum value | 0.00 | 0.00 | 0.00 | 0.00 | 0.00 | 0.00 | 0.00 | 43.61 | 27.15 | 100.00 | 96.70 |
| Average | 4.12 | 0.02 | 0.06 | 0.10 | 0.00 | 0.01 | 0.01 | 62.92 | 32.75 | 100.00 | 99.63 |
| Standard deviation | 4.89 | 0.15 | 0.20 | 0.39 | 0.03 | 0.10 | 0.06 | 4.72 | 3.23 | - | - |
| 2σ | 1.85 | 0.06 | 0.07 | 0.15 | 0.01 | 0.04 | 0.02 | 1.79 | 1.22 | - | - |

Table 3. Chalcopyrite.

| Sample | O | Mg | Al | Si | K | Ca | Ti | S | Fe | Cu | Zn | Σ at% | Σ wt% |
|---|---|---|---|---|---|---|---|---|---|---|---|---|---|
| 1867A-5-47 | 0.00 | 0.00 | 0.00 | 0.00 | 0.00 | 0.00 | 0.00 | 48.20 | 24.34 | 27.47 | 0.00 | 100.01 | 103.80 |
| 1867A-5-48 | 0.00 | 0.00 | 0.00 | 0.00 | 0.00 | 0.00 | 0.00 | 48.43 | 24.53 | 27.04 | 0.00 | 100.00 | 102.59 |
| 1872A-1-6 | 0.00 | 0.00 | 0.00 | 0.00 | 0.00 | 0.00 | 0.00 | 48.56 | 24.44 | 27.00 | 0.00 | 100.00 | 103.59 |
| 1872A-2-15 | 0.00 | 0.00 | 0.00 | 0.00 | 0.00 | 0.00 | 0.00 | 48.70 | 23.32 | 27.98 | 0.00 | 100.00 | 103.38 |
| 1872A-3-24 | 0.00 | 0.00 | 0.00 | 0.00 | 0.00 | 0.00 | 0.00 | 48.50 | 24.61 | 26.89 | 0.00 | 100.00 | 100.63 |
| 1872A-7-54 | 0.00 | 0.00 | 0.00 | 0.00 | 0.00 | 0.00 | 0.00 | 48.33 | 24.23 | 27.44 | 0.00 | 100.00 | 103.00 |
| 1872A-7-60 | 0.00 | 0.00 | 0.00 | 0.00 | 0.00 | 0.00 | 0.00 | 48.45 | 23.92 | 27.62 | 0.00 | 100.00 | 103.89 |
| 1915A-1-1 | 0.00 | 0.00 | 0.00 | 0.00 | 0.00 | 0.00 | 0.00 | 50.19 | 25.17 | 24.64 | 0.00 | 100.00 | 98.94 |
| 1915A-2-6 | 0.00 | 0.00 | 0.00 | 0.00 | 0.00 | 0.00 | 0.00 | 50.65 | 24.76 | 24.58 | 0.00 | 100.00 | 97.34 |
| 1915A-2-8 | 0.00 | 0.00 | 0.00 | 0.00 | 0.00 | 0.00 | 0.00 | 50.59 | 25.13 | 24.28 | 0.00 | 100.00 | 97.83 |
| 1915A-15-54 | 0.00 | 0.00 | 0.00 | 0.00 | 0.00 | 0.00 | 0.00 | 50.45 | 25.65 | 23.90 | 0.00 | 100.00 | 98.55 |
| 1915A-15-55 | 0.00 | 0.00 | 0.00 | 0.00 | 0.00 | 0.00 | 0.00 | 50.74 | 25.68 | 23.58 | 0.00 | 100.00 | 99.37 |
| 1915A-17-64 | 0.00 | 0.00 | 0.00 | 0.00 | 0.00 | 0.21 | 0.00 | 50.29 | 25.01 | 24.49 | 0.00 | 100.00 | 98.67 |
| 2A-9-23 | 0.00 | 0.00 | 0.00 | 0.00 | 0.00 | 0.00 | 0.00 | 50.33 | 24.68 | 24.99 | 0.00 | 100.00 | 97.42 |
| 2A-9-27 | 0.00 | 0.00 | 0.00 | 0.00 | 0.00 | 0.00 | 0.00 | 50.95 | 24.64 | 24.41 | 0.00 | 100.00 | 97.90 |
| 2A-15-63 | 0.00 | 0.00 | 0.00 | 0.00 | 0.19 | 0.00 | 0.00 | 50.48 | 24.42 | 24.92 | 0.00 | 100.01 | 96.73 |
| 2A-16-65 | 0.00 | 0.00 | 0.00 | 0.00 | 0.00 | 0.00 | 0.00 | 49.67 | 25.69 | 24.65 | 0.00 | 100.01 | 100.13 |
| 2A-16-66 | 0.00 | 0.00 | 0.00 | 0.00 | 0.00 | 0.00 | 0.00 | 49.63 | 24.95 | 25.42 | 0.00 | 100.00 | 100.16 |
| 2A-16-68 | 0.00 | 0.00 | 0.00 | 0.00 | 0.00 | 0.00 | 0.00 | 49.65 | 25.37 | 24.99 | 0.00 | 100.01 | 100.11 |
| 2B2-2-1 | 0.00 | 0.00 | 0.00 | 0.00 | 0.00 | 0.00 | 0.00 | 49.76 | 25.35 | 24.89 | 0.00 | 100.00 | 99.60 |
| 2B2-3-6 | 0.00 | 0.00 | 0.00 | 0.00 | 0.00 | 0.00 | 0.00 | 49.63 | 25.41 | 24.96 | 0.00 | 100.00 | 98.81 |
| 2B2-4-12 | 0.00 | 0.00 | 0.00 | 0.00 | 0.00 | 0.00 | 0.00 | 50.18 | 25.49 | 24.33 | 0.00 | 100.00 | 97.89 |
| 2B2-5-20 | 0.00 | 0.00 | 0.00 | 0.00 | 0.00 | 0.00 | 0.00 | 49.57 | 25.47 | 24.96 | 0.00 | 100.00 | 99.62 |
| 2B2-7-25 | 0.00 | 0.00 | 0.00 | 0.00 | 0.00 | 0.00 | 0.00 | 49.64 | 25.26 | 25.09 | 0.00 | 100.00 | 100.59 |
| 2B2-9-38 | 0.00 | 0.00 | 0.00 | 0.00 | 0.00 | 0.00 | 0.00 | 49.75 | 26.04 | 24.20 | 0.00 | 100.00 | 99.27 |
| 2B2-9-41 | 0.00 | 0.00 | 0.00 | 0.00 | 0.00 | 0.00 | 0.00 | 49.88 | 25.36 | 24.76 | 0.00 | 100.00 | 99.81 |
| 2B2-12-67 | 0.00 | 0.00 | 0.00 | 0.00 | 0.00 | 0.00 | 0.00 | 49.74 | 25.05 | 25.21 | 0.00 | 100.00 | 99.56 |
| 2B2-14-73 | 0.00 | 0.00 | 0.00 | 0.00 | 0.00 | 0.00 | 0.00 | 49.74 | 24.99 | 25.27 | 0.00 | 100.00 | 99.47 |
| 2B2-14-76 | 0.00 | 0.00 | 0.00 | 0.00 | 0.00 | 0.00 | 0.00 | 50.00 | 24.24 | 23.55 | 2.20 | 100.00 | 100.28 |
| 2B2-15-77 | 0.00 | 0.00 | 0.00 | 0.00 | 0.00 | 0.00 | 0.00 | 49.57 | 24.25 | 24.37 | 1.82 | 100.00 | 100.62 |
| 2B2-15-79 | 0.00 | 0.00 | 0.00 | 0.00 | 0.00 | 0.00 | 0.00 | 49.89 | 25.20 | 24.91 | 0.00 | 100.00 | 99.67 |
| 2B2-17-85 | 0.00 | 0.00 | 0.00 | 0.00 | 0.00 | 0.00 | 0.00 | 50.34 | 24.78 | 24.87 | 0.00 | 100.00 | 97.97 |
| 2B2-18-97 | 0.00 | 0.00 | 0.00 | 0.00 | 0.00 | 0.00 | 0.00 | 49.76 | 24.87 | 25.36 | 0.00 | 100.00 | 100.30 |
| 2B2-18-99 | 0.00 | 0.00 | 0.00 | 0.00 | 0.00 | 0.00 | 0.00 | 49.76 | 25.33 | 24.91 | 0.00 | 100.00 | 99.14 |
| 2B2-20-106 | 0.00 | 0.00 | 0.00 | 0.00 | 0.00 | 0.00 | 0.00 | 49.67 | 25.38 | 24.95 | 0.00 | 100.00 | 99.18 |
| 2B2-20-108 | 0.00 | 0.00 | 0.00 | 0.26 | 0.00 | 0.00 | 0.00 | 49.64 | 24.97 | 25.13 | 0.00 | 100.00 | 100.08 |
| 3A1-5-19 | 0.00 | 0.00 | 0.00 | 0.00 | 0.00 | 0.00 | 0.00 | 50.40 | 24.99 | 24.61 | 0.00 | 100.00 | 97.21 |
| 3A1-5-20 | 0.00 | 0.00 | 0.00 | 0.00 | 0.00 | 0.00 | 0.00 | 49.91 | 25.10 | 24.99 | 0.00 | 100.00 | 99.46 |
| 3A1-6-22 | 0.00 | 0.00 | 0.00 | 0.00 | 0.00 | 0.00 | 0.00 | 50.21 | 25.06 | 24.74 | 0.00 | 100.01 | 98.04 |
| 3A1-6-23 | 3.37 | 0.00 | 0.00 | 0.00 | 0.00 | 0.00 | 0.00 | 48.59 | 23.42 | 23.60 | 1.02 | 100.00 | 100.19 |
| 3A1-6-24 | 0.00 | 0.00 | 0.00 | 0.00 | 0.00 | 0.00 | 0.00 | 50.11 | 24.32 | 24.51 | 1.07 | 100.01 | 99.87 |
| 3A1-6-25 | 0.00 | 0.00 | 0.00 | 0.00 | 0.00 | 0.00 | 0.00 | 50.17 | 24.38 | 24.44 | 1.01 | 100.00 | 99.30 |
| 3A1-6-27 | 0.00 | 0.00 | 0.00 | 0.00 | 0.00 | 0.00 | 0.00 | 50.06 | 24.87 | 25.07 | 0.00 | 100.00 | 97.98 |
| 3A1-8-35 | 0.00 | 0.00 | 0.00 | 0.00 | 0.00 | 0.00 | 0.00 | 49.76 | 25.00 | 24.52 | 0.71 | 99.99 | 99.44 |
| 3A1-9-40 | 0.00 | 0.00 | 0.00 | 0.00 | 0.00 | 0.00 | 0.00 | 50.33 | 25.23 | 24.44 | 0.00 | 100.00 | 98.54 |
| 3A1-10-45 | 0.00 | 0.00 | 0.00 | 0.00 | 0.00 | 0.00 | 0.00 | 50.13 | 24.83 | 25.04 | 0.00 | 100.00 | 99.69 |
| 3A1-13-66 | 0.00 | 0.00 | 0.00 | 0.00 | 0.00 | 0.00 | 0.00 | 49.75 | 25.09 | 25.16 | 0.00 | 100.00 | 98.70 |
| 3A1-13-67 | 0.00 | 0.00 | 0.00 | 0.00 | 0.00 | 0.00 | 0.00 | 50.33 | 24.89 | 24.78 | 0.00 | 100.00 | 97.28 |
| 2A-4-11 | 0.00 | 0.00 | 0.00 | 0.00 | 0.00 | 0.00 | 0.19 | 51.47 | 25.89 | 22.44 | 0.00 | 99.99 | 98.95 |
| 2A-8-23 | 0.00 | 0.00 | 0.00 | 0.00 | 0.00 | 0.00 | 0.00 | 50.43 | 24.58 | 24.98 | 0.00 | 99.99 | 98.85 |
| 2A-8-24 | 0.00 | 0.00 | 0.00 | 0.00 | 0.00 | 0.00 | 0.00 | 50.16 | 25.01 | 24.83 | 0.00 | 100.00 | 98.32 |
| 2A-10-31 | 0.00 | 0.00 | 0.00 | 0.00 | 0.00 | 0.00 | 0.00 | 49.79 | 25.08 | 25.13 | 0.00 | 100.00 | 99.13 |
| 2A-10-32 | 0.00 | 0.00 | 0.00 | 0.00 | 0.00 | 0.00 | 0.00 | 49.93 | 25.39 | 24.68 | 0.00 | 100.00 | 97.74 |
| 2A-11-34 | 0.47 | 0.00 | 0.00 | 0.00 | 0.00 | 0.00 | 0.00 | 49.77 | 24.99 | 24.77 | 0.00 | 100.00 | 98.57 |
| 2A-11-37 | 0.00 | 0.00 | 0.00 | 0.00 | 0.00 | 0.00 | 0.00 | 50.16 | 25.66 | 24.19 | 0.00 | 100.01 | 98.72 |
| 2A-11-38 | 21.58 | 3.13 | 2.64 | 3.08 | 0.00 | 0.00 | 0.00 | 33.31 | 18.84 | 17.43 | 0.00 | 100.01 | 100.08 |
| 2A2-6-26 | 0.00 | 0.00 | 0.00 | 0.00 | 0.00 | 0.00 | 0.00 | 49.69 | 25.40 | 24.91 | 0.00 | 100.00 | 99.69 |
| 2A2-6-28 | 0.00 | 0.00 | 0.00 | 0.00 | 0.00 | 0.00 | 0.00 | 49.79 | 24.99 | 25.22 | 0.00 | 100.00 | 100.04 |
| 2A2-7-29 | 0.00 | 0.00 | 0.00 | 0.00 | 0.00 | 0.00 | 0.00 | 50.01 | 25.10 | 24.89 | 0.00 | 100.00 | 99.80 |
| 2A2-7-30 | 0.00 | 0.00 | 0.00 | 0.00 | 0.00 | 0.00 | 0.00 | 50.03 | 25.11 | 24.87 | 0.00 | 100.01 | 99.13 |
| n=60 | | | | | | | | | | | | | |
| Maximum value | 21.58 | 3.13 | 2.64 | 3.08 | 0.19 | 0.21 | 0.19 | 51.47 | 26.04 | 27.98 | 2.20 | 100.01 | 103.89 |
| Minimum value | 0.00 | 0.00 | 0.00 | 0.00 | 0.00 | 0.00 | 0.00 | 33.31 | 18.84 | 17.43 | 0.00 | 99.99 | 96.73 |
| Average | 0.42 | 0.05 | 0.04 | 0.06 | 0.00 | 0.00 | 0.00 | 49.56 | 24.85 | 24.87 | 0.13 | 100.00 | 99.51 |
| Standard deviation | 2.79 | 0.40 | 0.34 | 0.40 | 0.02 | 0.03 | 0.02 | 2.21 | 0.94 | 1.39 | 0.42 | - | - |
| 2σ | 1.01 | 0.15 | 0.12 | 0.14 | 0.01 | 0.01 | 0.01 | 0.80 | 0.34 | 0.50 | 0.15 | - | - |

Table 4. Sphalerite.

| Sample | O | Si | S | Fe | Cu | Zn | Cd | Σ at% | Σ wt% |
|---|---|---|---|---|---|---|---|---|---|
| 1867A-2-4 | 2.35 | 0.00 | 47.43 | 5.70 | 0.00 | 44.52 | 0.00 | 100 | 103.71 |
| 1867A-2-13 | 0.00 | 0.00 | 50.13 | 6.31 | 0.00 | 43.56 | 0.00 | 100 | 100.00 |
| 1867A-2-14 | 2.60 | 0.00 | 48.82 | 5.22 | 0.00 | 43.36 | 0.00 | 100 | 103.46 |
| 1867A-3-23 | 0.00 | 0.00 | 48.92 | 6.27 | 0.00 | 44.81 | 0.00 | 100 | 102.61 |
| 1867A-5-45 | 0.00 | 0.00 | 48.54 | 5.93 | 0.00 | 45.53 | 0.00 | 100 | 103.79 |
| 1867A-6-55 | 0.00 | 0.00 | 49.34 | 5.69 | 0.00 | 44.96 | 0.00 | 99.99 | 100.63 |
| 1867A-6-56 | 0.00 | 0.00 | 48.56 | 5.85 | 0.00 | 44.96 | 0.63 | 100 | 102.21 |
| 1867A-6-58 | 0.00 | 0.00 | 48.82 | 5.98 | 0.00 | 44.70 | 0.50 | 100 | 101.88 |
| 1867A-6-59 | 0.00 | 0.00 | 49.02 | 5.39 | 0.00 | 45.06 | 0.54 | 100.01 | 103.06 |
| 1915A-2-7 | 2.81 | 0.00 | 48.08 | 5.04 | 3.70 | 40.36 | 0.00 | 100 | 101.17 |
| 1915A-2-9 | 2.25 | 0.00 | 48.07 | 2.48 | 0.74 | 46.46 | 0.00 | 100 | 102.67 |
| 1915A-9-29 | 0.00 | 0.00 | 49.39 | 2.15 | 0.00 | 48.46 | 0.00 | 100 | 100.18 |
| 1915A-9-31 | 2.09 | 0.00 | 48.24 | 2.29 | 0.00 | 47.38 | 0.00 | 100 | 100.53 |
| 1915A-9-32 | 2.52 | 0.00 | 48.24 | 8.00 | 6.50 | 34.74 | 0.00 | 100 | 103.13 |
| 2B2-4-18 | 0.00 | 0.00 | 49.50 | 6.14 | 0.00 | 44.36 | 0.00 | 100 | 101.64 |
| 2B2-5-21 | 2.78 | 0.00 | 47.73 | 5.63 | 0.00 | 43.67 | 0.19 | 100 | 102.77 |
| 2B3-7-31 | 2.59 | 0.00 | 47.72 | 5.00 | 0.00 | 44.70 | 0.00 | 100 | 102.57 |
| 2B4-14-74 | 0.00 | 0.00 | 48.89 | 4.97 | 0.00 | 46.14 | 0.00 | 100 | 102.22 |
| 2B5-18-98 | 0.00 | 0.00 | 49.45 | 5.33 | 0.50 | 44.72 | 0.00 | 100 | 102.83 |
| 3A1-4-10 | 2.59 | 0.00 | 48.51 | 4.64 | 0.00 | 44.26 | 0.00 | 100 | 101.42 |
| 3A1-4-11 | 2.95 | 0.00 | 48.64 | 4.54 | 0.00 | 43.87 | 0.00 | 100 | 100.84 |
| 3A1-6-21 | 2.85 | 0.00 | 47.43 | 5.55 | 0.00 | 44.17 | 0.00 | 100 | 103.78 |
| 3A1-7-28 | 2.71 | 0.00 | 48.41 | 4.12 | 0.00 | 44.76 | 0.00 | 100 | 100.01 |
| 3A1-8-36 | 3.07 | 0.00 | 48.38 | 4.92 | 0.00 | 43.63 | 0.00 | 100 | 101.13 |
| 3A1-8-37 | 0.00 | 0.00 | 49.25 | 4.87 | 0.00 | 45.88 | 0.00 | 100 | 100.96 |
| 3A1-8-38 | 2.74 | 0.37 | 48.51 | 4.47 | 0.00 | 43.91 | 0.00 | 100 | 100.36 |
| 1923B-1-86 | 0.00 | 0.00 | 48.98 | 5.75 | 0.00 | 45.27 | 0.00 | 100 | 103.34 |
| 1923B-3-100 | 1.47 | 0.00 | 48.77 | 5.94 | 0.00 | 43.82 | 0.00 | 100 | 103.45 |
| n=28 | | | | | | | | | |
| Maximum value | 3.07 | 0.37 | 50.13 | 8.00 | 6.50 | 48.46 | 0.63 | 100.01 | 103.79 |
| Minimum value | 0.00 | 0.00 | 47.43 | 2.15 | 0.00 | 34.74 | 0.00 | 99.99 | 100.00 |
| Average | 1.37 | 0.01 | 48.63 | 5.15 | 0.41 | 44.36 | 0.07 | 100.00 | 102.01 |
| Standard deviation | 1.31 | 0.07 | 0.63 | 1.23 | 1.36 | 2.33 | 0.17 | - | - |
| 2σ | 0.69 | 0.04 | 0.34 | 0.65 | 0.72 | 1.24 | 0.09 | - | - |

Table 5. Galena.

| Sample | O | Al | Er | S | Fe | Cu | Pb | Σ at% | Σ wt% |
|---|---|---|---|---|---|---|---|---|---|
| 1915A-7-23 | 7.65 | 1.13 | 0.00 | 42.73 | 6.56 | 0.00 | 41.92 | 100.00 | 100.17 |
| 1915A-14-50 | 13.61 | 0.00 | 0.00 | 40.54 | 1.15 | 0.00 | 44.71 | 100.00 | 103.12 |
| 1915A-16-59 | 17.74 | 0.00 | 0.00 | 43.30 | 9.65 | 0.00 | 29.31 | 100.00 | 96.05 |
| 2A-9-24 | 6.73 | 0.00 | 0.00 | 44.36 | 0.00 | 0.00 | 48.91 | 100.00 | 102.04 |
| 2A-9-25 | 7.51 | 0.00 | 0.00 | 44.14 | 0.00 | 0.00 | 48.35 | 100.00 | 102.63 |
| 2A-13-42 | 6.69 | 0.00 | 0.00 | 43.65 | 0.00 | 0.00 | 49.65 | 99.99 | 102.05 |
| 2A-13-49 | 6.17 | 0.00 | 0.00 | 43.96 | 0.00 | 0.00 | 49.87 | 100.00 | 100.82 |
| 2A-15-58 | 5.49 | 0.00 | 0.90 | 43.74 | 2.22 | 0.00 | 47.64 | 99.99 | 103.89 |
| 2B2-10-45 | 7.58 | 0.00 | 0.00 | 43.56 | 0.00 | 0.00 | 48.87 | 100.00 | 101.79 |
| 2B2-10-48 | 7.40 | 0.00 | 0.00 | 43.45 | 1.16 | 0.00 | 48.00 | 100.00 | 103.21 |
| 2B2-10-53 | 6.55 | 0.00 | 0.00 | 44.22 | 0.00 | 0.00 | 49.23 | 100.00 | 100.7 |
| 2B2-11-55 | 6.94 | 0.00 | 0.00 | 44.29 | 0.00 | 0.00 | 48.77 | 100.00 | 101.67 |
| 2B2-13-69 | 7.14 | 0.00 | 0.00 | 43.38 | 1.34 | 0.00 | 48.15 | 100.00 | 102.19 |
| 2B2-13-71 | 7.79 | 0.00 | 0.00 | 43.68 | 0.00 | 0.00 | 48.53 | 100.00 | 101.3 |
| 2B2-17-86 | 8.02 | 0.00 | 0.00 | 43.76 | 0.00 | 0.00 | 48.22 | 100.00 | 102.33 |
| 2B2-17-89 | 7.34 | 0.00 | 0.00 | 44.16 | 0.00 | 0.00 | 48.50 | 100.00 | 101.6 |
| 2B2-17-91 | 8.32 | 0.00 | 0.00 | 41.92 | 1.36 | 1.85 | 46.55 | 100.00 | 102.86 |
| 1889A2-4-88 | 9.94 | 0.00 | 0.00 | 42.35 | 0.00 | 0.00 | 47.71 | 100.00 | 103.63 |
| 1889A2-4-91 | 11.28 | 0.00 | 0.00 | 42.00 | 0.00 | 0.00 | 46.72 | 100.00 | 103.52 |
| 1889A3-13-57 | 0.00 | 0.00 | 0.00 | 46.08 | 0.00 | 0.00 | 53.92 | 100.00 | 103.72 |
| 1889A3-9-28 | 7.08 | 0.00 | 0.00 | 43.46 | 2.72 | 0.00 | 46.73 | 100.00 | 103.98 |
| n=21 | | | | | | | | | |
| Maximum value | 17.74 | 1.13 | 0.90 | 46.08 | 9.65 | 1.85 | 53.92 | 100.00 | 103.98 |
| Minimum value | 0.00 | 0.00 | 0.00 | 40.54 | 0.00 | 0.00 | 29.31 | 99.99 | 96.05 |
| Average | 7.95 | 0.05 | 0.04 | 43.46 | 1.25 | 0.09 | 47.15 | 100.00 | 102.06 |
| Standard deviation | 3.27 | 0.24 | 0.19 | 1.10 | 2.41 | 0.39 | 4.54 | 0.00 | 1.72 |
| 2σ | 2.00 | - | 0.12 | 0.67 | 1.48 | - | 2.78 | 0.00 | 1.05 |

Table 6. Cobaltite

| Sample | S | Fe | Co | Ni | Cu | As | Σ at% | Σ wt% |
|---|---|---|---|---|---|---|---|---|
| 1872A-1-1 | 32.98 | 1.93 | 29.76 | 1.41 | 0.00 | 33.93 | 100.00 | 101.92 |
| 1872A-1-2 | 33.12 | 1.85 | 29.78 | 1.44 | 0.00 | 33.80 | 100.00 | 100.64 |
| 1872A-1-3 | 33.97 | 2.09 | 30.06 | 0.00 | 0.00 | 33.88 | 100.00 | 99.06 |
| 1872A-1-4 | 43.06 | 2.64 | 30.28 | 0.00 | 0.00 | 24.02 | 100.00 | 101.71 |
| 1872A-1-5 | 43.65 | 2.28 | 30.77 | 0.00 | 0.00 | 23.30 | 100.00 | 99.47 |
| 1872A-1-9 | 33.80 | 2.27 | 29.89 | 0.00 | 0.00 | 34.04 | 100.00 | 100.48 |
| 1872A-1-10 | 33.19 | 1.89 | 29.81 | 1.25 | 0.00 | 33.86 | 100.00 | 101.92 |
| 1872A-1-12 | 44.00 | 1.39 | 31.39 | 0.00 | 0.00 | 23.22 | 100.00 | 99.92 |
| 1872A-2-13 | 44.78 | 2.39 | 30.99 | 0.00 | 0.00 | 21.84 | 100.00 | 100.47 |
| 1872A-2-14 | 39.13 | 1.16 | 32.16 | 0.00 | 0.00 | 27.55 | 100.00 | 101.05 |
| 1872A-2-16 | 33.65 | 2.02 | 29.69 | 0.00 | 0.00 | 34.64 | 100.00 | 99.05 |
| 1872A-2-17 | 33.63 | 2.24 | 30.74 | 0.00 | 0.00 | 33.39 | 100.00 | 96.91 |
| 1872A-3-20 | 33.30 | 2.01 | 29.62 | 1.53 | 0.00 | 33.54 | 100.00 | 101.21 |
| 1872A-3-23 | 33.63 | 2.04 | 29.04 | 1.63 | 0.00 | 33.66 | 100.00 | 100.61 |
| 1872A-3-25 | 38.57 | 2.88 | 29.57 | 0.00 | 0.84 | 28.14 | 100.00 | 98.46 |
| 1872A-3-26 | 37.75 | 3.04 | 27.88 | 0.00 | 3.29 | 28.03 | 100.00 | 102.25 |
| 1872A-5-39 | 37.77 | 1.25 | 31.64 | 0.00 | 0.39 | 28.94 | 100.00 | 101.61 |
| 1872A-7-55 | 33.19 | 2.22 | 29.29 | 1.50 | 0.00 | 33.82 | 100.00 | 101.54 |
| 1872A-5-38 | 36.55 | 4.58 | 28.02 | 0.00 | 0.00 | 30.85 | 100.00 | 103.41 |
| 1872A-7-57 | 33.48 | 3.77 | 27.88 | 1.85 | 0.00 | 33.02 | 100.00 | 100.69 |
| 1872A-7-58 | 34.23 | 4.24 | 26.44 | 2.23 | 0.00 | 32.86 | 100.00 | 97.39 |
| 2A-7-17 | 33.23 | 2.08 | 30.29 | 1.16 | 0.00 | 33.25 | 100.01 | 103.28 |
| 3A1-5-17 | 33.61 | 2.38 | 30.27 | 0.57 | 0.00 | 33.17 | 100.00 | 102.46 |
| 1837A-1-320 | 32.62 | 2.56 | 28.42 | 2.39 | 0.00 | 34.02 | 100.00 | 101.83 |
| 1837A-8-350 | 33.66 | 1.00 | 31.51 | 0.00 | 0.00 | 33.83 | 100.00 | 100.09 |
| 1837A-8-351 | 33.08 | 1.02 | 31.62 | 0.00 | 0.00 | 34.29 | 100.00 | 99.11 |
| 1837A-11-358 | 32.90 | 0.91 | 31.55 | 0.00 | 0.00 | 34.63 | 100.00 | 98.92 |
| 1837A-11-359 | 32.93 | 1.09 | 31.63 | 0.00 | 0.00 | 34.35 | 100.00 | 102.22 |
| 1837A-12-361 | 32.49 | 1.02 | 31.50 | 0.90 | 0.00 | 34.08 | 100.00 | 103.75 |
| 1837A-13-363 | 33.11 | 0.88 | 31.20 | 0.79 | 0.00 | 34.02 | 100.00 | 103.97 |
| 1837A-14-365 | 33.22 | 0.82 | 31.73 | 0.00 | 0.00 | 34.24 | 100.00 | 102.31 |
| n=31 | | | | | | | | |
| Maximum value | 44.78 | 4.58 | 32.16 | 2.39 | 3.29 | 34.64 | 100.01 | 103.97 |
| Minimum value | 32.49 | 0.82 | 26.44 | 0.00 | 0.00 | 21.84 | 100.00 | 96.91 |
| Average | 35.43 | 2.06 | 30.14 | 0.60 | 0.15 | 31.62 | 100.00 | 100.89 |
| Standard deviation | 3.70 | 0.94 | 1.36 | 0.78 | 0.60 | 3.83 | - | - |
| 2σ | 1.86 | 0.47 | 0.69 | 0.39 | 0.30 | 1.93 | - | - |

Table 7. Arsenopyrite.

| Sample | S | Fe | Co | As | Σ at% | Σ wt% |
|---|---|---|---|---|---|---|
| 2A-3-4 | 31.39 | 27.18 | 6.36 | 35.08 | 100.01 | 102.76 |
| 2A-2-1 | 28.77 | 25.45 | 7.72 | 38.06 | 100.00 | 102.49 |
| 2A-3-6 | 31.37 | 26.65 | 6.66 | 35.32 | 100.00 | 102.55 |
| 2A-3-7 | 31.58 | 27.19 | 6.11 | 35.13 | 100.01 | 101.88 |
| 2A-4-9 | 28.30 | 23.94 | 9.43 | 38.33 | 100.00 | 102.61 |
| 2A-5-11 | 30.99 | 26.99 | 6.65 | 35.36 | 99.99 | 103.40 |
| 2A-5-13 | 27.28 | 22.72 | 9.04 | 36.27 | 100.00 | 103.66 |
| 2A-6-14 | 28.38 | 24.53 | 8.56 | 38.54 | 100.01 | 103.40 |
| 2A-11-33 | 28.51 | 24.56 | 8.87 | 38.06 | 100.00 | 103.41 |
| 2A-12-38 | 28.36 | 23.99 | 9.46 | 38.19 | 100 | 103.40 |
| 2A-14-53 | 31.31 | 26.58 | 6.79 | 35.32 | 100.00 | 103.29 |
| 2A-15-55 | 30.09 | 25.83 | 7.50 | 36.58 | 100.00 | 102.35 |
| 2A-15-57 | 31.24 | 26.59 | 6.52 | 35.65 | 100.00 | 102.54 |
| 3A1-2-2 | 29.29 | 25.56 | 7.97 | 37.18 | 100.00 | 103.46 |
| 3A1-2-3 | 29.40 | 25.52 | 7.58 | 37.50 | 100.00 | 102.39 |
| 3A1-11-49 | 32.01 | 27.23 | 6.16 | 34.59 | 99.99 | 102.77 |
| n=16 | | | | | | |
| Maximum value | 32.01 | 27.23 | 9.46 | 38.54 | 100.01 | 103.66 |
| Minimum value | 27.28 | 22.72 | 6.11 | 34.59 | 99.99 | 101.88 |
| Average | 29.89 | 25.66 | 7.59 | 36.57 | 100.00 | 102.90 |
| Standard deviation | 1.47 | 1.34 | 1.15 | 1.35 | - | - |
| 2σ | 1.03 | 0.94 | 0.80 | 0.95 | - | - |

Table 9. Co-bearing pyrite.

| Sample | O | S | Ca | Fe | Co | As | Σ at% | Σ wt% |
|---|---|---|---|---|---|---|---|---|
| 1915A-5-18 | 6.70 | 62.29 | 0.00 | 30.51 | 0.50 | 0.00 | 100.00 | 103.51 |
| 1915A-8-27 | 0.00 | 66.01 | 0.00 | 33.38 | 0.44 | 0.16 | 100.00 | 99.06 |
| 1915A-10-34 | 0.00 | 66.69 | 0.00 | 32.23 | 1.08 | 0.00 | 100.00 | 98.52 |
| 1915A-15-53 | 0.00 | 66.85 | 0.00 | 32.10 | 1.06 | 0.00 | 100.00 | 98.37 |
| 1915A-17-63 | 0.00 | 66.34 | 0.19 | 32.60 | 0.62 | 0.24 | 100.00 | 98.39 |
| 1915A-19-69 | 0.00 | 65.96 | 0.00 | 33.29 | 0.48 | 0.27 | 100.00 | 98.31 |
| 2B2-2-3 | 0.00 | 66.10 | 0.00 | 33.41 | 0.48 | 0.00 | 100.00 | 99.77 |
| 2B2-4-9 | 0.00 | 66.55 | 0.00 | 32.61 | 0.84 | 0.00 | 100.00 | 99.49 |
| 2B2-4-10 | 0.00 | 66.48 | 0.00 | 32.19 | 1.33 | 0.00 | 100.00 | 99.70 |
| 2B2-4-11 | 0.00 | 66.47 | 0.00 | 31.05 | 2.48 | 0.00 | 100.00 | 99.59 |
| 2B2-4-13 | 0.00 | 66.64 | 0.00 | 32.13 | 1.23 | 0.00 | 100.00 | 98.83 |
| 2B2-4-15 | 0.00 | 66.21 | 0.00 | 31.61 | 2.18 | 0.00 | 100.00 | 100.51 |
| 2B2-4-16 | 0.00 | 66.40 | 0.00 | 31.85 | 1.75 | 0.00 | 100.00 | 99.68 |
| 2B2-4-17 | 0.00 | 65.32 | 0.00 | 33.09 | 1.59 | 0.00 | 100.00 | 102.03 |
| 2B2-5-19 | 0.00 | 66.65 | 0.00 | 31.57 | 1.78 | 0.00 | 100.00 | 99.98 |
| 2B2-7-29 | 0.00 | 66.64 | 0.00 | 32.52 | 0.84 | 0.00 | 100.00 | 98.86 |
| 2B2-7-30 | 0.00 | 66.57 | 0.00 | 31.82 | 1.62 | 0.00 | 100.00 | 98.49 |
| 2B2-19-104 | 0.00 | 66.91 | 0.00 | 28.60 | 4.49 | 0.00 | 100.00 | 97.47 |
| 2B2-20-107 | 0.00 | 66.26 | 0.00 | 31.12 | 2.63 | 0.00 | 100.00 | 99.93 |
| 3A1-5-18 | 10.23 | 60.42 | 0.00 | 28.79 | 0.56 | 0.00 | 100.00 | 99.43 |
| 2A-4-8 | 0.00 | 66.61 | 0.00 | 32.85 | 0.54 | 0.00 | 100.00 | 100.29 |
| 2A-5-15 | 0.00 | 66.43 | 0.00 | 33.15 | 0.42 | 0.00 | 100.00 | 99.68 |
| 2A-7-18 | 0.00 | 66.51 | 0.00 | 33.01 | 0.48 | 0.00 | 100.00 | 99.65 |
| 2A2-1-1 | 0.00 | 66.19 | 0.00 | 33.33 | 0.48 | 0.00 | 100.00 | 99.48 |
| 2A2-1-4 | 0.00 | 53.00 | 0.00 | 46.48 | 0.52 | 0.00 | 100.00 | 99.43 |
| 2A2-2-5 | 0.00 | 66.16 | 0.00 | 33.41 | 0.43 | 0.00 | 100.00 | 99.73 |
| 2A2-2-6 | 0.00 | 53.11 | 0.00 | 46.19 | 0.70 | 0.00 | 100.00 | 100.15 |
| 2A2-3-14 | 7.07 | 61.09 | 0.00 | 31.45 | 0.38 | 0.00 | 100.00 | 101.05 |
| 2A2-10-43 | 0.00 | 66.29 | 0.00 | 32.75 | 0.97 | 0.00 | 100.01 | 99.93 |
| 2A2-12-53 | 7.00 | 61.17 | 0.00 | 31.44 | 0.39 | 0.00 | 100.00 | 101.43 |
| 2A2-12-54 | 7.62 | 61.00 | 0.00 | 30.96 | 0.42 | 0.00 | 100.00 | 101.54 |
| 1889A3-10-32 | 0.00 | 66.71 | 0.00 | 31.41 | 1.88 | 0.00 | 100.00 | 103.21 |
| n=32 | | | | | | | | |
| Maximum value | 10.23 | 66.91 | 0.19 | 46.48 | 4.49 | 0.27 | 100.01 | 103.51 |
| Minimum value | 0.00 | 53.00 | 0.00 | 28.60 | 0.38 | 0.00 | 100.00 | 97.47 |
| Average | 1.21 | 64.75 | 0.01 | 32.90 | 1.11 | 0.02 | 100.00 | 99.86 |
| Standard deviation | 2.88 | 3.80 | 0.00 | 3.95 | 0.94 | 0.05 | - | - |
| 2σ | 1.43 | 1.89 | - | 1.96 | 0.47 | 0.03 | - | - |

Table 10. Molybdenite.

| Sample | O | Na | Al | Si | K | S | Fe | Co | As | Mo | W | Pb | Σ at% | Σ wt% |
|---|---|---|---|---|---|---|---|---|---|---|---|---|---|---|
| 1872A-4-30 | 10.12 | 0.00 | 0.00 | 0.00 | 0.00 | 61.17 | 0.00 | 0.00 | 0.00 | 28.71 | 0.00 | 0.00 | 100.00 | 96.38 |
| 1872A-4-31 | 14.55 | 0.67 | 0.54 | 1.02 | 0.00 | 56.64 | 1.40 | 0.00 | 0.00 | 25.19 | 0.00 | 0.00 | 100.00 | 101.25 |
| 1872A-4-32 | 9.87 | 0.00 | 0.00 | 0.00 | 0.00 | 61.55 | 0.86 | 0.00 | 0.00 | 27.73 | 0.00 | 0.00 | 100.00 | 97.81 |
| 1872A-4-33 | 6.35 | 0.00 | 0.00 | 0.00 | 0.00 | 64.54 | 0.00 | 0.00 | 0.00 | 29.11 | 0.00 | 0.00 | 100.00 | 97.25 |
| 1872A-4-36 | 16.30 | 0.00 | 0.00 | 0.00 | 0.00 | 57.36 | 0.00 | 0.00 | 0.00 | 26.34 | 0.00 | 0.00 | 100.00 | 99.03 |
| 1872A-4-37 | 24.64 | 0.00 | 1.04 | 2.06 | 0.00 | 48.27 | 1.88 | 0.00 | 0.00 | 22.12 | 0.00 | 0.00 | 100.00 | 97.27 |
| 1872A-6-49 | 11.51 | 0.00 | 0.00 | 0.59 | 0.00 | 59.37 | 0.55 | 0.00 | 0.00 | 27.97 | 0.00 | 0.00 | 99.99 | 98.55 |
| 1872A-6-50 | 9.96 | 0.00 | 0.00 | 0.00 | 0.00 | 62.05 | 0.00 | 0.00 | 0.00 | 28.00 | 0.00 | 0.00 | 100.01 | 97.79 |
| 1915A-5-16 | 4.78 | 0.00 | 0.32 | 0.00 | 0.00 | 62.66 | 0.56 | 0.00 | 0.00 | 31.67 | 0.00 | 0.00 | 100.00 | 100.64 |
| 1915A-5-17 | 5.02 | 0.00 | 0.00 | 0.24 | 0.00 | 61.79 | 0.60 | 0.00 | 0.00 | 31.02 | 0.00 | 1.33 | 100.00 | 101.37 |
| 2A-10-31 | 6.09 | 0.00 | 0.00 | 0.00 | 0.00 | 62.82 | 0.00 | 0.71 | 0.18 | 30.19 | 0.00 | 0.00 | 99.99 | 100.09 |
| 2A-15-56 | 5.09 | 0.00 | 0.00 | 0.00 | 0.00 | 63.14 | 0.46 | 0.00 | 0.00 | 30.77 | 0.54 | 0.00 | 100.00 | 101.57 |
| 3A1-2-1 | 6.18 | 0.00 | 0.00 | 0.00 | 0.00 | 62.23 | 0.00 | 0.00 | 0.00 | 31.26 | 0.32 | 0.00 | 99.99 | 103.45 |
| 3A1-2-4 | 5.77 | 0.00 | 0.00 | 0.00 | 0.00 | 62.79 | 0.45 | 0.00 | 0.00 | 30.99 | 0.00 | 0.00 | 100.00 | 99.57 |
| 3A1-3-5 | 5.58 | 0.00 | 0.00 | 0.28 | 0.00 | 62.76 | 0.38 | 0.00 | 0.00 | 31.00 | 0.00 | 0.00 | 100.00 | 101.52 |
| 22A2-11-50 | 4.00 | 0.00 | 1.23 | 4.18 | 0.91 | 60.42 | 0.37 | 0.00 | 0.00 | 28.89 | 0.00 | 0.00 | 100.00 | 97.61 |
| 22A2-11-51 | 4.76 | 0.00 | 0.00 | 1.13 | 0.00 | 62.78 | 0.41 | 0.00 | 0.00 | 30.91 | 0.00 | 0.00 | 99.99 | 102.63 |
| n=17 | | | | | | | | | | | | | | |
| Maximum value | 24.64 | 0.67 | 1.23 | 4.18 | 0.91 | 64.54 | 1.88 | 0.71 | 0.18 | 31.67 | 0.54 | 1.33 | 100.01 | 103.45 |
| Minimum value | 4.00 | 0.00 | 0.00 | 0.00 | 0.00 | 48.27 | 0.00 | 0.00 | 0.00 | 22.12 | 0.00 | 0.00 | 99.99 | 96.38 |
| Average | 8.86 | 0.04 | 0.18 | 0.56 | 0.05 | 60.73 | 0.47 | 0.04 | 0.01 | 28.93 | 0.05 | 0.08 | 100.00 | 99.63 |
| Standard deviation | 5.29 | 0.16 | 0.38 | 1.06 | 0.21 | 3.70 | 0.51 | 0.17 | 0.04 | 2.49 | 0.14 | 0.31 | - | - |
| 2σ | 3.60 | 0.11 | 0.26 | 0.72 | 0.15 | 2.52 | 0.35 | 0.11 | 0.03 | 1.69 | 0.10 | 0.21 | - | - |

Table 11. Bismuthinite.

| Sample | O | Al | Si | S | Fe | Co | Ni | Cu | Zn | As | Tc | Sb | Bi | Σ at% | Σ wt% |
|---|---|---|---|---|---|---|---|---|---|---|---|---|---|---|---|
| 2A-13-41 | 5.56 | 0.96 | 0.00 | 52.58 | 1.04 | 0.00 | 0.00 | 0.00 | 0.00 | 0.00 | 10.18 | 0.00 | 29.69 | 100.00 | 101.89 |
| 2A-14-51 | 7.47 | 0.00 | 0.00 | 53.93 | 1.33 | 0.00 | 0.00 | 1.53 | 0.00 | 0.00 | 0.00 | 0.00 | 35.73 | 99.99 | 97.49 |
| 2A-14-52 | 8.52 | 0.00 | 0.00 | 54.69 | 0.00 | 0.00 | 0.00 | 0.60 | 0.00 | 0.00 | 0.00 | 0.00 | 36.20 | 100.01 | 97 |
| 2A-15-59 | 9.40 | 0.00 | 0.00 | 40.22 | 2.41 | 0.00 | 0.00 | 0.00 | 0.00 | 0.39 | 0.00 | 0.00 | 47.57 | 99.99 | 100.89 |
| 2A-15-60 | 6.43 | 0.00 | 0.00 | 55.67 | 1.68 | 0.00 | 0.00 | 0.00 | 0.00 | 0.00 | 0.00 | 0.00 | 36.21 | 99.99 | 97.13 |
| 2B2-17-90 | 7.26 | 0.00 | 0.00 | 52.83 | 0.00 | 0.00 | 0.00 | 1.12 | 0.00 | 0.00 | 10.31 | 0.00 | 28.48 | 100.00 | 98.24 |
| 2B2-17-93 | 9.95 | 0.00 | 0.00 | 38.66 | 0.00 | 0.00 | 0.00 | 0.00 | 0.00 | 0.00 | 0.00 | 0.00 | 51.39 | 100.00 | 98.41 |
| 3A1-7-31 | 9.34 | 0.00 | 1.13 | 52.39 | 0.00 | 0.00 | 0.00 | 0.00 | 3.71 | 0.00 | 0.00 | 0.00 | 33.43 | 100.00 | 99.12 |
| 1837A-13-364 | 5.86 | 0.00 | 0.00 | 52.27 | 0.00 | 3.29 | 0.22 | 0.00 | 0.00 | 0.00 | 8.48 | 0.62 | 29.27 | 100.00 | 102.8 |
| 1837A-14-366 | 19.99 | 0.00 | 0.00 | 42.43 | 1.19 | 2.68 | 0.00 | 4.89 | 0.00 | 0.00 | 0.00 | 0.00 | 28.82 | 100.00 | 103.17 |
| n=10 | | | | | | | | | | | | | | | |
| Maximum value | 19.99 | 0.96 | 1.13 | 55.67 | 2.41 | 3.29 | 0.22 | 4.89 | 3.71 | 0.39 | 10.31 | 0.62 | 51.39 | 100.01 | 103.17 |
| Minimum value | 5.56 | 0.00 | 0.00 | 38.66 | 0.00 | 0.00 | 0.00 | 0.00 | 0.00 | 0.00 | 0.00 | 0.00 | 28.48 | 99.99 | 97.00 |
| Average | 8.98 | 0.10 | 0.11 | 49.57 | 0.76 | 0.60 | 0.02 | 0.81 | 0.37 | 0.04 | 2.90 | 0.06 | 35.68 | 100.00 | 99.61 |
| Standard deviation | 3.95 | 0.29 | 0.34 | 6.12 | 0.84 | 1.20 | 0.07 | 1.46 | 1.11 | 0.12 | 4.45 | 0.19 | 7.55 | - | - |
| 2σ | 3.50 | 0.25 | 0.30 | 5.43 | 0.74 | 1.07 | 0.06 | 1.29 | 0.99 | 0.10 | 3.95 | 0.17 | 6.70 | - | - |

Table 12. Skutterudite.

| Sample | S | Fe | Co | As | Σ at% | Σ wt% |
|---|---|---|---|---|---|---|
| 2A-4-8 | 0.61 | 0.8 | 24.28 | 74.31 | 100 | 105 |
| 2A-10-30 | 0.51 | 0.83 | 23.91 | 74.76 | 100 | 105.11 |
| 2A-12-37 | 0.56 | 0.76 | 24.4 | 74.28 | 100 | 105.79 |
| 2A-12-39 | 0.58 | 0.61 | 24.4 | 74.4 | 100 | 104.06 |
| n=4 | | | | | | |
| Maximum value | 0.61 | 0.83 | 24.40 | 74.76 | 100.01 | 105.79 |
| Minimum value | 0.51 | 0.61 | 23.91 | 74.28 | 99.99 | 104.06 |
| Average | 0.57 | 0.75 | 24.25 | 74.44 | 100.00 | 104.99 |
| Standard deviation | 0.04 | 0.08 | 0.20 | 0.19 | - | - |
| 2σ | 0.05 | 0.12 | 0.28 | 0.27 | - | - |

Table 13. Pentlandite.

| Sample | S | Fe | Co | Ni | Σ at% | Σ wt% |
|---|---|---|---|---|---|---|
| 1988A2-3-5 | 46.98 | 6.01 | 44.47 | 2.54 | 100 | 100.2 |
| 1988A2-3-6 | 46.7 | 4.6 | 45.57 | 3.13 | 100 | 99.93 |
| 1988A2-4-9 | 47.56 | 8.33 | 41.58 | 2.53 | 100 | 101.76 |
| 1988A2-4-10 | 46.58 | 4.73 | 45.69 | 3 | 100 | 99.63 |
| 1988A2-4-11 | 46.59 | 5.01 | 45.5 | 2.9 | 100 | 101.19 |
| 1988A2-4-12 | 46.46 | 4.67 | 45.76 | 3.11 | 100 | 101.02 |
| 1988A2-6-19 | 46.83 | 4.26 | 45.85 | 3.05 | 99.99 | 100.76 |
| 1988A2-6-22 | 46.62 | 4.19 | 46.07 | 3.12 | 100 | 100.75 |
| 1988A2-8-25 | 46.94 | 4.18 | 45.75 | 3.13 | 100 | 100.21 |
| 1988A2-8-26 | 47.82 | 7.87 | 42.26 | 2.06 | 100.01 | 98.66 |
| 1988A2-8-27 | 46.84 | 6.47 | 43.93 | 2.75 | 99.99 | 99.69 |
| 1988A2-9-31 | 46.7 | 6.34 | 44.57 | 2.39 | 100 | 100.58 |
| 1988A2-9-32 | 48.17 | 15.13 | 34.76 | 1.94 | 100 | 99.69 |
| 1988A2-10-34 | 46.99 | 4.1 | 46.13 | 2.77 | 99.99 | 100.94 |
| 1988A2-10-35 | 46.89 | 4.37 | 45.48 | 3.26 | 100 | 100.57 |
| 1988A2-12-38 | 47.27 | 6.15 | 44.24 | 2.34 | 100 | 100.47 |
| 1988A2-12-39 | 46.95 | 4.43 | 46.18 | 2.44 | 100 | 100.53 |
| 1988A2-12-40 | 46.96 | 5.15 | 45.2 | 2.69 | 100 | 100.65 |
| 1988A2-13-42 | 47.05 | 5.02 | 44.79 | 3.14 | 100 | 101.08 |
| 1988A2-13-44 | 47.08 | 5.15 | 44.88 | 2.9 | 100.01 | 100 |
| 1988A2-14-56 | 46.98 | 4.74 | 45.72 | 2.55 | 99.99 | 99.68 |
| n=21 | | | | | | |
| Maximum value | 48.17 | 5.15 | 45.72 | 3.14 | 100.01 | 101.08 |
| Minimum value | 46.46 | 4.74 | 44.79 | 2.55 | 99.99 | 99.68 |
| Average | 47.00 | 5.02 | 45.15 | 2.82 | 100.00 | 100.35 |
| Standard deviation | 0.41 | 0.17 | 0.36 | 0.22 | - | - |
| 2σ | 0.25 | 0.10 | 0.22 | 0.14 | - | - |

Table 14. Carrolite.

| Sample | S | Fe | Co | Ni | Cu | Σ at% | Σ wt% |
|---|---|---|---|---|---|---|---|
| 1872A-1-7 | 56.18 | 0.99 | 29.24 | 0.00 | 13.59 | 100.00 | 100.36 |
| 1872A-3-21 | 56.96 | 0.00 | 28.84 | 0.00 | 14.20 | 100.00 | 99.1 |
| 1872A-3-22 | 55.91 | 0.81 | 28.99 | 0.00 | 14.28 | 100.00 | 100.55 |
| 1872A-3-28 | 56.74 | 0.00 | 29.19 | 0.00 | 14.07 | 100.00 | 98.83 |
| 1872A-4-34 | 56.37 | 1.23 | 29.94 | 0.00 | 12.46 | 100.00 | 97.6 |
| 1872A-5-40 | 56.40 | 0.00 | 31.00 | 0.00 | 12.60 | 100.00 | 100.56 |
| 1872A-5-41 | 56.00 | 0.00 | 32.12 | 0.00 | 11.88 | 100.00 | 101.15 |
| 1872A-6-47 | 55.93 | 0.00 | 31.97 | 0.00 | 12.10 | 100.00 | 102.66 |
| 1872A-6-48 | 55.94 | 0.00 | 31.96 | 0.00 | 12.10 | 100.00 | 102.77 |
| 1872A-6-51 | 56.07 | 0.00 | 31.52 | 0.00 | 12.41 | 100.00 | 101.4 |
| 1872A-7-56 | 55.29 | 0.00 | 29.04 | 1.17 | 14.49 | 100.00 | 102.61 |
| 1872A-7-59 | 56.00 | 0.00 | 29.55 | 0.00 | 14.45 | 100.00 | 98.62 |
| 1872A-8-64 | 56.31 | 0.00 | 31.51 | 0.00 | 12.18 | 100.00 | 100.75 |
| 1872A-8-65 | 55.92 | 0.00 | 31.78 | 0.00 | 12.30 | 100.00 | 102.94 |
| n=14 | | | | | | | |
| Maximum value | 56.96 | 1.23 | 32.12 | 1.17 | 14.49 | 100.00 | 102.94 |
| Minimum value | 55.29 | 0.00 | 28.84 | 0.00 | 11.88 | 100.00 | 97.60 |
| Average | 56.15 | 0.22 | 30.48 | 0.08 | 13.08 | 100.00 | 100.71 |
| Standard deviation | 0.39 | 0.42 | 1.27 | 0.30 | 0.99 | - | - |
| 2σ | 0.29 | 0.32 | 0.95 | 0.23 | 0.74 | - | - |

Table 15. Willyamite, costibite and ullmannite.

| Sample | O | Al | Si | S | Fe | Co | Ni | Zn | Tc | Sb | Bi | Σ at% | Σ wt% |
|---|---|---|---|---|---|---|---|---|---|---|---|---|---|
| 2B2-10-51 | 2.84 | 0.00 | 0.00 | 33.04 | 2.84 | 20.57 | 8.98 | 0.00 | 0.00 | 31.72 | 0.00 | 100.00 | 99.66 |
| 2B2-10-52 | 5.04 | 0.00 | 0.00 | 30.64 | 4.01 | 17.69 | 10.17 | 0.00 | 1.30 | 31.16 | 0.00 | 100.00 | 97.65 |
| 3A1-8-34 | 0.00 | 0.00 | 0.71 | 32.39 | 0.48 | 28.61 | 3.14 | 1.03 | 0.00 | 33.65 | 0.00 | 100.01 | 100.90 |
| 3A2-8-39 | 0.00 | 0.00 | 0.75 | 32.29 | 0.70 | 29.41 | 1.82 | 1.16 | 0.00 | 33.87 | 0.00 | 100.00 | 101.13 |
| 3A3-9-41 | 1.60 | 0.00 | 0.37 | 32.01 | 1.12 | 28.12 | 3.61 | 0.00 | 0.00 | 33.16 | 0.00 | 99.99 | 102.18 |
| 3A4-9-42 | 0.00 | 0.00 | 0.00 | 32.16 | 0.70 | 29.57 | 3.16 | 0.00 | 0.00 | 34.42 | 0.00 | 100.01 | 100.96 |
| 3A5-9-43 | 2.47 | 0.00 | 1.56 | 31.52 | 1.33 | 26.27 | 4.19 | 0.00 | 0.00 | 32.65 | 0.00 | 99.99 | 98.61 |
| 3A6-9-44 | 5.21 | 0.00 | 4.60 | 29.21 | 0.73 | 19.08 | 10.33 | 0.00 | 0.00 | 29.38 | 1.46 | 100.00 | 101.42 |
| 3A7-10-46 | 0.00 | 0.00 | 0.00 | 32.39 | 1.59 | 31.07 | 1.07 | 0.00 | 0.00 | 33.87 | 0.00 | 99.99 | 101.41 |
| 1889A2-4-87 | 0.00 | 0.00 | 0.00 | 33.10 | 0.00 | 30.43 | 2.38 | 0.00 | 0.00 | 34.08 | 0.00 | 99.99 | 101.99 |
| 1889A2-5-94 | 0.00 | 0.00 | 0.00 | 33.07 | 0.00 | 30.59 | 2.30 | 0.00 | 0.00 | 34.03 | 0.00 | 99.99 | 103.05 |
| 1889A3-10-36 | 0.00 | 0.00 | 0.00 | 33.35 | 1.40 | 30.66 | 0.00 | 0.00 | 0.00 | 34.59 | 0.00 | 100.00 | 102.19 |
| 1889A3-11-42 | 0.00 | 0.00 | 0.00 | 32.83 | 0.00 | 30.73 | 2.01 | 0.00 | 0.00 | 34.43 | 0.00 | 100.00 | 103.96 |
| 1889A3-12-50 | 1.90 | 0.00 | 0.00 | 32.84 | 0.00 | 31.24 | 0.00 | 0.00 | 0.00 | 34.01 | 0.00 | 99.99 | 102.70 |
| 1923B-3-98 | 2.06 | 1.37 | 0.00 | 1.48 | 27.08 | 3.34 | 0.00 | 0.00 | 0.00 | 32.85 | 0.00 | 68.18 | 103.63 |
| 1923B-4-106 | 2.46 | 1.06 | 0.00 | 1.62 | 28.74 | 0.00 | 0.00 | 0.00 | 0.00 | 33.00 | 0.00 | 66.89 | 101.99 |
| n=16 | | | | | | | | | | | | | |
| Maximum value | 5.21 | 1.37 | 4.60 | 33.35 | 28.74 | 31.24 | 10.33 | 1.16 | 1.30 | 34.59 | 1.46 | 100.01 | 103.96 |
| Minimum value | 0.00 | 0.00 | 0.00 | 1.48 | 0.00 | 0.00 | 0.00 | 0.00 | 0.00 | 29.38 | 0.00 | 66.89 | 97.65 |
| Average | 1.47 | 0.15 | 0.50 | 28.37 | 4.42 | 24.21 | 3.32 | 0.14 | 0.08 | 33.18 | 0.09 | 95.94 | 101.46 |
| Standard deviation | 1.74 | 0.41 | 1.14 | 10.19 | 8.95 | 9.55 | 3.39 | 0.36 | 0.31 | 1.36 | 0.35 | - | - |
| 2σ | 1.22 | 0.28 | 0.80 | 7.15 | 6.28 | 6.70 | 2.38 | 0.25 | 0.22 | 0.95 | 0.25 | - | - |

Table 16. Native Bi.

| Sample | O | Al | S | Fe | Co | Ni | Zn | As | Sb | Pb | Bi | Σ at% | Σ wt% |
|---|---|---|---|---|---|---|---|---|---|---|---|---|---|
| 2A-10-32 | 23.47 | 0.00 | 0.00 | 0.00 | 2.90 | 0.00 | 0.00 | 1.25 | 0.00 | 0.00 | 72.38 | 100.00 | 103.46 |
| 2A-13-45 | 16.84 | 2.09 | 0.00 | 0.00 | 0.00 | 0.00 | 0.00 | 0.00 | 0.00 | 0.00 | 81.07 | 100.00 | 102.42 |
| 2A-13-46 | 14.94 | 2.26 | 0.00 | 0.00 | 0.00 | 0.00 | 0.00 | 0.00 | 0.00 | 0.00 | 82.81 | 100.01 | 101.87 |
| 2A-15-61 | 17.20 | 0.00 | 0.00 | 4.87 | 1.86 | 0.00 | 0.00 | 5.55 | 0.00 | 0.00 | 70.51 | 99.99 | 98.10 |
| 2B2-10-42 | 15.27 | 0.00 | 0.00 | 0.00 | 0.00 | 0.00 | 0.00 | 0.00 | 0.00 | 0.00 | 84.73 | 100.00 | 102.88 |
| 2B3-10-44 | 21.30 | 0.00 | 0.00 | 0.00 | 0.00 | 0.00 | 0.00 | 0.00 | 0.00 | 0.00 | 78.70 | 100.00 | 102.47 |
| 2B4-10-46 | 29.18 | 0.00 | 0.00 | 0.00 | 0.00 | 0.00 | 0.00 | 0.00 | 0.00 | 0.00 | 70.82 | 100.00 | 100.72 |
| 2B5-10-49 | 22.48 | 0.00 | 0.00 | 2.15 | 0.00 | 0.00 | 0.00 | 0.00 | 0.00 | 0.00 | 75.37 | 100.00 | 102.90 |
| 2B6-10-50 | 25.25 | 0.00 | 7.69 | 0.00 | 0.00 | 0.00 | 0.00 | 0.00 | 0.00 | 0.00 | 67.05 | 100.00 | 101.63 |
| 2B7-11-56 | 24.22 | 0.00 | 0.00 | 0.00 | 0.00 | 0.00 | 2.84 | 0.00 | 0.00 | 0.00 | 72.94 | 100.00 | 100.43 |
| 2B8-11-57 | 22.91 | 0.00 | 0.00 | 0.00 | 0.00 | 0.00 | 0.00 | 0.00 | 0.00 | 0.00 | 77.09 | 100.00 | 102.49 |
| 2B9-11-58 | 23.12 | 0.00 | 0.00 | 0.00 | 0.00 | 0.00 | 0.00 | 0.00 | 0.00 | 0.00 | 76.88 | 100.00 | 102.63 |
| 2B10-11-61 | 27.92 | 0.00 | 0.00 | 0.00 | 0.00 | 0.00 | 0.00 | 0.00 | 0.00 | 0.00 | 72.08 | 100.00 | 96.52 |
| 3A1-7-29 | 13.25 | 0.00 | 0.00 | 0.00 | 0.00 | 0.00 | 8.71 | 0.00 | 0.00 | 0.00 | 78.04 | 100.00 | 103.17 |
| 3A1-11-51 | 28.24 | 0.00 | 8.55 | 5.23 | 2.44 | 1.68 | 0.00 | 0.00 | 0.00 | 3.66 | 50.21 | 100.01 | 103.04 |
| 1837A-1-323 | 21.02 | 0.00 | 0.00 | 0.00 | 0.00 | 0.00 | 0.00 | 0.00 | 2.43 | 0.00 | 76.55 | 100.00 | 100.31 |
| 1837A-1-325 | 23.63 | 0.00 | 0.00 | 0.00 | 0.00 | 0.00 | 0.00 | 0.00 | 1.75 | 0.00 | 74.61 | 100.00 | 103.14 |
| n=17 | | | | | | | | | | | | | |
| Maximum value | 29.18 | 2.26 | 8.55 | 5.23 | 2.90 | 1.68 | 8.71 | 5.55 | 2.43 | 3.66 | 84.73 | 100.01 | 103.46 |
| Minimum value | 13.25 | 0.00 | 0.00 | 0.00 | 0.00 | 0.00 | 0.00 | 0.00 | 0.00 | 0.00 | 50.21 | 99.99 | 96.52 |
| Average | 21.78 | 0.26 | 0.96 | 0.72 | 0.42 | 0.10 | 0.68 | 0.40 | 0.25 | 0.22 | 74.23 | 100.00 | 101.66 |
| Standard deviation | 4.67 | 0.70 | 2.62 | 1.66 | 0.93 | 0.40 | 2.12 | 1.32 | 0.68 | 0.86 | 7.48 | 0.00 | 1.86 |
| 2σ | 3.18 | 0.48 | 1.78 | 1.13 | 0.63 | 0.27 | 1.44 | 0.90 | 0.47 | 0.59 | 5.09 | 0.00 | 1.27 |

Table 17. Monazite.

| Sample | ALZ190015A-1 | VNA002A | | VNA002B2 | VNA003A1 | ALZ190037A-1 |
|---|---|---|---|---|---|---|
| Analysis | MNZ-1 | MNZ-2 | MNZ-3 | MNZ-4 | MNZ-5 | MNZ-6 |
| $P_2O_5$ | 28.28 | 29.52 | 29.97 | 27.38 | 29.74 | 30.27 |
| $SIO_2$ | 0.75 | | 0.34 | 1.50 | - | - |
| $ThO_2$ | - | - | - | 7.67 | - | - |
| $UO_2$ | - | - | 0.93 | 0.00 | - | - |
| $Y_2O_3$ | - | - | 1.54 | 1.99 | 2.78 | - |
| $La_2O_3$ | 15.25 | 16.37 | 15.97 | 13.99 | 15.43 | 32.58 |
| $Ce_2O_3$ | 33.10 | 31.91 | 31.10 | 28.60 | 29.66 | 29.54 |
| $Pr_2O_3$ | 3.48 | 3.52 | 2.93 | 3.39 | 2.96 | 0.00 |
| $Nd_2O_3$ | 12.49 | 12.19 | 11.38 | 11.33 | 11.93 | 4.39 |
| $Sm_2O_3$ | 2.19 | 2.19 | 2.40 | 2.06 | 1.88 | - |
| $Gd_2O_3$ | 1.63 | 2.20 | 1.69 | 1.98 | 1.63 | - |
| CaO | 0.34 | 0.25 | 0.62 | 0.64 | 0.60 | 0.55 |
| $Ag_2O$ | 1.40 | 0.44 | 1.21 | - | 1.39 | - |
| Total | 98.89 | 98.59 | 100.09 | 100.55 | 98.00 | 97.32 |
| Formula based on: | | 4 oxygens | | | | |
| P | 0.97 | 1.10 | 1.08 | 0.92 | 1.00 | 1.04 |
| Si | 0.03 | - | 0.01 | 0.06 | - | - |
| Th | - | 0.00 | - | 0.07 | - | - |
| U | - | 0.00 | 0.01 | - | - | - |
| Y | - | 0.00 | 0.03 | 0.04 | 0.06 | - |
| La | 0.23 | 0.27 | 0.25 | 0.21 | 0.23 | 0.49 |
| Ce | 0.49 | 0.52 | 0.49 | 0.42 | 0.43 | 0.44 |
| Pr | 0.05 | 0.06 | 0.05 | 0.05 | 0.04 | - |
| Nd | 0.18 | 0.19 | 0.17 | 0.16 | 0.17 | 0.06 |
| Sm | 0.03 | 0.03 | 0.04 | 0.03 | 0.03 | - |
| Gd | 0.02 | 0.03 | 0.02 | 0.03 | 0.02 | - |
| Ca | 0.01 | 0.01 | 0.03 | 0.03 | 0.03 | 0.02 |
| Ag | 0.03 | 0.01 | 0.03 | - | 0.03 | - |
| Total | 2.04 | 2.22 | 2.21 | 2.01 | 2.03 | 2.06 |
| La/(La+Ce) | 0.32 | 0.34 | 0.34 | 0.33 | 0.34 | 0.53 |
| Name | monazite-(Ce) | monazite-(Ce) | monazite-(Ce) | monazite-(Ce) | monazite-(Ce) | monazite-(La) |

Table 18. Allanite.

| Sample | ALZ190037A-1 | | | | |
|---|---|---|---|---|---|
| Analysis | AL-01 | AL-02 | AL-03 | AL-04 | AL-05 |
| $SIO_2$ | 33.16 | 35.81 | 32.15 | 33.20 | 33.24 |
| $AL_2O_3$ | 17.52 | 20.48 | 17.69 | 19.69 | 18.44 |
| FeO | 12.22 | 10.86 | 12.21 | 12.32 | 11.46 |
| MgO | 1.94 | 1.06 | 1.79 | 1.09 | 1.29 |
| CaO | 11.66 | 14.69 | 11.25 | 13.95 | 12.94 |
| $La_2O_3$ | 11.76 | 8.88 | 11.20 | 8.20 | 10.31 |
| $Ce_2O_3$ | 11.75 | 8.21 | 10.08 | 8.32 | 8.97 |
| $Nd_2O_3$ | - | - | 2.06 | - | - |
| Total | 100.00 | 99.99 | 98.44 | 96.77 | 96.66 |
| Formula based on: | | 12.5 oxygens | | | |
| Si | 3.05 | 3.12 | 2.88 | 2.87 | 2.90 |
| Al | 1.90 | 2.10 | 1.87 | 2.01 | 1.90 |
| $Fe^{2+}$ | 0.94 | 0.79 | 0.92 | 0.89 | 0.84 |
| Mg | 0.27 | 0.14 | 0.24 | 0.14 | 0.17 |
| Ca | 1.15 | 1.37 | 1.08 | 1.29 | 1.21 |
| La | 0.40 | 0.28 | 0.37 | 0.26 | 0.33 |
| Ce | 0.40 | 0.26 | 0.33 | 0.26 | 0.29 |
| Nd | - | - | 0.07 | - | - |
| Total | 8.10 | 8.06 | 7.76 | 7.73 | 7.63 |
| #Mg | 0.22 | 0.15 | 0.21 | 0.14 | 0.17 |
| La/(La+Ce) | 0.50 | 0.52 | 0.53 | 0.50 | 0.54 |
| Name | allanite | allanite-(La) | allanite-(La) | allanite | allanite-(La) |

Table 19. Xenotime.

| Sample | ALZ180076A-22 | | VNA001A |
|---|---|---|---|
| Analysis | XEN-01 | XEN-02 | XEN-03 |
| $Y_2O_3$ | 59.38 | 57.84 | 47.58 |
| $Gd_2O_3$ | 6.96 | 2.33 | 2.60 |
| $Dy_2O_3$ | 3.47 | 6.15 | 5.14 |
| $Er_2O_3$ | 5.83 | 5.72 | 3.77 |
| $Yb_2O_3$ | 5.11 | 3.60 | 0.00 |
| $UO_2$ | 0.00 | 0.00 | 0.91 |
| $P_2O_5$ | 42.51 | 41.48 | 34.53 |
| Total | 123.26 | 117.12 | 94.54 |
| Formula based on: | | 4 oxygens | |
| Y | 0.84 | 0.84 | 0.93 |
| Gd | 0.06 | 0.02 | 0.03 |
| Dy | 0.03 | 0.05 | 0.06 |
| Er | 0.05 | 0.05 | 0.04 |
| Yb | 0.04 | 0.03 | 0.00 |
| U | 0.00 | 0.00 | 0.01 |
| P | 0.95 | 0.96 | 1.08 |
| Total | 1.97 | 1.95 | 2.15 |
| Name | xenotime-(Y) | xenotime-(Y) | xenotime-(Y) |

Table 20. Magnetite.

| Sample | ALZ190034A-1 | | ALZ190037A-1 | | | |
|---|---|---|---|---|---|---|
| Analysis | MG-01 | MG-02 | MG-03 | MG-04 | MG-05 | MG-06 |
| $SIO_2$ | 3.89 | 7.19 | 0.00 | 0.00 | 0.00 | 0.00 |
| $AL_2O_3$ | 6.78 | 3.97 | 2.10 | 0.00 | 0.00 | 0.00 |
| FeO | 26.99 | 27.00 | 30.40 | 30.54 | 30.67 | 30.91 |
| $Fe_2O_3$ | 59.98 | 60.01 | 67.57 | 67.88 | 68.16 | 68.70 |
| Total | 97.64 | 98.16 | 100.06 | 98.42 | 98.82 | 99.61 |
| Formula based on: | | 4 oxygens | | | | |
| Si | 0.30 | 0.18 | 0.10 | 0.00 | 0.00 | 0.00 |
| Al | 0.15 | 0.27 | 0.00 | 0.00 | 0.00 | 0.00 |
| $Fe^{2+}$ | 0.85 | 0.85 | 1.00 | 1.06 | 1.05 | 1.04 |
| $Fe^{3+}$ | 1.70 | 1.69 | 2.00 | 2.12 | 2.10 | 2.09 |
| Total | 2.99 | 2.98 | 3.09 | 3.17 | 3.15 | 3.13 |
| Name | magnetite | magnetite | magnetite | magnetite | magnetite | magnetite |

# Appendix 5- Drill-cores

Drill core mineralization, alteration and stratigraphic representation. BH8903 (A, B and C), BH9002 (D and E), BH9003 (F and G) and BH9004 (H and I).

## A.

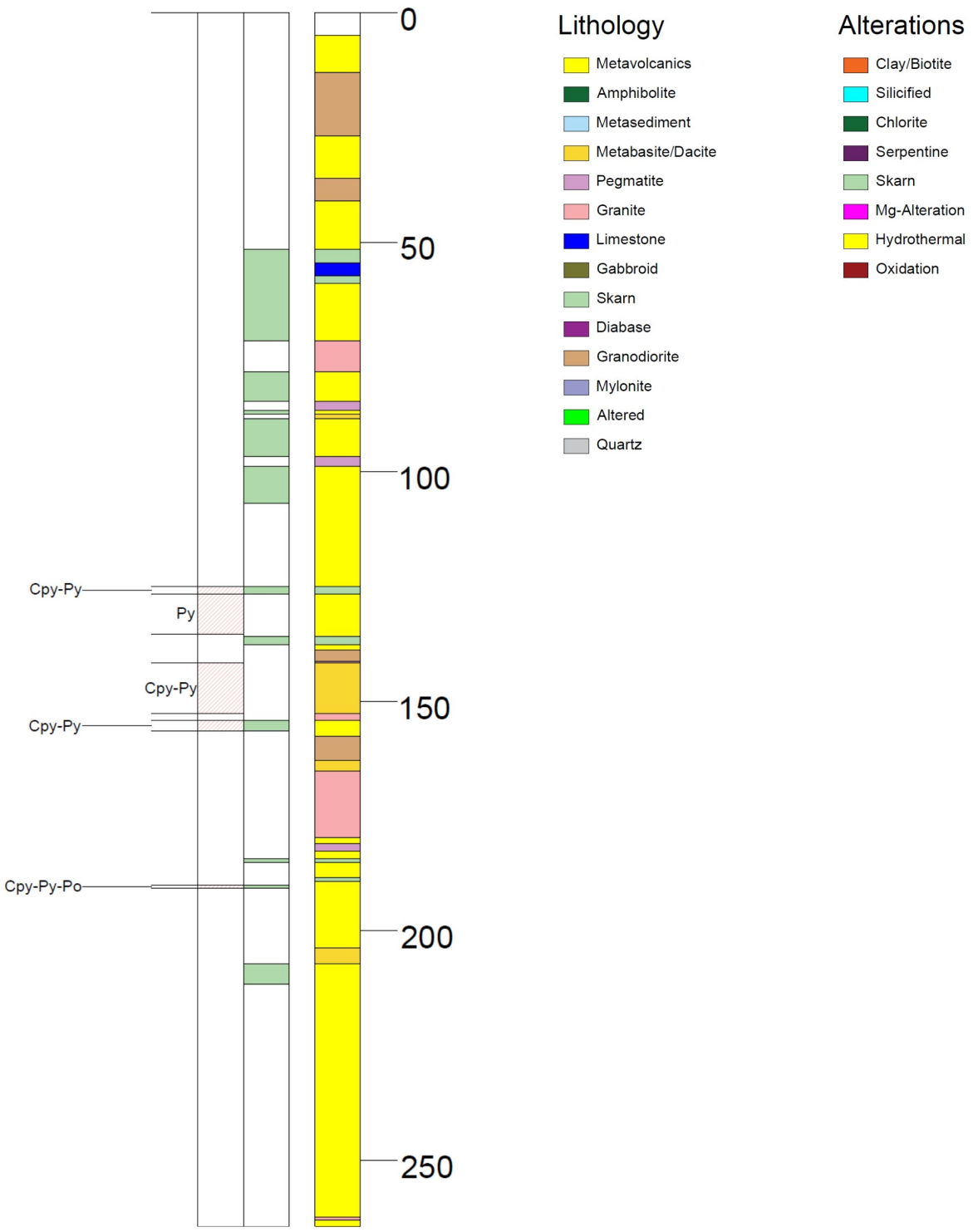

**B.**

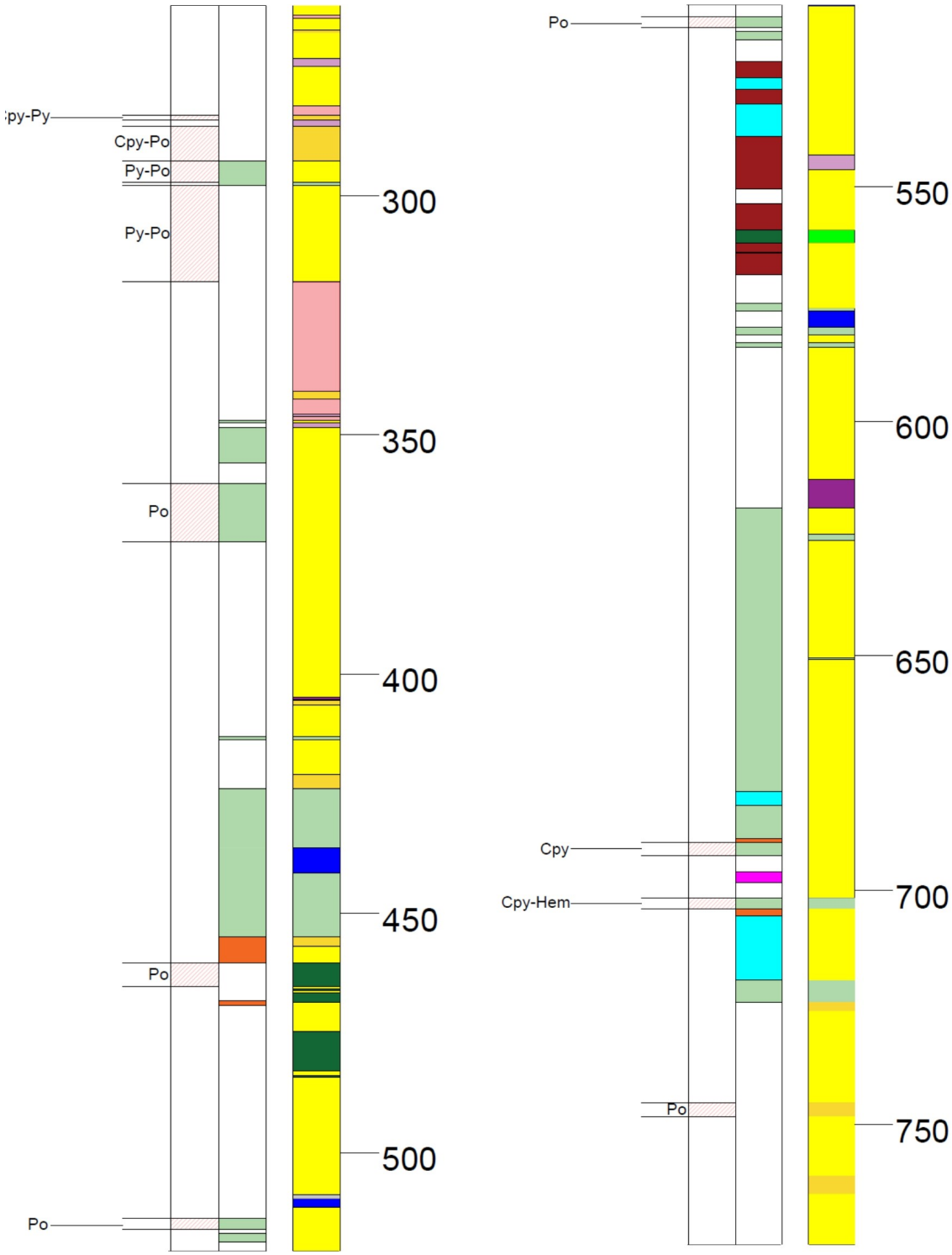
Cpy-Py
Cpy-Po
Py-Po
Py-Po
Po
Po
Po
300
350
400
450
500
Po
Cpy
Cpy-Hem
Po
550
600
650
700
750

**C.**

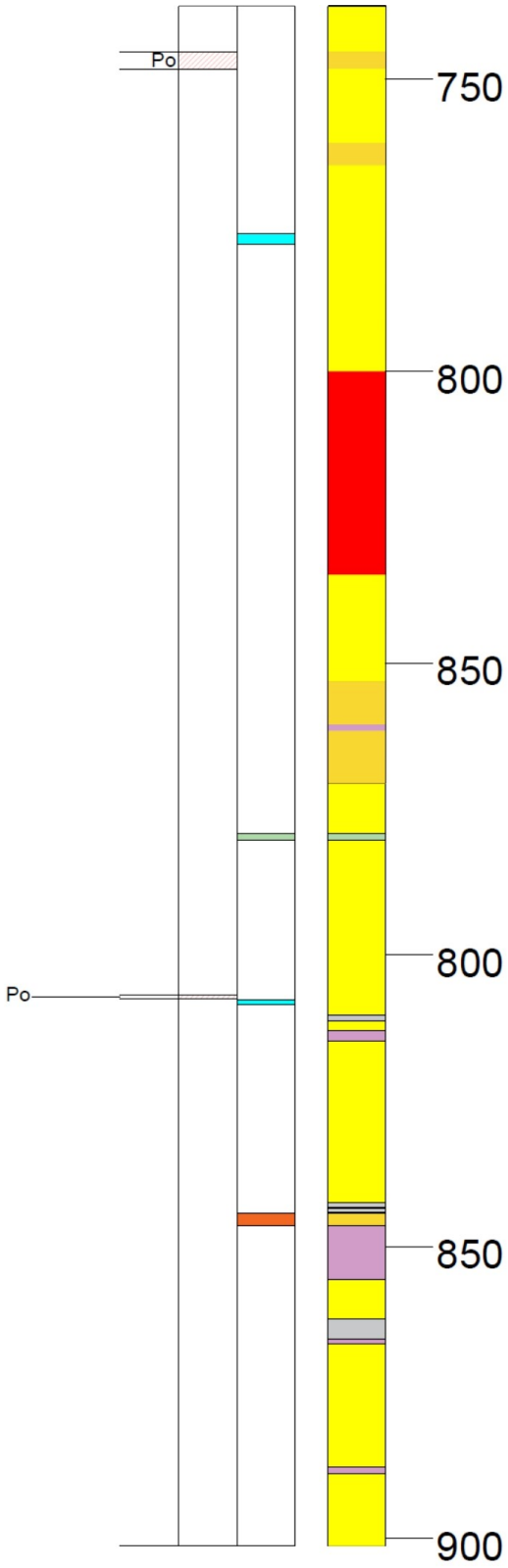

**D.**

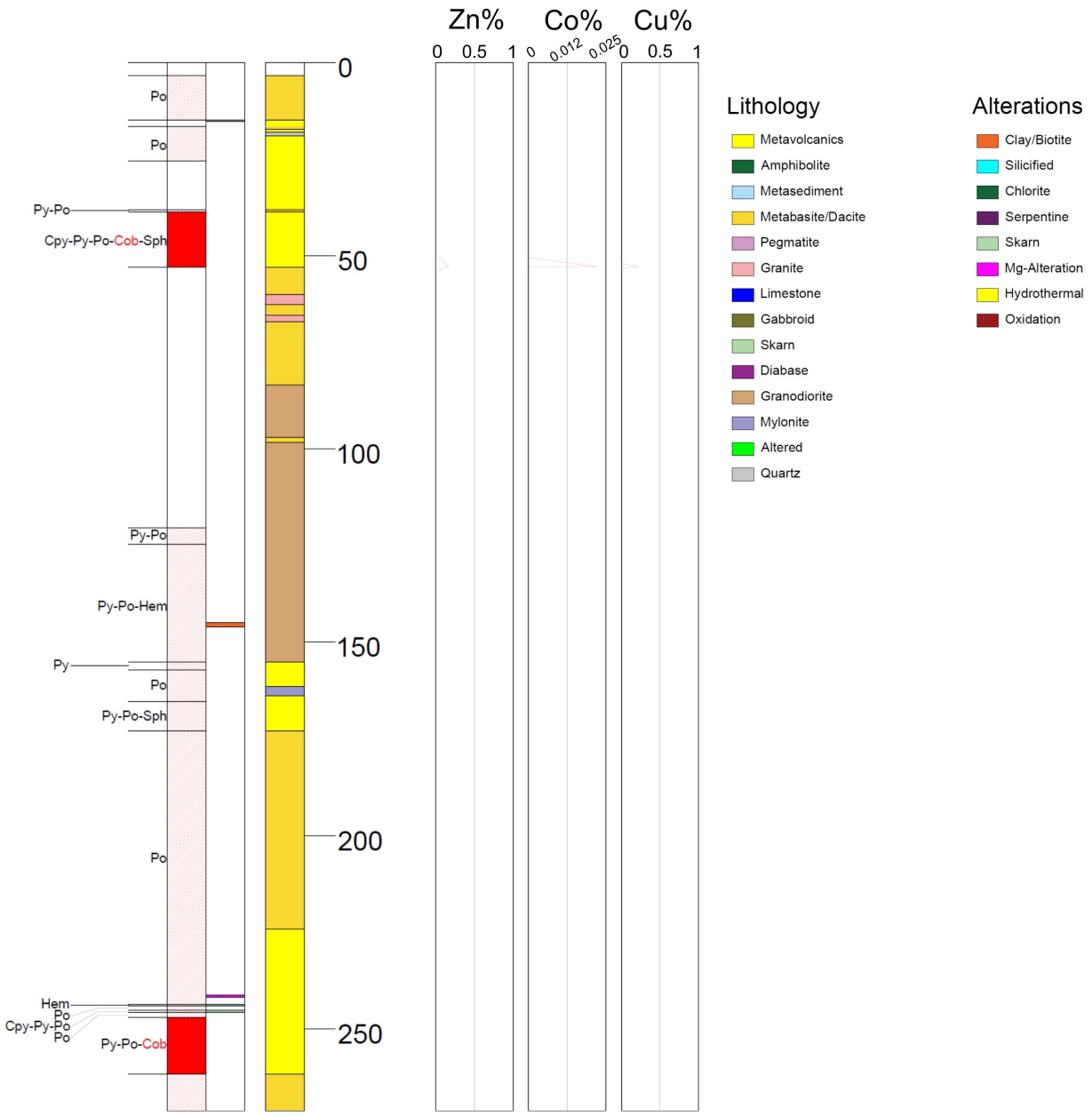
Zn%
Co%
Cu%
0 0.5 1
0 0.012 0.025
0 0.5 1
0
50
100
150
200
250
Po
Po
Py-Po
Cpy-Py-Po-Cob-Sph
Py-Po
Py-Po-Hem
Py
Po
Py-Po-Sph
Po
Hem
Po
Cpy-Py-Po
Po
Py-Po-Cob
Lithology
Metavolcanics
Amphibolite
Metasediment
Metabasite/Dacite
Pegmatite
Granite
Limestone
Gabbroid
Skarn
Diabase
Granodiorite
Mylonite
Altered
Quartz
Alterations
Clay/Biotite
Silicified
Chlorite
Serpentine
Skarn
Mg-Alteration
Hydrothermal
Oxidation

**E.**

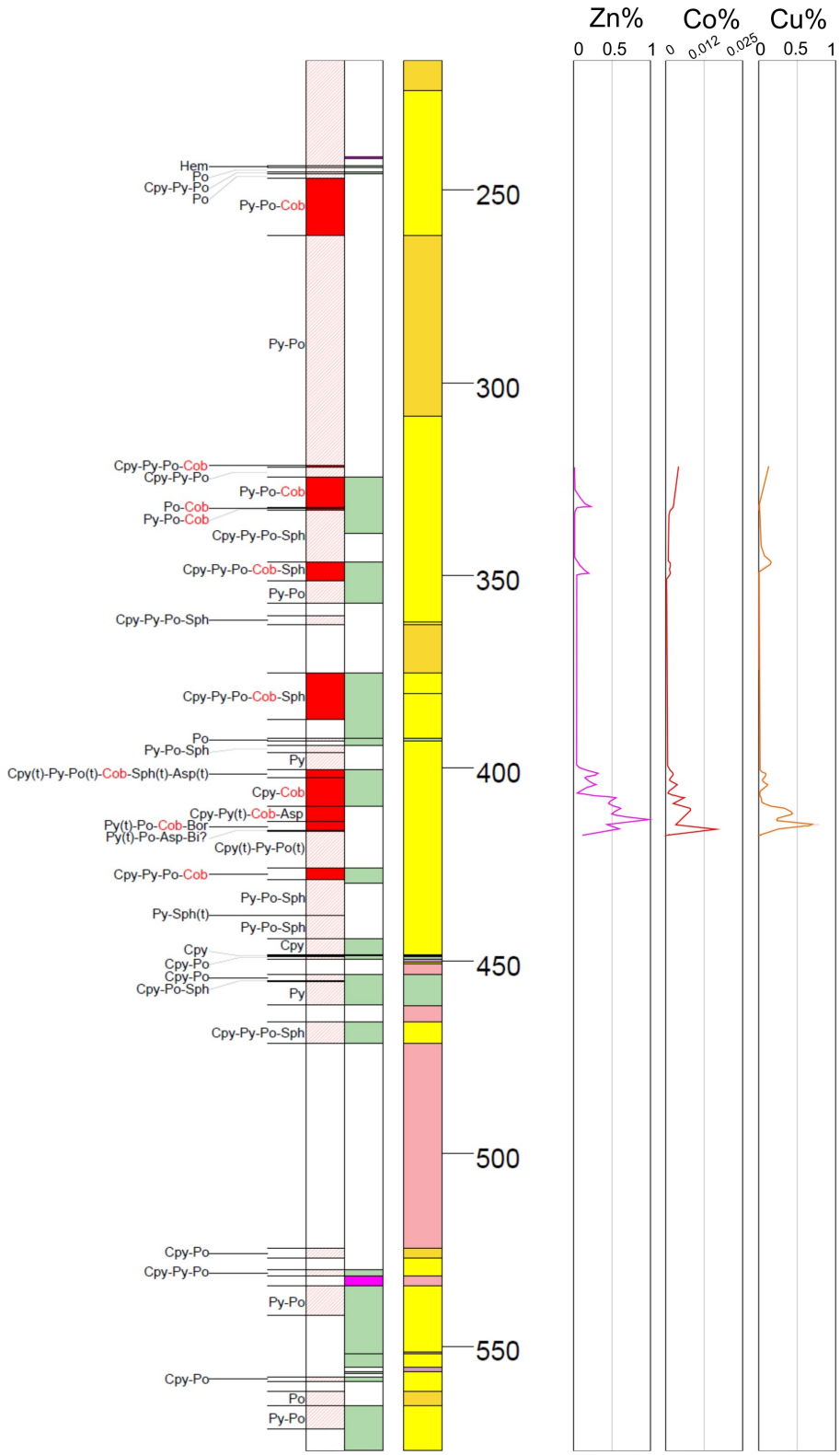
Zn%
Co%
Cu%
0
0.5
1
0
0.012
0.025
0
0.5
1
Hem
Po
Cpy-Py-Po
Po
Py-Po-Cob
Py-Po
Cpy-Py-Po-Cob
Cpy-Py-Po
Py-Po-Cob
Po-Cob
Py-Po-Cob
Cpy-Py-Po-Sph
Cpy-Py-Po-Cob-Sph
Py-Po
Cpy-Py-Po-Sph
Cpy-Py-Po-Cob-Sph
Po
Py-Po-Sph
Py
Cpy(t)-Py-Po(t)-Cob-Sph(t)-Asp(t)
Cpy-Cob
Cpy-Py(t)-Cob-Asp
Py(t)-Po-Cob-Bor
Py(t)-Po-Asp-Bi?
Cpy(t)-Py-Po(t)
Cpy-Py-Po-Cob
Py-Po-Sph
Py-Sph(t)
Py-Po-Sph
Cpy
Cpy
Cpy-Po
Cpy-Po
Cpy-Po-Sph
Py
Cpy-Py-Po-Sph
Cpy-Po
Cpy-Py-Po
Py-Po
Cpy-Po
Po
Py-Po
250
300
350
400
450
500
550

**F.**

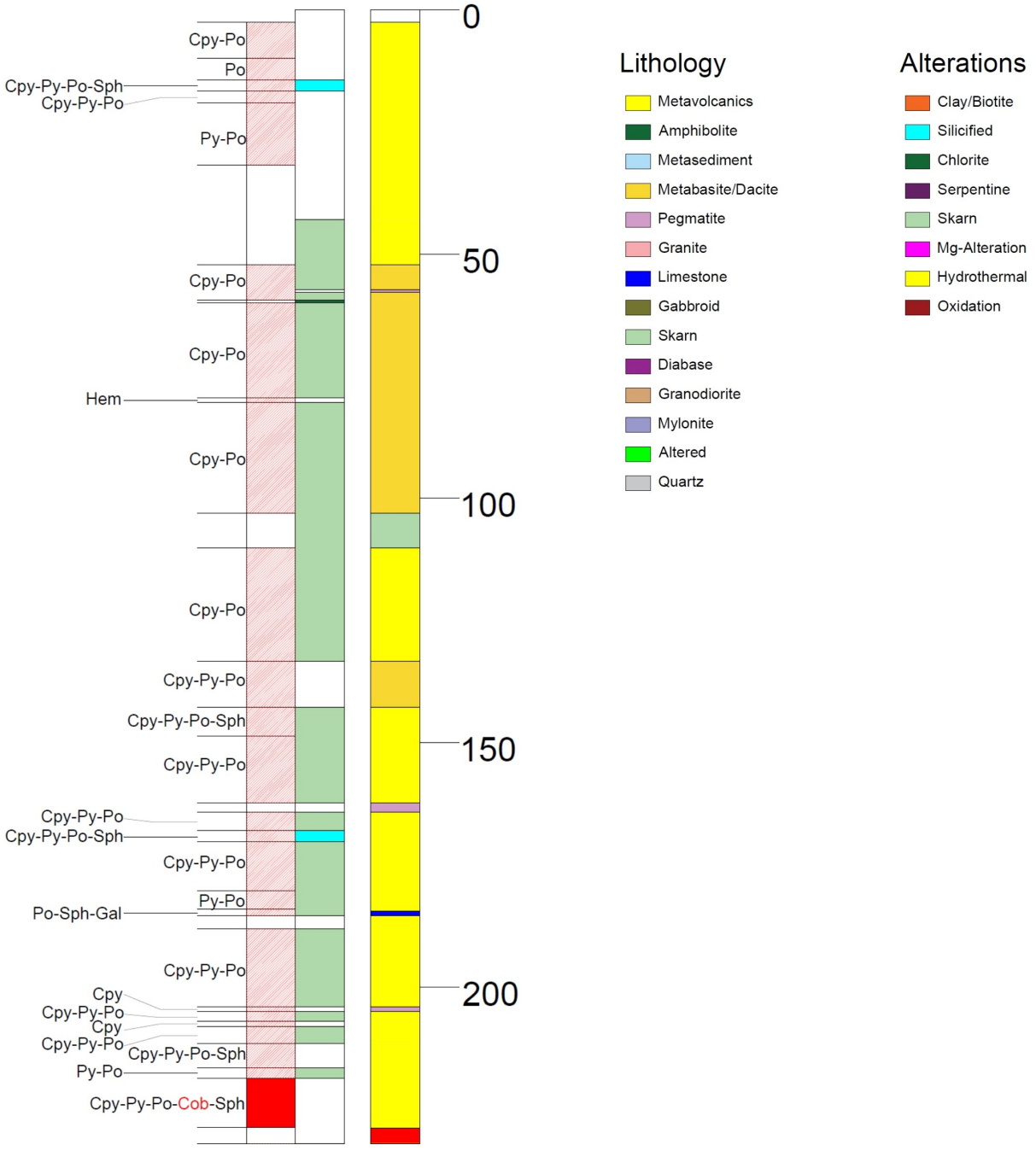
Cpy-Po
Po
Cpy-Py-Po-Sph
Cpy-Py-Po
Py-Po
Cpy-Po
Cpy-Po
Hem
Cpy-Po
Cpy-Po
Cpy-Py-Po
Cpy-Py-Po-Sph
Cpy-Py-Po
Cpy-Py-Po
Cpy-Py-Po-Sph
Cpy-Py-Po
Po-Sph-Gal
Py-Po
Cpy-Py-Po
Cpy
Cpy-Py-Po
Cpy
Cpy-Py-Po
Cpy-Py-Po-Sph
Py-Po
Cpy-Py-Po-Cob-Sph
0
50
100
150
200
Lithology
Metavolcanics
Amphibolite
Metasediment
Metabasite/Dacite
Pegmatite
Granite
Limestone
Gabbroid
Skarn
Diabase
Granodiorite
Mylonite
Altered
Quartz
Alterations
Clay/Biotite
Silicified
Chlorite
Serpentine
Skarn
Mg-Alteration
Hydrothermal
Oxidation

**G.**

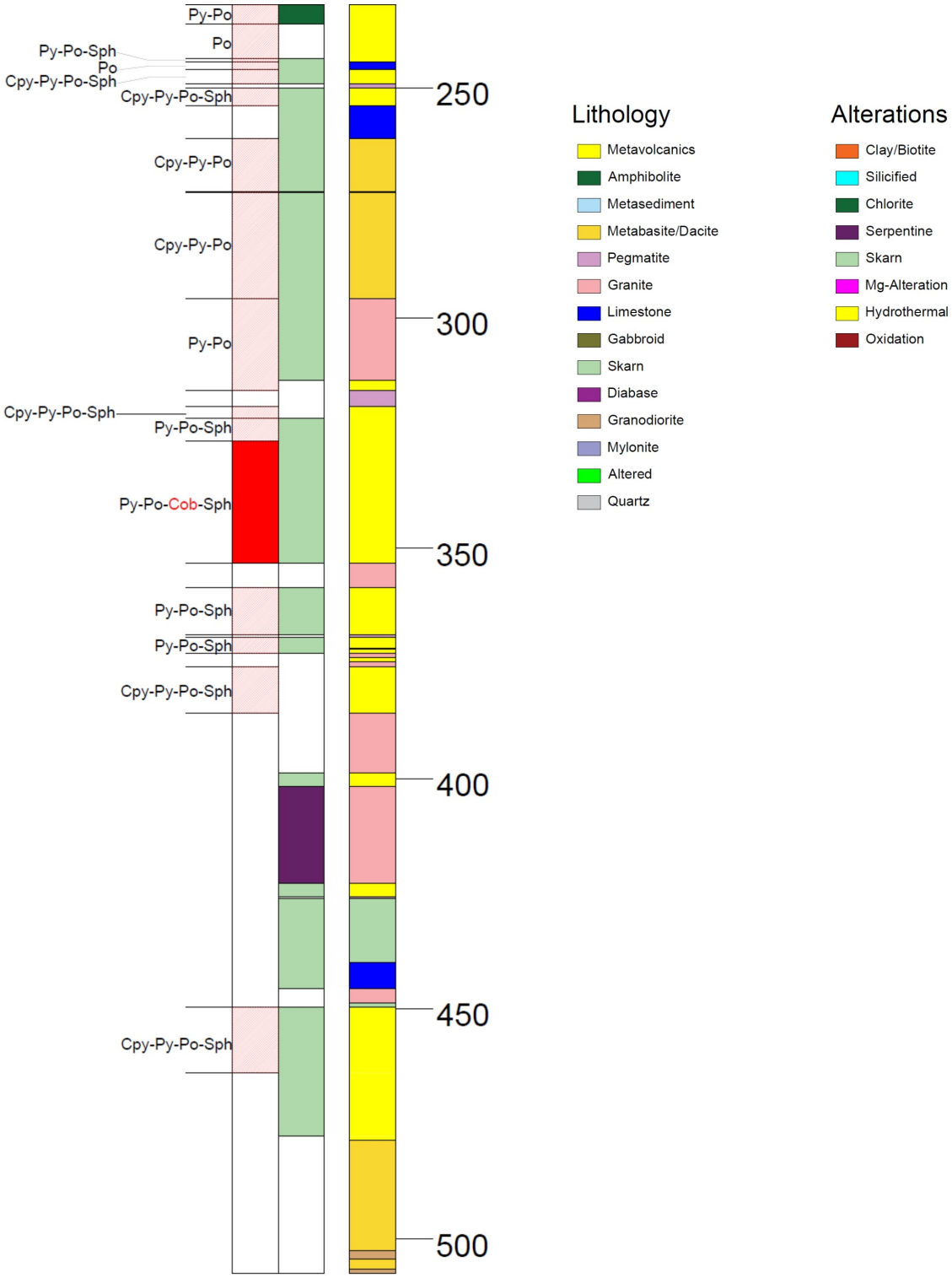
Py-Po
Py-Po-Sph
Po
Po
Cpy-Py-Po-Sph
Cpy-Py-Po-Sph
Cpy-Py-Po
Cpy-Py-Po
Py-Po
Cpy-Py-Po-Sph
Py-Po-Sph
Py-Po-Cob-Sph
Py-Po-Sph
Py-Po-Sph
Cpy-Py-Po-Sph
Cpy-Py-Po-Sph
250
300
350
400
450
500
Lithology
Metavolcanics
Amphibolite
Metasediment
Metabasite/Dacite
Pegmatite
Granite
Limestone
Gabbroid
Skarn
Diabase
Granodiorite
Mylonite
Altered
Quartz
Alterations
Clay/Biotite
Silicified
Chlorite
Serpentine
Skarn
Mg-Alteration
Hydrothermal
Oxidation

**H.**

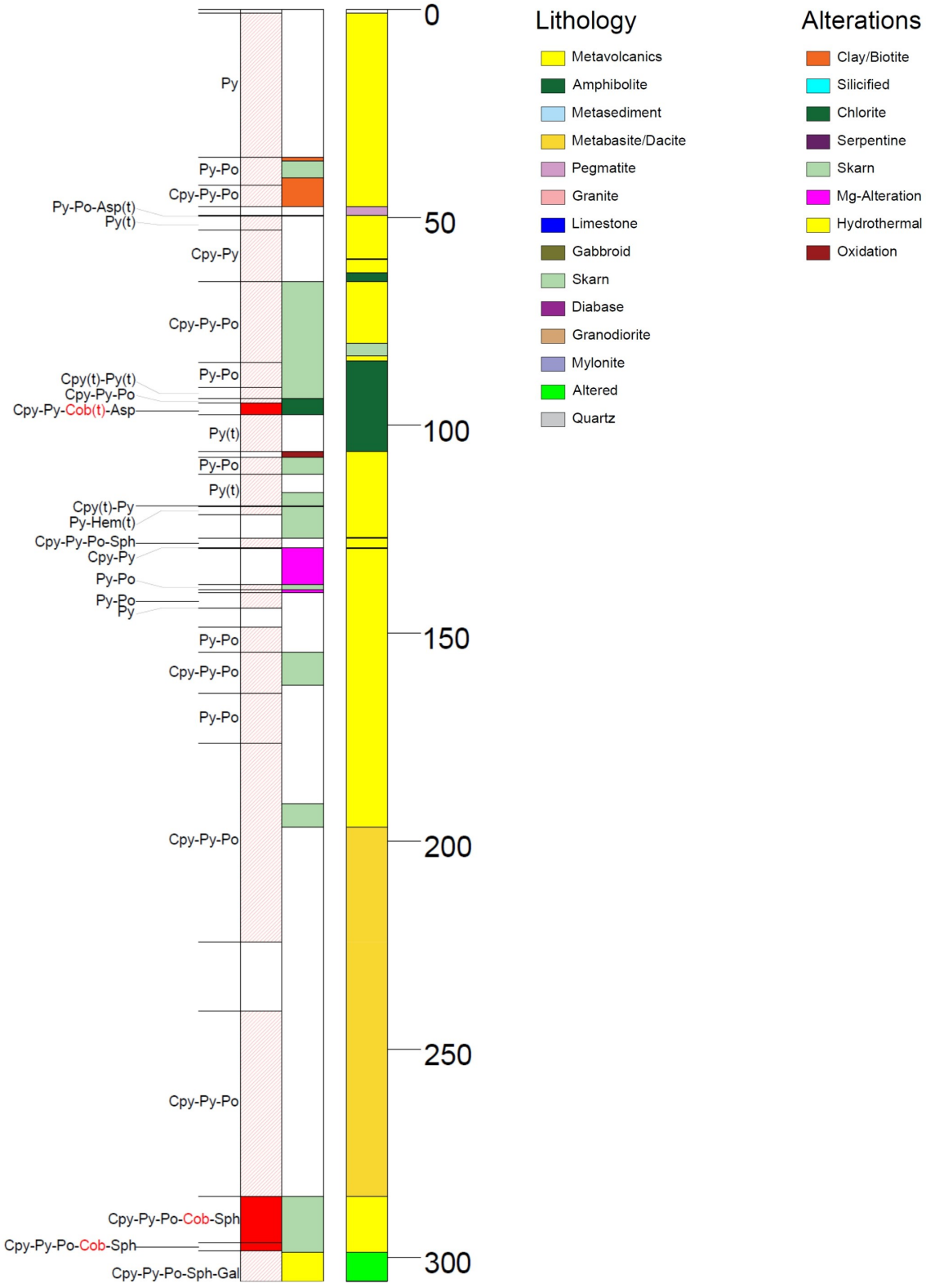
Py
Py-Po
Cpy-Py-Po
Py-Po-Asp(t)
Py(t)
Cpy-Py
Cpy-Py-Po
Py-Po
Cpy(t)-Py(t)
Cpy-Py-Po
Cpy-Py-Cob(t)-Asp
Py(t)
Py-Po
Py(t)
Cpy(t)-Py
Py-Hem(t)
Cpy-Py-Po-Sph
Cpy-Py
Py-Po
Py-Po
Py
Py-Po
Cpy-Py-Po
Py-Po
Cpy-Py-Po
Cpy-Py-Po
Cpy-Py-Po-Cob-Sph
Cpy-Py-Po-Cob-Sph
Cpy-Py-Po-Sph-Gal
0
50
100
150
200
250
300
Lithology
Metavolcanics
Amphibolite
Metasediment
Metabasite/Dacite
Pegmatite
Granite
Limestone
Gabbroid
Skarn
Diabase
Granodiorite
Mylonite
Altered
Quartz
Alterations
Clay/Biotite
Silicified
Chlorite
Serpentine
Skarn
Mg-Alteration
Hydrothermal
Oxidation

**I.**

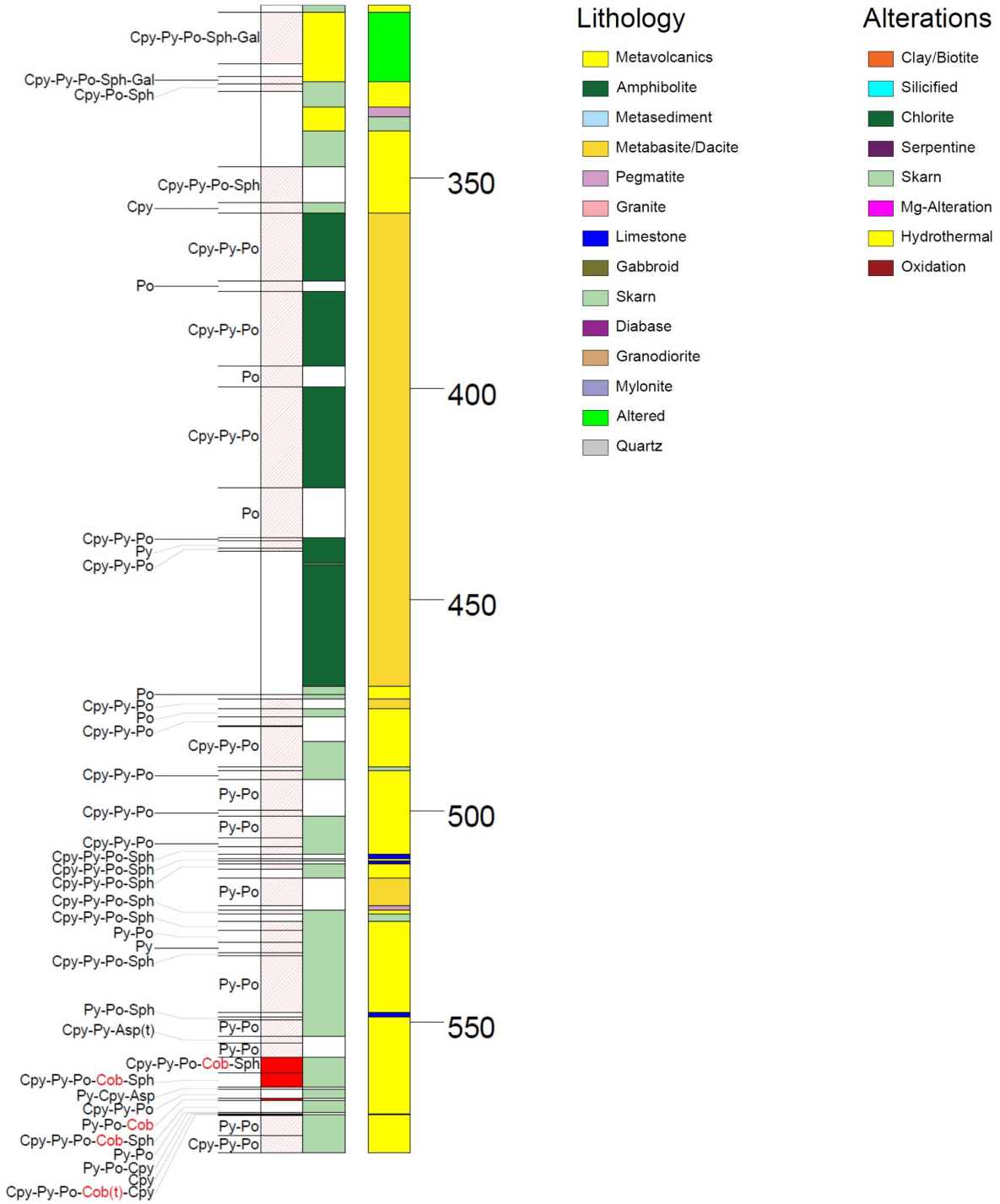
Cpy-Py-Po-Sph-Gal
Cpy-Py-Po-Sph-Gal
Cpy-Po-Sph
Cpy-Py-Po-Sph
Cpy
Cpy-Py-Po
Po
Cpy-Py-Po
Po
Cpy-Py-Po
Po
Cpy-Py-Po
Py
Cpy-Py-Po
Po
Cpy-Py-Po
Po
Cpy-Py-Po
Cpy-Py-Po
Cpy-Py-Po
Py-Po
Cpy-Py-Po
Py-Po
Cpy-Py-Po
Cpy-Py-Po-Sph
Cpy-Py-Po-Sph
Cpy-Py-Po-Sph
Py-Po
Cpy-Py-Po-Sph
Cpy-Py-Po-Sph
Py-Po
Py
Cpy-Py-Po-Sph
Py-Po
Py-Po-Sph
Cpy-Py-Asp(t)
Py-Po
Py-Po
Cpy-Py-Po-Cob-Sph
Cpy-Py-Po-Cob-Sph
Py-Cpy-Asp
Cpy-Py-Po
Py-Po-Cob
Cpy-Py-Po-Cob-Sph
Py-Po
Py-Po-Cpy
Cpy
Cpy-Py-Po-Cob(t)-Cpy
Py-Po
Cpy-Py-Po
350
400
450
500
550
Lithology
Metavolcanics
Amphibolite
Metasediment
Metabasite/Dacite
Pegmatite
Granite
Limestone
Gabbroid
Skarn
Diabase
Granodiorite
Mylonite
Altered
Quartz
Alterations
Clay/Biotite
Silicified
Chlorite
Serpentine
Skarn
Mg-Alteration
Hydrothermal
Oxidation

## Tidigare skrifter i serien ”Examensarbeten i Geologi vid Lunds universitet”:

528. Jansson, Robin, 2018: Multidisciplinary perspective on a natural attenuation zone in a PCE contaminated aquifer. (45 hp)
529. Larsson, Alfred, 2018: Rb-Sr sphalerite data and implications for the source and timing of Pb-Zn deposits at the Caledonian margin in Sweden. (45 hp)
530. Balija, Fisnik, 2018: Stratigraphy and pyrite geochemistry of the Lower–Upper Ordovician in the Lerhamn and Fågelsång -3 drill cores, Scania, Sweden. (45 hp)
531. Höglund, Nikolas, 2018: Groundwater chemistry evaluation and a GIS-based approach for determining groundwater potential in Mörbylånga, Sweden. (45 hp)
532. Haag, Vendela, 2018: Studie av mikrostrukturer i karbonatslagkäglor från nedslagsstrukturen Charlevoix, Kanada. (15 hp)
533. Hebrard, Benoit, 2018: Antropocen – vad, när och hur? (15 hp)
534. Jancsak, Nathalie, 2018: Åtgärder mot kusterosion i Skåne, samt en fallstudie av erosionsskydden i Löderup, Ystad kommun. (15 hp)
535. Zachén, Gabriel, 2018: Mesosideriter – redogörelse av bildningsprocesser samt SEM-analys av Vaca Muertameteoriten. (15 hp)
536. Fägersten, Andreas, 2018: Lateral variability in the quantification of calcareous nannofossils in the Upper Triassic, Austria. (15 hp)
537. Hjertman, Anna, 2018: Förutsättningar för djupinfiltration av ytvatten från Ivösjön till Kristianstadbassängen. (15 hp)
538. Lagerstam, Clarence, 2018: Varför svalde svanödlor (Reptilia, Plesiosauria) stenar? (15 hp)
539. Pilser, Hannes, 2018: Mg/Ca i bottenlevande foraminiferer, särskilt med avseende på temperaturer nära 0°C. (15 hp)
540. Christiansen, Emma, 2018: Mikroplast på och i havsbotten - Utbredningen av mikroplaster i marina bottensediment och dess påverkan på marina miljöer. (15 hp)
541. Staahlnacke, Simon, 2018: En sammanställning av norra Skånes prekambriska berggrund. (15 hp)
542. Martell, Josefin, 2018: Shock metamorphic features in zircon grains from the Mien impact structure - clues to conditions during impact. (45 hp)
543. Chitindingu, Tawonga, 2018: Petrological characterization of the Cambrian sandstone reservoirs in the Baltic Basin, Sweden. (45 hp)
544. Chonewicz, Julia, 2018: Dimensionerande vattenförbrukning och alternativa vattenkvaliteter. (15 hp)
545. Adeen, Lina, 2018: Hur lämpliga är de geofysiska metoderna resistivitet och IP för kartläggning av PFOS? (15 hp)
546. Nilsson Brunlid, Anette, 2018: Impact of southern Baltic sea-level changes on landscape development in the Verkeån River valley at Haväng, southern Sweden, during the early and mid Holocene. (45 hp)
547. Perälä, Jesper, 2018: Dynamic Recrystallization in the Sveconorwegian Frontal Wedge, Småland, southern Sweden. (45 hp)
548. Artursson, Christopher, 2018: Stratigraphy, sedimentology and geophysical assessment of the early Silurian Halla and Klinteberg formations, Altajme core, Gotland, Sweden. (45 hp)
549. Kempengren, Henrik, 2018: Att välja den mest hållbara efterbehandlingsmetoden vid sanering: Applicering av beslutsstödsverktyget SAMLA. (45 hp)
550. Andreasson, Dagnija, 2018: Assessment of using liquidity index for the approximation of undrained shear strength of clay tills in Scania. (45 hp)
551. Ahrenstedt, Viktor, 2018: The Neoproterozoic Visingsö Group of southern Sweden: Lithology, sequence stratigraphy and provenance of the Middle Formation. (45 hp)
552. Berglund, Marie, 2018: Basaltkuppen - ett spel om mineralogi och petrologi. (15 hp)
553. Hernnäs, Tove, 2018: Garnet amphibolite in the internal Eastern Segment, Sveconorwegian Province: monitors of metamorphic recrystallization at high temperature and pressure during Sveconorwegian orogeny. (45 hp)
554. Halling, Jenny, 2019: Characterization of black rust in reinforced concrete structures: analyses of field samples from southern Sweden. (45 hp)
555. Stevic, Marijana, 2019: Stratigraphy and dating of a lake sediment record from Lyngsjön, eastern Scania - human impact and aeolian sand deposition during the last millennium. (45 hp)
556. Rabanser, Monika, 2019: Processes of Lateral Moraine Formation at a Debris-covered Glacier, Suldenferner (Vedretta di Solda), Italy. (45 hp)
557. Nilsson, Hanna, 2019: Records of environmental change and sedimentation processes over the last century in a Baltic coastal inlet. (45 hp)
558. Ingered, Mimmi, 2019: Zircon U-Pb con-

straints on the timing of Sveconorwegian migmatite formation in the Western and Median Segments of the Idefjorden terrane, SW Sweden. (45 hp)

559. Hjorth, Ingeborg, 2019: Paleomagnetisk undersökning av vulkanen Rangitoto, Nya Zeeland, för att bestämma dess utbrottshistoria. (15 hp)
560. Westberg, Märta, 2019: Enigmatic worm-like fossils from the Silurian Waukesha Lagerstätte, Wisconsin, USA. (15 hp)
561. Björn, Julia, 2019: Undersökning av påverkan på hydraulisk konduktivitet i förorenat område efter in situ-saneringsförsök. (15 hp)
562. Faraj, Haider, 2019: Tolkning av georadarprofiler över grundvattenmagasinet Verveln - Gullringen i Kalmar län. (15 hp)
563. Bjermo, Tim, 2019: Eoliska avlagringar och vindriktningar under holocen i och kring Store Mosse, södra Sverige. (15 hp)
564. Langkjaer, Henrik, 2019: Analys av Östergötlands kommande grundvattenresurser ur ett klimtperspektiv - med fokus på förstärkt grundvattenbildning. (15 hp)
565. Johansson, Marcus, 2019: Hur öppet var landskapet i södra Sverige under Atlantisk tid? (15 hp)
566. Molin, Emmy, 2019: Litologi, sedimentologi och kolisotopstratigrafi över krita–paleogen-gränsintervallet i borrningen Limhamn-2018. (15 hp)
567. Schroeder, Mimmi, 2019: The history of European hemp cultivation. (15 hp)
568. Damber, Maja, 2019: Granens invandring i sydvästa Sverige, belyst genom pollenanalys från Skottenesjön. (15 hp)
569. Lundgren Sassner, Lykke, 2019: Strandmorfologi, stranderosion och stranddeposition, med en fallstudie på Tylösand sandstrand, Halland. (15 hp)
570. Greiff, Johannes, 2019: Mesozoiska konglomerat och Skånes tektoniska utveckling. (15 hp)
571. Persson, Eric, 2019: An Enigmatic Cerapodian Dentary from the Cretaceous of southern Sweden. (15 hp)
572. Aldenius, Erik, 2019: Subsurface characterization of the Lund Sandstone – 3D model of the sandstone reservoir and evaluation of the geoenergy storage potential, SW Skåne, South Sweden. (45 hp)
573. Juliusson, Oscar, 2019: Impacts of subglacial processes on underlying bedrock. (15 hp)
574. Sartell, Anna, 2019: Metamorphic paragenesis and P-T conditions in garnet amphibolite from the Median Segment of the Idefjorden Terrane, Lilla Edet. (15 hp)
575. Végvári, Fanni, 2019: Vulkanisk inverkan på klimatet och atmorsfärcirkulationen: En litterarurstudie som jämför vulkanism på låg respektive hög latitud. (15 hp)
576. Gustafsson, Jon, 2019: Petrology of platinum-group element mineralization in the Koillismaa intrusion, Finland. (45 hp)
577. Wahlquist, Per, 2019: Undersökning av mindre förkastningar för vattenuttag i sedimentärt berg kring Kingelstad och Tjutebro. (15 hp)
578. Gaitan Valencia, Camilo Esteban, 2019: Unravelling the timing and distribution of Paleoproterozoic dyke swarms in the eastern Kaapvaal Craton, South Africa. (45 hp)
579. Eggert, David, 2019: Using Very-Low-Frequency Electromagnetics (VLF-EM) for geophysical exploration at the Albertine Graben, Uganda - A new CAD approach for 3D data blending. (45 hp)
580. Plan, Anders, 2020: Resolving temporal links between the Högberget granite and the Wigström tungsten skarn deposit in Bergslagen (Sweden) using trace elements and U-Pb LA-ICPMS on complex zircons. (45 hp)
581. Pilser, Hannes, 2020: A geophysical survey in the Chocaya Basin in the central Valley of Cochabamba, Bolivia, using ERT and TEM. (45 hp)
582. Leopardi, Dino, 2020: Temporal and genetical constraints of the Cu-Co Vena-Dampetorp deposit, Bergslagen, Sweden. (45 hp)

LUNDS UNIVERSITET

**Geologiska institutionen**
**Lunds universitet**
**Sölvegatan 12, 223 62 Lund**